

A Thesis Submitted for the Degree of PhD at the University of Warwick

Permanent WRAP URL:

<http://wrap.warwick.ac.uk/164640>

Copyright and reuse:

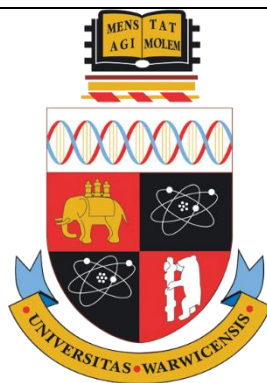
This thesis is made available online and is protected by original copyright.

Please scroll down to view the document itself.

Please refer to the repository record for this item for information to help you to cite it.

Our policy information is available from the repository home page.

For more information, please contact the WRAP Team at: wrap@warwick.ac.uk



Studying Humid Creep Inhibitors of Gypsum Plaster with Electrochemical and Analytical Techniques

by

Tom Scott

Thesis

Submitted to the University of Warwick
for the degree of
Doctor of Philosophy

Supervisors: Prof. Patrick R. Unwin and Prof. Richard I. Walton

Department of Chemistry

January 2020

Contents

List of Figures	v
List of Tables	viii
Abbreviations	ix
Acknowledgements	xi
Declaration	xii
Abstract	xiii
1 Introduction	1
1.1 Gypsum	1
1.1.1 Gypsum Applications	1
1.2 Humid Creep	4
1.3 Gypsum Humid Creep Additives	8
1.4 Crystal Growth and Dissolution Reactions	17
1.5 Crystal Growth Theory	19
1.5.1 Nucleation	19
1.5.2 Crystal Growth	21
1.5.3 Crystal Dissolution Theory	22
1.6 Scanning Probe Microscopy	23
1.6.1 SICM and Nanoprecipitation	24
1.6.2 SECCM	28
1.7 Analytical Techniques	30
1.7.1 Surface Area Measurements	30
1.7.2 Confocal Fluorescence Microscopy	31
1.7.3 Finite Element Method (FEM) Modelling	32
1.7.4 Raman Spectroscopy	33
1.8 Thesis Aims	34
1.9 References	36
2 Studying Plaster Humid Creep Inhibitors via Droplet Evaporation – Nucleation of Gypsum Due to the Coffee-Ring Effect	49
2.1 Abstract	49
2.2 Introduction	50
2.3 Materials and Methods	52
2.3.1 Solutions	52
2.3.2 Video Setup	52
2.3.3 Mass Measurement Setup	53
2.3.4 FEM Simulations	54
2.3.5 Scanning Electron Microscopy (SEM)	55
2.3.6 Raman Spectroscopy	55
2.4 Results and Discussion	57
2.4.1 Evaporation of a Calcium Sulfate Solution Droplet	57
2.4.2 FEM Simulations of the Coffee-Ring Effect	59

2.4.3	Mass Measurements	62
2.4.4	Contact Angle Measurement Studies	63
2.4.5	SEM Study	66
2.5	Conclusions	72
2.6	References	73
3	Utilizing SICM Nanoprecipitation for Studying Dissolution and Crystallisation Kinetics of Gypsum with Humid Creep Inhibitor Incorporation	74
3.1	Abstract	74
3.2	Introduction	75
3.3	Materials and Methods	76
3.3.1	Solutions	76
3.3.2	Nanoprecipitation Setup	76
3.3.3	Data Analysis	77
3.3.4	FEM Simulations	78
3.3.5	Scanning Electron Microscopy (SEM)	79
3.3.6	Raman Spectroscopy	79
3.3.7	Transmission Electron Microscopy (TEM)	80
3.4	Results and Discussion	81
3.4.1	FEM Simulations and Initial Blocking of the Nanopipette ..	81
3.4.2	In-Situ Raman Spectroscopy	87
3.4.3	Cycling Nanoprecipitation and Dissolution	89
3.5	Nanoprecipitation of HKUST-1	94
3.5.1	Introduction	94
3.6	Materials and Methods	99
3.6.1	Solutions	99
3.6.2	Experimental Setup	99
3.6.3	FEM Simulations	101
3.7	Results and Discussion	103
3.7.1	Nanoprecipitation of HKUST-1 with Different Copper Precursors	103
3.7.2	HKUST-1 Seeds as a Precursor	106
3.7.3	HKUST-1 Formation from Copper Acetate	110
3.8	Conclusions	112
3.9	References	115
4	Studying the Wetting of Gypsum Plaster and Common Humid Creep Inhibitors via SECCM	119
4.1	Abstract	119
4.2	Introduction	120
4.3	Materials and Methods	122
4.3.1	Solutions and Sample Preparation	122
4.3.2	SECCM Setup	122
4.3.3	BET Theory	124
4.3.4	Video Analysis	124
4.3.5	Scanning Electron Microscopy (SEM)	124
4.3.6	Atomic Force Microscopy (AFM)	125

4.4 Results and Discussion	126
4.4.1 SEM and Creation of Samples	126
4.4.2 Wetting, SECCM and BET	127
4.4.3 Changing Humidity	130
4.4.4 Wetting with Micropipettes	133
4.5 Conclusions	140
4.6 References	141
5 Fluorescein as a Potential Plaster Humid Creep Additive	142
5.1 Abstract	142
5.2 Introduction	143
5.3 Materials and Methods	146
5.3.1 Solutions	146
5.3.2 Tests for Water Demand, Set Time with Additives	146
5.3.3 Fluorescence Microscopy	148
5.3.4 Sag Testing	148
5.4 Results and Discussion	150
5.4.1 Fluorescence Microscopy	150
5.4.2 The Viability of Fluorescein in Industry	151
5.4.3 Droplet Evaporation Experiment and SEM	152
5.4.4 Sag Testing	152
5.5 Conclusions	155
5.6 References	156
6 Conclusions and Outlook	158
7 Appendix	162

List of Figures

Figure 1.1. Crystal structure of gypsum	2
Figure 1.2. Crystal structure of the (010) face	2
Figure 1.3. SEM image of plaster	4
Figure 1.4. Crystal structure of α and β bassanite polymorphs	5
Figure 1.5. SEM images of gypsum crystals in the presence of acid	5
Figure 1.6. Plasterboard sag schematic	6
Figure 1.7. Sketch of pressure solution creep between gypsum crystals	7
Figure 1.8. Water absorption isotherm of plaster	8
Figure 1.9. Chemical structure of STMP	8
Figure 1.10. The stand-up conformation of tartaric acid on the (010) surface of gypsum	10
Figure 1.11. Average surface flux comparison of additives on gypsum	11
Figure 1.12. Dissolution rate constant comparison of the (010) gypsum face under additive effects	13
Figure 1.13. Dissolution rate constant comparison of the (010) gypsum face with different STMP concentrations	14
Figure 1.14. SEM images of gypsum made from different calcium sulfate hemihydrate precursors	16
Figure 1.15. Creep velocity as a function of gypsum solubility	17
Figure 1.16. Gibbs free energy diagrams for crystal nucleation and temperature dependence of the critical radius	20
Figure 1.17. Schematic of the crystallisation pathways under thermodynamic and kinetic control	21
Figure 1.18. Example of a dissolution etch pit	23
Figure 1.19. SICM schematic	25
Figure 1.20. SEM and TEM images of nanopipettes	27
Figure 1.21. SECCM schematic	29
Figure 2.1. Schematic of flow inside an evaporating droplet	50
Figure 2.2. Droplet evaporation experiment schematic	53
Figure 2.3. Schematic of FEM simulation of a droplet evaporating	55
Figure 2.4. Snapshots of an evaporating droplet taken from underneath	57
Figure 2.5. Raman spectra of gypsum with additives	58
Figure 2.6. Time to average first optically visible crystallisation of gypsum	59
Figure 2.7. FEM simulations of an evaporating droplet looking at flow and supersaturation of gypsum	61
Figure 2.8. The mass of an evaporating droplet over time	63
Figure 2.9. Average contact angle of evaporating calcium sulfate droplets on clean glass	64
Figure 2.10. Average contact angle of evaporating calcium sulfate droplets on the (010) gypsum plane	65
Figure 2.11. SEM image of an evaporated calcium sulfate droplet	67
Figure 2.12. SEM comparisons of gypsum crystals with different additives incorporated	68
Figure 2.13. SEM comparisons of evaporated droplets with no additive, STMP and SHMP	68
Figure 2.14. Snapshots of a droplet containing calcium sulfate with citric acid evaporating	69

Figure 2.15. SEM image of an evaporated droplet containing calcium sulfate and gallic acid	70
Figure 2.16. SEM images of unusual crystal formations formed from various calcium sulfate droplets evaporating	70
Figure 3.1. SICM setup for nanoprecipitation of gypsum	77
Figure 3.2. FEM simulation of nanoprecipitation	81
Figure 3.3. Simulated maximum calcium sulfate saturations at different applied potentials in nanoprecipitation	82
Figure 3.4. First blocking transients of a nanopipette after applying 10 V	83
Figure 3.5. Further examples of first blocking transients	83
Figure 3.6. Average time to complete gypsum blocking in nanoprecipitation	87
Figure 3.7. Experimental setup of nanoprecipitation under a Raman beam	88
Figure 3.8. Raman spectra taken during a nanoprecipitation experiment	88
Figure 3.9. Example of how the current changes during blocking and unblocking in nanoprecipitation	90
Figure 3.10. Example of a full set of blocking/unblocking transients	90
Figure 3.11. Average crystallisation and dissolution times of gypsum inside a nanopipette	92
Figure 3.12. The structure of HKUST-1	95
Figure 3.13. Reaction schematic for creating HKUST-1	97
Figure 3.14. SICM setup for nanoprecipitation of HKUST-1	100
Figure 3.15. FEM simulation setup for nanoprecipitation	101
Figure 3.16. Example of a blocking transient of HKUST-1 when copper nitrate is the precursor	103
Figure 3.17. Example of a blocking transient of HKUST-1 when copper acetate is the precursor	104
Figure 3.18. Example of a blocking transient of HKUST-1 when copper acetate is the precursor from $t=0$	105
Figure 3.19. FEM simulation data of the current drop expected depending on the size of the nanoparticle passing through seen in Figure 3.16	105
Figure 3.20. Particle sizing calculated from the data shown in Figure 3.16	106
Figure 3.21. Comparison of solutions of HKUST-1 made with and without pre-seeding	107
Figure 3.22. Raman spectra of HKUST-1.....	108
Figure 3.23. SEM images of HKUST-1	109
Figure 3.24. SEM images of HKUST-1 at higher magnification	109
Figure 3.25. Optical image of a HKUST-1 formation inside a nanopipette	110
Figure 3.26. Raman spectra of HKUST-1 formed inside a nanopipette	111
Figure 4.1. Radius of a droplet base against time	121
Figure 4.2. Schematic of the wetting area under a droplet inside a dry porous substrate.....	121
Figure 4.3. SECCM setup for wetting study	123
Figure 4.4. SEM and AFM images of plaster before and after grinding	127
Figure 4.5. Optical images of plaster before and after wetting	129
Figure 4.6. Wetting radii of different plaster samples at 50% humidity with a 50 nm pipette	130
Figure 4.7. Wetting radii of plaster at differing humidities with a 50 nm pipette ..	131
Figure 4.8. Average wetting radii of plaster samples at 97% humidity with a 50 nm pipette	132

Figure 4.9. Average wetting radii of plaster samples at 50% humidity with a 50 nm pipette	133
Figure 4.10. Average wetting radii of plaster samples at 97% humidity with a 50 μ m pipette	134
Figure 4.11. Average wetting radii of plaster samples at 50% humidity with a 50 μ m pipette	135
Figure 4.12. Images of silicone oil incorporated plaster before and after the droplet is contacted	136
Figure 4.13. Surface area of plaster samples measured by BET.....	137
Figure 5.1. Chemical structure of fluorescein	143
Figure 5.2. Schematic of setup for viscosity of gypsum slurry	146
Figure 5.3. Schematic of setup for testing set time of plaster	147
Figure 5.4. Schematic of sag testing setup	148
Figure 5.5. Fluorescence microscopy images of gypsum containing fluorescein formed from droplet evaporation	150
Figure 5.6. SEM images of evaporated droplets of gypsum with and without fluorescein	153
Figure 5.7. The magnitude of sag of plasterboards made with fluorescein and tartaric acid compared with pure plaster	154

List of Tables

Table 1.1. Structure of synthetic polycarboxylates used as additives in Reference 50 of Chapter 1	16
Table 3.1. Distribution of initial blocking transient shapes after application of 10 V to the nanopipette in a nanoprecipitation experiment	84
Table 5.1. Comparison of some properties of plaster setting with and without fluorescein as an additive	151

Abbreviations

2D	Two-Dimensional
AC	Alternating Current
AFM	Atomic Force Microscopy
BCF	Burton-Cabrera-Frank
BET	Brunauer-Emmett-Teller
BTC	Benzene-1,3,5-tricarboxylate
CFC	Channel Flow Cell
CLSM	Confocal Laser Scanning Microscopy
CNT	Classical Nucleation Theory
DC	Direct Current
DMSO	Dimethyl Sulfoxide
FEM	Finite Element Method
FTIR	Fourier-Transform Infrared
ICP-OES	Inductively Coupled Plasma-Optical Emission Spectroscopy
KSV	Kossel-Stranksi-Volmer
LED	Light Emitting Diode
MOF	Metal-Organic Framework
PAM	Polyacrylamide
PC	Polycarboxylate
PEG	Polyethylene Glycol
PVA	Polyvinyl Alcohol
QRCE	Quasi-Reference Counter Electrode

SDS	Sodium Dodecyl Sulfate
SECCM	Scanning Electrochemical Cell Microscopy
SECM	Scanning Electrochemical Microscopy
SEM	Scanning Electron Microscopy
SEPM	Scanning Electrochemical Probe Microscopy
SHMP	Sodium Hexametaphosphate
SICM	Scanning Ion Conductance Microscopy
SPM	Scanning Probe Microscopy
STM	Scanning Tunnelling Microscopy
STMP	Sodium Trimetaphosphate
TEM	Transmission Electron Microscopy
TMA	Trimesic Acid
UME	Ultramicroelectrode
UV	Ultra-Violet
VCVA	Vinyl Chloride-Vinyl Acetate
XRD	X-Ray Diffraction
α -H	α -Hemihydrate
β -H	β -Hemihydrate

Acknowledgements

First and foremost, I would like to thank my supervisors Prof. Patrick R. Unwin and Prof. Richard I. Walton for their extensive guidance and encouragement throughout these years of my studies, and for always pushing me to do my best. I would also like to thank Saint-Gobain Gypsum for funding this project, and in particular Dr. Kane Ironside and Dr. Robin Fisher who have both been tremendous help in guiding the project and giving an industrial perspective.

I would also like to thank the Warwick Electrochemistry and Interfaces Group for always being so friendly and helpful, in particular the Crystal Crew for sitting through my endless presentations on gypsum. I must also personally thank Dr. Ashley Page for all the help writing the custom MATLAB script for my wetting studies, and for keeping me sane with the occasional lunchtime pool match and/or pint. Many thanks to Dr. David Perry who performed the majority of the FEM simulations for me and has been a constant source of ideas and solutions. I would also like to thank Peter Morris, who studied under me and did all the experimental work for the nanoprecipitation study of HKUST-1.

Finally thank you to my friends and family, especially Sarah for keeping me sane and constantly pushing me forward when I was struggling, your love has kept me positive throughout the last five years even when you glaze over when I start talking about my experiments. Thank you also to Ian, who saved my hard drive when it broke halfway through writing my thesis. Thank you to my Warwick chemistry friends who always make me laugh and always understood when I complained about experiments not working properly.

Declaration

The work presented in this thesis is entirely original and my own work, except for the following collaborations: finite element simulations carried out in Chapters 3 and 4 were performed by Dr. David Perry, and most of the experimental work on the nanoprecipitation of HKUST-1 in Chapter 4 was performed by Peter Morris. Set-time experiments performed at Saint Gobain in Chapter 6 were performed by Dr. Robin Fisher, and sag tests were performed at the R&D centre in Saint Gobain Research Shanghai.

I confirm that this thesis has not been submitted for a degree at another university.

Abstract

This thesis is concerned with the humid creep mechanism of gypsum plaster, and how additives inhibit this effect. The crystallisation and dissolution of gypsum are studied under these additive effects in a collaborative project sponsored by Saint-Gobain Gypsum.

Multiple approaches are taken to understand the additive effects, studying the crystallisation, dissolution and wetting of gypsum. The crystal behaviour was studied through a simple droplet evaporation experiment, with the formed crystals studied by SEM. Nanoprecipitation was employed using a SICM setup which allows the study of the very early stages of nucleation as well as the dissolution of gypsum, allowing for repeat experiments and good statistical analysis of the crystallisation and dissolution. To study plaster wetting, a SECCM setup was utilised to allow controlled application of water droplets to a plaster surface, and the wetting analysed through a video setup coupled with advanced image software and custom-made programmes. Analytical methods are employed throughout, including Raman spectroscopy, powder X-ray diffraction and BET theory to characterise gypsum and its porosity. These studies led to the investigation of new potential anti-sag additives, which yielded the untested fluorescein. Its effect on the sag of gypsum plaster is explored and the potential uses as a unique tag in plaster explained, with fluorescence microscopy utilised to show how additives are incorporated in gypsum.

To demonstrate the effectiveness of the nanoprecipitation technique further, crystallisation of the MOF HKUST-1 was performed. The unique advantages of nanoprecipitation give new proof to the proposed literature mechanism of HKUST-1, which depends on the copper precursor used as a reagent. Finite element method simulations were employed alongside both nanoprecipitation setups in order to quantify the supersaturation of gypsum and HKUST-1 respectively.

Chapter 1: Introduction

1.1 Gypsum

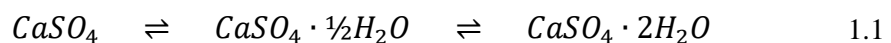
Gypsum is the most hydrated form of crystallised calcium sulfate ($\text{CaSO}_4 \cdot 2\text{H}_2\text{O}$) and can be commonly found in large quantities underground.¹ The first people to deduce the crystal structure of gypsum were Atoji and Rundle, with Cole and Lancucki refining the structure using X-ray diffraction data.^{2,3} Gypsum has a monoclinic structure (space group $C2/c$) and exhibits repeating layers of Ca^{2+} and SO_4^{2-} units perpendicular to the b axis.⁴ Its lattice parameters are $a = 5.679 \text{ \AA}$, $b = 15.202 \text{ \AA}$, $c = 6.522 \text{ \AA}$, with $\alpha = \gamma = 90^\circ$ and $\beta = 118.43^\circ$. Ca^{2+} ions are sandwiched between two SO_4^{2-} layers in such a way that each SO_4^{2-} ion is tetrahedrally bound to four Ca^{2+} ions (Figure 1.1).^{4,5} The SO_4^{2-} planes are linked together by weak H-bonds that originate from the H_2O molecules held between the Ca^{2+} and SO_4^{2-} layers. This arrangement allows for easy perfect cleavage of the (010) faces, leaving the surface comprising of a single CaSO_4 bilayer (Figure 1.2).³

1.1.1 Gypsum Applications

Gypsum is a heavily studied material due to its use in many industries such as architecture, as a fertilizer and even as a food additive for its high calcium content.⁶ It is the most abundant sulfate material found in the Earth's crust,⁷ although it is being increasingly synthesised due to its availability as a by-product from power plants, where excess sulfur dioxide is created from the burning of fossil fuels in the flue gas desulfurisation process.⁸ However with the demand for cleaner methods of generating energy and the reduction of fossil fuel use, mined gypsum is the primary natural source.⁹ Its main commercial use is as plasterboard for ceilings and walls in buildings;

it has been around for centuries, with examples dating back as far as Ancient Egypt.¹⁰ Gypsum has many attractive properties in architecture such as the ease of application, fire resistance and its favourable processing conditions, with only relatively mild temperatures needed.¹¹ The universal demand for gypsum is huge with ~260 million metric tonnes being mined worldwide in 2017.¹²

For production of gypsum in architecture (plasterboard), gypsum is exposed to a calcination process, which involves the gypsum being exposed to elevated temperatures for prolonged periods.¹³ This process removes the majority of the water from the crystal structure, leaving calcium sulfate hemihydrate ($\text{CaSO}_4 \cdot \frac{1}{2}\text{H}_2\text{O}$) or bassanite (not to be confused with basanite, the igneous volcanic rock), more commonly referred to as ‘stucco’.^{14,15} This calcination is necessary for the production of gypsum materials as bassanite can be hydrated to form gypsum in moulds, going from a powder to a solid crystalline matrix that has mechanical strength.¹⁶ Further heating of bassanite leads to complete dehydration of the crystal leaving just calcium sulfate (CaSO_4), also known as anhydrite.^{17,18} The dehydration of gypsum leading to these phase transitions is detrimental to the mechanical properties of plaster so processing of gypsum plaster is never higher than 45 °C; the temperature required for phase transition to bassanite. These processes are illustrated in Equation 1.1:



Gypsum plasterboard is made by the simple re-hydration of bassanite which forms a matrix of interlocking, polycrystalline, needle shaped gypsum crystals, shown in Figure 1.3.¹⁹ The mass ratio of water to calcium hemihydrate necessary to complete a hydration reaction is 18.6 %, ²⁰ with an excess of water introducing porosity into the structure. The porosity in gypsum is microporous, while the bassanite it originates

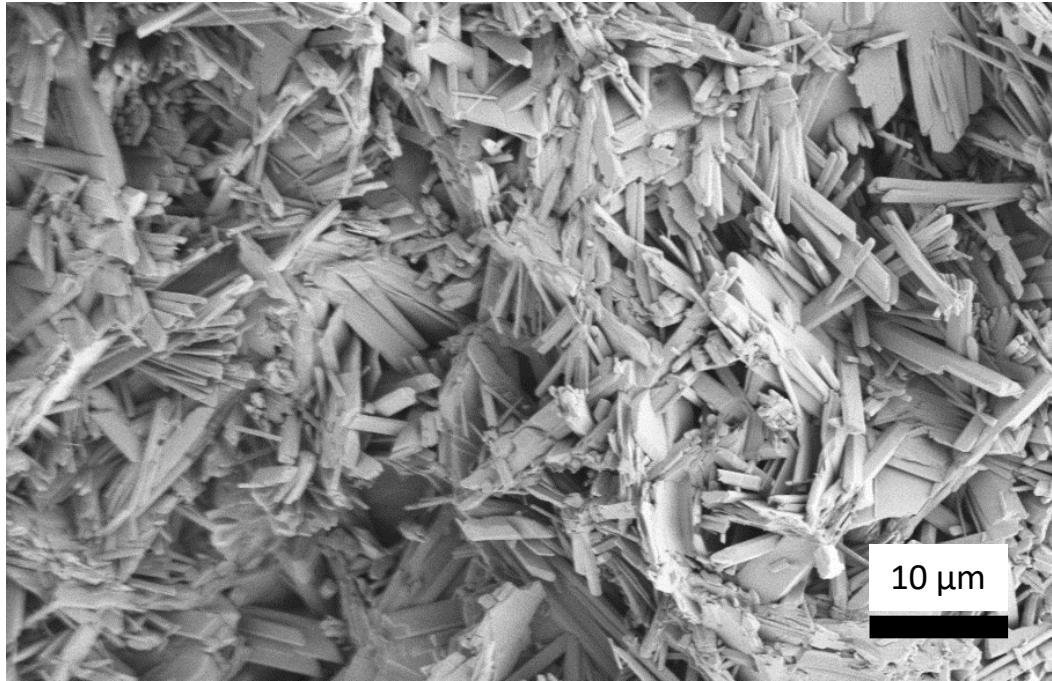


Figure 1.3: SEM image of gypsum plaster created from the hydration of calcium sulfate hemihydrate and heated at 40 °C overnight.

from is nanoporous, with water molecules filling the nanopores in bassanite (Figure 1.4).⁵ The crystal morphology of gypsum can be modified in different ways, for example in the presence of strong acid to form thick elongated plates (Figure 1.5).¹⁹

1.2 Humid Creep

One of the major issues with gypsum for building use is its poor water resistance; in the presence of water and applied stress the gypsum can deflect or ‘creep’, a process that has been suggested to be responsible for the instability of old gypsum mines.²² The phenomenon is also apparent in industrial plasterboard; in high humidity countries (humidity ≥ 90 %) plasterboard will absorb water vapour from the air, leading to a reduction in aesthetic and mechanical properties in a process called “humid creep” or “sag” (Figure 1.6). The mechanism behind this phenomenon has been extensively investigated, with Chappuis *et al.* proposing a model for humid creep

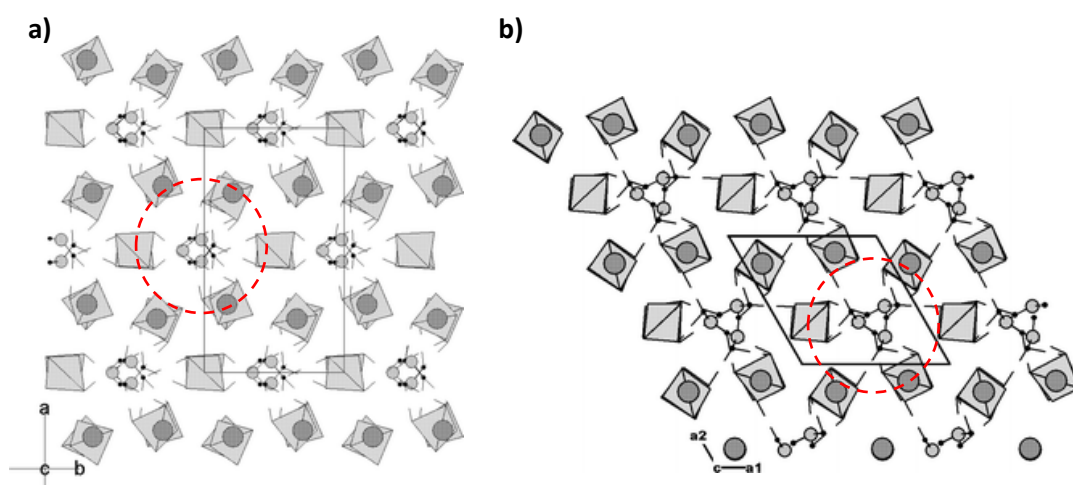


Figure 1.4: The crystal structure of a) α -bassanite and b) β -bassanite viewed along the 001 direction showing the packing of calcium ions (dark grey circles). Water molecules (oxygen = light grey circles and hydrogen = small black circles) reside in channels (red dashed circles) created by sulfate tetrahedra. The water molecules are non-identical, with the water oxygen atoms sharing slightly different spaces in the unit cell. The channel diameter in α -bassanite is ~ 5.5 Angstroms. Images taken from Christensen *et al.*²¹

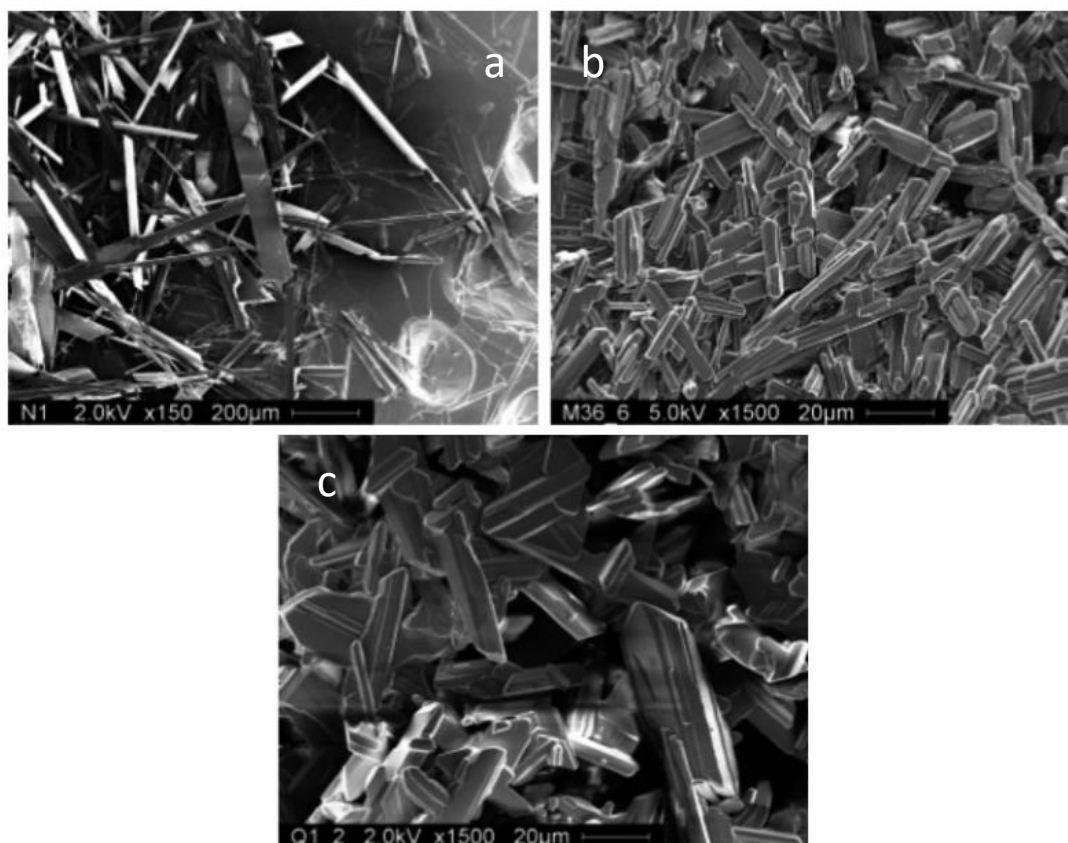


Figure 1.5: SEM images of gypsum crystals grown under different crystallisation conditions: a) in presence of 200 mM H_2SO_4 for 24 h; b) in presence of 6.4 M H_2SO_4 for 6 h; c) in presence of seed gypsum crystals and 6.29 M HCl for 2 h. Images taken from Feldmann and Demopoulos.¹⁸

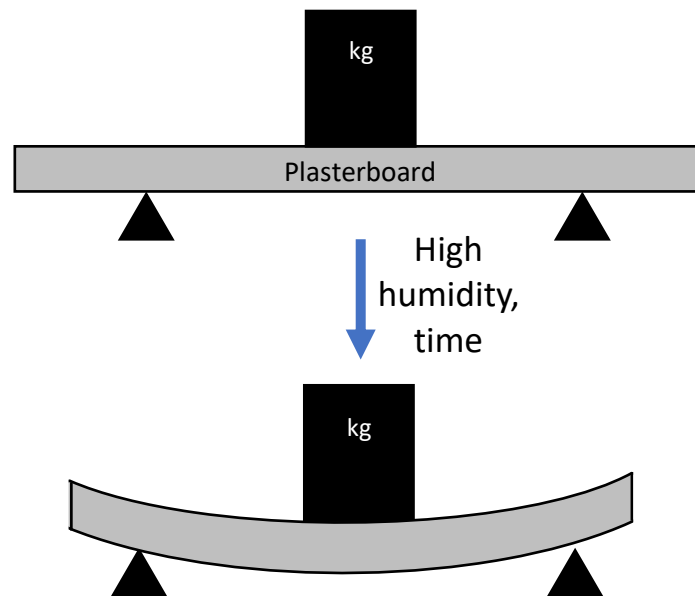


Figure 1.6: Schematic of humid creep of gypsum plasterboard due to water uptake from the atmosphere. The plasterboard deforms over time under the application of a load.

involving local dissolution and recrystallisation of gypsum at the points between interlocking crystals (Figure 1.7).²³ Chappuis suggested that the gypsum needles in plaster are not welded together by solid connections but are separated by thin liquid films of water. These water films form from the growth of the crystals, as the water brings the calcium and sulfate ions together necessary for the crystalline growth. He believed the thin water layers provide capillary forces that give the plaster its mechanical strength. Chappuis also explained how completely dry plaster (not dehydrated plaster) keeps its mechanical strength. In the absence of liquid there should be no capillary forces; however Chappuis observed very ordered packing of the water molecules in the film, in the order of 4-6 molecules thickness of the water layer. This leads to an effectively solid water layer, which constitutes a solid linker, and thus a higher adhesion force than the force obtained by the capillary forces in thin liquid films. Colombani *et al.* recently added further weight to this argument by using holographic interferometry experiments to prove that the wet creep effect of plaster is dissolution driven, but changed the description from dissolution-recrystallisation to

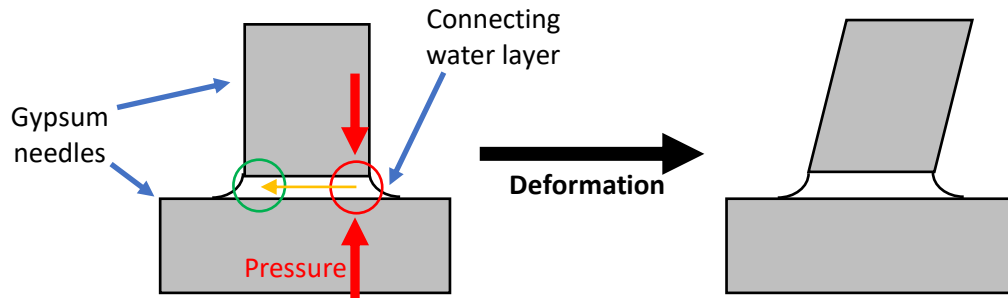


Figure 1.7: Sketch of the steps of pressure solution creep in gypsum plaster: an external load (red arrows) creates a local compression stress between two gypsum needles (red circle), which induces dissolution, diffusion of the dissolved species (yellow arrow), and recrystallisation in a non-stressed area (green circle). This sequence induces a local transfer of matter, so a macroscopic plastic strain.

pressure-solution creep.²² He suggested that the external load induces local compressive stresses between adjacent gypsum needles which leads to a change in the chemical potential of the solid. This invokes dissolution of the gypsum in the confined water layers to reduce the stress on the plaster and the resultant dissolved species diffuse through the thin water layer and precipitates in areas where there is less stress.²⁴ This process happens spontaneously at many different locations throughout the plaster, leading to the macro-level deformation of the plaster.

Badens *et al.* suggested a different mechanism in which the bonds between crystals are weakened by ingress water at grain boundaries.²⁵ They concluded that the weight increase in a high humidity environment (Figure 1.8) is due to ingress water increasing the thickness of the water layers in between grain boundaries, and the thicker water layers behave more like bulk water, thus allowing the crystals to slide over each other.²⁵ It follows from this that the humid creep effect is a combination of these ideas, where an increased humidity increases the size and volume of the water layers, leading to more dissolution within the water layers but preferentially at sites where the stress is greater to reduce the internal energy. Humid creep does not occur at low humidity as the water layer constitutes a solid linker, not allowing dissolution

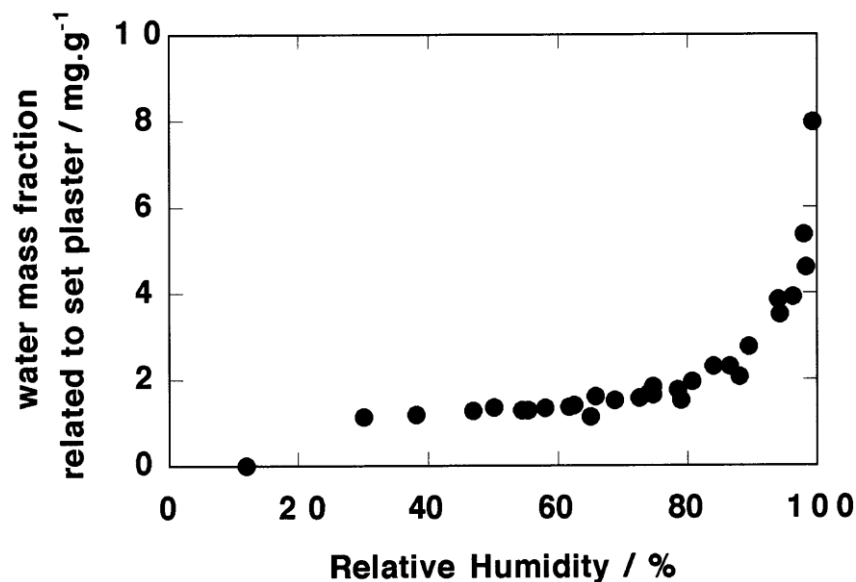


Figure 1.8: Water absorption isotherm for a sample of pure set plaster with a porosity of 57% recorded at 291 K. Image taken from Badens *et al.*²⁵ A sharp increase of water intake can be seen at 90% humidity.

or any flow of matter until the volume of the water layer is sufficiently increased so it can be thought of as a liquid again.

1.3 Gypsum Humid Creep Additives

Chemical additives such as tartaric acid,^{25,26} gallic acid,²⁷ boric acid²⁸ and sodium trimetaphosphate (STMP, Figure 1.9)²⁹ have been reported in the patent literature as a means of inhibiting the macroscopic humid creep effect. Other previous studies have shown that tartaric acid can also inhibit dissolution of other calcium minerals.³⁰ The mechanism behind the chemical additive modes of action is unclear,

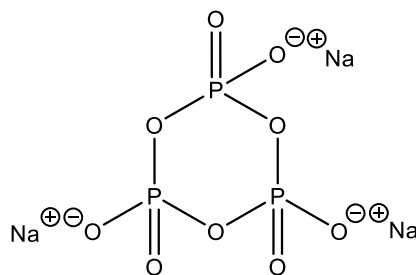


Figure 1.9: Chemical structure of STMP.

however separate studies have shown that the presence of carboxylic acid groups (*e.g.* tartaric acid) have an effect on the crystal growth rate of gypsum.^{25,31} It was discovered that the majority of the carboxylic acid group was adsorbed within the first minutes of crystallisation (60 mol% D,L-malic acid adsorbed within the first three minutes).³¹ It was also observed that deformation in the gypsum crystals was apparent in the presence of some carboxylic acids; namely those that had the highest mol% adsorption for additive concentrations of 100 – 1000 μM ,³¹ but it is now stated that the morphology of the crystals is unaffected (or at least negligibly affected) by lower concentrations of additives.³² A recent study showed that tartaric acid changed the morphology forming short plate and spherulitic crystals alongside the usual thin, needle-like crystals using low concentrations of additive (1 g L⁻¹).²⁰

Badens *et al.* theorised two modes of action for the chemical additives: complexation of the additive carboxylate groups onto the gypsum surfaces containing calcium ions, or complexation of the additive within the crystal structure, with a sulfate oxygen atom exchanged for an additive carboxylate oxygen atom, and a complexed water molecule oxygen atom exchanged with an additive hydroxyl group oxygen atom.³¹ Badens *et al.* stated that only the (120) and (-111) faces have calcium ions present; the other two faces, (011) and (010), have negative superficial charges and no calcium ions present. Thus, they conclude that surface additives should only bind to the (120) and (-111) surfaces. The (120) face is neutrally charged and the closest distance between two calcium ions is 4.0 Å. The (-111) face has the same closest calcium ion distance but is positively charged.³¹ This is completely contradictory to what Chen *et al.* recently reported, as they confirmed with AFM (atomic force microscopy), μ -FTIR (Fourier-transform infrared spectroscopy) and advanced molecular dynamics simulations that L-(+)-tartaric acid and citric acid

bound strongly with the (010) plane, forming a monolayer organic-inorganic structure.³³ They stated that the (010) plane has calcium ions present and citric acid and tartaric acid favour a stand up conformation with one carboxylic acid group interacting with the top most calcium ions (Figure 1.10).

Fisher and Mbogoro *et al.* recently studied gypsum dissolution with some of the aforementioned additives using a channel flow cell (CFC) technique (described previously^{34,35}) complimented by inductively coupled plasma-optical emission spectroscopy (ICP-OES).^{36,37} Their study found that STMP had some small retarding effect on the crystal dissolution rate as previously reported^{29,36} (Figure 1.11), but the other additives did not. Their discovery sheds some doubt on the dissolution-precipitation mechanism proposed by Chappuis mentioned earlier,²³ as the additives do not inhibit dissolution. Singh *et al.* proposed that the chemical additives alter the crystal area and the faces that are in contact with each other,³⁸ although the SEM (scanning electron microscopy) images taken by Fisher *et al.* showed no noticeable crystal modification.³⁶ They instead proposed the theory put forward first by Finot *et al.*, who determined that the adhesion between crystal faces was dependant on the Miller planes in contact,³⁹⁻⁴¹ and it could be that the chemical additives alter the crystal

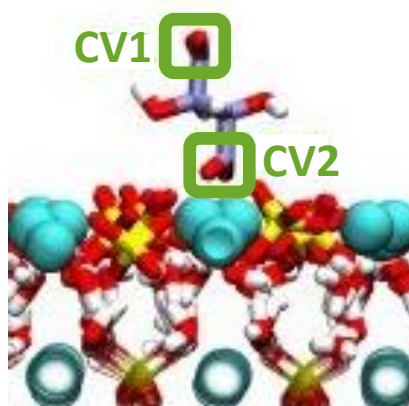


Figure 1.10: Diagram taken from Chen *et al.* showing the stand-up conformation of L-tartaric acid on the (010) surface of gypsum.³³ CV1 and CV2 correspond to the two carboxyl groups.

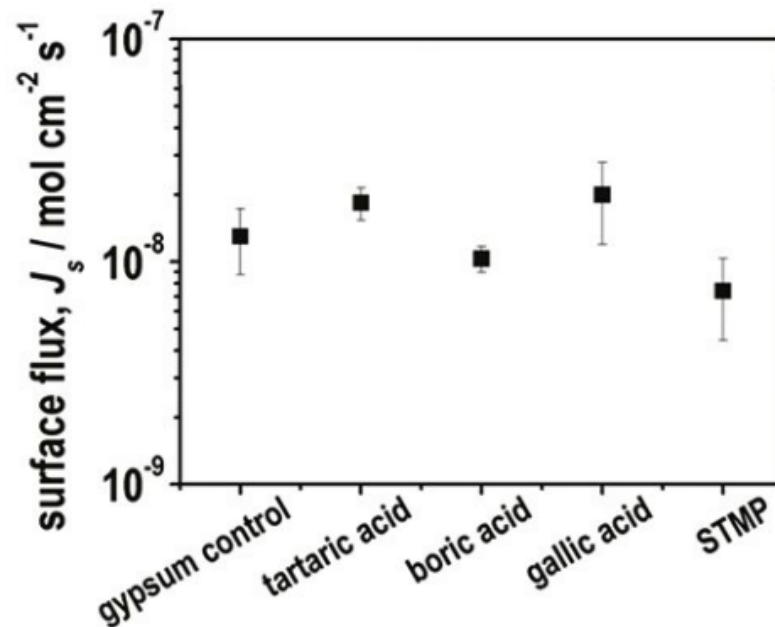


Figure 1.11: Plot of the average surface fluxes, J_s , of gypsum and four chemical additives. STMP has the greatest crystal dissolution retarding effect. Graph taken from Mbogoro *et al.*³⁵

faces somehow to increase the adhesion. They also proposed that the inhibitors could reduce the amount of water present at the crystal surfaces, thus preventing the degenerative effect of water.³⁶

Kato *et al.* discovered that polar liquids such as ethanol reduced the mechanical properties of gypsum and proposed that this was due to a decrease in surface energy, which thus lowers the binding energy of the crystals.⁴² Reynauld *et al.* used internal friction measurements to come up with a visco-elastoplastic rheological model to describe the plastic flow of gypsum, where the adsorbed liquid layer shields some electrostatic interactions between the crystals leading to the crystals sliding over each other.⁴³ This stance was previously taken by Coquard and Boistelle, who disputed the mechanism of crystal dissolution-precipitation and proposed that the gypsum crystals were held together by electrostatic interactions and water in the structure would shield these electrostatic interactions, thus reducing the binding strength.⁴⁴

Other chemical additives have been tested, with Khalil *et al.* reporting on the effects of waste additives such as unburnt rice husk, slag, calcium carbonate and commercial poly vinyl alcohol polymer (PVA).⁴⁵ They reported that each of these additives reduced the setting time, increased the porosity (each effect more pronounced with increasing additive concentration) and small amounts of additives increased the compressive strength of gypsum. Their study also recorded that the additives sit in the gypsum pores without interacting or binding with the gypsum crystals. The increased mechanical strength is given by a different mechanism for each additive: rice husk acts as a reinforcing agro fibre,⁴⁶ slag is a hydraulic binder; whereas calcium carbonate and PVA apparently sit at the pores between plaster grains.⁴⁶ A separate study showed PVA has no effect on the crystal morphology.²⁰

Colombani *et al.* tested a number of additives using digital holographic interferometry.⁴⁷ They believed that the dissolution-recrystallisation mechanism was responsible for the creep effect as they had discovered in a previous study²⁴ and thus investigated the dissolution kinetics of gypsum under a variety of additives: a 1/6 tartaric/boric acid mix, Trilon® P (a sodium salt of a polyamino carboxylic acid), Sequion 50K33, Dequest 2054 (both potassium salts of hexamethylenediamine tetra(methylene phosphonic acid) with six and one potassium ions respectively) and STMP. Their results are shown in Figure 1.12. They show that STMP clearly has the largest dissolution inhibition and suggest this is due to the salts chelating to the surface calcium ions, effectively blocking them from dissolution. They suggest STMP has the highest dissolution inhibition due to it being the most strongly bound complex because of its ring geometry. They also note that their measured dissolution rate

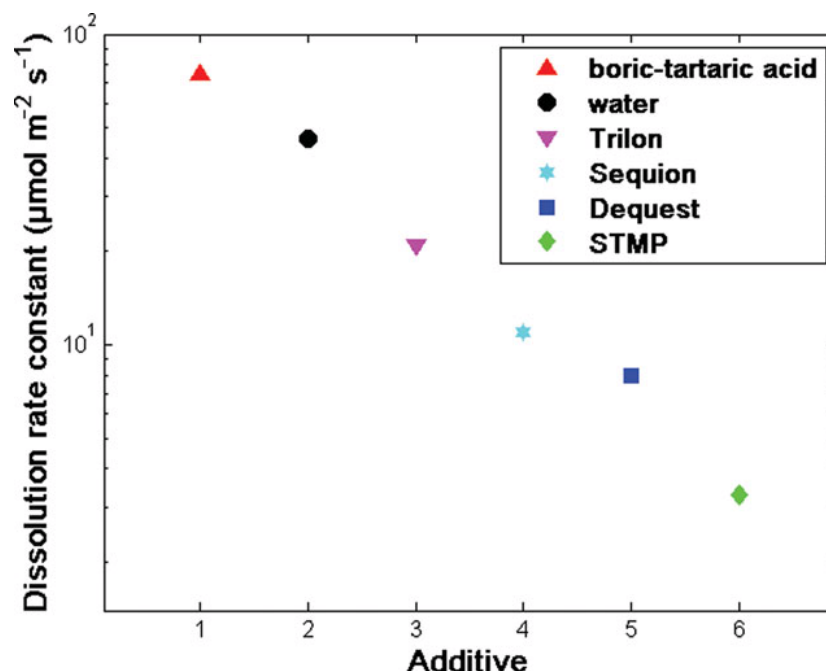


Figure 1.12: Pure dissolution rate constant of the (010) face of a gypsum single crystal in water containing various additives. Graph taken from Colombani *et al.*⁴⁵

constant is four times lower than the rate constant measured by Fisher *et al.* and explained that this is due to the hydrodynamical assumptions made by Fisher *et al.* for their data analysis.³⁶ Fisher *et al.* used a technique in which the solvent is flowing over the crystal, always replenishing the surface with fresh solvent devoid of any dissolved species, whereas Colombani's holographic interferometry had a gypsum crystal dissolving in a stagnant solution.^{36,47} This would have led to a higher measured rate constant for Fisher *et al.*, as the solution is always undersaturated with regards to gypsum whereas Colombani's solution would eventually become gypsum saturated. Colombani noted the tartaric/boric acid mixture gave an increase in the dissolution rate constant which was put down to the weak nature of the second dissociation of sulfuric acid. The lowering of the pH due to the acid mix presence leads to a rise in the HSO_4^- concentration and thus a decrease in the SO_4^{2-} concentration. The dissolution is then accelerated as SO_4^{2-} ions are liberated from the gypsum crystals in order to supply new SO_4^{2-} ions into the acidic solution.⁴⁷ Also of note in Colombani's paper are the concentrations of additives used. Figure

1.13 shows that the dissolution rate constant is effectively independent of the concentration of additive used at about 0.05 wt%.

Colombani *et al.* went further in the studies of these additives and discovered that none affected the crystal morphology.⁴⁸ They again used holographic interferometry to investigate the creep mechanism and discovered that the kinetics were not driven by the diffusion of the dissolved species moving through the thin water film (Figure 1.7). They also demonstrated that the wet creep rate is linked to the dissolution rate of the gypsum material and that STMP was again the most effective dissolution/creep resistive additive for plaster. They put forward the theory that this mechanism may also contribute to the creep of hydrated Portland cement.

A few years prior, Gartner had discussed how the presence of “bridging” is necessary to obtain a more comprehensive interpretation of the set plaster properties.⁴⁹ In her paper, Gartner also tested the effects of some different chemical additives in the form of calcium carboxylate salts: $\text{Ca}(\text{HCOO})_2$, $\text{Ca}(\text{CH}_3\text{COO})_2$ and

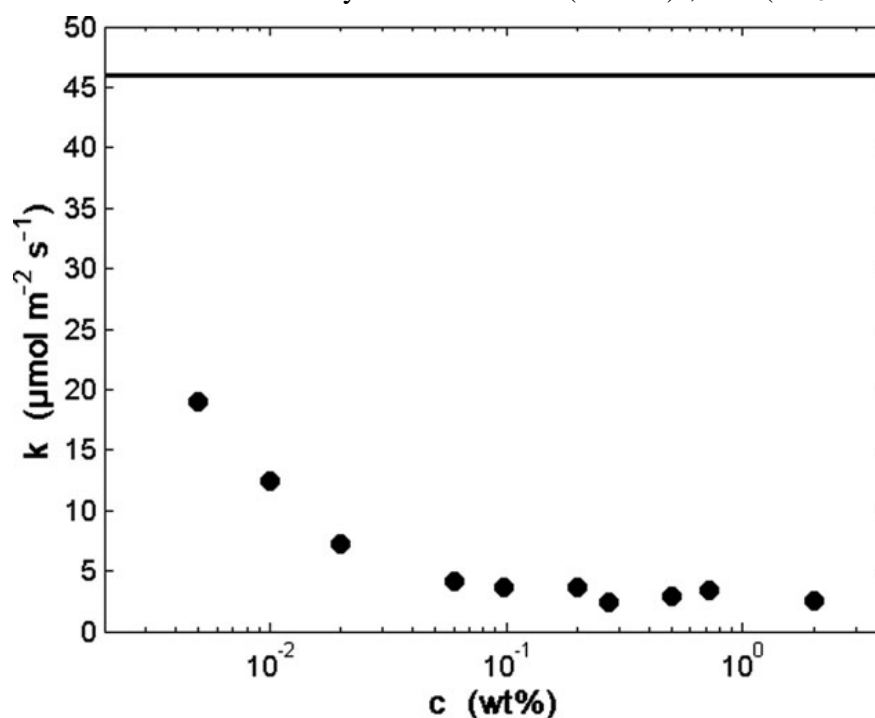


Figure 1.13: Evolution of the pure dissolution rate constant of the cleavage plane of gypsum with the STMP concentration in the aqueous solution where the crystal dissolves. The horizontal line is the value in pure water. Graph taken from Colombani *et al.*⁴⁵

$\text{Ca}(\text{CH}_3\text{CH}_2\text{COO})_2$, of which the latter two (when used at aqueous concentrations of 10 % or more) caused large expansions of the crystal matrix while still retaining its cohesion. It was suggested that these specific adsorbates deposit on and stabilise certain crystal faces and can modify the tendency of these faces to form the bridging interactions she speaks of. The additives also retarded the setting.

It is common knowledge in industry that there are two polymorphs of calcium hemihydrate: the α form and β form.⁵⁰⁻⁵² The β form is formed when gypsum is calcined in an open container such as a kiln. This rapid heating leads to fast calcining but porous and irregular powder particles. The α form is created when gypsum is calcined under steam pressure in a closed container. This method releases the water of crystallisation slowly, leading to more uniform powder particles that have less porosity. Wu *et al.* recently demonstrated that the two different polymorphs have different water absorbance and compressive strengths; the α -hemihydrate (α -H) is stronger and absorbs less water, although the β -H form is used more in industry due to its lower cost.⁵³ Wu *et al.* tested various polymer additives in the attempt to find a way to increase both the mechanical strength and the water absorption for modelling plaster, but the results still apply for construction plaster. They tested eight different polymers: PC-1, PC-2, PC-3, PC-4 (all of which are detailed in Table 1.1), PEG (polyethylene glycol), PVA (polyvinyl alcohol), PAM (polyacrylamide) and VCVA (vinyl chloride-vinyl acetate). They discovered that the more hydrophilic polymers (PVA and PEG) provided an increase in mechanical strength whereas the more hydrophobic polymers (VCVA and PAM) have a negative effect on both the strength and the water absorption (i.e. for the case of construction plaster, the strength decreases and the water absorption increases). PVA also seemed to alter the crystal morphology from β -H to α -H (Figure 1.14). All of the polycarboxylate polymers (PC-

Table 1.1: Structure of the synthetic polycarboxylates taken from Wu *et al.*⁵¹

Polymer	Structure
PC-1	$\begin{array}{ccccccc} \text{COONa} & & \text{CH}_3 & & \text{CONHOH} & & \text{CH}_2\text{SO}_3\text{Na} \\ & & & & & & \\ -\text{CH}-\text{CH}- & \text{---} & \text{CH}_2-\text{C}- & \text{---} & \text{CH}_2-\text{CH}- & \text{---} & \text{CH}_2-\text{CH}- \\ & & & & & & \\ \text{COONa} & & \text{CH}_2\text{CH}_2\text{O}- & \text{---} & \text{CH}_2\text{CH}_2\text{O}- & \text{---} & \text{CH}_2-\text{CHO}-\text{H} \\ & & & & & & \\ & & & & & & \text{CH}_3 \end{array}$ <p style="text-align: center;">$a_1 \quad b_1 \quad c_1 \quad d_1 \quad m \quad n$</p>
PC-2	$\begin{array}{ccccccc} \text{COONa} & & \text{CH}_3 & & \text{CH}_2\text{SO}_3\text{Na} & & \\ & & & & & & \\ -\text{CH}-\text{CH}- & \text{---} & \text{CH}_2-\text{C}- & \text{---} & \text{CH}_2-\text{CH}- & \text{---} & \text{CH}_3 \\ & & & & & & \\ \text{COONa} & & \text{CH}_2\text{CH}_2\text{O}- & \text{---} & \text{CH}_2\text{CH}_2\text{O}- & \text{---} & \text{CH}_2-\text{CHO}-\text{H} \\ & & & & & & \\ & & & & & & \text{CH}_3 \end{array}$ <p style="text-align: center;">$a_2 \quad b_2 \quad c_2 \quad m \quad n$</p>
PC-3	$\begin{array}{ccccccc} & \text{CH}_3 & & \text{COONa} & & \text{CH}_2\text{SO}_3\text{Na} & \\ & & & & & & \\ -\text{CH}_2-\text{C}- & \text{---} & \text{CH}_2-\text{CH}- & \text{---} & \text{CH}_2-\text{CH}- & \text{---} & \text{CH}_3 \\ & & & & & & \\ & \text{CH}_2\text{CH}_2\text{O}- & \text{---} & \text{CH}_2\text{CH}_2\text{O}- & \text{---} & \text{CH}_2-\text{CHO}-\text{H} \\ & & & & & & \\ & & & & & & \text{CH}_3 \end{array}$ <p style="text-align: center;">$a_3 \quad c_3 \quad d_3 \quad m \quad n$</p>
PC-4	$\begin{array}{ccccccc} & \text{CH}_3 & & \text{CONHOH} & & \text{CH}_2\text{SO}_3\text{Na} & \\ & & & & & & \\ -\text{CH}_2-\text{C}- & \text{---} & \text{CH}_2-\text{CH}- & \text{---} & \text{CH}_2-\text{CH}- & \text{---} & \text{CH}_3 \\ & & & & & & \\ & \text{CH}_2\text{CH}_2\text{O}- & \text{---} & \text{CH}_2\text{CH}_2\text{O}- & \text{---} & \text{CH}_2-\text{CHO}-\text{H} \\ & & & & & & \\ & & & & & & \text{CH}_3 \end{array}$ <p style="text-align: center;">$a_4 \quad b_4 \quad c_4 \quad m \quad n$</p>

1 to PC-4) led to an increase in water absorption in β -H and only PC-4 (the one polycarboxylate without a carboxyl group) led to an increase in mechanical strength. This leads to the proposition that the carboxyl group detrimentally affects the β -H crystal structure or crystal binding by ‘capturing’ the Ca^{2+} ions which reduces the availability of calcium in the crystallisation. For the α -H polymorph, PC-3 and PC-4 increased the strength. This polymer route could be an effective pathway in reducing the water absorption which it seems would logically reduce the humid creep effect.

One of the more recent studies by Schug *et al.* into gypsum humid creep seems to confirm the model of pressure-solution creep. They showed evidence that the creep

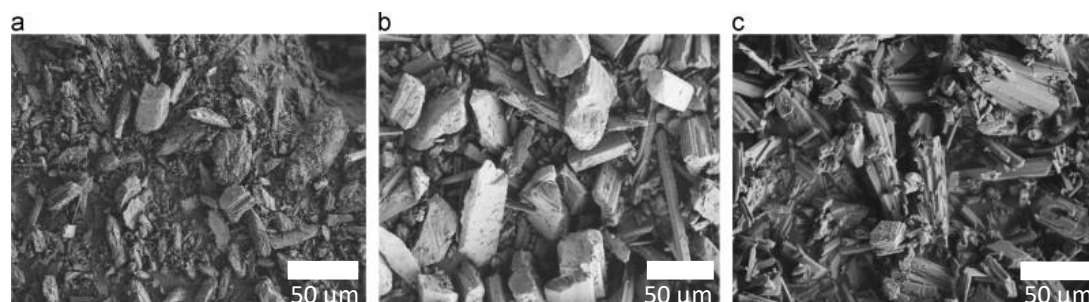


Figure 1.14: SEM profiles of the hardened gypsum made from (a) α -H, (b) β -H, (c) β -H pretreated with 0.2% PVA. Image taken from Wu *et al.*⁵¹

velocity of gypsum is directly proportional to the solubility of gypsum, shown in Figure 1.15.⁵⁴ Schug *et al.* were able to modify the solubility of gypsum using varying concentrations of nitric acid and were able to study the creep on the nanometre scale with a special SEM setup. The fact that the amount of creep is directly proportional to the solubility of the gypsum probably confirms the pressure-solution mechanism proposed by Chappuis, as an increase in pressure between two gypsum needles would artificially increase the solubility of the plaster, thus leading to more dissolution and the characteristic plastic deformation.²³

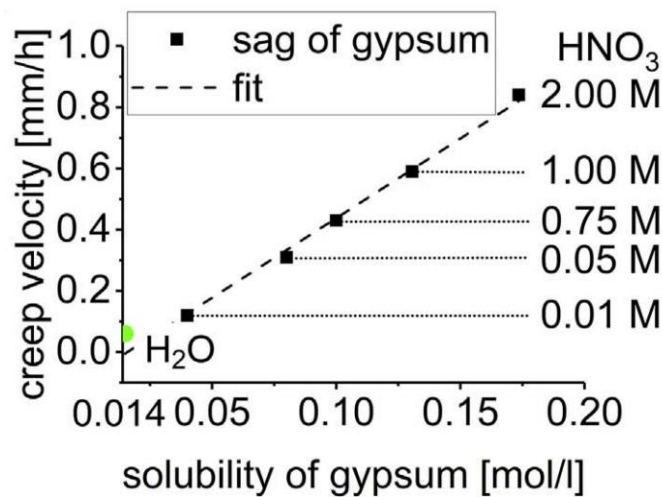
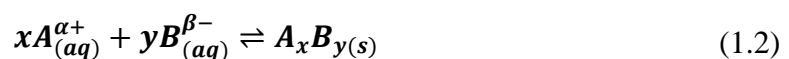


Figure 1.15: Data showing that the creep velocity of gypsum is directly proportional to the solubility of the gypsum. The gypsum solubility was altered by incorporating varying concentrations of nitric acid into the dissolving solution. Image taken from Schug *et al.*⁵²

1.4 Crystal Growth and Dissolution Reactions

Crystal growth and dissolution is a process that can be expressed by the equation:



where $A^{\alpha+}$ and $B^{\beta-}$ are the reagents of the solid crystal A_xB_y . In the case of gypsum $A^{\alpha+}$ and $B^{\beta-}$ are Ca^{2+} and SO_4^{2-} respectively. The saturation level of the system is denoted by S :

$$S = \sqrt{(\alpha+\beta) \frac{(a_A \times a_B)}{K_{sp}}} \quad (1.3)$$

where a_A and a_B are the activities of the A and B ions respectively. K_{sp} is the crystal solubility product.

When the system is in equilibrium such that the forward and backward reaction rates in Equation 1.2 are equal, $S = 1$. When the reaction is not in equilibrium and new states are being formed, $S \neq 1$. When $S < 1$ the system is considered undersaturated, leading to dissolution of the solid, and when $S > 1$ the system is considered supersaturated leading to formation of the solid, or crystal growth. The extent to which the system is away from equilibrium is proportional to the thermodynamic driving force for the process. The change in chemical potential difference, $\Delta\mu$, can be denoted as:

$$\Delta\mu = k_B T \ln \left[\frac{(a_A \times a_B)}{K_{sp}} \right] \quad (1.4)$$

where k_B is the Boltzmann constant and T is the temperature. The illustrative case where there is a high supersaturation and crystal growth is heavily favoured ($S \gg 1$) corresponds to a large $\Delta\mu$ and thus a high driving force for nucleation/growth.⁵⁵ In order to re-establish equilibrium in the system, precipitate forms and continues to form until the dissolved ion concentration is equal to the solubility product, resulting in a reduction in the total free energy of the system. The opposite occurs in the case of crystal dissolution with the precipitate dissolving into solution until $\Delta\mu = 0$.

1.5 Crystal Growth Theory

1.5.1 Nucleation

Crystal nucleation is the process by which ions in a solution arrange and aggregate to form an agglomeration, ending in a solid with a size that is thermodynamically stable.⁵⁶ If the nucleation is homogeneous, nuclei form in the bulk solution only with no influence from a pre-existing solid.^{57,58} The induction time of the nuclei forming is determined by the thermodynamics of the system and the reaction kinetics of the crystal. Heterogeneous nucleation occurs when there is a pre-existing solid or surface to nucleate on. These surfaces can be impurities in the solution, cracks or imperfections in the crystallising vessel.

Homogenous nucleation is well described by Classical Nucleation Theory (CNT) which considers the energetics involved in the formation of crystal nuclei.⁵⁹⁻⁶² CNT describes the forming of a spherical nucleus as a result of collisions and aggregations of atoms, the shape being a sphere as a sphere exhibits the lowest surface tension. The total free energy change (ΔG) of the nucleus formation is described as the sum of its volume and surface free energies:

$$\Delta G = -\left(\frac{4}{3}\pi r^3 \Delta g_v\right) + (4\pi r^2 \Delta g_s) \quad (1.5)$$

where r is the radius of the nucleus, g_v is the free energy per unit volume and g_s is the free energy per unit area. When ΔG is negative, this indicates a lower energy and a new stable solid phase prevails. Δg_v decreases with nucleus size while Δg_s increases with nucleus size (Figure 1.16a), striking a balance between the two bracketed terms in Equation 1.5. Thus, the overall ΔG increases as the nucleus radius increases up to a maximum (ΔG^*) where the critical radius (r^*) is reached and growth is favoured over new nucleation. Nuclei with radii smaller than r^* tend to dissolve back to ions.⁶³ Due to the high activation barrier (ΔG^*) and the strong prevalence on ambient

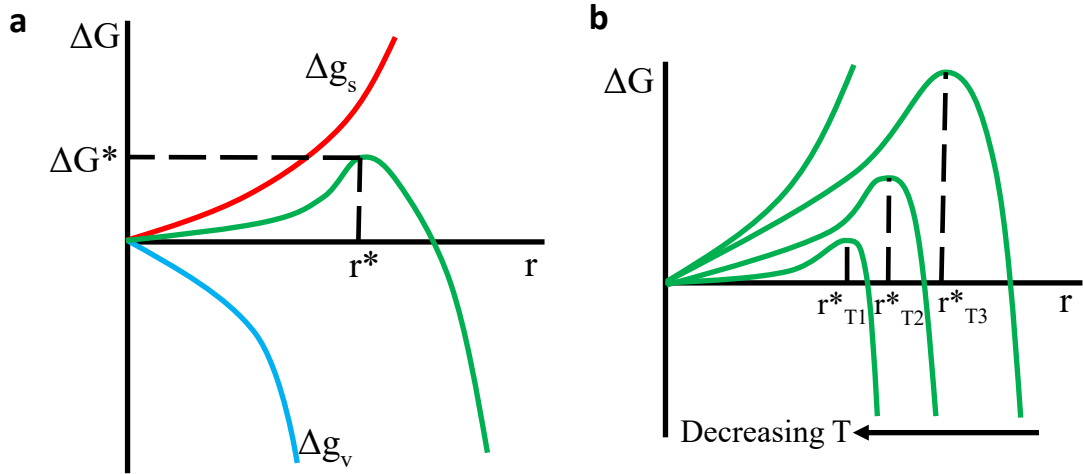


Figure 1.16: a) Gibbs free energy diagram for crystal nucleation and b) temperature dependence of the critical radius.

temperatures, (Figure 1.16b) homogenous nucleation tends to only occur at high supersaturations ($S \gg 1$).

The nucleation rate, J , follows an Arrhenius-style relation:

$$J_n = A e^{\left(-\frac{\Delta G^*}{k_B T}\right)} \quad (1.6)$$

where A is a kinetic parameter related to the number of available nucleation sites on the nucleus.⁶⁴ One of the limitations of CNT is the assumption that the nucleus formed exhibits similar properties to the bulk crystal.⁵⁷

There exist meta-stable phases preceding the formation of the thermodynamically stable final crystalline phase due to the availability of kinetic products.⁶⁵ These kinetically favoured products give rise to polymorphism, where phases are formed before reorganisation into the thermodynamically stable polymorph (Figure 1.17).⁶⁶⁻⁶⁹

Heterogenous crystallisation occurs due to the lower energy needed to bond to the pre-existing impurities or imperfections in the crystallisation vessel. The bonds formed here are stronger and thus lead to a smaller contribution of enthalpy to bond formation, reducing the activation barrier to nucleation.⁷⁰

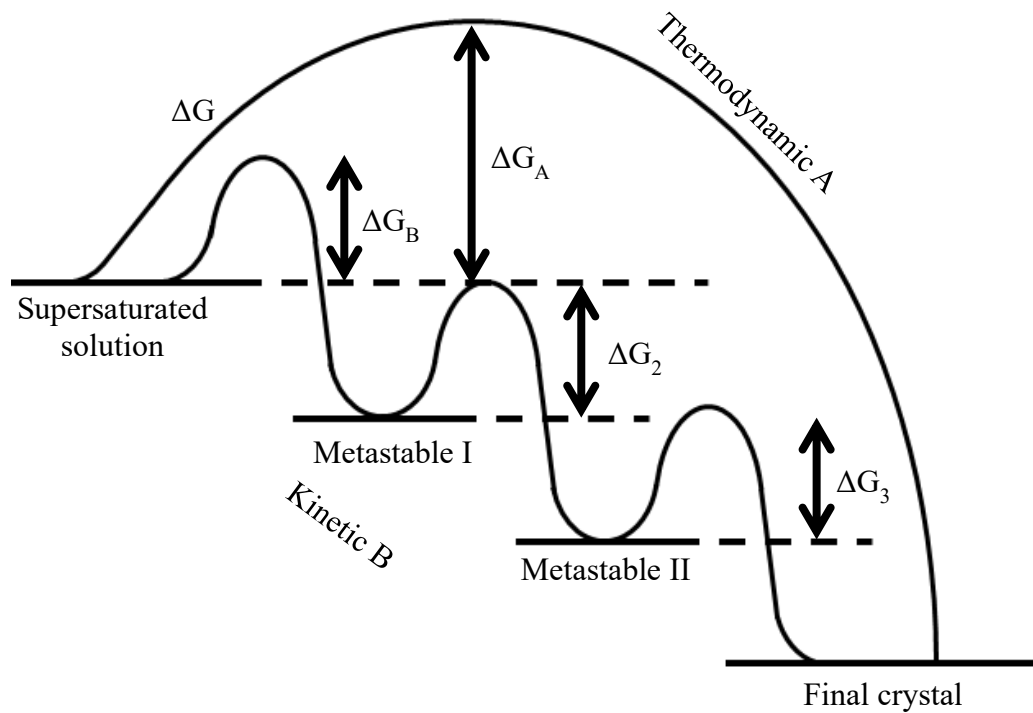


Figure 1.17: Simplified schematic of the crystallisation pathways under thermodynamic and kinetic control, showing the two pathways of the one-step route to the final mineral phase (path A) or sequential precipitation (path B).⁶⁶

1.5.2 Crystal Growth

Crystal growth involves the mass transport of the relevant ions from the bulk solution to the solid-liquid interface and then adsorption of the molecule onto the surface. It is energetically favourable for the molecule to attach to a defect site on the surface such as a kink or a step due to the loss of degrees of freedom.⁷¹ The molecules that reach the surface have mobility across the surface until such a defect site is found. This was first described in the Kossel, Stranski and Volmer (KSV) model.⁷²⁻⁷⁴ This continuous growth of molecules attaching to surfaces and propagating layer by layer affects the crystal macro-morphology depending on the growth rates on different crystal faces.⁶⁴

The KSV model was extended by Burton, Cabrera and Frank (BCF) who modelled the crystal growth as the movement of crystal steps across the surface.⁷⁵⁻⁸⁰ BCF theory also explains that a defect on the surface can lead to a mismatch in the crystal structure and produce a screw dislocation. Screw dislocations are a source of infinite steps from which the crystal can continuously grow.⁸¹⁻⁸³

1.5.3 Crystal Dissolution Theory

Crystal dissolution has been much less widely explored than crystal growth, despite its importance in a number of different fields.^{84,85} The thermodynamic force for dissolution is the opposite of growth, where undersaturation ($S < 1$) favours dissolution. Similar and opposite to crystal growth, dissolution starts preferentially at crystal surface sites that exhibit excess energy such as kinks, steps and adatoms.

While BCF theory describes screw dislocations for crystal growth, Cabrera and Levine applied similar principles to dissolution.^{86,87} They explained how at low saturation conditions ($S < 1$) the strain field of a dislocation opens up, creating a cavity which forms a stable etch pit. The stability of the etch pit requires the driving force of the dissolution (the extent of undersaturation) to be above a certain critical energy level (ΔG_{crit}) and the etch pit to reach its critical radius (r_{crit}), similar to crystal nucleation (but opposite).^{86,87} The dissolution then follows a spiral dissolution mechanism which, again similar to the crystal growth mechanism, provides an infinite source of steps in which the crystal can continuously dissolve (Figure 1.18).⁸⁸

With latest advances in sophisticated computer models that simulate crystal dissolution, recent attempts to further develop crystal dissolution theories have been studied, relating the dependence of dissolution rates to the state of undersaturation or the differing dissolution rates of different crystal faces.⁸⁶⁻⁹²

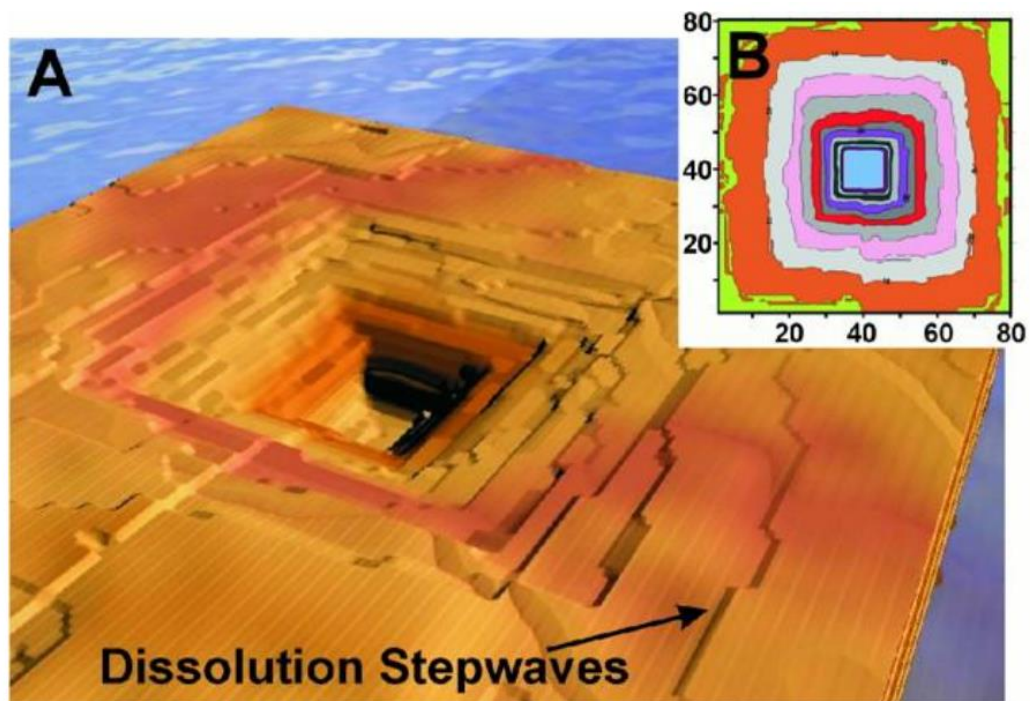


Figure 1.18: A dissolution etch pit as a source of infinite steps.⁸⁶

1.6 Scanning Probe Microscopy

Conventional microscopy techniques tend to irradiate a sample with light or an electron beam but scanning probe microscopy (SPM) utilises equipment that requires no contact or irradiation of the sample.⁹³ There are many types of SPM, all of which involve an interaction between the probe and the surface being imaged. The information collected may be used to understand the surface topography though some techniques are capable of investigating surface charge or porosity.

One of the first SPM techniques created was scanning tunnelling microscopy (STM) which relies on the quantum tunnelling of electrons across the gap between the surface and the probe which is ideally only one atom thick at the point. This technique can build images of surfaces with atomic resolution.⁹³⁻⁹⁵ AFM is a similar technique on a larger scale: a probe is passed across a surface and the probe is deflected by repulsive forces from the surface. These deflections are detected by the

probe which is mounted to a cantilever, the movements of which are measured by the reflections of a laser onto a photodiode detector.^{96,97} AFM is best known and mostly used for imaging surface topography, but it can also be used for force measurements at the surface.⁹⁸⁻¹⁰⁰ While STM typically gives higher resolution images than AFM, AFM still gives images several orders of magnitude higher in resolution than what could be achieved with conventional optical microscopes.¹⁰¹⁻¹⁰³

While STM and AFM use physical forces to detect a surface topography, some techniques require no physical interaction with a surface, only an electrochemical signal. These techniques are referred to as scanning electrochemical probe microscopies (SEPMs), with the most common probing technique being scanning electrochemical microscopy (SECM).¹⁰⁴⁻¹⁰⁷ SECM involves sealing a thin conducting wire (typically platinum, gold or carbon fibre) of 1-25 μm diameter inside glass, and then polishing back the glass until the wire is revealed, creating an ultramicroelectrode (UME).¹⁰⁸ This probe is then used for electrochemical reactions and the current measured, tracking topography or surface functionalities.^{106, 109-112}

Other SEPM techniques include open channel techniques such as scanning ion conductance microscopy (SICM)¹¹³⁻¹¹⁵ and droplet-based techniques such as scanning electrochemical cell microscopy (SECCM).¹¹⁶⁻¹¹⁸

1.6.1 SICM and Nanoprecipitation

SICM typically works through the application of a bias between two quasi-reference counter electrodes (QRCEs, usually Ag/AgCl wire), one inside a glass or quartz nanopipette, and the other in bulk solution outside of a nanopipette (Figure 1.19).¹¹³⁻¹¹⁵ The current measured between the electrodes gives information on the environment around the end of the nanopipette, and has thus been used extensively

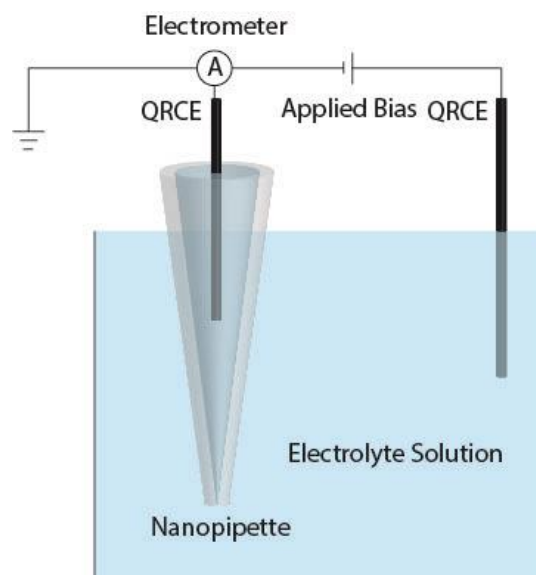


Figure 1.19: Schematic of SICM setup. For imaging a surface, a nanopipette would be tracked over the surface.

for topographical imaging, especially with delicate samples that are damaged by other SPM techniques such as living cells.¹¹⁶⁻¹¹⁹ SICM is suitable for these delicate samples as the probe never comes in to physical contact with the sample, avoiding any potential damage. The magnitude of the current passing between the two electrodes is mostly dependent on the size of the opening of the nanopipette, the concentration of the electrolyte and the bias applied to the electrode to measure the current.

Typically, the SICM setup is used for surface studies, but for this study the nucleation/growth and dissolution of crystals inside a nanopipette is employed, with no need for a surface. This technique is referred to as nanoprecipitation, a SICM technique that has been utilised in the past to study very early stages of crystallisation and has also shown to be an effective screening method for additives.¹²⁰⁻¹²³ The technique involves the separation of the two ionic species of a crystal – one species in a nanopipette and the other in bulk (either in a bath or a droplet). The movement of the ionic species is controlled by application of the electrical bias for controlled mixing, and the saturation level of the ionic species leads to precipitation of crystals,

thus blocking the tip and dropping the current that passes through the nanopipette, which can be tracked to give an understanding of the extent of crystallisation. The current can drop indicating partial blocking of the nanopipette, or the current can become zero, indicating complete blocking of the nanopipette. Sometimes periodic partial blocking can be seen, indicating crystal growth inside the nanopipette which is then pushed out through electrophoretic forces.¹²⁰

Preparation of the nanopipettes for SICM studies are relatively simple, a glass or quartz capillary, typically with an inner diameter of 0.5-1 mm, are placed into a laser puller where a laser heats the centre of the capillary to the point of melting. A pulling force is applied to either end of the capillary while the heating occurs, narrowing the centre to a fine point, eventually breaking, creating two nanopipettes of similar diameter and geometry. The diameter of the nanopipette opening depends on the parameters of the heating, the pulling force as well as the material the capillary is made from. Tuning of these parameters leads to extremely consistent production of nanopipettes. Some studies demonstrate consistent nanopipette sizes of 10-20 nm at the smallest end of the scale.^{124,125}

As the current detected in the SICM experiment is very dependent on the geometry of the nanopipette, precise characterisation of the nanopipettes is critical. Several methods exist for characterisation, the most common and simple being cyclic voltammetry where the ionic response in a nanopipette is measured at different potential differences. The opening size is then calculated from the current response with the assumption that the pipette is conically shaped. A more reliable method to determine nanopipette geometry is SEM (Figure 1.20a), which can provide accurate images of the nanopipette opening, giving dimensions of the aperture as well as the wall size.^{124,126-128} However some of the limitations of SEM are that nanopipettes with

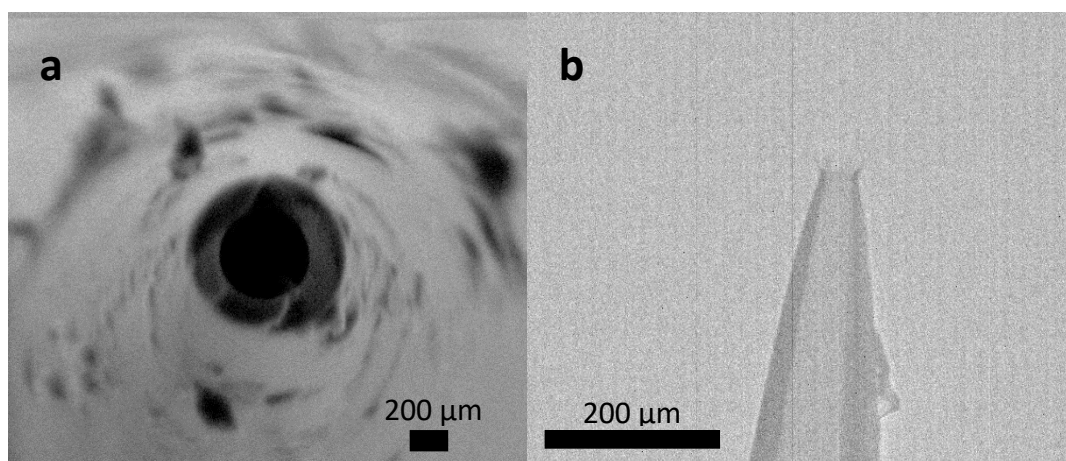


Figure 1.20: a) SEM image of a nanopipette showing the opening diameter and the glass thickness at the end of the nanopipette and b) TEM image of a nanopipette showing the opening diameter as well as the inner geometry.

diameter < 50 nm are difficult to image due to the limitations in SEM resolution as well as the inside wall in the nanopipette being invisible to SEM. It has been predicted that the external geometry of the nanopipette alone is not sufficient to fully predict the ionic current response on a nanopipette, due to the fact that the assumption of the conical internal geometry is incorrect.¹²⁹ Transmission electron microscopy (TEM, Figure 1.20b) has become the new key method for imaging nanopipettes for full characterisation due to the ability of the electron beam to penetrate the walls of the nanopipette. This allows for more geometrical parameters to be measured along the length of the nanopipette aperture, such as the glass thickness and inner cone angle, which has been shown to vary significantly along the length of the nanopipette.¹²⁹ This cone angle is considered fixed in the assumption of a conical geometry. Another advantage of TEM is that the resolution is typically much higher, with the ability of giving much more accurate images of even the smallest nanopipettes with aperture diameters down to 10 nm.

1.6.2 SECCM

SICM requires the surface being analysed to be submerged in solution which is not necessarily always possible due to surfaces dissolving. One technique that can be done in air is scanning electrochemical cell microscopy (SECCM).¹³⁰ In SECCM there is no bath solution and instead of a single barrel nanopipette being employed as a probe, a dual barrelled (or theta) nanopipette is used (Figure 1.21). These dual barrelled pipettes have been used before for SICM delivery, allowing two different samples to be delivered from either channel.¹³¹ In SECCM, each channel can be filled with solution forming a meniscus at the end of the pipette, which acts as a localised electrochemical cell, with an ionic current being measured across the meniscus. The technique can be used for controlled mixing of two solutions at the end of the nanopipette or as a controlled droplet to be applied to a surface of interest.^{132,133} SECCM has been used in part to study local dissolution of a substrate,¹³⁴⁻¹³⁷ substrate reactivity¹³⁸⁻¹⁴⁰ and precise deposition onto a surface.¹⁴¹⁻¹⁴³

SECCM is a useful technique as it allows precise yet gentle application of a droplet onto any surface, with the droplet size depending on the nanopipette aperture, thus making it tuneable. During a scan, the nanopipette is mounted onto a vertical piezoelectric positioning system that allows for precise movement normal to the surface, without the possibility of human error to crash the nanopipette into the surface. The micropositioner is controlled via computer, and for SECCM, the bias that is applied to the piezoelectric positioner to control the movement is oscillated,

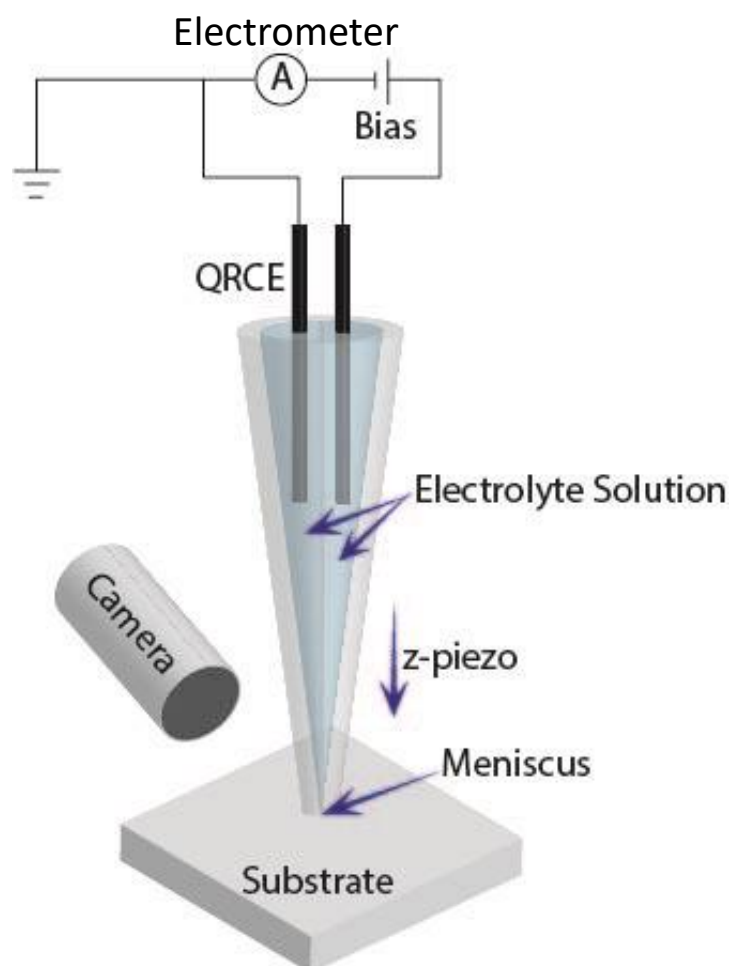


Figure 1.21: Schematic of SECCM setup. A meniscus forms at the end of the nanopipette which can be carefully placed onto the surface of interest.

providing an AC current. The AC current is tracked in real time as once the droplet reaches a surface and attaches, the AC current being recorded will change, thus telling the micropositioner to stop moving, and stop the nanopipette from ever touching the surface.¹⁴⁴

1.7 Analytical Techniques

1.7.1 Surface Area Measurements

For characterisation of the surface area of porous solids, gas adsorption is much more accurate than liquid adsorption. Adsorption from solution measurements are easier to carry out but often difficult to interpret.¹⁴⁵ Langmuir was one of the pioneers of surface adsorption, bringing together the unifying concept of the monolayer.¹⁴⁶ Langmuir theory proposes that the plateau of an adsorption isotherm of a gas represented completion of the monolayer, and if the area occupied by each adsorbed molecule was known, it is possible to predict the surface area of the corresponding adsorbent.

While this may still hold true for planar surfaces, Langmuir had already pointed out that surface areas of highly porous materials cannot be easily defined, and that the equations Langmuir defined for planar surfaces should not be applied to the adsorption of highly porous materials.^{146,147}

This problem was partially solved by Brunauer and Emmett who made their first attempts of determining the surface area of an iron ammonia catalyst by means of low temperature gas adsorption.¹⁴⁸ Eventually they published their findings and proposed the Brunauer-Emmett-Teller (BET) theory.¹⁴⁹ BET theory is still used now as a standard procedure for surface area determination of porous solids, although it has come under some criticism for being based on an over-simplified model of Langmuir multilayer adsorption.¹⁵⁰ BET theory tries to extend on Langmuir theory stating that: gas molecules adsorb infinitely in layers; gas molecules only interact with adjacent layers and that the Langmuir theory can be applied to each layer. BET theory also comes with assumptions such as adsorption only occurring on well-defined sites

of the sample surface and that the molecules can act as a single adsorption site for a molecule of the layer above it. BET theory also assumes that at saturation pressure the molecule layer tends to infinity, implying that the sample is surrounded by a liquid phase.

The application of BET theory analyses the adsorption of nitrogen molecules within the porous structure due to the inertness of nitrogen and are employed at the boiling temperature of nitrogen, 77 K. It is generally agreed that the method is unreliable when applied to ultramicroporous materials which contain pores of molecular dimensions due to the size of the nitrogen molecule. BET theory thus provides a surface area of a porous solid, but its accuracy and reliability have come under much scrutiny for the amount of assumptions made.¹⁵⁰

1.7.2 Confocal Fluorescence Microscopy

Fluorescence microscopy has been used in the past to provide insight into concentration profiles within structures, penetrating the surface in real time.¹⁴⁹ Confocal laser scanning microscopy (CLSM) reduces out-of-focus blur from light sources out of the plane of focus. CLSM allow non-invasive optical sectioning of objects and profiling of multilayer structures.¹⁵²

Fluorescein is one of the most commonly employed fluorophores that exhibits a pH-sensitive fluorescence signal above pH 6.5. It has been used previously in many fluorescence microscopy studies and its pH sensitivity makes it ideal for studying reactions that generate protons or hydroxide ions.^{153,154}

1.7.3 Finite Element Method (FEM) Modelling

The complex list of variables present in studies such as SICM and nanoprecipitation make the interpretation of the current responses sometimes difficult to process. To combat these challenges, the experiments are often compared with theoretical studies using the parameters from the experiment.^{129,155} The partial differential equations that treat both the transport of species in solution and electric field distribution cannot be solved analytically so they are treated numerically to provide estimations. One such method is finite element method (FEM) modelling, where a set domain is divided into a finite number of regions using a technique known as “meshing” using software such as COMSOL Multiphysics (used herein). The domains can be one, two or three-dimensional, with some systems being liable to simplification by turning a three-dimensional system into a two-dimensional one through clever use of geometry customisation. This is a technique often employed with SICM by using an axis of rotation around the centre of the nanopipette, as usually all of the environments around this axis are identical (as in Chapter 3 of this thesis). The meshing slices the domain into several smaller domains, often yielding several thousand small meshes. The meshing extent can vary, being very fine at areas of particular interest, but being very large in areas of less interest such as in bulk solution. Most of these shortcuts are used to reduce computation power, as at each mesh point (the intersection of each mesh), the necessary equations are solved numerically using an iterative solving method.

After a geometry has been built and the necessary differential equations included, boundary conditions and initial conditions are input. In a SICM simulation, initial conditions are parameters like the starting conditions for a time-dependant simulation or an initial estimate of a steady-state simulation. Typical boundary

conditions refer to a concentration, applied potentials or surface charges, among other parameters such as an interfacial flux. For example the wall of a nanopipette would be deemed a zero flux boundary as no solution can pass through, but it would be given a slightly negative surface charge.¹⁵⁶ This negative surface charge is usually a considerable factor for small nanopipettes at lower electrolyte concentrations, inducing ion current rectification,^{129,157-164} but the extent of rectification has been shown to decrease with electrolyte concentration.¹⁵⁷ In the studies undertaken herein the concentrations are large enough that ion current rectification is negligible.

FEM simulations are employed in Chapters 2 and 3, to analyse supersaturations of species in an evaporating droplet (Chapter 2) and to look at supersaturations in the case of nanoprecipitation inside a nanopipette (Chapter 3). FEM simulations give quantitative information usually unobtainable experimentally and are always complimentary to experimental data.

1.7.4 Raman Spectroscopy

Raman spectroscopy has proved useful in studying crystal systems due to its ability to accurately distinguish between different polymorphs or hydrates of crystals, as every crystal structure has a unique fingerprint.^{165,166} Raman spectroscopy works from the near infrared through to the near ultraviolet spectrum and relies on inelastic scattering of monochromatic light. The technique probes vibrational, rotational and other low-frequency modes from Raman scattering.¹⁶⁷ Raman scattering occurs when the monochromatic light source (from a laser) is absorbed by the target substance and re-emitted but at a different frequency. This behaviour occurs when the molecule of interest is excited into a higher virtual energy state by the incoming photon from the

laser, and then relaxes into a lower vibrational energy state that is non-identical to the starting energy state, releasing energy as it relaxes.

In the case of gypsum, the dihydrate can be differentiated from the hemihydrate and dehydrated forms of calcium sulfate, albeit by less than ten wavenumbers. Gypsum shows a categorically large sulfate S=O vibrational stretch peak at 1008 cm^{-1} while bassanite and anhydrite have large sulfate peaks at 1015 cm^{-1} and 1017 cm^{-1} respectively.

1.8 Thesis Aims

The main aim of this thesis is to better understand the main mechanism of action of humid creep inhibitors in gypsum plaster, and how these additives can affect certain gypsum characteristics such as the dissolution, crystallisation and nucleation kinetics, as well as the wettability of plaster. Through these investigations, new additives are explored for the purpose of stalling humid creep further, and failing that, finding additives that have a useful impact on the plasterboard industry.

Chapter 2 focusses on studying the crystallisation of gypsum in an evaporative study. Many different humid creep inhibitors are used and the changes in the crystal behaviour of gypsum highlighted. FEM simulations are used to explain the crystallisation patterns seen, and this study also shows the droplet contact angle and evaporation rate of the droplet are unaffected by each of the additives.

Chapter 3 introduces the nanoprecipitation technique and utilizes this technique to show that the early nucleation, crystallisation and dissolution kinetics of gypsum crystals are all altered under the additives – the nucleation, growth and dissolution times are all increased. The technique is also used to study the early

nucleation of the MOF HKUST-1, proving a nucleation theory presented before in literature and highlighting how diverse and useful nanoprecipitation can be for studying crystal kinetics. FEM simulations are employed in both of these studies to quantify the saturation of the represented species during experimentation.

Chapter 4 aims to show how water spreads through gypsum plaster with the use of SECCM to apply microscale droplets to a surface. This study shows that even when plaster is treated with small concentrations of common humid creep inhibitors, the rate of wetting does not appear to change.

Chapter 5 introduces fluorescein as a new additive for the use of tagging in industrial plasterboard. Fluorescein shows no negative effects on the sagging of gypsum plaster or on the processing conditions but has the utility of being fluorescent, meaning it could be used as an invisible tag to prevent counterfeit issues.

Chapter 6 finally considers the contributions to the gypsum plasterboard industry with concluding remarks.

1.9 References

- ¹ D. C. Ford, P. W. William, *Karst Geomorphology and Hydrology*, Unwin Hyman, Chippenham, Wiltshire, U.K., **1989**
- ² M. Atoji, R. E. Rundle, *Chem. Phys.*, **1958**, 29, 1306
- ³ W. F. Cole, C. Lancucki, *J. Acta. Crystal.*, **1974**, B 30, 921
- ⁴ C. Fan, H. H. Teng, *Chem. Geol.*, **2007**, 245, 242
- ⁵ C. Yan, J. Nishida, R. Yuan, M. Fayer, *J. Am. Chem. Soc.*, **2016**, 138, 9694
- ⁶ “Food Additives & Ingredients – Overview of Food Ingredients, Additives & Colors.” U S Food and Drug Administration Home Page. Center for Food Safety and Applied Nutrition, **2nd Dec. 2014**. Accessed **17th Apr. 2017**
- ⁷ D. Freyer, W. Voigt, *Monatsh. Chem.*, **2003**, 134, 693
- ⁸ D. J. Peterson, N. W. Kaleta, L. W. Kingston, Kirk-Othmer Encyclopaedia of Chemical Technology, *Calcium Compounds (Calcium Sulfate)*, 4th ed., Howe-Grant, M., Ed. Wiley-Interscience, New York, **1992**, 4, 812
- ⁹ F. Wirsching, Encyclopaedia of Industrial Chemistry, *Calcium Sulfate*, VCH Verlagsgesellschaft mbH., Weinheim, **1985**, A4, 555
- ¹⁰ T. Heldal, E. G. Bloxam, P. Degryse, P. Storemyr, A. Kelany, *Geo. Sur. Nor. Spec. Pub.*, **2009**, 12, 51
- ¹¹ H. J. Arpe, Ullmans Encyclopaedia of Industrial Chemistry, 5th ed., VCH, Weinheim, **1985**, A4, 555
- ¹² R. D. Crangle, *U.S. Geological Survey, Mineral Commodity Summaries*, Reston, Virginia, U.S., **January 2018**

- ¹³ O. J. G. Vetter, R. C. Philips, *J. Petrol. Technol.*, **1970**, 22, 1299
- ¹⁴ A. C. Lasaga, A. E. Blum, *Geochim. Cosmochim. Acta*, **1986**, 50, 2363
- ¹⁵ J. Schott, O. S. Pokrovsky, E. Oelkers, *Rev. Mineral.*, **2009**, 70, 207
- ¹⁶ *Building Materials in Civil Engineering*, Woodhead Publishing, **2011**, 30
- ¹⁷ A. C. Lasaga, A. Leuttge, *Eur. J. Mineral.*, **2003**, 15, 603
- ¹⁸ A. Lüttge, *J. Electron Spectrosc. Relat. Phenom.*, **2006**, 150, 248
- ¹⁹ E. M. Gartner, *Cem. Concr. Res.*, **2009**, 39, 289
- ²⁰ T. Feldmann, G. P. Demopoulos, *J. Chem. Technol. Biotechnol.*, **2014**, 89, 1523
- ²¹ A. N. Christensen T. R. Jensen, A. Nonat, *Dalton Trans.*, **2010**, 39, 2044-2048
- ²² D. Hoxha, F. Homand, C. Auvray, *Eng. Geol.*, **2006**, 86, 1
- ²³ J. Chappuis, *Colloid Surf.*, **1999**, 156, 223
- ²⁴ E. A. Pachon-Rodriguez, E. Guillon, G. Houvenaghel, J. Colombani, *Phys. Rev. E*, **2011**, 84, 066121
- ²⁵ E. Badens, S. Veessler, R. Boistelle, D. Chatain, *Colloid Surf.*, **1999**, 156, 373
- ²⁶ R. Arese, D. Martin, M. Rigaudon, *Process for reducing creep in a gypsum plaster-based element, gypsum plaster-based composition and method for making a gypsum plaster-based element with reduced creep*, U.S. Patent 2006/0048680, **2003**
- ²⁷ B. K. Wilson, K. W. Jones, *Production of shaped gypsum articles*, GB Patent 1481788, **1977**
- ²⁸ R. E. Muller, P. L. Henkels, B. M. O'Kelly, *Gypsum board*, U.S. Patent 3190787, **1965**

- ²⁹ Q. Yu, S. Sucheck, B. Groza, R. Mlinac, F. Jones, F. Boehnert, *Process for reducing creep in a gypsum plaster-based element, gypsum plaster-based composition and method for making a gypsum plaster-based element with reduced creep*, U.S. Patent 6632550, **2003**
- ³⁰ J. Colombani, *Geochim. Cosmochim. Acta*, **2008**, 72, 5634
- ³¹ E. Badens, S. Veessler, R. Boistelle, *J. Cryst. Growth*, **1999**, 198, 704
- ³² L. Amathieu, *J. Cryst. Growth*, **1988**, 88, 183
- ³³ W. Chen, W. Zhao, Y. Wu, Y. Wang, B. Zhang, L. Fengteng, Q. Chen, Z. Qi, Z. Xu, *CrystEngComm*. **2018**, 20, 3581
- ³⁴ M. E. Snowden, P. H. King, J. A. Covington, J. V. Macpherson, P. R. Unwin, *Anal. Chem.*, **2010**, 82, 3124
- ³⁵ P. R. Unwin, J. V. Macpherson, *Chem. Soc. Rev.*, **1995**, 24, 109
- ³⁶ R. D. Fisher, M. M. Mbogoro, M. E. Snowden, M. B. Joseph, J. A. Covington, P. R. Unwin, R. I. Walton, *ACS Appl. Mater. Interfaces*, **2011**, 3, 3528
- ³⁷ M. M. Mbogoro, M. E. Snowden, M. A. Edwards, M. Peruffo, P. R. Unwin, *J. Phys. Chem. C*, **2011**, 115, 10147
- ³⁸ N. B. Singh, B. Middendorf, *Prog. Cryst. Growth Charact. Mater.*, **2007**, 53, 57
- ³⁹ E. Finot, E. Lesniewska, J. C. Mutin, J. P. Goudonnet, *Langmuir*, **2000**, 16, 4237
- ⁴⁰ E. Finot, E. Lesniewska, J. P. Goudonnet, J. C. Mutin, *App. Surf. Sci.*, **2000**, 161, 316
- ⁴¹ E. Finot, E. Lesniewska, J. P. Goudonnet, J. C. Mutin, M. Domenech, A. A. Kadi, *Sol. State Ion.*, **2001**, 141-142, 39

- ⁴² Y. Kato, M. Matsui, K. Umeya, *Gypsum Lime*, **1980**, 166, 83
- ⁴³ P. Reynauld, M. Saadaoui, S. Meille, G. Fantozzi, *ICIFMS-14*, Elsevier Science Sa: Kyoto, Japan, **2005**, 500
- ⁴⁴ P. Coquard, R. Boistelle, *Int. J. Rock Mech. Min. Sci. & Geomech. Abstr.*, **1994**, 31, 517
- ⁴⁵ A. A. Khalil, A. Tawfik, A. A. Hegazy, M. F. El-Shahat, *Construction and Building Mater.*, **2014**, 68, 580
- ⁴⁶ A. A. Khalil, *J. Interceram. Int. Refract Manual*, **2010**, 39, 289
- ⁴⁷ E. A. Pachon-Rodriguez, J. Colombani, *AIChE J.*, **2013**, 59, 1622
- ⁴⁸ E. A. Pachon-Rodriguez, E. Guillon, G. Houvenaghel, J. Colombani, *Cement and Concrete Research*, **2014**, 63, 67
- ⁴⁹ E. Gartner, *Cement and Concrete Research*, **2009**, 39, 289
- ⁵⁰ K. K. Kelley, J. C. Southard, C. T. Anderson, *U.S. Bur. Mines Tech.*, **1941**, 625
- ⁵¹ H. B. Welser, W. O. Milligan, *J. Amer. Chem. Soc.*, **1937**, 59, 1456
- ⁵² D. A. Powell, *Nature Lett.*, **1960**, 185, 375
- ⁵³ H. Wu, Y. Xia, X. Hu, X. Liu, *Ceram. Int.*, **2014**, 40, 14899
- ⁵⁴ B. Schug, K. Mandel, G. Schottner, A. Shmeliov, V. Nicolosi, R. Baese, B. Pietschmann, M. Biebl, G. Sestl, *Cement and Concrete Research*, **2017**, 98, 122
- ⁵⁵ S. L. Brantley, J. D. Kibicki, A. F. White, *Kinetics of Water-rock Interaction*, Springer Science: New York, **2008**

- ⁵⁶ A. C. Lasaga, *Kinetic Theory and Applications in Earth Sciences*, Princeton Press, Princeton, **1998**
- ⁵⁷ S. L. Brantley, J. D. Kibicki, A. F. White, *Kinetics of Water-Rock Interaction*, Springer Science, New York, **2008**
- ⁵⁸ B. K. Chakreverty, *Crystal Growth: An Introduction*, North-Holland Publishing Company, **1973**
- ⁵⁹ J. Frenkel, *J. Chem. Phys.*, **1939**, 7, 538
- ⁶⁰ D. Turnbull, J. C. Fisher, *J. Chem. Phys.*, **1949**, 17, 71
- ⁶¹ D. Becker, W. Doring, *Ann. Phys-Berlin*, **1935**, 24, 719
- ⁶² M. Volmer, A. Weber, *Z. Phys. Chem.*, **1925**, 119, 277
- ⁶³ K. Sangwal, *Etching of Crystals, Theory, Experiment and Application*, North Holland Publishing, Amsterdam, **1987**
- ⁶⁴ K. Sangwal, *Additives and Crystallisation Processes: From Fundamentals to Applications*, John Wiley & Sons Ltd, Chichester, **2007**
- ⁶⁵ J. Merikanto, E. Zapadinsky, A. Lauri, H. Vehkamäki, *Phys. Rev. Lett.*, **2007**, 98, 145702
- ⁶⁶ H. Cölfen, M. Antonietti, *Langmuir*, **1998**, 14, 582
- ⁶⁷ J. Rieger, J. Thieme, C. Schmidt, *Langmuir*, **2000**, 16, 8300
- ⁶⁸ F. C. Meldrum, H. Cölfen, *Chem. Rev.*, **2008**, 108, 4332
- ⁶⁹ A. E. S. Van Driessche, L. G. Benning, J. D. Rodriguez-Blanco, M. Ossorio, P. Bots, J. M. Garcia-Ruiz, *Science*, **2012**, 336, 69

- ⁷⁰ J. J. De Yoreo, P. G. Velikov, *Biomineralization, Reviews in Mineralogy and Geochemistry*, **2003**, 54, 57
- ⁷¹ A. G. Jones, *Crystallization Process Systems*, Butterworth-Heinemann, Oxford, U.K. **2002**
- ⁷² W. Kossel, *Nachr. Ges. Wiss. Gottigen. Math.-Phys. Klasse*, **1927**, 135
- ⁷³ I. N. Stranski, *Z. Phys. C.*, **1928**, 136, 259
- ⁷⁴ H. Brandes, M. Volmer, *Inter. J. Research Phys. Chem. Chem. Phys.*, **1931**, 155, 466
- ⁷⁵ R. Boistelle, J. Astier, *J. Cryst. Growth*, **1988**, 90, 14
- ⁷⁶ P. Bennema, *J. Cryst. Growth*, **1967**, 1, 287
- ⁷⁷ W. Burton, N. Cabrera, *Discuss. Faraday Soc.*, **1949**, 5, 33
- ⁷⁸ N. Cabrera, W. Burton, *Discuss. Faraday Soc.*, **1949**, 5, 40
- ⁷⁹ F. Frank, *Discuss. Faraday Soc.*, **1949**, 5, 48
- ⁸⁰ Y. I. Kwon, B. Dai, J. J. Derby, *Prog. Cryst. Growth Charact. Mater.*, **2007**, 553, 167
- ⁸¹ H. H. Teng, P. M. Dove, J. J. De Yoreo, *Geochim. Cosmochim. Acta*, **1999**, 63, 2507
- ⁸² P. S. Dobson, L. A. Bindley, J. V. Macpherson, P. R. Unwin, *Langmuir*, **2005**, 21, 1255
- ⁸³ M. Adobes-Vidal, A. G. Shtukenberg, M. D. Ward, P. R. Unwin, *Cryst. Growth Des.*, **2017**, 17, 1766

- ⁸⁴ A. Lüttge, *J. Electron Spectrosc. Relat. Phenom.*, **2006**, 150, 248
- ⁸⁵ R. Tang, G. H. Nancollas, C. A. Orme, *J. Am. Chem. Soc.*, **2001**, 123, 5437
- ⁸⁶ N. Cabrera, M. M. Levine, J. S. Plaskett, *Phys. Rev.*, **1954**, 96, 1153
- ⁸⁷ N. Cabrera, M. M. Levine, *Philos. Mag.*, **1956**, 1, 450
- ⁸⁸ A. C. Lasaga, A. Lüttge, *Science*, **2001**, 291, 2400
- ⁸⁹ J. Cama, L. Zhang, J. M. Soler, G. D. Giudici, R. S. Arvidson, A. Lüttge, *Geochim. Cosmochim. Acta*, **2010**, 74, 4298
- ⁹⁰ M. Adobes-Vidal, F. M. Maddar, D. Momotenko, L. P. Hughes, S. A. C. Wren, L. N. Poloni, M. D. Ward, P. R. Unwin, *Cryst. Growth Des.*, **2016**, 16, 4421
- ⁹¹ M. Adobes-Vidal, H. Pearce, P. R. Unwin, *Phys. Chem. Chem. Phys.*, **2017**, 19, 17827
- ⁹² F. M. Maddar, M. Adobes-Vidal, L. P. Hughes, S. A. C. Wren, P. R. Unwin, *Cryst. Growth Des.*, **2017**, 17, 5108
- ⁹³ E. Meyer, H. J. Hug, R. Bennewitz, *Scanning probe microscopy: the lab on a tip*, Springer Berlin Heidelberg, **2013**
- ⁹⁴ G. Binnig, H. Rohrer, *Surf. Sci.*, **1983**, 126, 236
- ⁹⁵ P. K. Hansma, J. Tersoff, *J. Appl. Phys.*, **1987**, 67, R1
- ⁹⁶ G. Binnig, C. F. Quate, *Phys. Rev. Lett.*, **1986**, 56, 930
- ⁹⁷ D. Rugar, P. Hansma, *Phys. Today*, **1990**, 43, 23
- ⁹⁸ H. J. Butt, B. Cappella, M. Kappl, *Surf. Sci. Rep.*, **2005**, 59, 1

- ⁹⁹ J. D. Willott, T. J. Murdoch, G. B. Webber, E. J. Wanless, *Macromolecules*, **2016**, *49*, 2327
- ¹⁰⁰ J. P. Froning, P. Lazar, M. Pykal, Q. Li, M. Dong, R. Zbořil, M. Otyepka, *Nanoscale*, **2017**, *9*, 119
- ¹⁰¹ S. Ido, H. Kimiya, K. Kobayashi, H. Kominami, K. Matsushige, H. Yamada, *Nat. Mater.*, **2014**, *13*, 264
- ¹⁰² J. Zhou, D. Liang, S. Contera, *Nanoscale*, **2015**, *7*, 17102
- ¹⁰³ S. Shi, X. Chen, X. Liu, X. Wu, F. Liu, Z. Zhang, Y. Li, T. P. Russell, D. Wang, *ACS Appl. Mater. Interfaces*, **2017**, *9*, 24451
- ¹⁰⁴ A. J. Bard, F. F. Fan, J. Kwak, O. Lev, *Anal. Chem.*, **1989**, *61*, 132
- ¹⁰⁵ J. Kwak, A. J. Bard, *Anal. Chem.*, **1989**, *61*, 1794
- ¹⁰⁶ S. Amemiya, A. J. Bard, F. F. Fan, M. V. Mirkin, P. R. Unwin, *Annu. Rev. Anal. Chem.*, **2008**, *1*, 95
- ¹⁰⁷ C. G. Zoski, *J. Electrochem. Soc.*, **2016**, *163*, H3088
- ¹⁰⁸ C. G. Zoski, *Electroanalysis*, **2002**, *14*, 1041
- ¹⁰⁹ J. V. Macpherson, P. R. Unwin, *J. Phys. Chem.*, **1995**, *99*, 14824
- ¹¹⁰ A. Schulte, M. Nebel, W. Schuhmann, *Annu. Rev. Anal. Chem.*, **2010**, *3*, 299
- ¹¹¹ J. Kim, M. Shen, N. Nioradze, S. Amemiya, *Anal. Chem.*, **2012**, *84*, 3489
- ¹¹² T. Sun, Y. Yu, B. J. Zacher, M. V. Mirkin, *Angew. Chem.*, **2014**, *53*, 14120
- ¹¹³ P. K. Hansma, B. Drake, O. Marti, S. A. Gould, C. B. Prater, *Science.*, **1989**, *243*, 641

- ¹¹⁴ C. C. Chen, Y. Zhou, L. A. Baker, *Annu. Rev. Anal. Chem.*, **2012**, 5, 207
- ¹¹⁵ A. Page, D. Perry, P. R. Unwin, *Proc. R. Soc. A.*, **2017**, 473, 2200
- ¹¹⁶ Y. E. Korchev, J. Gorelik, M. J. Lab, E. V. Sviderskaya, C. L. Johnston, C. R. Coombes, I. Vodyanoy, C. R. Edwards, *Biophys J.*, **2000**, 78, 451
- ¹¹⁷ J. Gorelik, L. Q. Yang, Y. Zhang, M. Lab, Y. Korchev, S. E. Harding, *Cardiovasc. Res.*, **2006**, 72, 422
- ¹¹⁸ D. Perry, B. P. Madappuram, D. Momotenko, P. D. Voyias, A. Page, G. Tripathi, B. G. Frenguelli, P. R. Unwin, *J. Am. Chem. Soc.*, **2016**, 138, 3152
- ¹¹⁹ A. Page, M. Kang, A. Armitstead, D. Perry, P. R. Unwin, *Anal. Chem.*, **2017**, 89, 3021
- ¹²⁰ B. Vilozy, P. Actis, R. A. Seger, N. Pourmand, *ACS Nano*, 2011, 5, 3191
- ¹²¹ A. Perry, *Quantitative Microscopic Methods for Crystal Growth and Dissolution Processes: PhD Thesis*, University of Warwick **2011**, 152
- ¹²² F. M. Maddar, D. Perry, and P. R. Unwin, *Cryst. Growth Des.*, **2017**, 17 (12), 6565
- ¹²³ D. Perry, A. S. Parker, A. Page, and P. R. Unwin, *ChemElectroChem*, **2016**, 3 (12), 2212
- ¹²⁴ A. I. Shevchuk, G. I. Frolenkov, D. Sanchez, P. S. James, N. Freedman, M. J. Lab, R. Jones, D. Klenerman, Y. E. Korchev, *Angew. Chem., Int. Ed.*, **2006**, 45, 2212
- ¹²⁵ Y. Takahashi, K. Ito, X. Wang, Y. Matsumae, H. Komaki, A. Kumatani, K. Ino, H. Shiku, T. Matsue, *Electrochemistry*, **2014**, 82, 331
- ¹²⁶ J. Rheinlaender, T. E. Schäffer, *Soft Matter*, **2013**, 9, 3230

- ¹²⁷ E. M. Yuill, W. Shi, J. Poehlman, L. A. Baker, *Anal. Chem.*, **2015**, 87, 11182
- ¹²⁸ M. Karhanek, J. T. Kemp, N. Pourmand, R. W. Davis, C. D. Webb, *Nano Lett.*, **2005**, 5, 403
- ¹²⁹ D. Perry, D. Momotenko, R. A. Lazenby, M. Kang, P. R. Unwin, *Anal. Chem.*, **2016**, 88, 5523
- ¹³⁰ C. L. Bentley, M. Kang, P. R. Unwin, *Current Op. Electrochemistry*, **2017**, 6, 23
- ¹³¹ K. T. Rodolfa, A. Bruckbauer, D. Zhou, Y. E. Korchey, D. Klenerman, *Angew. Chem. Int. Ed.*, **2005**, 44, 6854
- ¹³² M. E. Snowden, A. G. Güell, S. C. S. Lai, K. McKelvey, N. Ebejer, M. A. O-Connell, A. W. Colburn, P. R. Unwin, *Anal. Chem.*, **2012**, 84, 2483
- ¹³³ N. Ebejer, A. D. Güell, S. C. S. Lai, K. McKelvey, M. E. Snowden, P. R. Unwin, *Annu. Rev. Anal. Chem.*, **2013**, 6, 329
- ¹³⁴ A. G. Güell, N. Ebejer, M. E. Snowden, J. V. Macpherson, P. R. Unwin, *J. Am. Chem. Soc.*, **2012**, 134, 7258
- ¹³⁵ C. H. Chen, K. E. Meadows, A. Cuharuc, S. C. S. Lai, P. R. Unwin, *Phys. Chem. Chem. Phys.*, **2014**, 16, 18545
- ¹³⁶ A. G. Güell, A. S. Cuharuc, Y. R. Kim, G. Zhang, S. Y. Tan, N. Ebejer, P. R. Unwin, *ACS Nano*, **2015**, 9, 3558
- ¹³⁷ H. V. Patten, S. C. S. Lai, J. V. Macpherson, P. R. Unwin, *Anal. Chem.*, **2012**, 84, 5427
- ¹³⁸ S. L. Kinnear, K. McKelvey, M. E. Snowden, M. Peruffo, A. W. Colburn, *Langmuir*, **2013**, 29, 15565

- ¹³⁹ A. S. Parker, R. Al Botros, S. L. Kinnear, M. E. Snowden, K. McKelvey, A. T. Ashcroft, M. Carvell, A. Joiner, M. Peruffo, C. Philpotts, P. R. Unwin, *J. Colloid Interface Sci.*, **2016**, 476, 94
- ¹⁴⁰ A. S. Parker, A. N. Patel, R. Al Botros, M. E. Snowden, K. McKelvey, P. R. Unwin, A. T. Ashcroft, M. Carvell, A. Joiner, M. Peruffo, *J. Dentistry*, **2014**, 4251, 521
- ¹⁴¹ K. McKelvey, M. A. O'Connell, P. R. Unwin, *Chem. Commun.*, **2003**, 49, 2986
- ¹⁴² E. E. Oseland, Z. J. Ayres, A. Basile, D. Haddleton, D. M. Wilson, P. R. Unwin, *Chem. Commun.*, **2016**, 52, 9929
- ¹⁴³ D. Momotenko, A. Page, M. Adobes-Vidal, P. R. Unwin, *ACS Nano*, **2016**, 10, 8871
- ¹⁴⁴ N. Ebejer, M. Schnippering, A. W. Colburn, M. A. Edwards, P. R. Unwin, *Anal. Chem.*, **2010**, 82, 9141
- ¹⁴⁵ K. S. W. Sing, *Adv. Colloid. Interface Sci.*, **1998**, 76, 3
- ¹⁴⁶ I. Langmuir, *J. Am. Chem. Soc.*, **1916**, 38, 2221
- ¹⁴⁷ E. K. Rideal, *Disc. Faraday Soc.*, **1932**, 139
- ¹⁴⁸ S. Brunauer, P. H. Emmett, *J. Am. Chem. Soc.*, **1935**, 57, 1754
- ¹⁴⁹ S. Brunauer, P. H. Emmett, E. Teller, *J. Am. Chem. Soc.*, **1938**, 60, 309
- ¹⁵⁰ J. Rouquerol, P. L. Llewellyn, F. Rouquerol, *Studies Surf. Sci. Catal.*, **2007**, 160, 49
- ¹⁵¹ C. Amatore, A. Chovin, P. Garrigue, L. Servant, N. Sojic, S. Szunerits, L. Thouin, *Anal. Chem.*, **2004**, 76, 7202
- ¹⁵² C. J. R. Sheppard, D. M. Shotton, *Confocal Laser Scanning Microscopy*, **1997**

- ¹⁵³ F. M. Boldt, J. Heinze, M. Diez, J. Petersen, M. Börsch, *Anal. Chem.*, **2004**, 76, 3473
- ¹⁵⁴ N. C. Rudd, S. Cannan, E. Bitziou, I. Ciani, A. L. Whitworth, P. R. Unwin, *Anal. Chem.* **2005**, 77, 6205
- ¹⁵⁵ D. Perry, R. Al Botros, D. Momotenko, S. L. Kinnear, P. R. Unwin, *ACS Nano*, **2015**, 9, 7266
- ¹⁵⁶ S. H. Behrens, D. G. Grier, *J. Chem. Phys.*, **2001**, 115, 6716
- ¹⁵⁷ C. Wei, A. J. Bard, S. W. Feldberg, *Anal. Chem.*, **1997**, 69, 4627
- ¹⁵⁸ Z. Siwy, E. Heins, C. C. Harrell, P. Kohli, C. R. Martin, *J. Am. Chem. Soc.*, **2004**, 126, 10850
- ¹⁵⁹ H. S. White, A. Bund, *Langmuir*, **2008**, 24, 2212
- ¹⁶⁰ D. Momotenko, F. Cortes-Salazar, J. Josserand, S. Liu, Y. Shao, H. H. Girault, *Phys. Chem. Chem. Phys.*, **2011**, 13, 5430
- ¹⁶¹ D. Momotenko, H. H. Girault, *J. Am. Chem. Soc.*, **2011**, 133, 14496
- ¹⁶² W. J. Lan, D. A. Holden, H. S. White, *J. Am. Chem. Soc.*, **2011**, 133, 13300
- ¹⁶³ X. Yin, S. Zhang, Y. Dong, S. Liu, J. Gu, Y. Chen, X. Zhang, X. Zhang, Y. Shao, *Anal. Chem.*, **2015**, 87, 9070
- ¹⁶⁴ L. Rosentsvit, W. Wang, J. Schiffbauer, H. C. Chang, G. Yossifon, *J. Chem. Phys.*, **2015**, 143, 22470
- ¹⁶⁵ A. C. Ferrari, J. C. Meyer, V. Scardaci, C. Casiraghi, M. Lazzeri, F. Mauri, S. Piscanec, D. Jiang, K. S. Novoselov, S. Roth, A. K. Geim, *Phys. Rev. Lett.*, **2006**, 97, 187401

¹⁶⁶ N. Prieto-Taboada, O. Gómez-Laserna, I. Martínez-Arkarazo, M. Á. Olazabal, J. M. Madariaga, *Anal. Chem.*, **2014**, 86, 10131

¹⁶⁷ D. J. Gardiner, P. R. Graves, *Practical Raman Spectroscopy*, **1989**

Chapter 2: Studying Plaster Humid Creep Inhibitors via Droplet Evaporation

– Nucleation of Gypsum due to the Coffee-Ring Effect

2.1 Abstract

Gypsum crystallisation is studied with different additives by evaporation of a calcium sulfate saturated droplet and confirmed with Raman spectroscopy. Crystals are formed in a circular pattern matching the diameter of the droplet due to the coffee-ring effect, which is explained with the help of finite element method models. These crystals are imaged by SEM and the different effects the additives have on the crystal behaviour commented on. Some additives show little effect whereas other additives show a reduction in crystal size, with the exception of gallic acid that shows an increase in size of single crystals, but a reduction in the number of individual crystals. It is shown that the droplet contact angle and rate of droplet evaporation are independent of the additive used inside the droplet.

2.2 Introduction

Nucleation of matter from an evaporating droplet has been extensively studied due to its importance in the industrial application of inkjet printing, self-assembly and biological detection fields.¹⁻⁶ The “coffee-ring” effect is a phenomenon in which solute particles are drawn to the outer edges of the droplet as it evaporates due to the pinning of the droplet edges.^{1, 7, 8} As the droplet evaporates at the edges, liquid from the centre must move outwards to replenish the edge to keep the pin, thus leading to an outward capillary flow, which draws with it any solid still in solution (Figure 2.1).

The crystallisation of gypsum is an important step in the humid creep process as the humid creep mechanism is believed to be a process of 3 steps: dissolution of a crystal within the thin water layers binding crystals due to increased pressure, movement of matter through the thin water layer, and then recrystallisation at a point in the thin water layer where the pressure is lower.

In this Chapter, various humid creep additives are investigated with respect to the recrystallisation step in the humid creep process. This work shows optical studies of nucleation and growth of gypsum with additives through the evaporation of a droplet. The response of crystallisation around the edge of the droplet is semi-

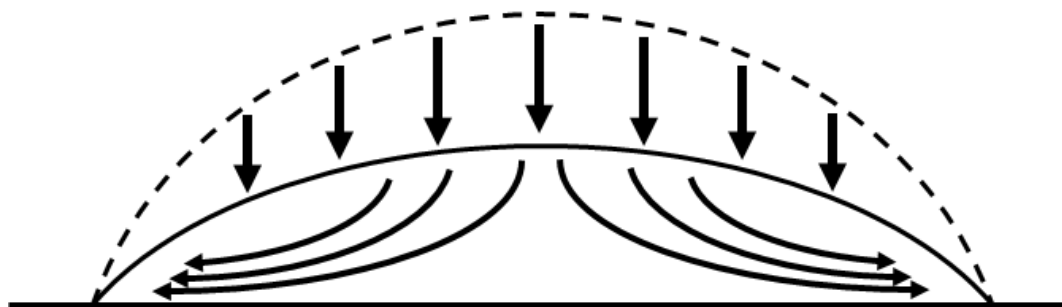


Figure 2.1: Cross-sectional schematic of the flow inside an evaporating droplet. Precipitate is drawn to the outer rim as the droplet evaporates and shrinks.

quantified using finite element method (FEM) modelling that shows the locations of highest saturation of calcium sulfate. An SEM study of the gypsum crystals grown through this droplet method is then also considered, examining the different nucleation and crystallisation behaviours under different additive effects.

2.3 Materials and Methods

2.3.1 Solutions

All solutions were made in ultrapure 18.2 M Ω water (Purite, Select HP). Calcium sulfate hemihydrate powder (α -plaster, 99%) was supplied by Saint Gobain, while large single gypsum crystals were provided by Saint Gobain Gyproc. All additives were purchased from Sigma-Aldrich: acetic acid ($\geq 99\%$), ascorbic acid ($\geq 99\%$), L-aspartic acid ($\geq 98\%$), boric acid ($\geq 99.5\%$), citric acid, ($\geq 99.5\%$), gallic acid ($\geq 97.5\%$), maleic acid ($\geq 99\%$), STMP ($\geq 95\%$), SHMP (reagent grade) and tartaric acid ($\geq 99\%$). Solutions for droplets contained 10 mM calcium sulfate hemihydrate and 0.5 mM respective additive. This additive concentration was chosen to best replicate the conditions used in plasterboard factories.

2.3.2 Video Setup

Thin glass slides (0.16 mm thickness) were cleaned via a process of sonication in de-ionised water, isopropanol and then acetone for 15 minutes each, drying with nitrogen in between the changes of cleaning solution. The glass slide was then mounted on an inverted Zeiss Axiovert 25 microscope and viewed through a 2.5X lens, with a PL-B871CU PixeLink camera for video capture. Upon this glass slide, 0.5 μ l droplets were deposited by hand using a Hamilton syringe ($0.5\ \mu\text{l} \pm 0.05\ \mu\text{l}$).

The droplet was simultaneously recorded perpendicularly with a PL-B776U PixeLink camera. Images were taken every second on both cameras and converted into time lapse captures via the ImageJ software.⁶ The droplet was illuminated from the opposite sides of the video cameras by LED cold lights (Figure 2.2). The entire setup was placed inside of a Faraday cage to minimise temperature fluctuations.

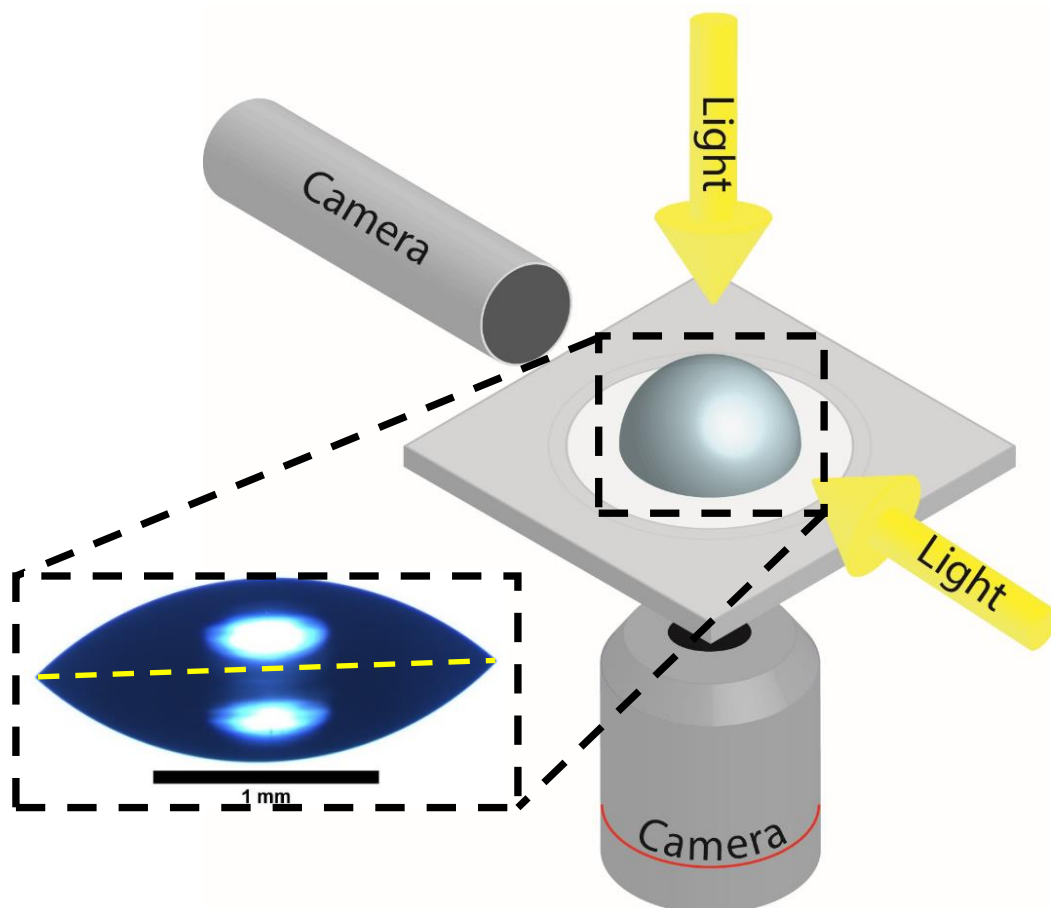


Figure 2.2: Schematic of droplet experiment setup. This allows for simultaneous recording of evaporation from below and the side. Inset: example image of a droplet image from the side camera. The dotted line shows the reflection line in the glass slide the droplet is sat on.

Various saturated salt solutions of magnesium nitrate hexahydrate (Sigma-Aldrich, 99.999 %) were placed around the Faraday cage to keep the humidity as constant as possible ($51\% \pm 3\%$).

2.3.3 Mass Measurement Setup

5 μl droplets were deposited by hand on to a clean glass slide (same cleaning procedure) which in turn were placed on a 4-decimal place Sartorius Analytic A200S mass balance. A humidity sensor was placed inside the balance along with a small

bath of saturated magnesium chloride to monitor and control the humidity ($51\% \pm 3\%$), respectively. Readings were taken every minute and recorded.

2.3.4 FEM Simulations

FEM simulations were constructed in COMSOL Multiphysics v5.3a using the transport of diluted species and deformed geometry modules.⁷ The upper boundary of the droplet was set to move downwards at a rate calculated from optical measurements of the droplet whilst the width of the domain was held fixed to represent a pinned droplet. 10 mM Ca^{2+} and SO_4^{2-} ions were initially present in the droplet as well as 55 M water. A flux of water was applied to the bottom right corner of the simulation domain to drive the movement of water from bulk solution to the edge, to mimic the flow profile in an evaporating droplet. From the resulting diffusive flux of water, a velocity profile could be calculated which was used to calculate the convective movement of the Ca^{2+} and SO_4^{2-} ions. Diffusive fluxes were calculated using Equation 2.1:

$$R_i = \frac{\partial c_i}{\partial t} + \nabla(-D_i \nabla c_i) + u \nabla c_i \quad (2.1)$$

where the respective radial and vertical components of u were set to equal the local radial and vertical components of the diffusive flux divided by the local concentration of water. In this equation R_i is the net volumetric source for c_i , the concentration; t is time, D_i is the diffusion coefficient and u is the chemical potential.

At each time step, the top moving boundary of the droplet was shrunk by 1.6 $\mu\text{m/s}$ (measured experimentally) and the concentration changes of Ca^{2+} and SO_4^{2-} ions were calculated. At the same time water was set to leave a small vertical boundary at

the corner of the droplet at the same rate ($1.6 \mu\text{m/s}$) in order to promote a flow profile. A flux was applied to the ionic species such that as the boundary moved downwards (evaporated) there was a flux along the boundary based on the amount of the two species that was in the volume of droplet lost, meaning that the ionic species did not escape out of the top boundary. A simulation schematic is shown in Figure 2.3.

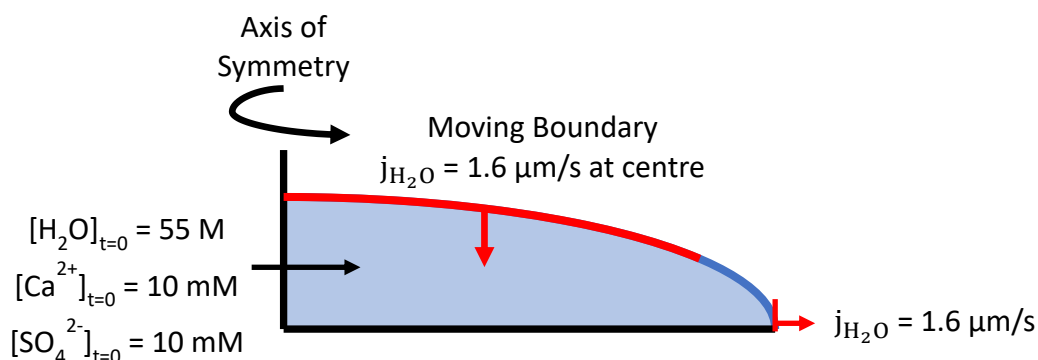


Figure 2.3: Schematic of the FEM setup used to study concentration changes inside an evaporating droplet. The movement of the top boundary was governed by experimental data and water was set to leave the vertical boundary at the same rate. An axis of symmetry is used to reduce computational strain.

2.3.5 Scanning Electron Microscopy (SEM)

SEM images were taken with a Zeiss Gemini ultra-high resolution SEM with a resolution of 0.6 nm at >1 kV. Samples were coated with ~ 80 nm gold Quorum Sputter Coater to combat local charging of samples.

2.3.6 Raman Spectroscopy

Raman spectra of crystals left after droplet evaporation were obtained using a Renishaw inVia Reflex Raman Microscope fitted with a Charge Coupled Device (CCD) detector with a 442 nm HeCd laser. In situ Raman spectroscopy for nanoprecipitation was performed by focussing the Raman beam at the end of the

nanopipette as the potential was applied. Raman spectroscopy for studying HKUST-1 used a 532 nm He-Cd laser.

2.4 Results and Discussion

2.4.1 Evaporation of a Calcium Sulfate Solution Droplet

Small droplets of calcium sulfate solution were recorded while evaporating through a two-camera setup as shown in Figure 2.2. These concentrations were chosen to replicate as close as possible the sort of additive concentrations used in industrial formulations, while also leaving the solution completely devoid of any precipitate $\text{CaSO}_4 \cdot \frac{1}{2}\text{H}_2\text{O}$. Droplets of $0.5 \mu\text{l}$ were used to fit the whole of the droplet in the microscope aperture. As the droplet evaporates, the crystals grow large enough to be seen by microscope (Figure 2.4), and thus some kinetics for crystallisation can be obtained. The moment for exact nucleation cannot be seen from this method, as the average nucleation site would be on the order of tens of nanometres.⁹ The resolution

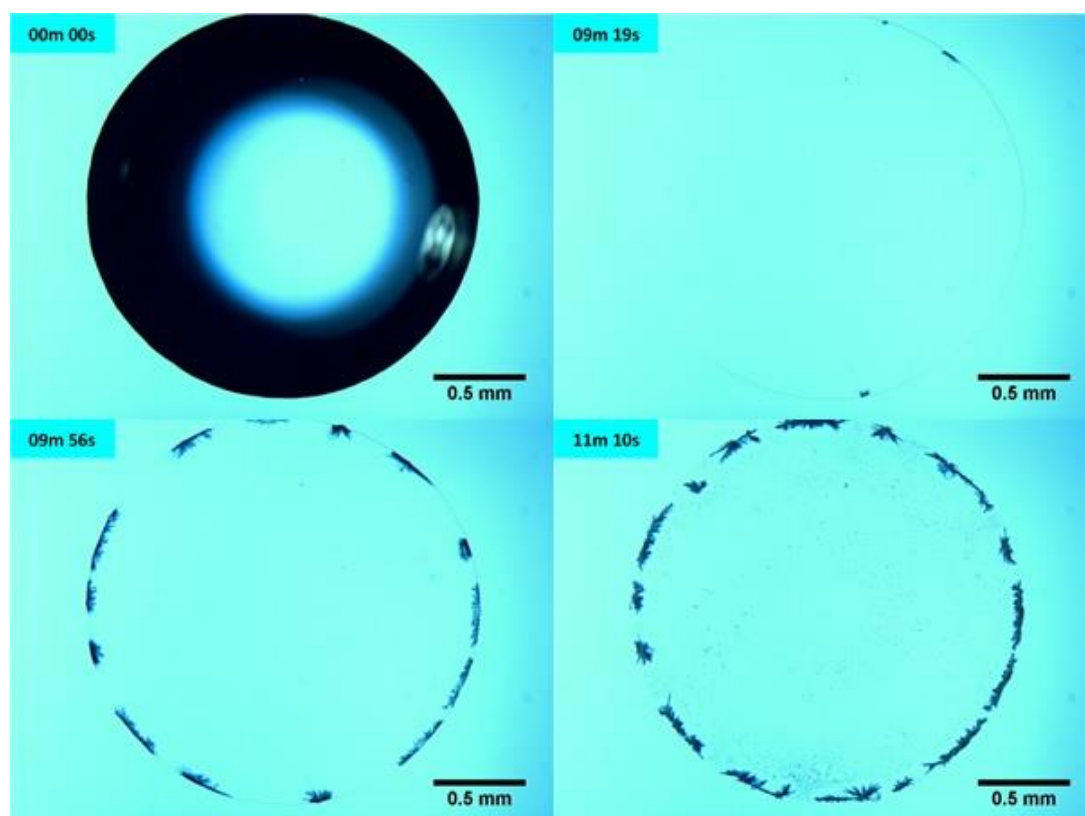


Figure 2.4: Snapshots of a video of a droplet of 10 mM CaSO_4 with no additive evaporating acquired through optical microscopy. From these videos the exact time for visible crystallisation can be extracted, down to a 1 second resolution.

of an optical microscope is limited by the wavelength of light, so nothing smaller than a few hundreds of nanometres is visible. So, from this data, the moment when a critical nucleus reaches a diameter of a few hundred nanometres can be viewed, down to a time resolution of a second.

The crystals obtained were always calcium sulfate dihydrate (gypsum), as confirmed by Raman spectroscopy, even when additives were included (Figure 2.5). The characteristic 1008 cm^{-1} peaks are always present. The other large peaks at $\sim 3500\text{ cm}^{-1}$ are due to water in the gypsum structure, and all of the other peaks are characteristic of gypsum. Data for the nucleation kinetics are shown in Figure 2.6. STMP, SHMP and citric acid show the average time to first visibly optical crystallisation to be longer than any other additive but from these data it was concluded that any differences between the majority of additives were negligible

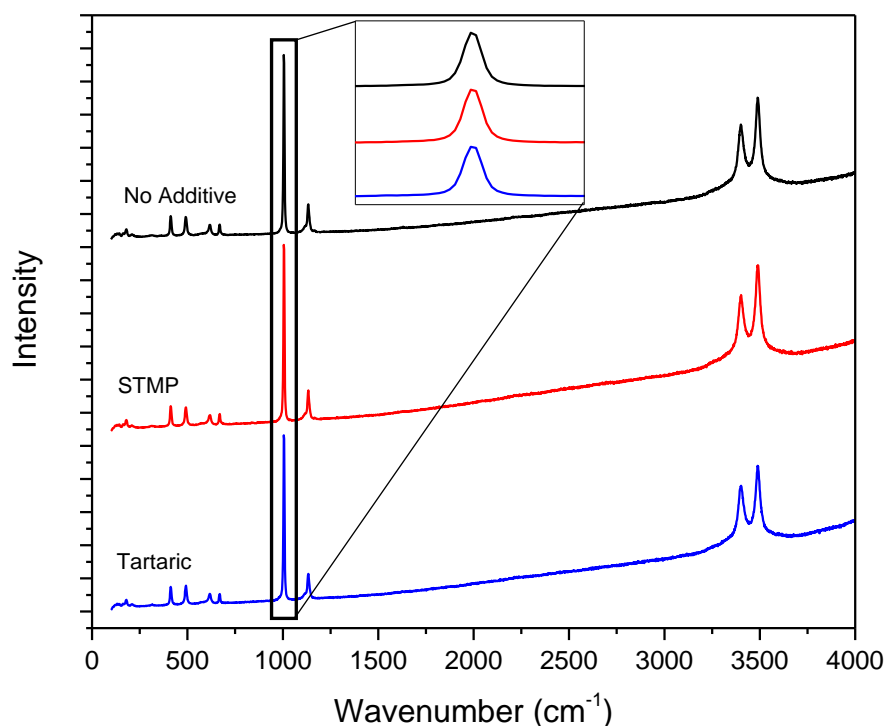


Figure 2.5: Raman spectra of gypsum crystals with additives incorporated. The additives do not change the Raman spectra.

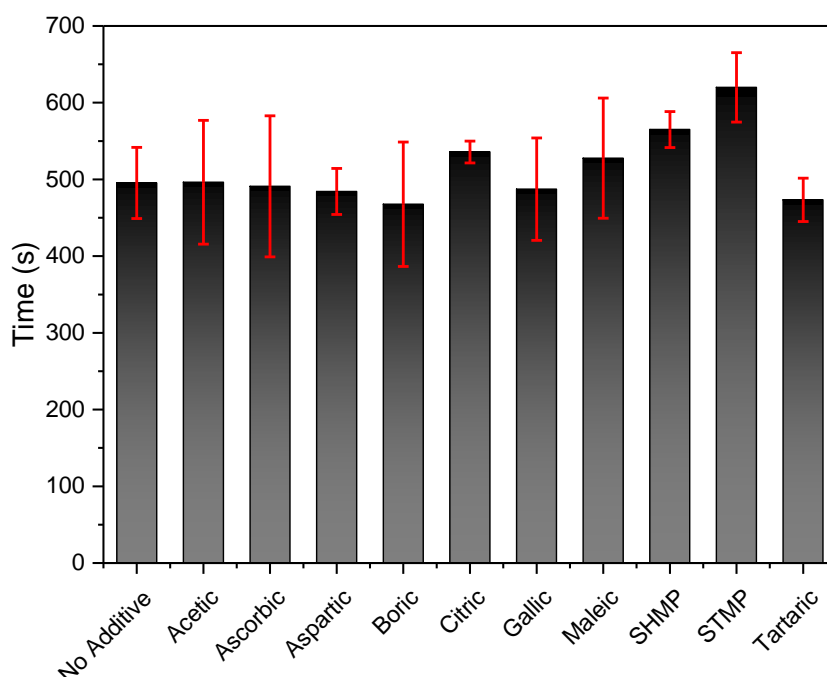


Figure 2.6: Time to average first optically visible crystallisation of gypsum, observed from videos.

when it comes to visible crystal formations as the standard deviations of each data series overlap with each other. The crystal shapes for these gypsum crystals with the additives incorporated are also different, as discussed later.

2.4.2 FEM Simulations of the Coffee Ring Effect

It has been seen that the crystal products that can be observed in these evaporation experiments are found around the circumference of the droplet. As mentioned above, this is attributed to the “coffee ring effect”, whereby, as a droplet containing particles evaporates, a ring like deposit is left at the end. The unequal distribution of evaporation across the surface of a pinned droplet leads to a flow profile that carries material to the edge where the droplet is pinned. In order to remain pinned, water needs to be drawn from the centre of the droplet to the edge to replace the water that evaporates, and this carries particles with it towards the edge.

Herein, time dependent FEM simulations were employed to mimic the flow profile found in such a droplet to approximate the saturation levels that would be typically achieved in experiments performed in this work. The movement of the droplet boundary with time was matched to the dimensions taken from typical optical measurements of the droplet. The flow profile was achieved through applying a flux of water out of the droplet from the point of pinning whilst, at this point, not allowing the droplet dimensions to change. This led to a diffusion gradient in the droplet of water from inside the droplet towards the edge. The convective flux experienced by the Ca^{2+} and SO_4^{2-} (initially present at 10 mM in the original droplet geometry) was calculated from the diffusive flux of water towards the edge.

Saturation level profiles were then extracted at different time points taken within the 550 second simulation run and are shown in Figure 2.7 along with the approximate flow profile in Figure 2.7a. It is important to note that these saturation values, Ω , defined as the positive square root of the product of the Ca^{2+} and SO_4^{2-} concentrations divided by the solubility of CaSO_4 in water (taken to be 14.5 mM/l)¹⁰, are semi-quantitative as the simulations do not take into account the effect of nucleation and growth processes that would begin once the value exceeds 1. While the calculation for saturation was defined by activity in Chapter 1, we use concentration here to simplify the model, as calculating the individual activities of ions at every time step requires a lot more time and computer power. The activity coefficient for each ion will be less than 1 (salt solutions are more energetically stable than ideal solutions due to electrostatic stabilisations) but for the purpose of visualising where the relative saturation is highest inside the droplet, using concentration gives an accurate visualisation.

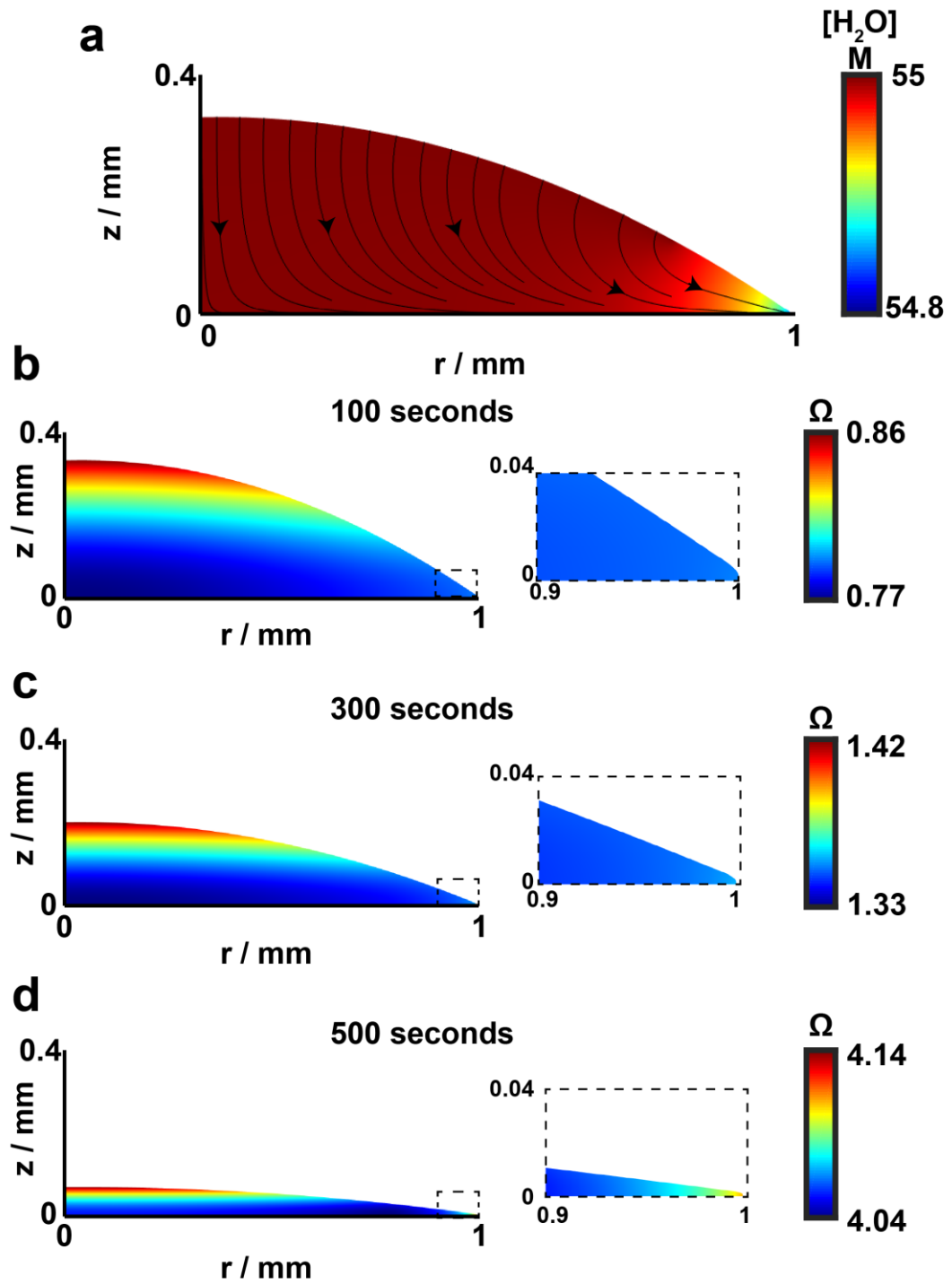


Figure 2.7: a) Flow profile in an evaporating droplet as a result of a movement of water from inside the droplet to the pinned edge. b-d) Saturation levels in the evaporating droplet after 100 s (b), 300 s (c) and 500 s (d) with insets showing a zoom of the pinned edge of the droplet.

The saturation profiles show that there is a greater saturation level at the top of the droplet where there is a high rate of evaporation in the vertical direction. The insets reveal that at the edge of the droplet there is a slightly enhanced saturation level and so these are the two places where initial nucleation events are most likely. It is also important to note that were nucleation and growth to initially occur near the top boundary of the droplet or indeed within the bulk of the droplet, the product would then move, as a result of the flow profile, to the edge and this is where the crystallisation products are observed experimentally.

2.4.3 Mass Measurements

To see if the additives had any significant effect on the evaporation rate of the droplet, the mass of 5 μ l droplets were recorded as they evaporated. The data are shown in Figure 2.8 for an average of 4 droplets with each additive. The scale used had a sensitivity of 0.1 mg, so the error in each measurement was relatively large. While the data shows some deviation in the evaporation rate between the additives, the error bars are large enough that they all overlap, so it is uncertain whether this evaporation deviation is real or not. Issues with keeping the humidity constant throughout the experiment throws some more doubt into the results, as the scale had to be opened for every new droplet application, and the environment inside the scale takes time to equilibrate to the desired humidity. The scale was also not airtight – ideally this experiment needs to be repeated in a glovebox to ensure no fluctuations in humidity, and with many more droplets with each additive to increase reliability.

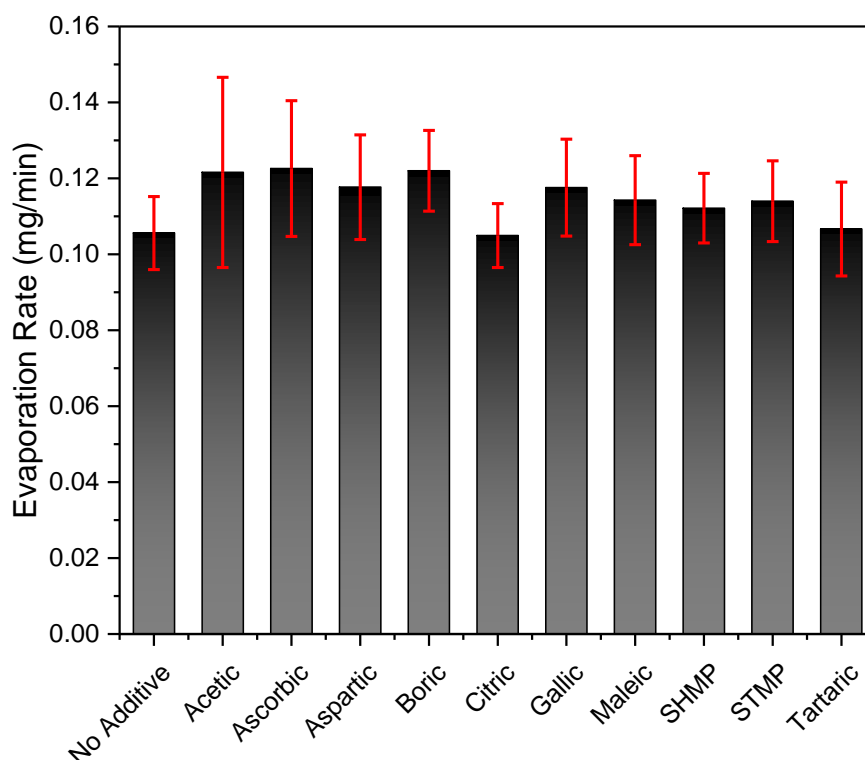


Figure 2.8: The changing mass of an evaporating 5 μ l droplet of 10 mM CaSO_4 and 0.5 mM additive over time. This data shows the average of 4 droplets of each additive evaporating at room temperature in a 50 ± 3 % humidity environment.

The evaporation rate of the droplets under different additive effects may be slightly different, but ultimately the deviations between each droplet are minor – as the sensitivity of the scale used to measure the mass was to the nearest 0.1 mg and the discrepancies between each evaporation rate is about ± 0.1 mg, conclusions from this study are hard to justify.

2.4.4 Contact Angle Measurement Studies

The contact angle of the droplet is of interest within the plaster industry due to the microstructure of plaster: the gypsum crystals are held together by thin water layers, and if the contact angle of these water layers change with each additive in solution, then this could be important when considering the mechanism of humid

creep inhibition. During droplet experiments, a camera was positioned perpendicularly so that the contact angle is clearly visible (example shown in Figure 2.2). The contact angle was seen to vary slightly between droplets, and the average contact angle over three droplets is shown in Figure 2.9. The contact angle can be seen to barely change across all of the samples, leading to the conclusion that none of the solutions tested affected the contact angle of the droplet. Any changes between contact angles of the droplets was put down to error in applying the droplet to the glass.

While the contact angle of the droplet on glass was easily measured, this is not necessarily similar to how the droplet behaves within the plaster structure due to there being no glass in gypsum. It is therefore of interest to measure the contact angle of water droplets on actual gypsum crystals, so droplets were applied to (001) gypsum

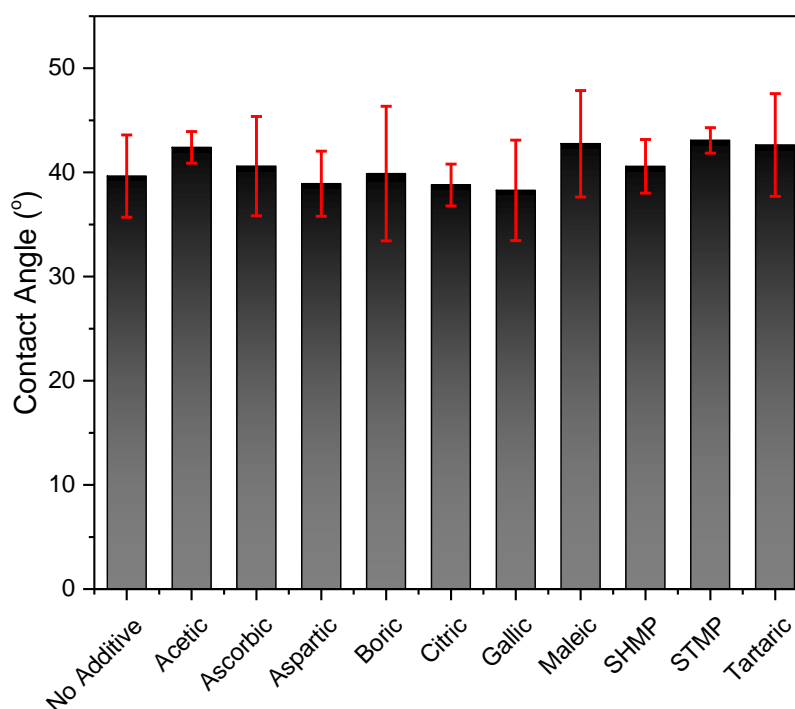


Figure 2.9: Contact angle of droplets containing 10 mM calcium sulfate and 0.5 mM respective additive on glass. This data shows the average of 3 droplets of each additive evaporating at room temperature.

crystal planes to better simulate two gypsum crystals being held together by the thin water layer. The droplets were saturated with $\text{CaSO}_4 \cdot 2\text{H}_2\text{O}$ to negate dissolution of the crystal face while the droplet was in contact. The crystal was treated by exposing the crystal surface to a 50 mM solution of additive, and the solution was allowed to evaporate, leaving a thin coating of the specific additive. Contact angles were then measured by the same procedure as before, presented in Figure 2.10. The large spread in data could be due to the gypsum (001) surfaces not being perfect, slight deformations in the surface could have appeared during cleaving. Another cause could be the amount of additive solution used to treat each sample – the surface areas of each gypsum surface were non-identical, yet the same volume of additive solution was used each time for treating. This would probably lead to a slightly different amount of additive on each gypsum surface, leading to potential skewing of results.

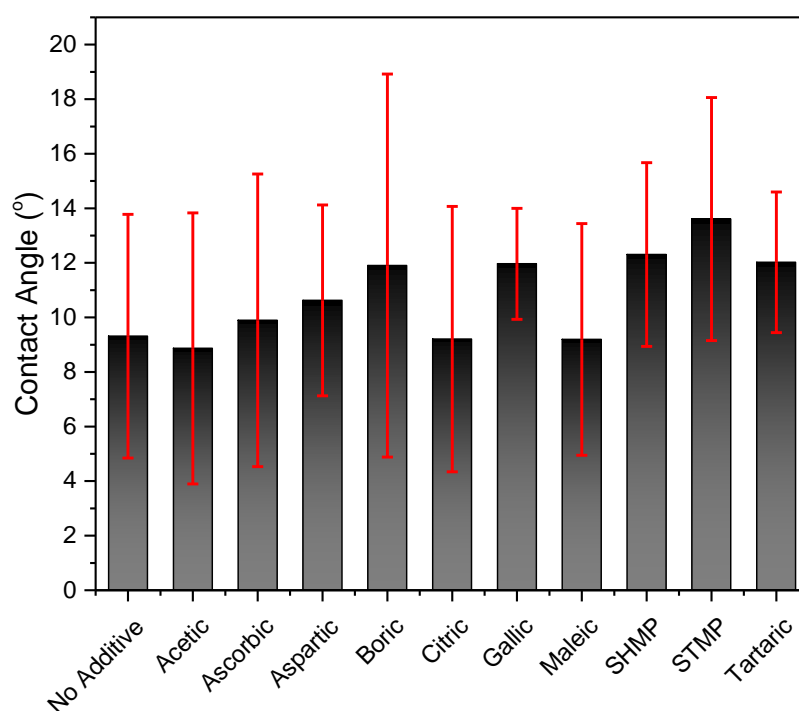


Figure 2.10: Contact angles of droplets containing 10 mM calcium sulfate and 0.5 mM respective additive on cleaved aged (010) gypsum basal plane. This data shows the average of 7 droplets of each additive evaporating at room temperature.

Droplets containing the additives were also tested on untreated gypsum crystal planes, but it was found that differences between the contact angles were negligible. While the data presented in Figure 2.10 may be unreliable, this could be early evidence that the contact angle is altered depending on what additive is upon the gypsum surface. Of interest is that STMP shows the largest contact angle, implying a slightly higher hydrophobicity of the gypsum than other additives. This hypothetically could be a reason as to why STMP works as the best additive – the water is allowed to spread less leading to a slightly more rigid structure.

2.4.5 SEM Study

The crystals formed by evaporation of the droplets from Section 3.2.1 (10 mM calcium sulfate hemihydrate and 0.5 mM additive) were analysed under SEM. Via SEM, differences in the crystal habits were visible depending on the additive. Distinct areas were also distinguishable within the remnants of the droplet (Figure 2.11), and were labelled (1) the outer edge where the majority of gypsum nucleated into larger crystals, (2) an ‘inner ring’ where much smaller and yet numerous crystals appeared, and (3) the centre of the droplet, where there was either a small amount of solid or no visible solid. All samples showed this inner circle matter with the exceptions of gallic acid and ascorbic acid. Only the control sample, the STMP sample, the aspartic acid sample and the acetic acid sample showed crystallisation in the centre of the droplet ring. The matter in the centre and inner-ring could be due to the Marangoni effect, where small convection currents within the droplet bring some of the solid back away from the edges.¹¹ The effect is not expected to be large as the glass slide is not heated, and efforts were taken to avoid any temperature increases.

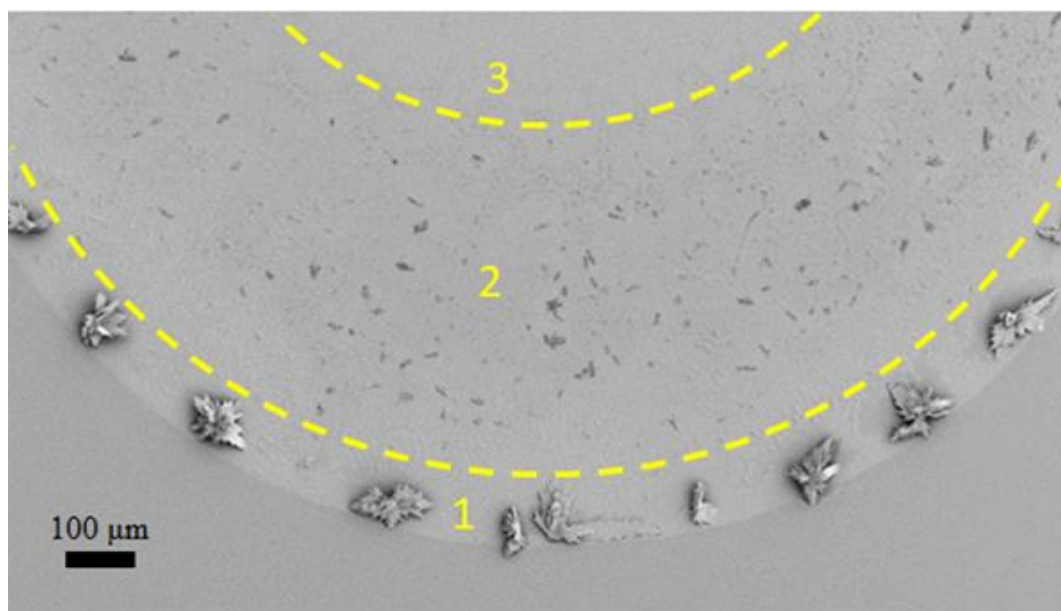


Figure 2.11: SEM image of an evaporated gypsum droplet. 3 distinct areas can be seen with different extents of gypsum nucleation.

Images showing the differences in gypsum crystal behaviour with the 10 different additives are shown in Figure 2.12. Of particular interest is the fact that with STMP and SHMP, the gypsum crystals formed were much smaller than anticipated, implying these additives inhibit the growth of gypsum crystals, but the amount of nucleation sites around the edge of the droplet remains largely the same (Figure 2.13). Given that STMP is widely considered one of the most effective humid creep inhibitors within the gypsum industry, this behaviour could be something that determines what makes it such an effective anti-sag inhibitor. It could be that if the crystals are smaller then there are more anchor points between crystals, meaning a tighter structure that is potentially less susceptible to humid creep. This droplet evaporation technique could then be a viable method for screening new additives and looking for crystallisation behaviour like that of STMP incorporated gypsum crystals.

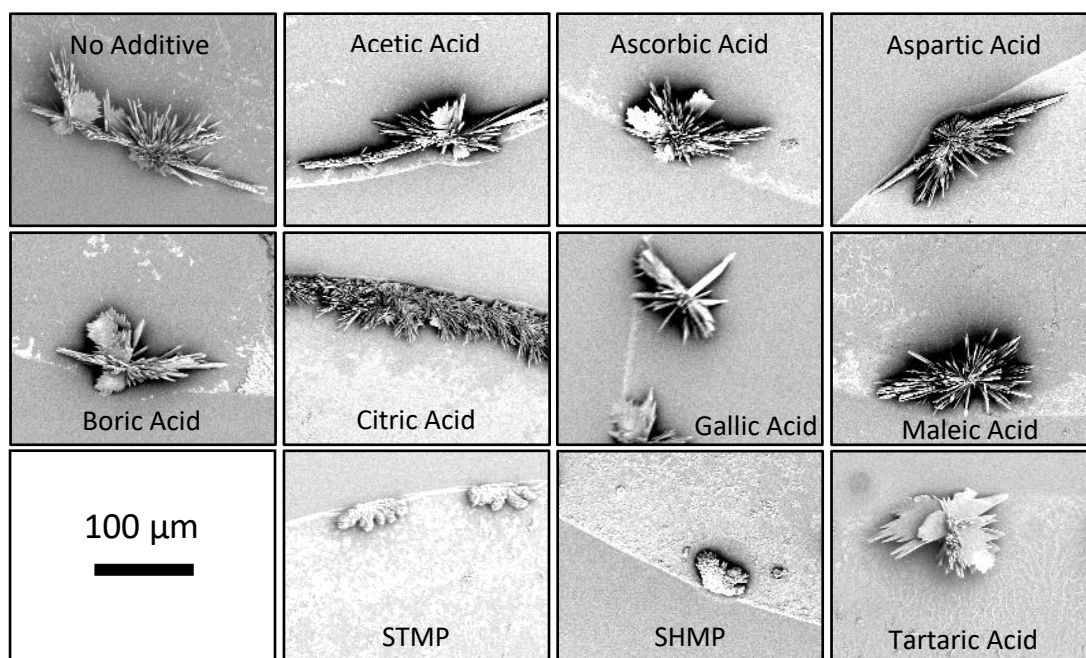


Figure 2.12: SEM comparisons of crystals around the outer edge of the evaporated droplet.

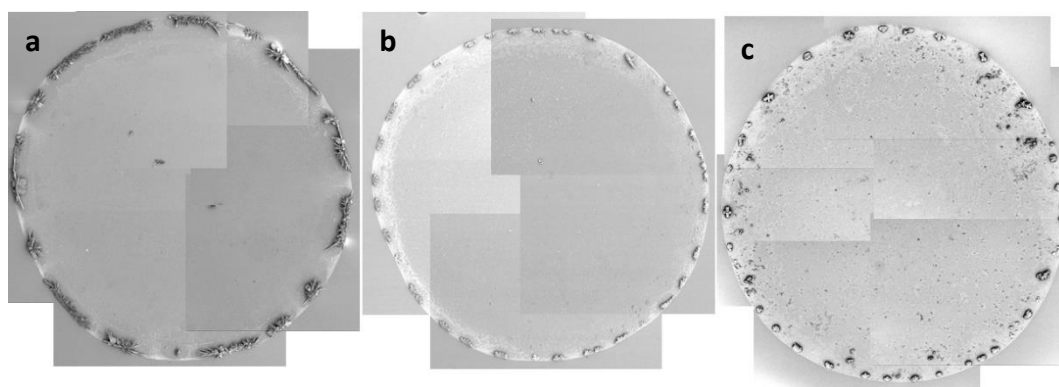


Figure 2.13: SEM comparisons of gypsum crystals around the outer edge of evaporated droplets. The nucleation density remains mostly the same when b) STMP or c) SHMP are added. The left image a) shows gypsum with the presence of no additives.

The majority of the additives do not seem to affect the crystal behaviour of the gypsum crystals that much, with acetic acid, ascorbic acid, aspartic acid, boric acid, maleic acid and tartaric acid giving similar results to the crystals with no additives. The only differences are the aforementioned STMP, SHMP, and citric acid. Citric acid seems to form a larger number of smaller individual crystals (compared to the crystals formed using other additives) that effectively fused together to form a constant ring of crystals, shown clearer in Figure 2.14. Gallic acid forms larger

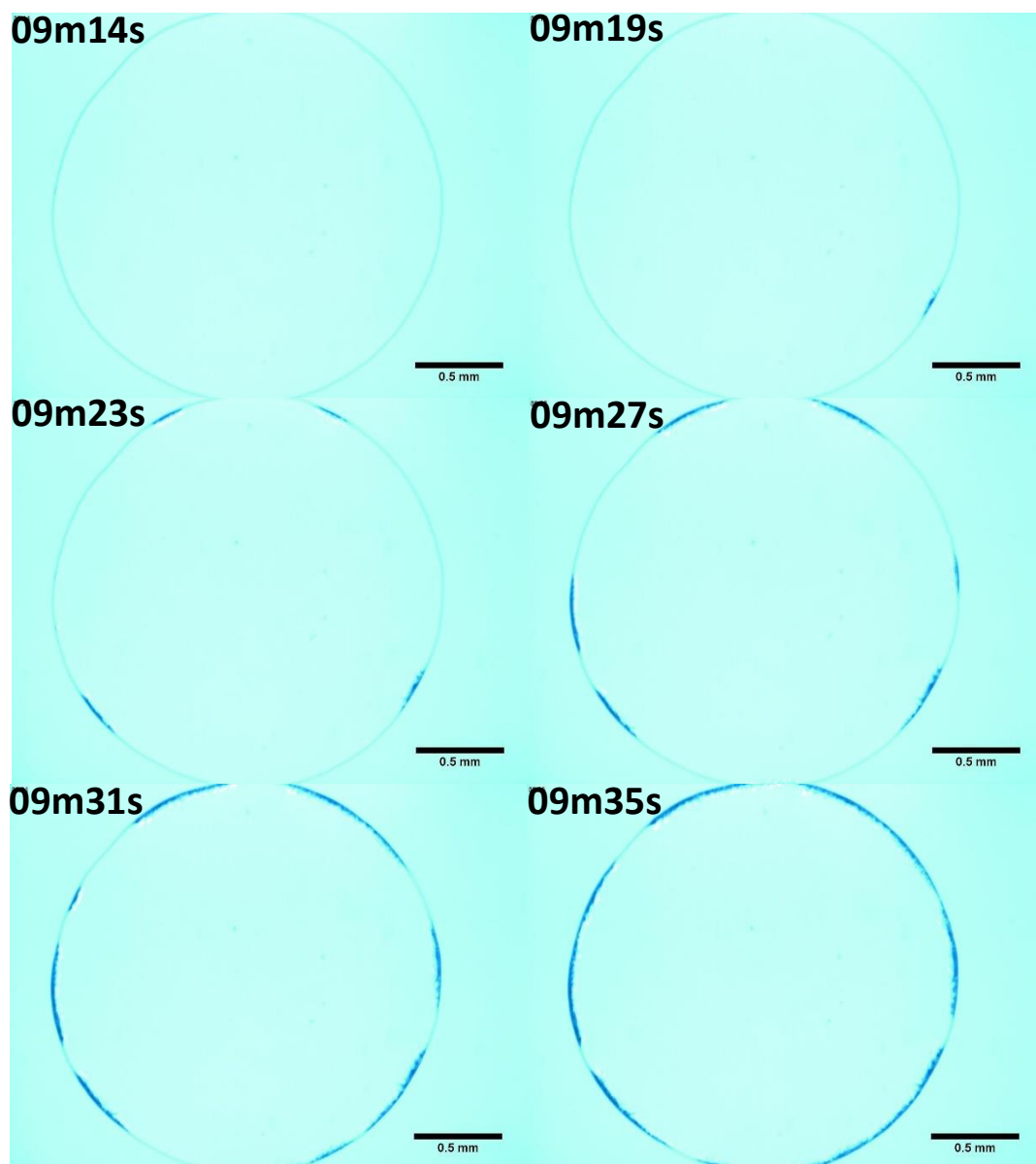


Figure 2.14: Snapshots of the nucleation of gypsum crystals with citric acid incorporated. The initial nucleation sites grow around the edge and eventually merge. Visible crystals only appear at the 9 minute and 19 second mark.

crystals, and not as many smaller crystals, which is even more obvious in Figure 2.15, but gallic acid is a known gypsum crystal growth inhibitor, so fewer crystals were expected.

In the inner ring of the evaporated droplet (area 2 referring to Figure 2.11), a variety of different size and shape of matter was seen. When no additive was present, curved crystallisation were observed in this inner ring (Figure 2.16). The crystals were

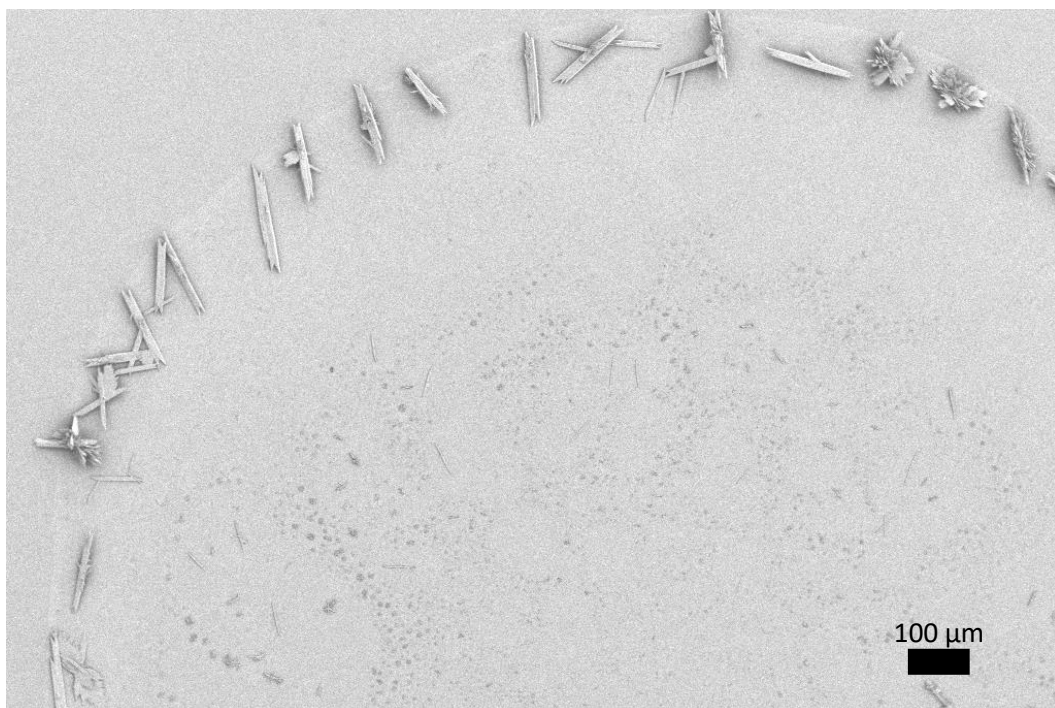


Figure 2.15: SEM image of an evaporated droplet of 10 mM calcium sulfate and 0.5 mM gallic acid.

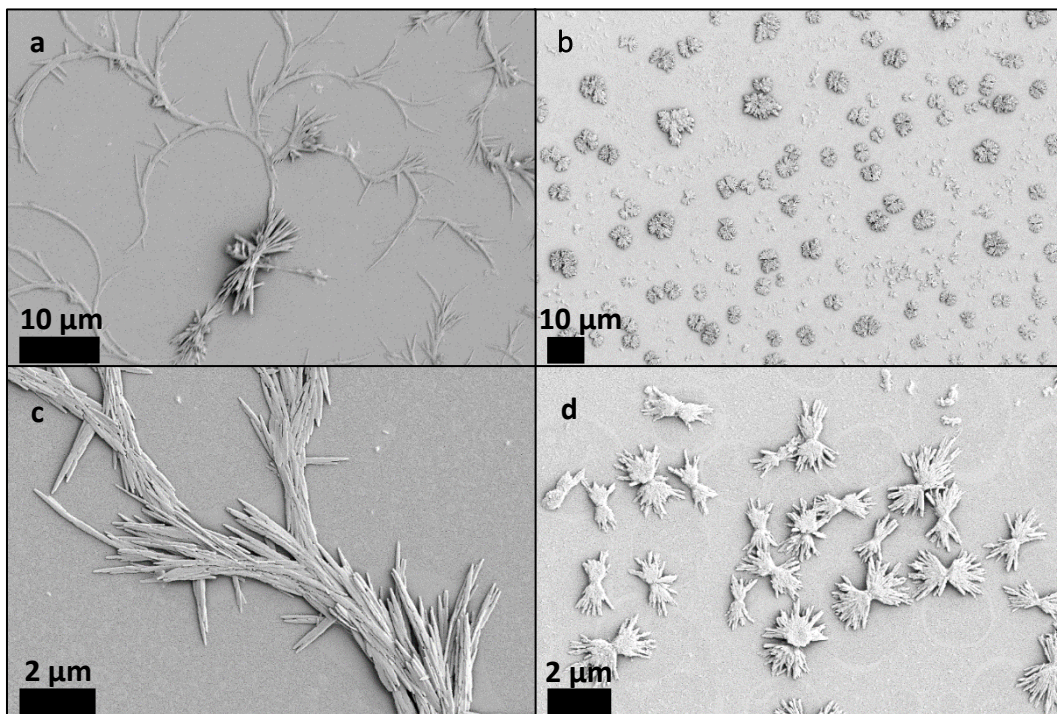


Figure 2.16: SEM images of a), d) curved crystals seen in the inner ring of some droplet areas and b), d) small crystal clusters seen in the inner ring of the STMP droplet areas. These are also visible in the SHMP samples (not shown here).

confirmed to be very thin gypsum crystals that stuck together and seemed to grow from each end, occasionally splitting off. This phenomenon was only observed for gypsum crystals with tartaric acid included. Tartaric acid also produced a number of small gypsum clusters, which were also observed for crystals with acetic acid, aspartic acid, boric acid, citric acid, gallic acid (to a much lesser extent), and maleic acid. These clusters were formed very late on in the droplet evaporation cycle – so the coffee-ring effect has not had time to take effect and the crystals nucleate and grow right where they are formed as the last of the liquid evaporates. In the inner ring of the STMP and SHMP droplets many small clusters of a different shape were observed, (Figure 2.16).

All of these additives clearly have some different effects on how the gypsum crystals nucleate and grow. The additives are all carboxylic acids or phosphates (with the exception of boric acid, which is a weak acid) which probably has something to do with how these additives behave with regards to the gypsum. It has been shown before that the ‘best’ additive, i.e. the additive that has the most humid creep inhibition for the smallest effect on the crystallisation behaviours of gypsum, STMP, has a favourable shape and size to bond with gypsum crystals. The O-O distance between STMP phosphate groups matches up with to Ca-Ca distances on the (120) and (-111) faces of gypsum.¹² In the case of the other additives, they bind through the attachment of the oxygen atoms in the carboxyl group, but the distance between them will not be as good a match as the O-O distances between the STMP phosphonate groups. It could be that the next best additive that has not been discovered yet could be a carboxylic acid or phosphonic acid where the O-O distance matches exactly with the Ca-Ca nearest distances.

2.5 Conclusions

In this study the relatively simple yet effective droplet evaporation experiment has shown how some common plasterboard additives effect gypsum nucleation and growth. The most effective anti-sag additives in STMP and SHMP show a severe slowing of the growth of gypsum crystals, but no slowing in the nucleation of gypsum crystals. There were also many more tiny nucleation sites in the inner ring of the droplet, showing that nucleation may be accelerated by STMP/SHMP, but the individual growth of these sites was severely hindered.

Most of the other additives do not show any significant difference from control gypsum samples with no additive used. The only other major difference was citric acid, which showed many small crystals being formed, so much so that the nucleation sites joined together and formed a large ring.

These findings have shown a potential easy to replicate screening technique for new additives. This technique could be used to study gypsum crystal behaviour and good candidates for new additives would show similar nucleation and growth behaviour to STMP and SHMP shown here.

Some of the experiments presented herein do deserve further attention, such as measuring the mass of a calcium sulfate droplet as it evaporates and seeing if including additives in the droplet affects the evaporation rate. Also worth considering is studying the contact angle of these droplets on perfectly cleaved gypsum planes – not just the (001) plane but also the other available planes, (011) and (120). Better control of the surface area of the planes would lead to a more reliable measurements of the contact angle, as well as making large single gypsum crystals with the additive already incorporated rather than treating the gypsum surface post-cleavage.

2.6 References

- ¹ R. D. Deegan, O. Bakajin, T. F. Dupont, G. Huber, S. R. Nagel, T. A. Witten, *Nature*, **1997**, 389, 827-829
- ² B. J. De Gans, P. C. Duineveld, U. S. Schubert, *Adv. Mater.*, **2004**, 16, 203-213
- ³ E. Tekin, P. J. Smith, U. S. Schubert, *Soft Matter*, **2008**, 4, 703-713
- ⁴ L. Wang, Y. Song, *Adv. Mater.*, **2014**, 26, 6950–6958
- ⁵ J. Jenczyk, M. Wozniak-Budych, M. Jarek, M. Grzeszkowiak, G. Nowaczyk, S. Jurga, *Appl. Surf. Sci.*, **2017**, 406, 235–244
- ⁶ Y. Hu *et al.*, *Applied Surface Science*, **2018**, 434, 626–632
- ⁷ R. D. Deegan, O. Bakajin, T. F. Dupont, G. Huber, S. R. Nagel, T. A. Witten, *Phys. Rev.*, **2002**, 62, 756.
- ⁸ R. D. Deegan, *Phys. Rev.*, **2000**, 61, 475
- ⁹ H. El-Shall, M. M. Rashad, E. A. Abdel-Aal, *Cryst. Res. Technol.*, **2002**, 37, 1264
- ¹⁰ E. Bock, *Canadian J. Chemistry*, **1961**, 39, 1746
- ¹¹ H. Hu, R. G. Larson, *J. Phys. Chem.*, **2006**, B 110, 7090
- ¹² E. Badens, S. Veessler, R. Boistelle, *J. Cryst. Growth*, **1999**, 198, 704

Chapter 3: Utilizing SICM Nanoprecipitation for Studying Dissolution and Crystallisation Kinetics of Gypsum with Humid Creep Additive Incorporation

3.1 Abstract

The nucleation, growth and dissolution kinetics of gypsum under additive effects are all examined via nanoprecipitation. All of the additives studied hinder the nucleation of new crystals and growth of existing crystals. Dissolution is slowed down by additives popular in the industry (tartaric acid, STMP) whereas some other additives seem to accelerate the dissolution (ascorbic, boric and gallic acid). FEM simulations show that at the concentrations used, the saturation of calcium sulfate is so high inside the nanopipette that precipitation of gypsum should be apparent, but it is theorised that total blockage of the nanopipette is difficult due to the needle-like geometry of the gypsum crystals and requires many crystals to be formed for complete blockage, with Raman spectroscopy data being used to back this up. The nanoprecipitation technique also proves a HKUST-1 nucleation theory presented previously in the literature showing the difference between the formation of HKUST-1 from either a copper acetate precursor or a copper nitrate precursor. The technique allows for an estimate of the HKUST-1 particle size when the copper nitrate precursor is used, limited only by the accuracy of the FEM simulation. Evidence for use of the HKUST-1 particles formed from copper nitrate as seeds for accelerated further MOF formation is shown.

3.2 Introduction

While the dissolution of single gypsum crystals has been explored in the presence of some additives,¹⁻⁸ and the crystallisation of gypsum also extensively explored,⁹ the early initial stages of nucleation and growth have not been studied as extensively. One of the issues with plaster is that the single crystal will not necessarily behave the same as the gypsum matrix present in plasterboard. In this study the nanoprecipitation and dissolution of gypsum crystals are studied in the presence of various additives. The relatively high solubility of gypsum makes for an interesting experiment as the crystals can be dissolved by a reversal of the bias, thus leading to the unique situation where the initial crystallisation and dissolution kinetics can be studied on the same specimen with the same apparatus. The effects additives have on the crystallisation and dissolution are also directly compared herein.

3.3 Materials and Methods

3.3.1 Solutions

All solutions were made in ultrapure 18.2 M Ω water (Purite, Select HP). Calcium sulfate hemihydrate powder (α -plaster, 99%) was supplied by Saint Gobain. Calcium chloride dihydrate ($\geq 99\%$) and sodium sulfate ($\geq 99\%$) were purchased from Sigma-Aldrich, along with all additives: ascorbic acid ($\geq 99\%$), boric acid ($\geq 99.5\%$), gallic acid ($\geq 97.5\%$), STMP ($\geq 95\%$) and tartaric acid ($\geq 99\%$). Nanopipettes were filled with 800 mM CaCl₂ and respective baths contained a solution of 200 mM Na₂SO₄ and 0.5 mM respective additive.

3.3.2 Nanoprecipitation Setup

Single barrel quartz nanopipettes of 50 nm \pm 10 nm were fabricated from Intracel item Q100-70-7.5 capillaries using a P-2000 Sutter Instruments laser puller and the diameter confirmed by TEM. The experimental setup is shown in Figure 3.1. Concentrations of 800 mM Na₂SO₄ and 200 mM CaCl₂ were used inside the nanopipette and the bath, respectively; concentrations this high were used to ensure that the supersaturation of calcium sulfate was high enough at the tip end to force crystallisation. The disparity between the two solution concentrations was to neutralise the difference in diffusion field shapes of the nanopipette and the bath. In the bath there is hemispherical diffusion towards the nanopipette tip, whereas in the nanopipette the diffusion field is effectively linear, so there would be many more cations from the bath meeting at the tip than anions from the nanopipette. Thus, a higher concentration was used in the tip to ensure a more stoichiometric system. A two-electrode system was used with two Ag/AgCl quasi-reference counter electrodes

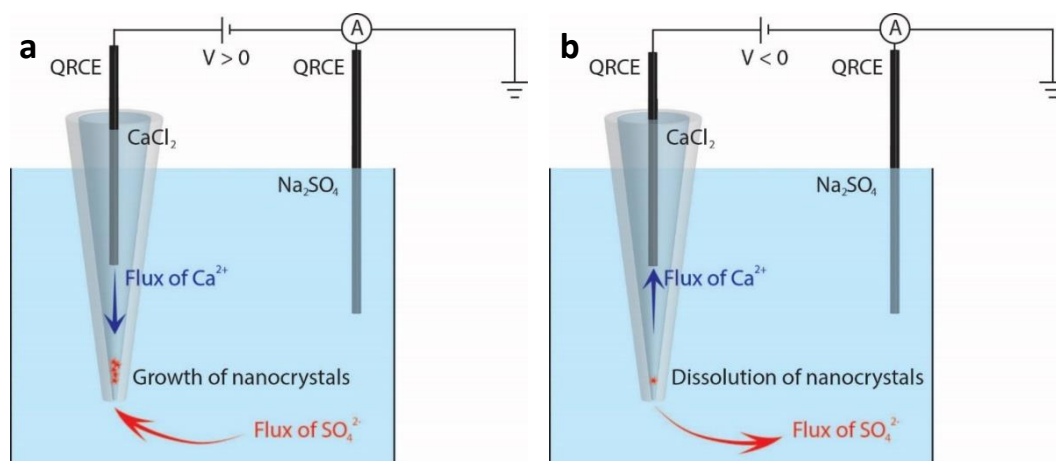


Figure 3.1: Schematic of SICM setup where a) the tip is being blocked by applying a positive potential to the nanopipette thus raising the saturation level of CaSO_4 and b) the crystals formed are being dissolved by a reversal of the potential and the consequential drop in CaSO_4 saturation.

(QRCE) fabricated freshly for the experiments from silver wire and a KCl solution. A potential of $+0.5 \text{ V}$ or -0.5 V was applied to the nanopipette to induce crystallisation or dissolution of gypsum respectively.

The electrode in the nanopipette was connected to a computer through a home-built potentiostat, and the current measured by a current follower through the QRCE in the bath. The data were visualised and the potential controlled through the LabView Design System Software, which has been tailored to the needs of the Warwick Electrochemistry and Interfaces Group (WEIG). Data were then saved and analysed through MATLAB in order to gather crystallisation and dissolution kinetics.⁸

3.3.3 Data Analysis

Data were analysed in MATLAB using a custom script made for this project. The script separated the crystallisation and dissolution events and analysed them separately by checking the voltage applied at the nanopipette. The script analyses and calculates the time taken for the current to drop to 10% of the open nanopipette

current, and then pulls out the time taken for the current to return to 90% of the open current once the potential was reversed. In each experiment the potential was reversed at least 20 times, so an average of repeated crystallisation and dissolution was obtained. The first crystallisation/dissolution event for each experiment was ignored so the analysis does not give false readings as the system was equilibrating.

3.3.4 FEM Simulations

Finite element method simulations were performed in COMSOL Multiphysics using the transport of diluted species and electrostatics modules to visualise where the saturation of CaSO_4 is highest inside the nanopipette. A 2D axisymmetric geometry representing a 50 nm diameter nanopipette in bulk solution was constructed based on transmission electron microscopy (TEM) data. The saturation level of CaSO_4 was calculated at each time step at each mesh point as stated previously in Chapter 2. Again, the activity coefficient will be less than 1 in this system meaning the calculations are only semi-quantitative but for the purpose of visualisation this simplification was deemed acceptable. Steady state simulations were performed with a fixed bias which was applied at the top of the nanopipette domain, that was varied in multiple simulations between 0 V and 0.5 V. The nanopipette domain contained 800 mM calcium chloride solution, relative to the outer domain of the bath solution, which contained 200 mM sodium sulfate. As all currents in the simulation were normalised, this did not affect the outcome or accuracy of the simulation. Ionic transport was assumed to follow the Nernst-Planck relationship, where the flux, J_i , of species, i , is given as:

$$J_i = -D_i \Delta c_i - z_i \frac{F}{RT} D_i c_i \nabla \phi \quad 3.1$$

and the Poisson equation describes the electrical potential, ϕ :

$$\nabla^2 \phi = -\frac{F}{\varepsilon \varepsilon_0} \sum_i z_i c_i \quad 3.2$$

where c_i denotes the species concentration, D_i and z_i denote the diffusion coefficient and charge number of the charge of species i and F , R , T , ε and ε_0 specify constants: the Faraday constant, gas constant, temperature, relative permittivity and vacuum permittivity, respectively.

3.3.5 Scanning Electron Microscopy (SEM)

SEM images were taken with a Zeiss Gemini ultra-high resolution SEM with a resolution of 0.6 nm at >1 kV. Samples were coated with ~80 nm gold Quorum Sputter Coater to combat local charging of samples.

3.3.6 Raman Spectroscopy

Raman spectra of crystals left after droplet evaporation were obtained using a Renishaw inVia Reflex Raman Microscope fitted with a Charge Coupled Device (CCD) detector with a 442 nm HeCd laser. In situ Raman spectroscopy for nanoprecipitation was performed by focussing the Raman beam at the end of the nanopipette as the potential was applied. Raman spectroscopy for studying HKUST-1 used a 532 nm He-Cd laser.

3.3.7 Transmission Electron Microscopy (TEM)

A JEOL 2000FX transmission electron microscope was used to image nanopipettes where SEM was not effective enough. A 200 kV accelerating voltage was used in order to get information on the inner geometry of the nanopipettes.

3.4 Results and Discussion

3.4.1 FEM Simulations and Initial Blocking of the Nanopipette

FEM simulations were first set up in order to gain some understanding of the saturation level of CaSO_4 . A simulation result is shown in Figure 3.2. The figure shows that after 10 seconds of +0.5 V applied voltage at the nanopipette, the saturation level is already very high, thus leading to the conclusion that the concentrations used were acceptable. Figure 3.3 shows the effect of the applied potential at the tip using 800 mM CaCl_2 and 200 mM Na_2SO_4 in the nanopipette and bath respectively, and shows that even at no potential applied, the saturation is already very high, so some crystallisation would be expected. However, when it came to the real experiment, no crystallisation was seen from following the current flowing through the nanopipette. This seems to be due to the crystallisation behaviour of gypsum – namely that gypsum

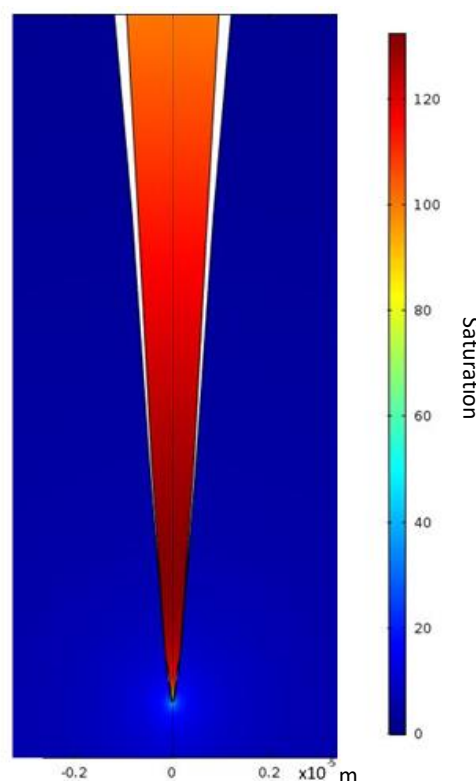


Figure 3.2: FEM simulation of the saturation inside a nanopipette after applying 0.5V at the tip for 10 seconds.

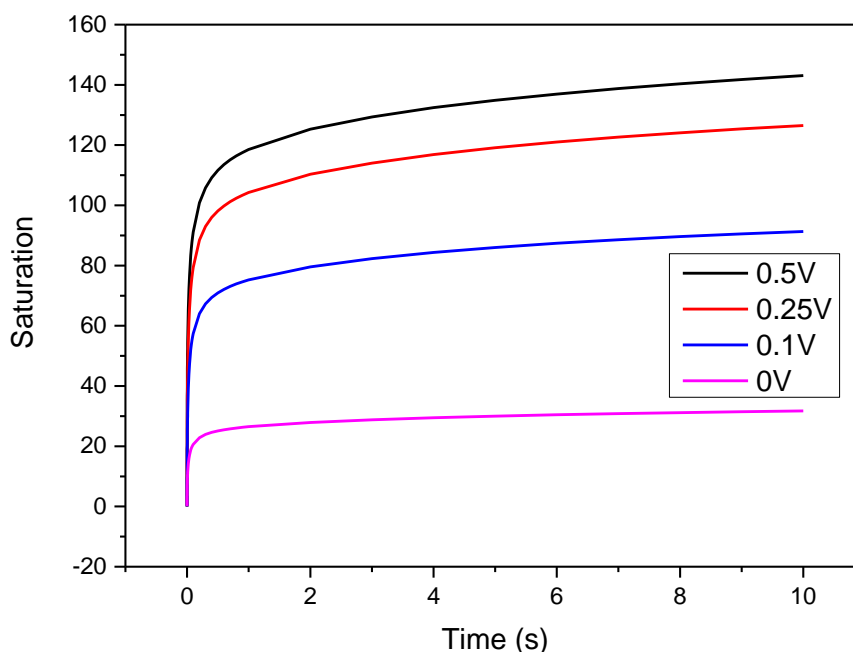


Figure 3.3: Simulated maximum saturations as a function of potential applied to the nanopipette. The saturation is already greater than zero even when no potential is applied.

crystals are needle-like in shape. Needles do not block the circular hole of a nanopipette efficiently, so multiple gypsum crystals need to be layered and meshed together to achieve full blocking. It was discovered that the best way to accomplish this was to apply a very strong potential to the nanopipette. In this case +10 V was used.

This 10 V application lead to the nucleation of enough crystal seeds that the crystals were dissolved upon application of -0.5 V, but then recrystallised to complete blocking upon application of $+0.5$ V. One interesting feature of the initial nanopipette blocking at 10 V is that the current transients looked different and distinct patterns were visible. As shown in Figures 3.4 and 3.5, there were 3 distinct transient shapes; a) a fairly constant current measurement followed by a sudden drop to zero current indicative of complete blocking of the nanopipette, b) large variations in current before a sudden drop and shape c) which shows a ‘parabola’ shaped transient in which

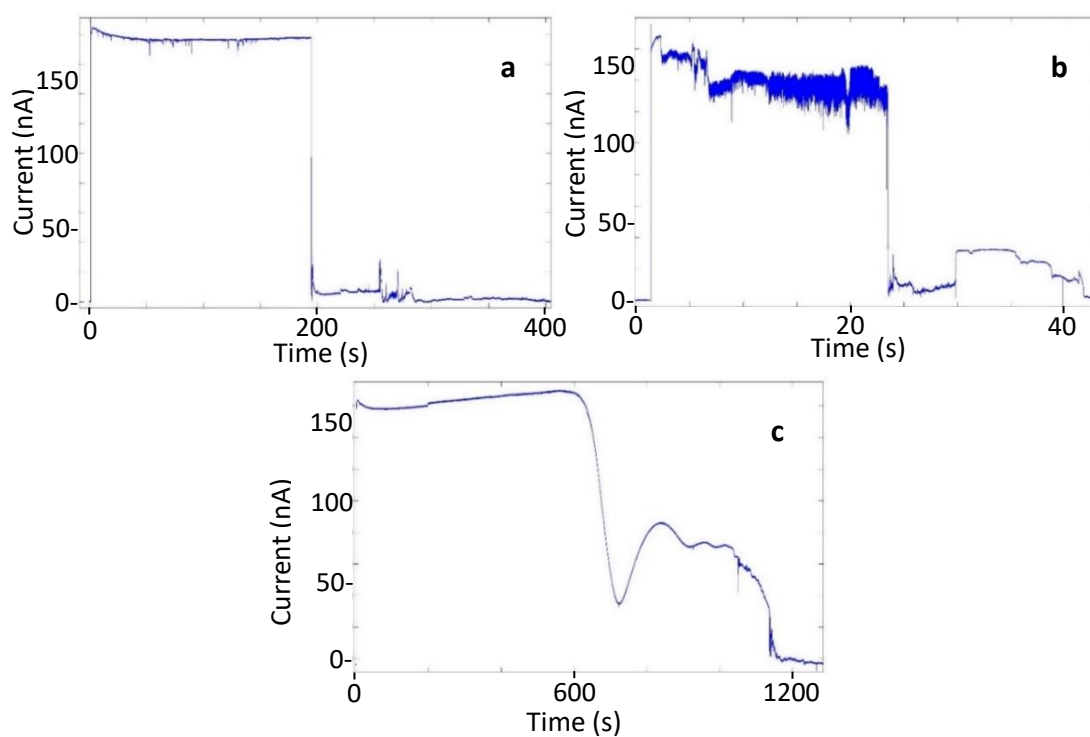


Figure 3.4: Blocking transients after applying 10 V to the nanopipette. 3 different shapes are seen; a) little activity followed by very sudden blocking, b) large electrical noise followed by sudden blocking, c) 'parabola' shaped transient followed by blocking.

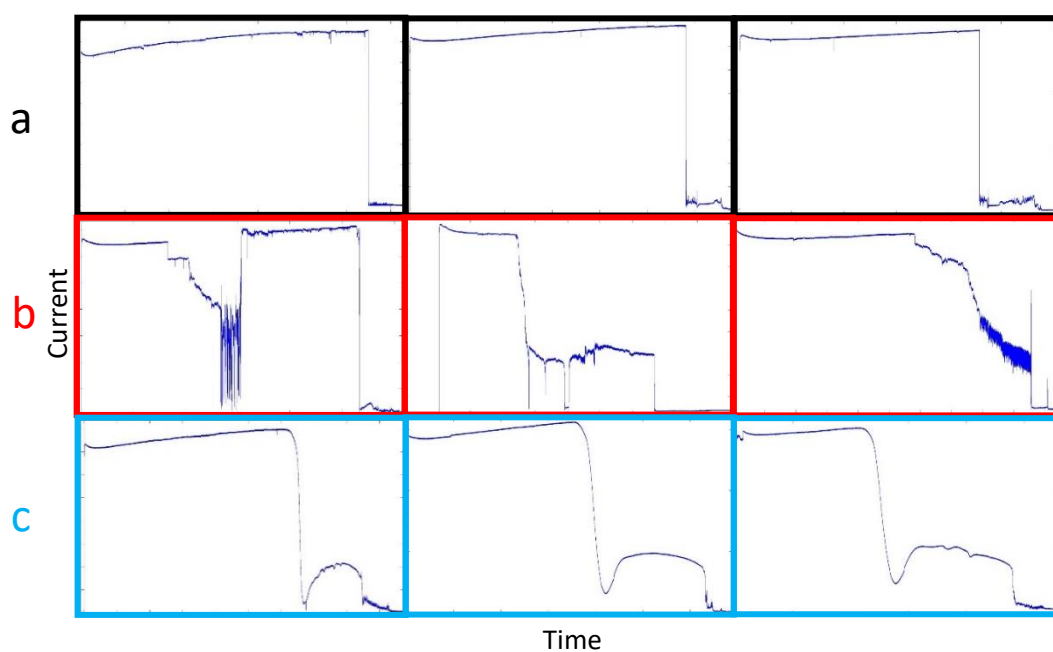


Figure 3.5: More examples of each blocking shape; black: shape a), red: shape b), blue: shape c).

the current reaches a local minimum before rising and then quickly dropping towards zero current.

The hypotheses for these transient shapes are that a) very small crystals are formed but do not block the nanopipette until they aggregate or find the “correct” orientation to block the nanopipette, b) slightly larger crystals form and move around inside the nanopipette (leading to large variations in current) before complete blocking similar to shape a), and finally shape c) which could be the formation of a larger crystal that moves or rotates slowly inside the nanopipette before locking into a blocking position. This is a difficult hypothesis to prove as previous work has only been performed with the crystallisation of amorphous clusters of crystals, and gypsum is slightly unique with its needles shape crystal structure. The eventual full blocking shows some similar aspects to shapes a) and b) in that the blocking is either slow after the large crystal settles, or the transient is noisy and then the blocking is very sudden, indicating lots of smaller crystals settling around the large crystal.

These different shapes are more common among certain additives as shown by Table 3.1 (data shown in Appendix). Not using any additive shows a high affinity for shape b), where lots of small crystals seem to form and move around inside the

Table 3.1: Distribution of transient shapes for gypsum forming inside a nanopipette. Entries highlighted are the majority shape seen for that additive. n=23 for no additive and tartaric, 22 for STMP, 10 for boric and ascorbic, and 7 for gallic

Shape	No Additive	Tartaric	STMP	Boric	Gallic	Ascorbic
a	13%	28%	59%	20%	0%	20%
b	57%	8%	14%	60%	0%	60%
c	17%	56%	27%	10%	14%	10%
No Block	13%	8%	0%	10%	86%	10%

nanopipette before the sudden blocking. STMP has a high proportion of shape a) which implies an abundance of small crystals (too small to cause significant electrical noise as seen in shape b) are blocking the nanopipette. Tartaric acid seems to more likely form a larger crystal as shown by the high percentage of shape c). These findings shed some light on early crystallisation of gypsum under these additive conditions. STMP forms many smaller crystals, implying that the nucleation is not slowed, but the growth of these crystals is slowed. Tartaric acid tends to form a mix of large crystals and smaller crystals. Some of this behaviour has been confirmed previously, with Chen *et al* showing that STMP incorporation leads to much smaller gypsum crystals.¹¹ This observation has also been seen in Chapter 2, the evaporative study where growth of gypsum crystals is hindered. Boric acid and ascorbic acid seem to show similar crystallisation behaviour to when no additive is used, implying that these additives do not affect the crystallisation to any significant extent.

The largest outlier though is gallic acid, with no blocking seen (except in one case) within the timeframe of the experiment, which was cut off at 2700 seconds (45 minutes). This doesn't necessarily mean that there are no crystals forming inside the nanopipette, but that they never grow big enough to block the nanopipette. From Chapter 2 we see that gypsum crystals grown with gallic acid are much larger than any other gypsum crystals with any other additives (Figure 2.15), so gallic acid does not necessarily restrict the size of gypsum crystals. The difference in the droplet evaporation experiment and the nanoprecipitation experiments are the methods that the crystals are forming from: in the droplet evaporation experiment the water has to evaporate and the solute has to precipitate somewhere, whereas in the nanopipette the water is not leaving the environment, meaning that precipitation is not guaranteed. The saturation inside the nanopipette is extremely high but growth of crystals to the

extent of blocking the nanopipette is still not possible. These studies combine to show that gallic acid slows down the growth of gypsum crystals considerably, but if forced, will form larger but fewer crystals. However, from the droplet experiment, we also see that some smaller crystals are formed in the inner ring of the droplet (Figure 2.11, zone 2). If these crystals form inside the nanopipette, they clearly rarely grow big enough to block the nanopipette completely. Hypothetically rather than forming a large number of smaller crystals that can block the nanopipette, the gypsum with gallic acid favours fewer, larger crystals meaning there are large gaps in between the crystals – thus no complete blocking of the nanopipette. Both of these hypotheses are feasible but given that the nanopipette did completely block in one of the experiments, the latter seems more likely than gallic acid just stopping nucleation and growth of gypsum.

Another interesting aspect of this study is determining how long the additives affect the initial nanopipette blocking, shown in Figure 3.6. The full blocking event is extremely stochastic in nature, as can be seen from the large error bars in the figure. The results in Figure 3.6 are an average of 25 blocking events so the random nature of the experiment is clearly inherent and not down to a small sample size. It is clear from this figure though that all of the additives hinder the formation of this initial blocking of the nanopipette, so it can be confirmed that the additives are slowing down the initial nucleation of gypsum crystals. Gallic acid clearly affects the growth the most, but the high average blocking time is due to the large percentage of nanopipettes that did not block after 2700 seconds. The one nanopipette that did block took 2443 seconds and showed the parabola shaped transient from shape c) (see Appendix for current-time data).

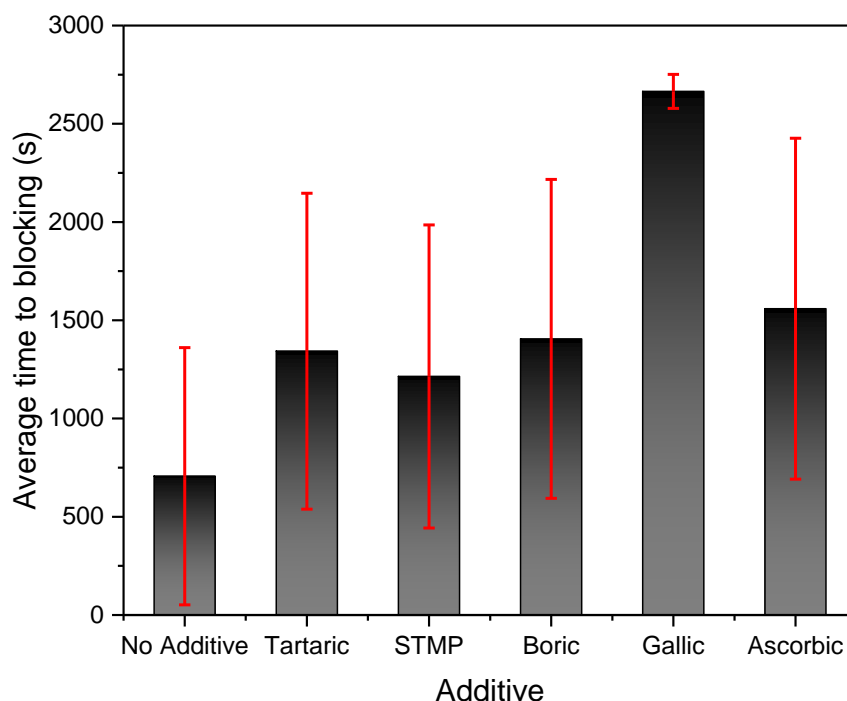


Figure 3.6: Average time to full tip blocking (current drop to zero) after application of 10 V to the nanopipette. $n = 25$.

3.4.2 In-Situ Raman Spectroscopy

To confirm that the formation of solid inside the nanopipette was in fact gypsum and not any other polymorph or hydrate of calcium sulfate, in-situ Raman spectroscopy was performed. The setup is shown in Figure 3.7, which is effectively the same SICM setup from Chapter 2, but the nanopipette is almost perpendicular to the surface of the bath. In this configuration a beam from a Raman microscope can be focussed on the end of the nanopipette as the voltage is applied. Raman spectra were taken at the end of the pipette every 30 seconds and the resulting spectra are shown in Figure 3.8a. There is only a few wavenumbers difference between the characteristic bands of gypsum and the other two calcium sulfate hydrates of bassanite and anhydrite ($\text{CaSO}_4 \cdot \frac{1}{2}\text{H}_2\text{O}$ and CaSO_4 respectively) but Raman spectroscopy is sensitive enough to distinguish the hydrates (Figure 3.8b).¹² A gypsum peak (1008 cm^{-1}) appears after about 510 seconds (Raman spectrum 17) and proves that blocking

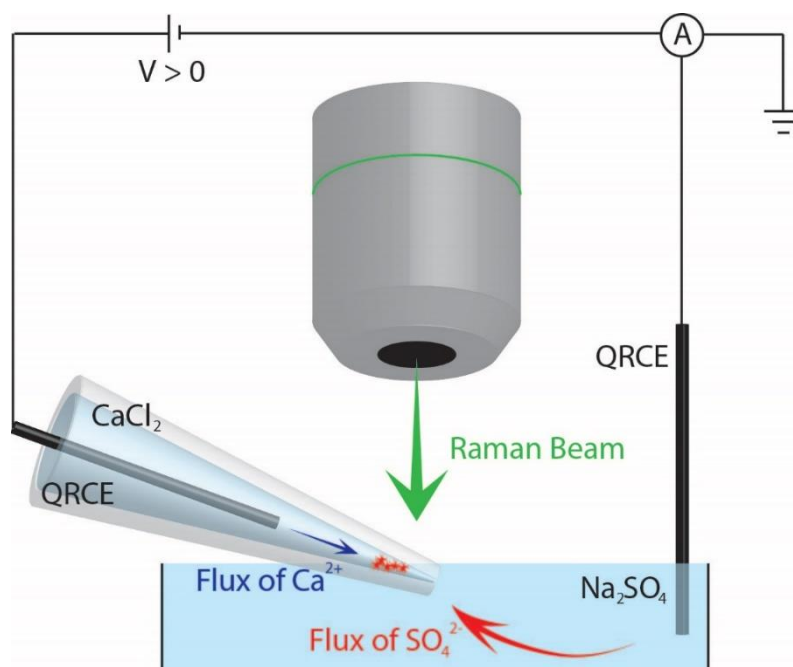


Figure 3.7: Experimental setup of SICM under a Raman beam showing the formation of CaSO_4 crystals due to application of a positive potential at the nanopipette.

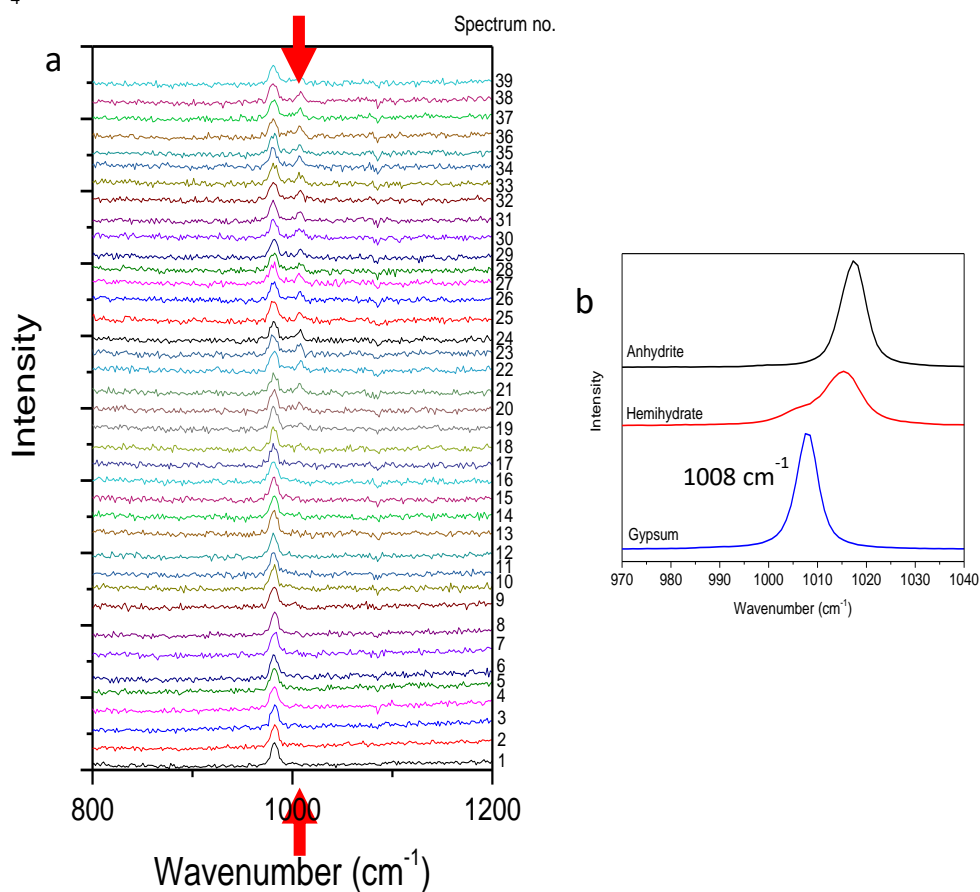


Figure 3.8: a) Raman spectra taken every 30 seconds while applying +10 V to the nanopipette and b) the Raman spectra of gypsum compared to the other CaSO_4 hydrates. The peak at $\sim 950 \text{ cm}^{-1}$ is from the sodium sulfate in solution. The red arrow in a) alludes to a peak at 1008 cm^{-1} , which matches the peak for gypsum in inset b).

of the nanopipette and resultant drop in current is due to the formation of gypsum only and no other calcium sulfate hydrate. Theoretically gypsum is formed instantaneously upon application of a pushing voltage, but the Raman required the luck of a crystal forming directly under the Raman beam, or for an existing crystal to move under the beam.

3.4.3 Cycling Nanoprecipitation and Dissolution

Once the nanopipette has been blocked once by application of +10 V to form the seeds, cycling of crystallisation and dissolution was possible. Application of -0.5 V unblocked the pipette after the initial blocking, and then reversing the potential to +0.5 V would re-block the pipette. This process was utilized in order to study the growth/dissolution kinetics of gypsum inside a nanopipette. The fact that the initial nanoprecipitation is so stochastic in nature proved a challenge between different nanopipettes, as any slight difference in geometry could change the crystallisation behaviour. This problem was solved by using the same nanopipette for all additives, with the CaCl_2 solution in the tip containing no additive, and the bath containing all of the additive. This meant that the nanopipette was able to be reused and the bath switched out for a bath containing a different additive, thus studying different additives removing the error of different nanopipette geometries.

A typical crystallisation/dissolution transient is shown in Figure 3.9 and a full set of 20 transients shown in Figure 3.10. The first step is as a positive voltage is applied (+0.5 V), an initial positive current is measured before rapidly dropping to zero as the gypsum crystals inside grow and block the nanopipette. When the potential is reversed (to -0.5 V), the crystals rapidly dissolve, which can be seen from the rapid

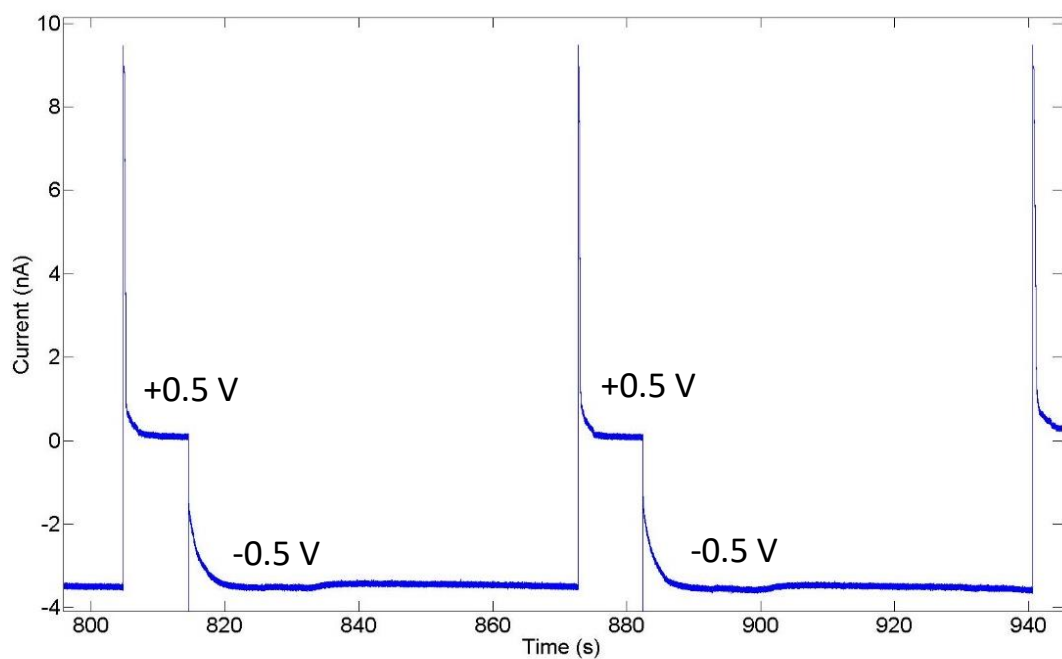


Figure 3.9: Example of blocking/unblocking transients inside a nanopipette. The current drops to zero as a positive potential is applied and then opens again upon reversal of the potential.

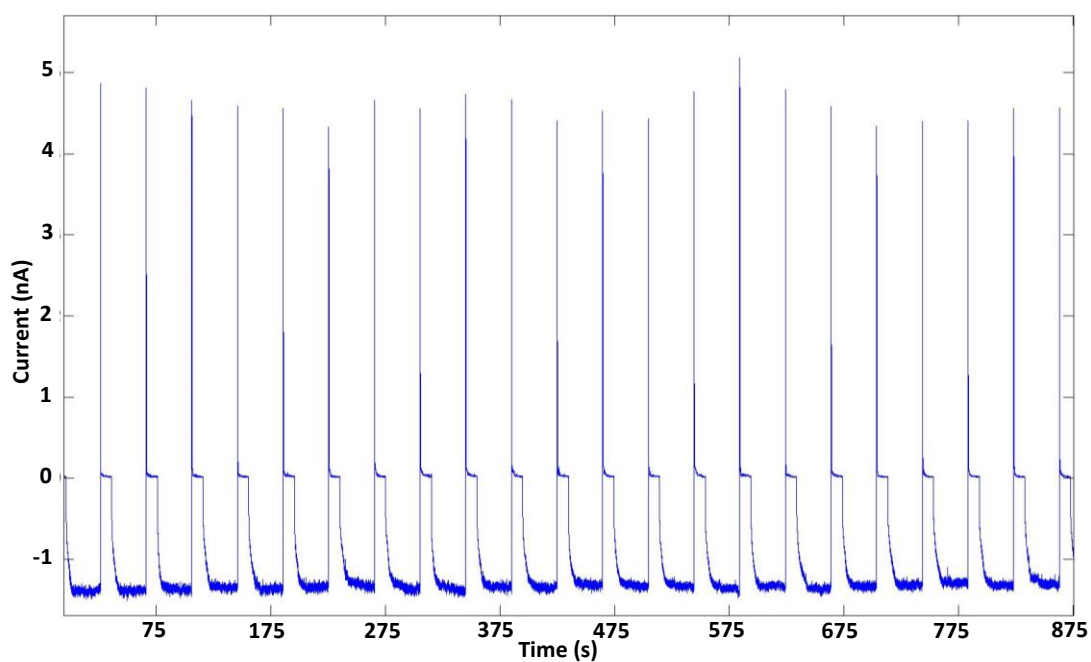


Figure 3.10: Example of a full set of blocking/unblocking transients inside a nanopipette. The nanopipette is left at a negative potential long enough so that the pipette unblocks reliably.

modular increase in negative current, which reaches a plateau as the nanopipette opens again, reaching a steady state current. The process is then repeated 10 or 25 times to get a good statistical average. The difference in the currents applied is due to the difference in the concentrations of the two solutions in the nanopipette and bath.

Averages of crystallisation and dissolution for 20 crystallisation/dissolution cycles with the same nanopipette using different additives are shown in Figure 3.11. Tartaric acid and STMP clearly significantly hinder both the crystallisation and dissolution of gypsum. These facts are fairly widely known^{12,15} but do not necessarily show how these additives work as humid creep inhibitors, given that STMP is the most effective anti-creep additive yet tartaric acid slows the crystallisation and dissolution slightly more effectively in this experiment. This implies that STMP works as a humid creep additive by doing more than just inhibiting the crystallisation and dissolution.

Tip blocking experiments with the other additives (ascorbic acid, boric acid and gallic acid) showed that these additives are not nearly as effective at hindering the dissolution of gypsum, but they severely slow the crystallisation. Both of these effects are bad for humid creep additives as the crystallisation being slowed down so much would lead to a much slower process inside the factory when making plasterboard. A faster dissolution would indicate that the sag effect would be reduced as the most likely mechanism of humid creep is the pressure-solution creep effect.¹⁰ These findings point to why ascorbic acid, boric acid and gallic acid are not commonly used in the plasterboard industry, whereas STMP and tartaric acid are.

While the crystallisation and dissolution are important steps in the pressure-creep mechanism, it has been shown by Schug *et al.* that STMP preferentially binds

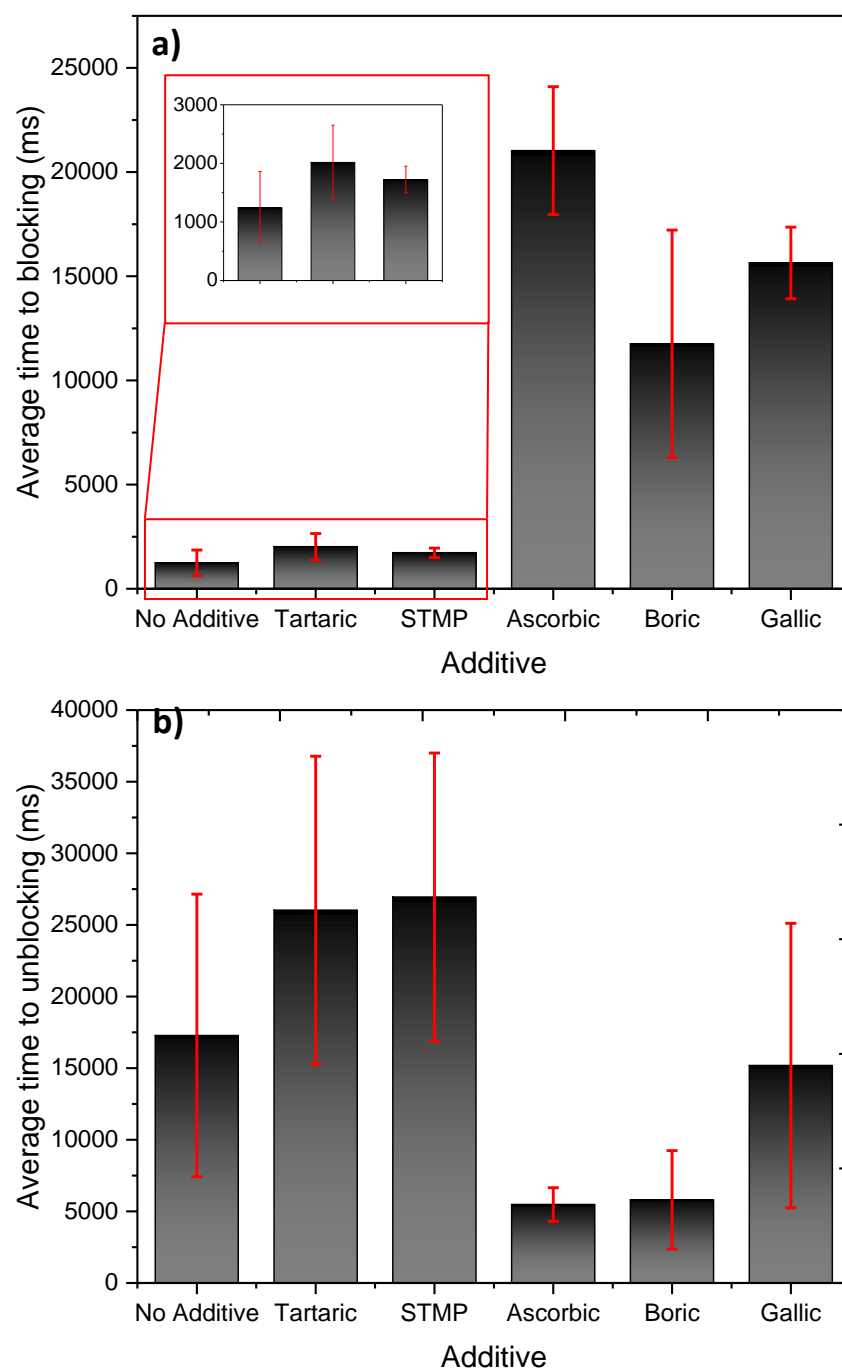


Figure 3.11: Average crystallisation (a) and dissolution (b) times inside a nanopipette upon reversing the potential applied to the tip between +0.5 V and -0.5 V.

with calcium sites on the (100) and (001) gypsum crystal planes, and they suggest that STMP sits in the thin water layers that bind crystals to act as a glue to hold crystals together, which would grant the gypsum crystal matrix much higher mechanical strength.¹³ These sorts of studies are not possible within the SICM setup used herein as the crystals form in-situ, meaning that water is still heavily present around each crystal. For STMP to become active as a humid creep inhibitor, the samples must be dry so that these thin water layers between crystals can form. Insight into how other humid creep additives is yet unknown, but it could be theorised that other additives work in the same manner, STMP is believed to be the most effective due to its O-O distances being very similar to the Ca-Ca distances on gypsum surfaces. Analysing the crystallisation and dissolution kinetics of these additives does not provide all of the information needed to determine what will make a good additive. This problem in studying additives is almost unique to gypsum due to the interesting growth patterns it forms (a matrix of needles), whereas other previously studied crystals with this technique (such as CaCO_3) form amorphous growths of crystals with little macro-interactions between crystals.¹⁰

3.5 Nanoprecipitation of HKUST-1

3.5.1 Introduction

Metal organic frameworks (MOFs) are a category of porous solids made from the reaction between organic and inorganic (metal ion) species to create a three-dimensional framework connected by strong bonds. Unlike zeolites that require the use of templates, MOFs require only a solvent in which to dissolve the organic and inorganic species.¹⁴ The exact structure adopted by a MOF will depend on the typical coordination geometry of the metal ion and the connectivity of the multidentate ligand used. MOFs exhibit some level of porosity and this porosity can be tailored and used in a variety of fields including catalysis and sensors.¹⁵⁻²⁰

MOFs which can be functionalised without compromising chemical or thermal stability are of interest. One such material is HKUST-1, or $\text{Cu}_3(\text{BTC})_2(\text{H}_2\text{O})_3$ (BTC = benzene-1,3,5-tricarboxylate), first synthesised by Chui *et al.* in 1999.²¹ The stability of HKUST-1, ease of synthesis, and high porosity have led to it becoming a focus of research concerning the mechanisms of formations and behaviour of MOFs as a whole.²² It is thermally stable up to temperatures of 240 °C and also has many potentially useful applications including heterogeneous catalysis, gas purification, separation and storage.²³

In HKUST-1, dimers are formed from the co-ordination of oxygen atoms from the BTC ligand bridging pairs of Cu^{2+} ions (shown in Figure 3.12.²⁴ Each Cu^{2+} is coordinated to 4 oxygen atoms from the ligands, and also an additional oxygen atom from a coordinated water molecule (or other solvent). These dimers are linked by others via the BTC ligands to form a three-dimensional system of square-shaped pores (each pore measuring 9 Å by 9 Å), and sub-nanometre pore channels, similar to

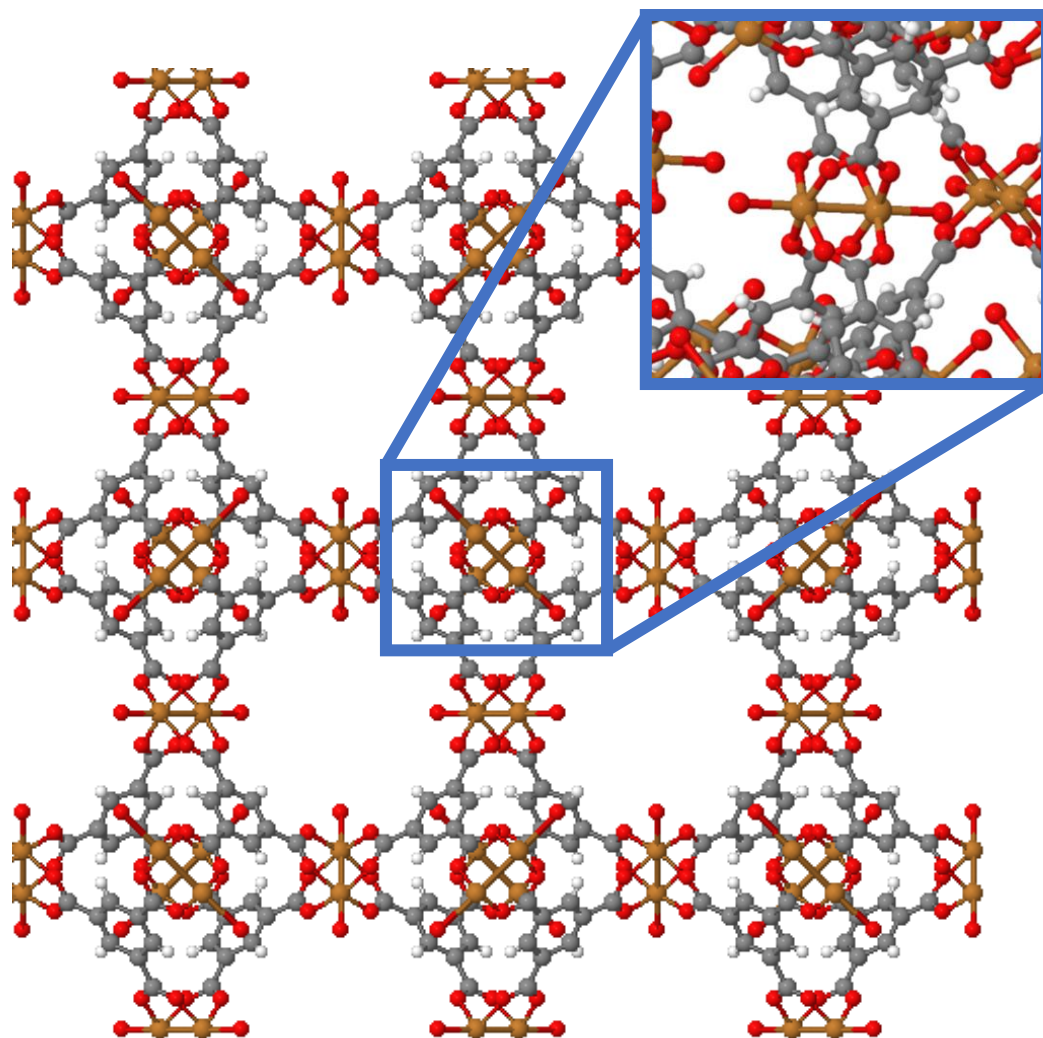


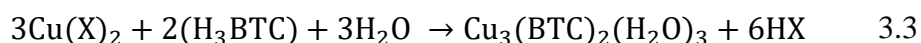
Figure 3.12: The crystalline structure of HKUST-1 (courtesy of ChemTube3D). Brown = Cu, grey = TMA, red = oxygen. The large pores can be seen in in this schematic. Inset: a clearer image of the copper dimers

zeolites. HKUST-1 is blue in colour and extremely hydrophilic, but it can be dehydrated, removing all water ligands, while preserving its overall crystalline structure.^{24,25}

When dehydrated, metal sites in the nanopore walls can coordinate to gas molecules such as dihydrogen, nitric oxide, nitrogen and carbon dioxide.²⁶ Wang *et al.* used HKUST-1 as a molecular sieve for the separation and purification of gases, in particular showing how it can be used for the separation of mixtures such as carbon dioxide-carbon monoxide, carbon dioxide-methane and ethylene-ethane.²⁷ The

adsorption properties of HKUST-1 also make it useful as a sensor. Wang *et al.* also found that HKUST-1 can adsorb up to 40 wt % water, which allowed Allendorf *et al.* to develop a microcantilever coated with a thin film of HKUST-1 which responded rapidly and reversibly to the presence of gaseous H₂O, methanol and ethanol.²⁸ Upon the removal of the copper-bound water, the copper sites of HKUST-1 can act as Lewis acids, making HKUST-1 a potentially useful catalyst. Schlichte *et al.* found that chemisorption by HKUST-1 activates benzaldehyde for liquid phase cyanosilylation, with a 57% yield and high selectivity (compared with a control of 10 % yield).²⁹ Alaerts *et al.* showed that the active sites of dehydrated HKUST-1 are hard Lewis acids, and that HKUST-1 can be used as a catalyst for the isomerisation of terpene derivatives including the rearrangement of α -pinene oxide to campholenic aldehyde, and the cyclisation of citronellal to isopulegol.³⁰

A versatile and commercially viable synthesis of HKUST-1 was proposed by Huo *et al.*, in which a one-pot synthetic route is used involving vigorous mixing of a copper (Cu²⁺) salt solution with a suspension of trimesic acid (H₃BTC) at 298 K in a reaction medium of water (Equation 3.3).³¹



where X can be an acetate, nitrate or chloride ion. The ease of this synthesis makes it a significant improvement over previous methods for its relatively low temperatures, while its convenience and versatility make it easy to replicate and adapt. This synthetic method was used to show that the copper precursor used has a dramatic effect on the precursors formed before the generation of bulk HKUST-1 (Figure 3.13). When Cu(NO₃)₂ is used as the precursor, slow nucleation is observed, followed by

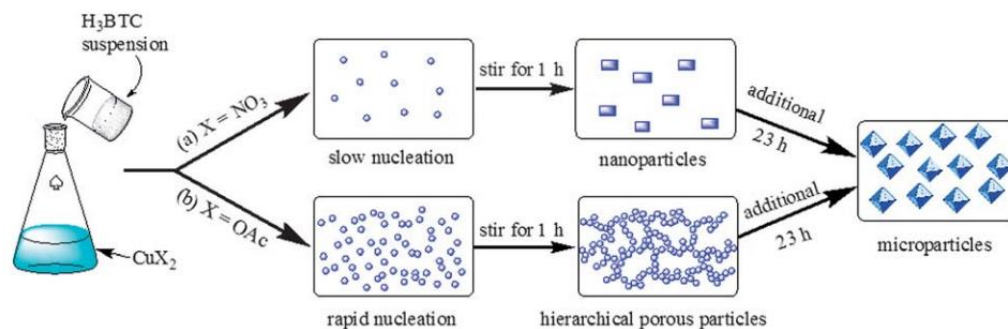


Figure 3.13: Schematic of the one pot reaction route for HKUST-1 presented by Huo *et al.* Depending on the copper precursor used, different synthetic routes are taken.³¹

the formation of discrete nanoparticles after an hour of stirring. Alternatively, when the same experimental set up was applied using a $\text{Cu}(\text{OAc})_2$ precursor, the result was fast nucleation, and the formation of hierarchical porous HKUST-1 particles, where particles of HKUST-1 agglomerate to form a porous structure. After a further 23 hours of stirring, each precursor resulted in microparticles of HKUST-1, each with a similar yield of ~90%. It is worth noting that other precursors can be used, with a CuCl_2 precursor showing successful HKUST-1 formation, but with a <40 % yield. Other studies as well have shown that the ratio of copper precursor to trimesic acid is important, with an excess of trimesic acid leading to a decreased formation of HKUST-1 due to the formation of over-coordinated species at the expense of less coordinated building units.²²

Given that the one-pot synthesis presented by Huo *et al.* needs only two reagents, and can be performed at room temperature, the system seems well suited to follow in the nanoprecipitation blocking experiment shown with gypsum previously. While the synthesis shown by Huo *et al.* and subsequent analysis is performed *ex situ*., the introduction of nanopipettes into the system allow for an *in situ*. examination of the HKUST-1 formation. Herein the mechanism presented by Huo *et al.* for HKUST-

1 particle formation is tested, with implications of the effects that HKUST-1 particle formation inside a confined environment shows.

3.6 Materials and Methods

3.6.1 Solutions

All solutions were made in ultrapure 18.2 M Ω water (Purite, Select HP). Benzene-1,3,5-tricarboxylic acid (≥ 95 %, also referred to as trimesic acid or TMA) solutions were made in dimethyl sulfoxide (≥ 99.7 %, DMSO), both purchased from Sigma-Aldrich. While the original suspension proposed by Huo *et al.*⁹ used only water as a reaction medium, trimesic acid was not soluble in water, so DMSO was used as it was miscible with water.

3.6.2 Experimental Setup

Single barrel nanopipettes of ~ 30 nm diameter were fabricated from quartz capillaries (outer diameter of 1.00 mm and an inner diameter of 0.50 mm) using a laser puller (P-2000, Sutter Instruments). Larger single barrel nanopipettes with diameter ~ 5 μ m were fabricated from borosilicate glass capillaries (outer diameter of 1.00 mm and an inner diameter of 0.58 mm) using the same laser puller but under different parameters.

The experimental setup for nanoprecipitation is shown in Figure 3.14. A two-electrode setup was used with quasi-reference counter electrodes of Ag/AgCl inside the nanopipette and droplet. The change in solvent should not change the structure of the HKUST-1 as DMSO molecules are much larger than water molecules, and they should not fit in the structure. The concentration ratio between the copper salt and trimesic acid was 5:2. A 1:2 ratio of copper to BTC reagents is normally needed, as reported in the literature³¹, but the difference in the diffusion fields means that a larger proportion of BTC⁻ ions will reach the nanopipette than Cu²⁺ ions. The difference in

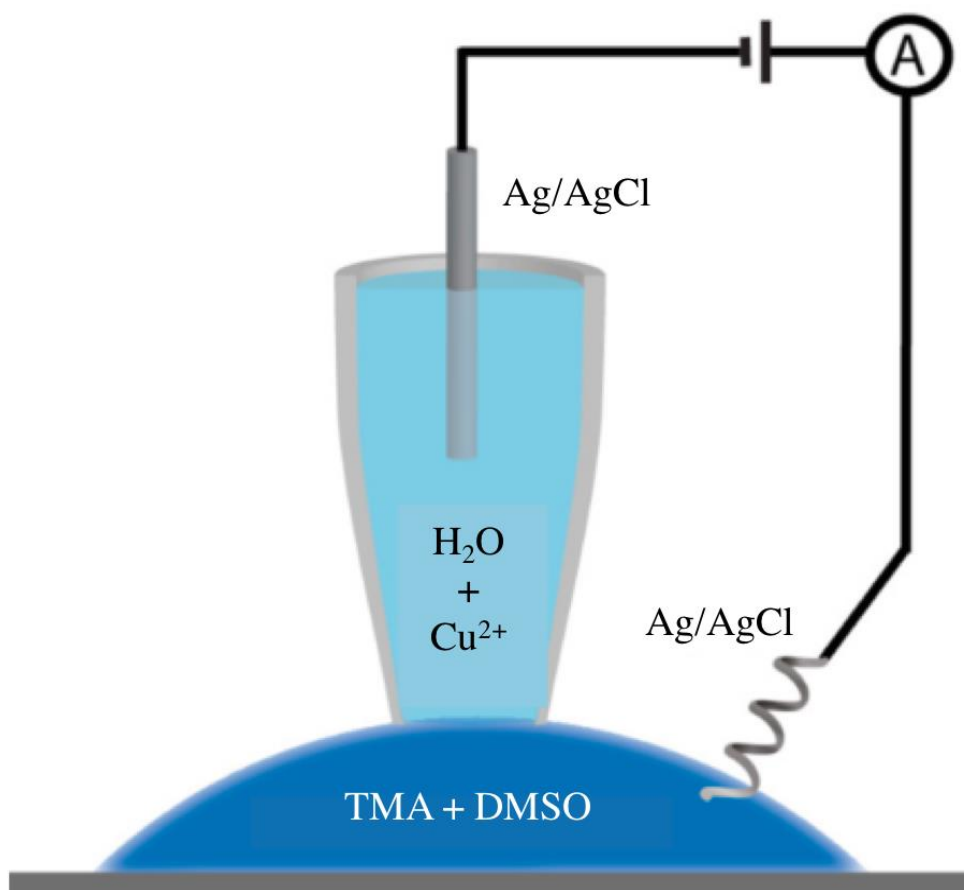


Figure 3.14: Schematic setup of the SICM setup for formation of HKUST-1.

diffusion fields means that ionic movement from the bath to the nanopipette is about 5 times faster than inside the nanopipette, so this was compensated for by using a 5 times higher concentration of Cu^{2+} ions inside the nanopipette, leading to a total ratio of 5:2 $\text{Cu}^{2+}:\text{BTC}^-$. Concentrations of 1 M copper acetate/nitrate and 200 mM BTC were used in the nanopipette and bath respectively.

The current was measured as a function of time with a constant potential applied to the nanopipette. Potential control and data acquisition were achieved using a field-programmable gate array card (7852R, National Instruments) controlled by a LabVIEW 2013 interface, National Instruments. The bias was applied for 15 minutes for each experiment, with variations in current being detected and then analysed after with MATLAB software.

3.6.3 FEM Simulations

Finite element method simulations were performed in COMSOL Multiphysics similar to as mentioned previously in Section 3.3.4 but used here to estimate the size of HKUST-1 particles that were formed inside the nanopipette. The nanopipette diameter was set to 30 nm and the concentrations of the solutions were 1 M copper acetate and 100 mM trimesic acid in the nanopipette and bath respectively. The concentration of trimesic acid in the simulation was lower than that of the actual experiments to reduce the time taken to run a simulation. Simulations were performed with spherical particles of varying radii positioned at the nanopipette orifice and the corresponding drop in current detected in order to create a calibration curve of current drop compared to particle size. A schematic of the simulation setup included in the FEM simulation is shown in Figure 3.15. The predicted ionic currents calculated from

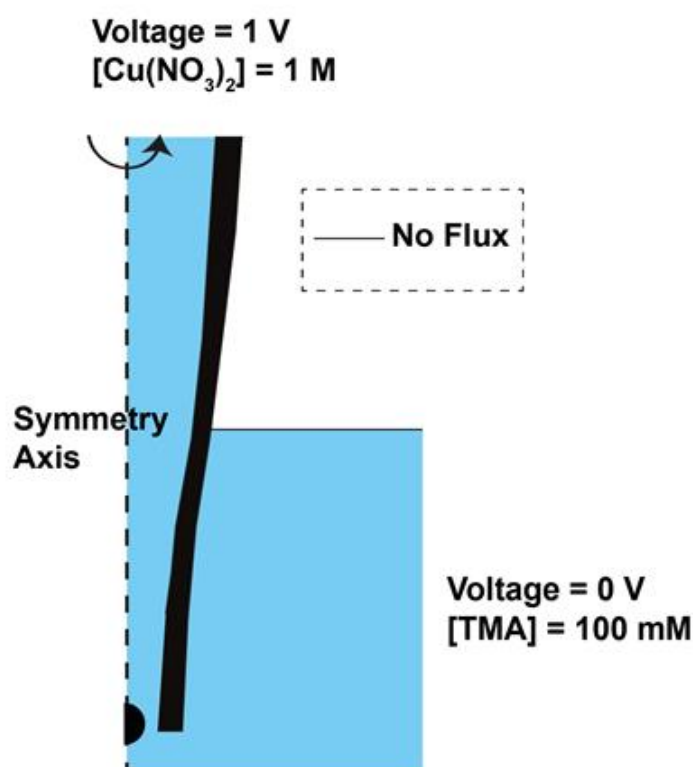


Figure 3.15: Schematic of the FEM simulation setup showing some of the conditions applied.

these simulations could then be compared to that of an open nanopipette. Surface charge of the nanopipette walls and particle was not considered and flow was not included for simplicity. A potential of 1 V was applied to the upper boundary of the nanopipette domain.

3.7 Results and Discussion

3.7.1 Nanoprecipitation of HKUST-1 with Different Copper Precursors

The formation of HKUST-1 is shown by Huo *et al.* to be relatively basic, so creating HKUST-1 inside a nanopipette is also simple. As can be seen from the results in Figures 3.16, 3.17 and 3.18, HKUST-1 forms upon application of a bias due to the mixing applied by the electric field and the subsequent current drop. The differences in the copper precursors can also be clearly seen, with $\text{Cu}(\text{NO}_3)_2$ showing very short sharp drops in the current (Figure 3.16), indicative of nanoparticles being formed and then expelled. $\text{Cu}(\text{OAc})_2$ simply shows a blocking of the nanopipette with no unblocking (Figures 3.17 and 3.18). These findings confirm *in situ* what Huo *et al.* presented, with the copper nitrate precursor forming nanoparticles before growing into larger microparticles, and that copper acetate yields very rapid nucleation and then quickly forms a larger conglomerate.

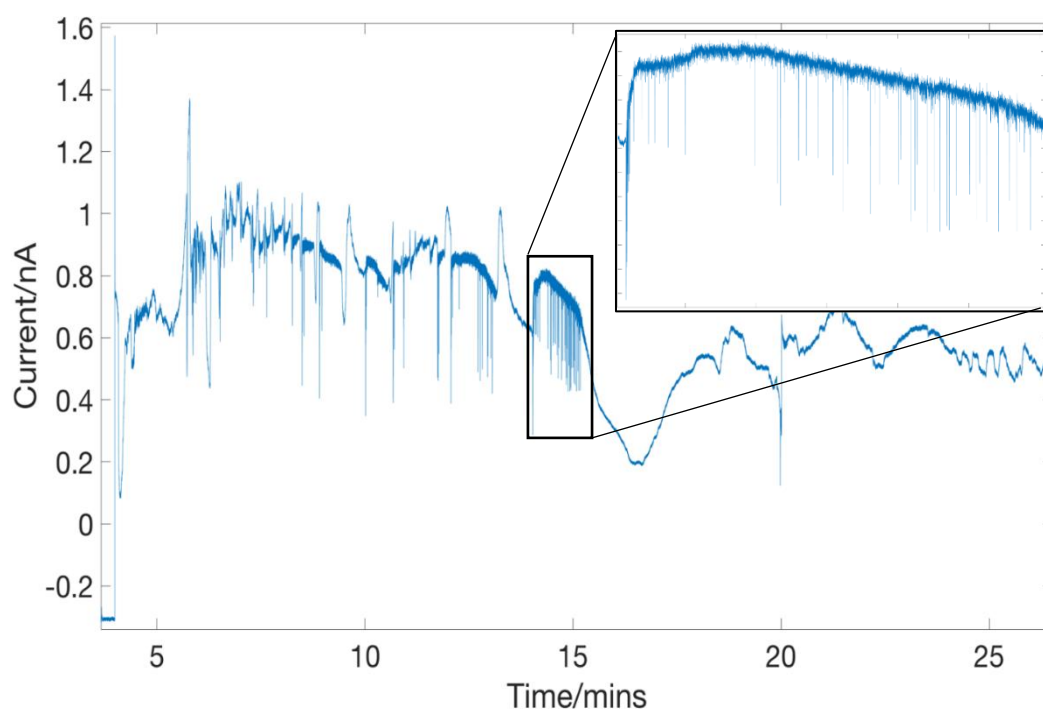


Figure 3.16: Example of an I/t transient of a nanopipette with copper nitrate as the precursor. Note the erratic current drops indicative of a nanoparticle passing through the nanopipette opening. A bias was only applied after ~4 minutes.

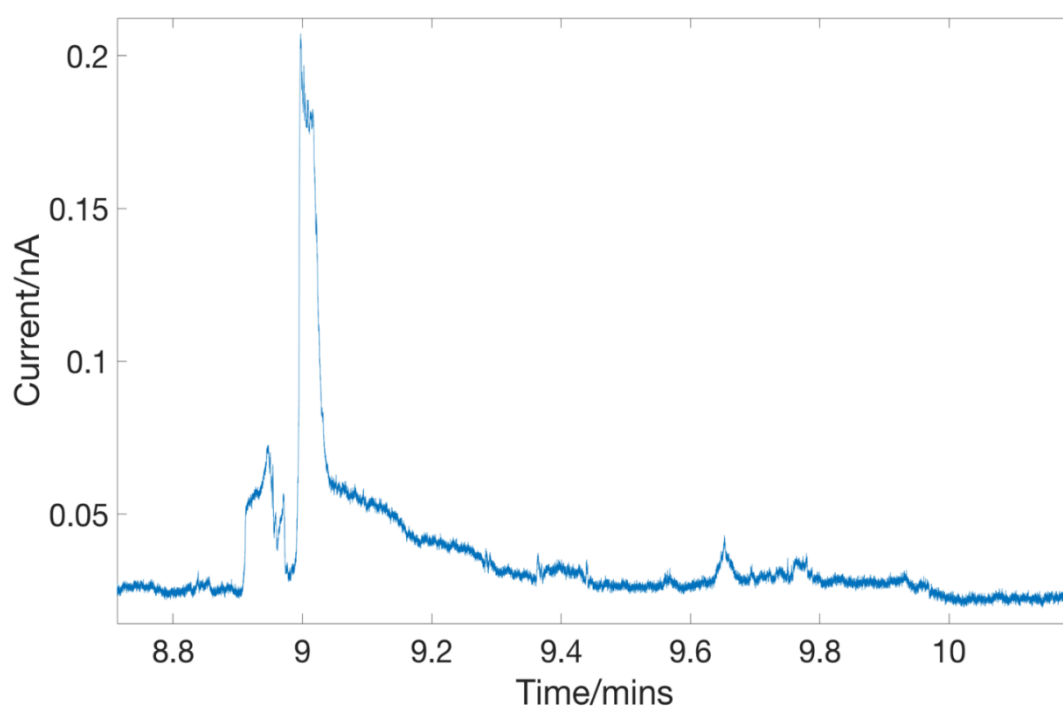


Figure 3.17: Example of an I/t transient of a nanopipette with copper acetate as the precursor. The nanopipette blocks very quickly and stays blocked. A bias was applied after ~ 8.9 minutes.

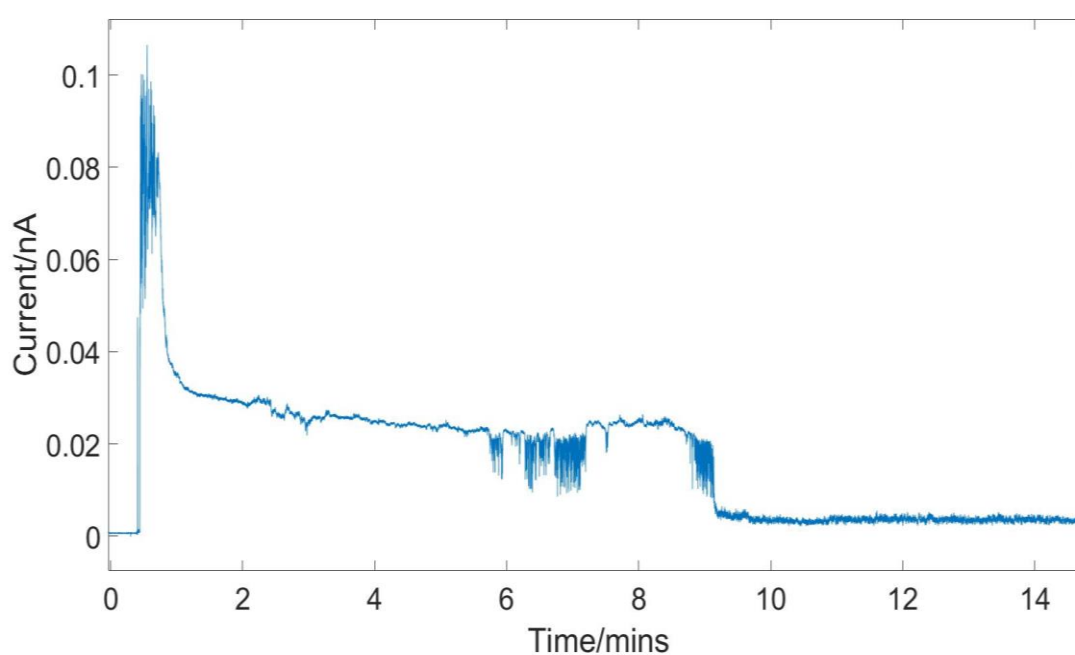


Figure 3.18: Example of an I/t transient of a nanopipette with copper acetate as the precursor. The nanopipette blocks almost completely after 9 minutes and stays blocked.

The nanoparticles that were formed by the copper nitrate precursor can be sized by analysing the magnitude of the drop in current. In order to calibrate this size to current drop ratio, FEM simulations were performed on spherical nanoparticles passing through a nanopipette and the corresponding current drop calculated (Figure 3.19). These FEM simulation results gave a calibration curve, which were then applied to the current drops shown in the inset in Figure 3.16. Figure 3.19 also shows the distribution of magnitude in current drops, which follows a pseudo-binomial distribution. Comparing these data to the calibration curve yields Figure 3.20 which shows the particle size distribution. Any current drops greater than 30 % were given the arbitrary particle size of >28 nm diameter as this was the limit of the FEM simulation and assumed that the particles completely blocked the nanopipette while passing through. These particles accounted for ~25 % of the total particles analysed. This indicates nanoparticle size could be limited by simply altering the nanopipette diameter. The HKUST-1 nanoparticles synthesised by Huo *et al.* had an average diameter of 74 nm after an hour.³¹ The nanoparticles synthesised here were created within a significantly shorter timeframe of 15 minutes and are thus expected to be

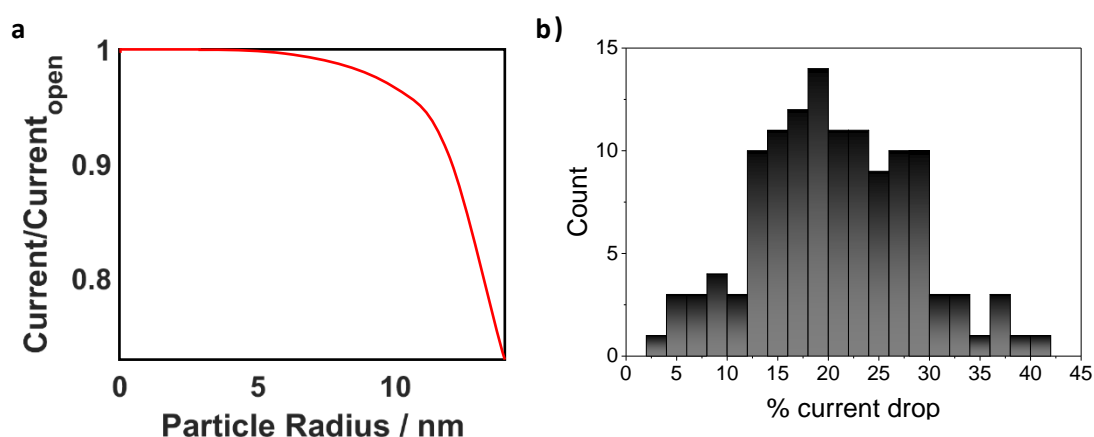


Figure 3.19: a) The current drop for different sized particles passing through a 30 nm nanopipette, as calculated by FEM simulations and b) the magnitude in current drop distribution from experimental data shown in Figure 3.16.

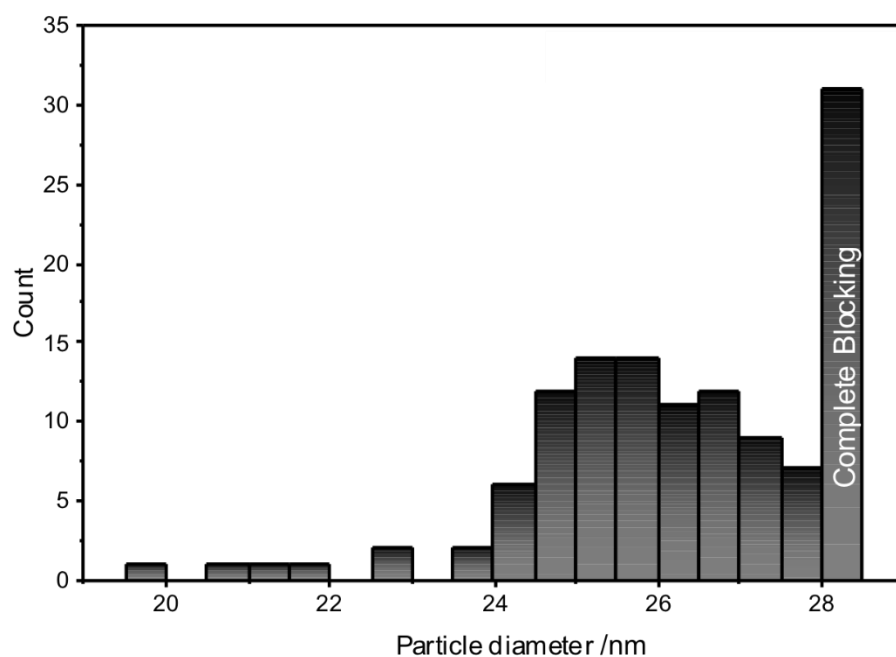


Figure 3.20: Particle size distribution for the particles travelling through the nanopipette in Figure 3.16, inset. Particles that led to a >30 % drop in current were assumed to completely block the nanopipette.

smaller, but the large percentage of nanoparticles formed can potentially be used as seeds for a much faster and facile synthesis of HKUST-1.

3.7.2 HKUST-1 Seeds as a Precursor

The nanoparticles formed from $\text{Cu}(\text{NO}_3)_2$ in a nanopipette were investigated as seeds to catalyse the bulk formation of HKUST-1. After applying a bias of 1 V to a tip containing 1M $\text{Cu}(\text{NO}_3)_2$ for 15 minutes, and directly combining the contents of the bath (trimesic acid in DMSO with the nanoparticle seeds) with a solution of 1M $\text{Cu}(\text{NO}_3)_2$ in water, a visible formation of a precipitate can be observed almost immediately without any stirring (Figure 3.21). The same precipitate is not seen in a combination without the seeding first. To confirm the presence of HKUST-1, the precipitate was centrifuged, then washed with water and ethanol to remove unreacted

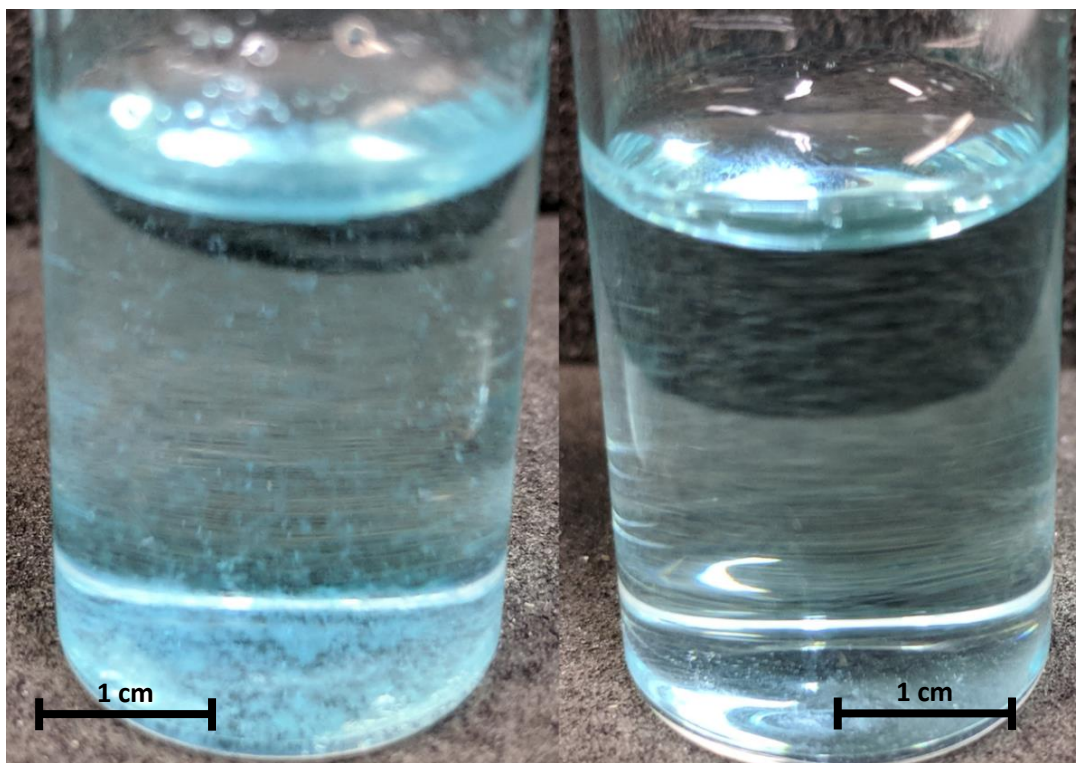


Figure 3.21: A comparison of synthesis of HKUST-1 with (left) and without (right) the seeding process. A precipitate can be clearly seen in the sample that had seeding before.

$\text{Cu}(\text{NO}_3)_2$ and trimesic acid. This left a blue crystalline substance which was identified as HKUST-1 by Raman spectroscopy (Figure 3.22). An extremely small amount of precipitate was also recovered from the unseeded solution, barely enough to even do Raman analysis.

A direct comparison of the solids from the two solutions with Raman microscopy is shown in Figure 3.20, from which we can see that the unseeded solution did not produce HKUST-1, whereas the seeded solution did. The solid from the seeded solution and a sample of pure HKUST-1 share some characteristic peaks: the C-H stretch at $\sim 750\text{ cm}^{-1}$, the C-H bend at $\sim 825\text{ cm}^{-1}$, the C=C symmetrical stretch at $\sim 1000\text{ cm}^{-1}$ (although this is far more intense in the spectra for seeded HKUST-1), the C-O-O symmetrical stretch at $\sim 1400\text{ cm}^{-1}$, the C-O-O asymmetrical stretch at $\sim 1550\text{ cm}^{-1}$, and the C=C symmetrical stretch at $\sim 1600\text{ cm}^{-1}$. This spectrum is consistent with the literature.³² There are also some key differences worth noting: the

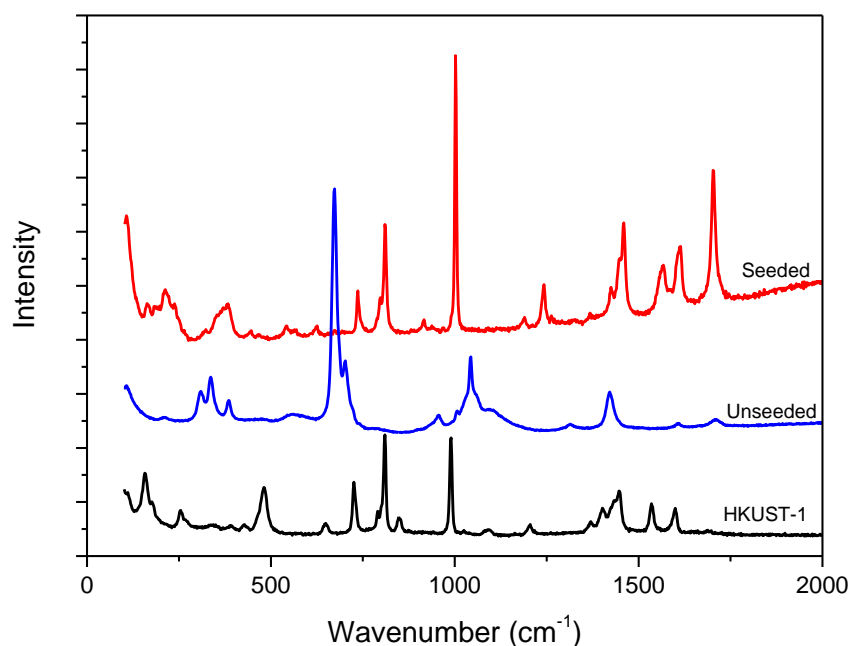


Figure 3.22: Raman spectroscopy of the solutions from Figure 3.21. The seeded precipitate shows a much greater resemblance to HKUST-1 than the precipitate from the unseeded solution.

characteristic Cu-O_{TMA} stretch at $\sim 500\text{ cm}^{-1}$ that appears in the spectrum for conventional HKUST-1 appears to have been significantly downshifted to around $\sim 400\text{ cm}^{-1}$ in seeded HKUST-1. This may be due to the presence of moisture within the seeded sample.³² A peak at $\sim 850\text{ cm}^{-1}$ can be seen in the spectra of conventional HKUST-1 that is not present in the spectra for seeded HKUST-1 (this appears to be part of the C-H bend). Additionally, there is a small peak at $\sim 900\text{ cm}^{-1}$ in the spectrum for seeded HKUST-1 which can be attributed to the presence of unreacted copper nitrate (a similar peak can be seen in the unseeded solution). An additional strong peak can be observed in the seeded HKUST-1 at $\sim 1700\text{ cm}^{-1}$. Any differences in the Raman spectra could be due to the introduction of DMSO into the system, which could fill the pores of HKUST-1 or coordinate to the Cu²⁺ ions. They could also be due to unreacted trimesic acid still present. A Raman study of HKUST-1 formed in the presence of DMSO has been performed previously by Worrall *et al.* who

electrodeposited HKUST-1 particles onto gold nanostructures.³³ Their study showed no difference to conventional HKUST-1 however their samples were stirred overnight in methanol to remove additional DMSO, whereas herein the samples were centrifuged for 10 minutes with both water and ethanol, a much less rigorous cleaning cycle. If the samples made in this study had been washed as vigorously, these extra peaks in the Raman spectra may disappear.

The seeded HKUST-1 was compared to conventional HKUST-1 by SEM, and they both show some similarity in the shape and size of the formed crystals at $\sim 1000\times$ and $10000\times$ magnification, despite the vastly different synthetic time frames (Figures 3.23 and 3.24). A few noticeable differences can be observed at a closer magnification, the conventional HKUST-1 crystals generated through combination of aqueous solutions over the course of 24 hours generally have smoother surfaces and

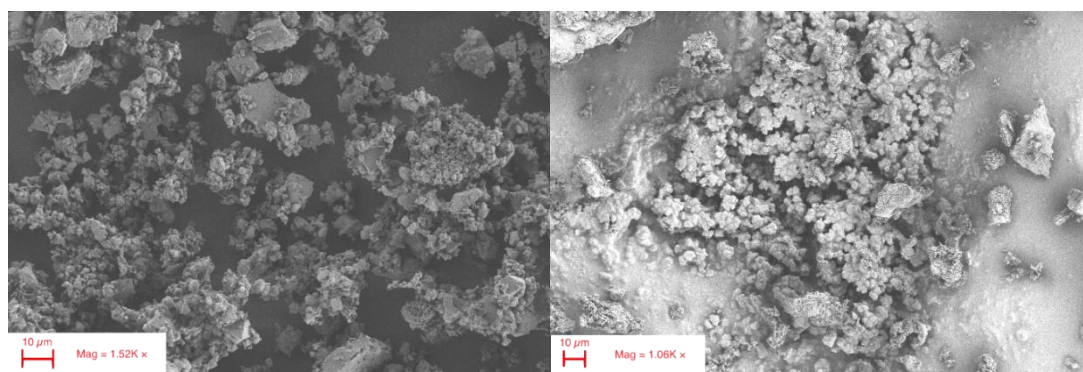


Figure 3.23: SEM images of a) HKUST-1 prepared from conventional methods and b) a sample of HKUST-1 synthesised using the seeding method.

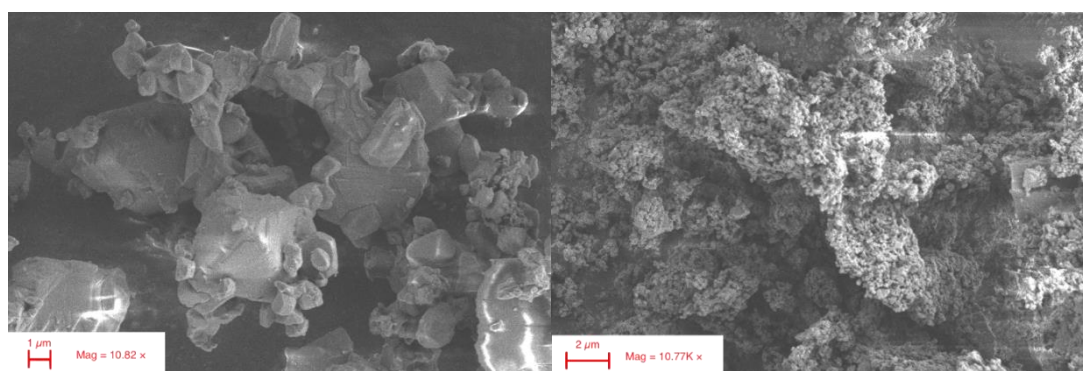


Figure 3.24: SEM images of a) HKUST-1 prepared from conventional methods and b) a sample of HKUST-1 synthesised using the seeding method both at higher magnification.

appear very crystalline. The sample generated through the seeding method over the course of less than 1 hour has a rougher surface, indicating that the small crystals have not had sufficient time to merge together (Figure 3.24). Unfortunately, these samples were too small in quantity to perform powder X-ray diffraction studies, more studies would need to be undertaken in order to produce enough solid.

3.7.3 HKUST-1 Formation from Copper Acetate

To confirm that the blocking of the nanopipette from a copper acetate precursor was due to the formation of HKUST-1, the same SICM experiment was performed with a larger diameter tip, in this case $\sim 5\text{ }\mu\text{m}$. A dark blue mass was observed to have formed in the micropipette after application of 1 V for a few minutes (Figure 3.25). The mass was studied under Raman microscopy alongside the reagents and a HKUST-1 sample prepared from the method described by Huo *et al.* The Raman

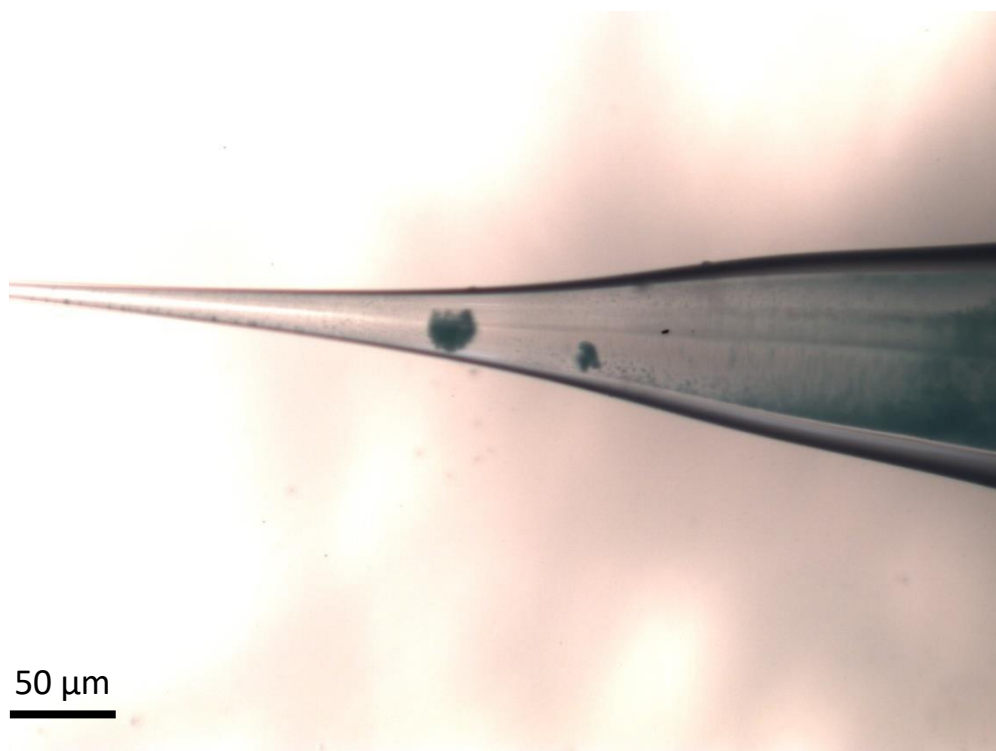


Figure 3.25: HKUST-1 formation inside of a micropipette with diameter $\sim 5\mu\text{m}$, observed by optical microscopy.

spectra are shown in Figure 3.2, where it can be seen that the mass inside the micropipette shares the majority of the peaks from the Raman spectrum of HKUST-1, thus confirming that HKUST-1 was formed inside the micropipette to block it.

It is worth noting the similarities and differences between the Raman spectrum of the HKUST-1 sample synthesised using a conventional method (Figure 3.24, black), and that of the sample synthesised inside the micropipette in just a few minutes (Figure 3.24, red). The two share many characteristic peaks, which are also in line with literature values.³³ The peaks at $\sim 700\text{ cm}^{-1}$ and $\sim 725\text{ cm}^{-1}$ in the micropipette generated spectrum match the peaks for DMSO at room temperature.³⁴ A peak that appears at $\sim 850\text{ cm}^{-1}$ in the HKUST-1 spectra does not seem to be visible (or possibly is shifted to be part of the peak at $\sim 825\text{ cm}^{-1}$) in the species created in the micropipette. Todaro *et al.* attributed this to a C-H bend.³² A peak that appears at $\sim 900\text{ cm}^{-1}$ in the micropipette can again be observed in the spectrum for copper acetate and attributed to some unreacted $\text{Cu}(\text{OAc})_2$.

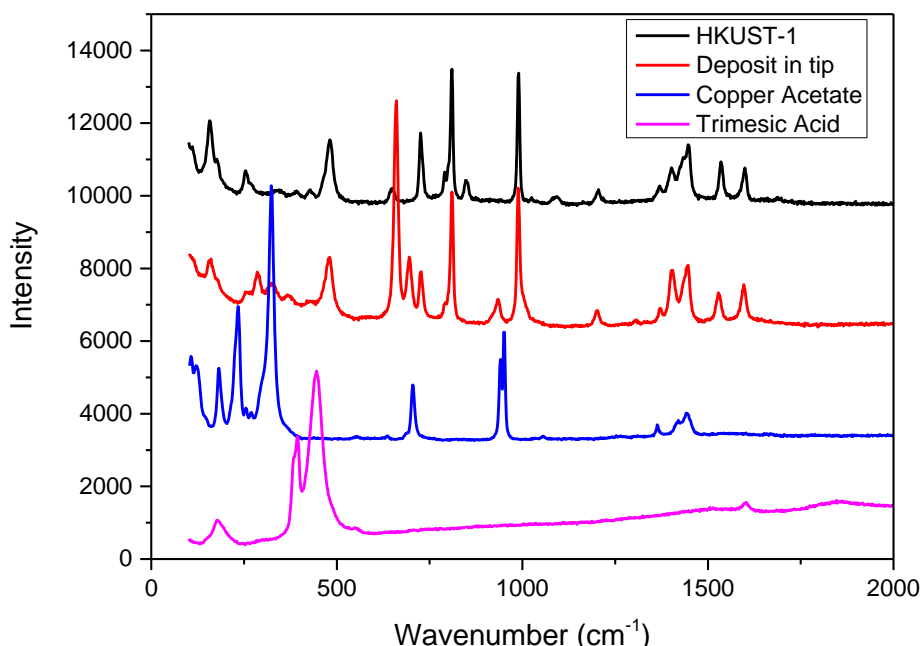


Figure 3.26: Raman spectra of HKUST-1 prepared by conventional methods (black), a deposit confirmed to be HKUST-1 inside of the micropipette after application of a bias (red), copper acetate (blue) and trimesic acid (pink).

3.8 Conclusions

Herein the nanoprecipitation of gypsum inside a nanopipette has been shown, and some common humid creep additives have been analysed for their effects on the crystallisation and dissolution of gypsum. The additives have a clear effect on how the gypsum initially nucleates and forms, with tartaric acid showing a tendency to form what is presumed to be a larger single crystal, while STMP forms many extremely small crystals. Boric acid and ascorbic acid show no real change from how the crystal forms with no additive, and gallic acid is a clear nucleation inhibitor, given the lack of blocking seen in the nanopipette.

It can also clearly be seen that the additives have an effect on the crystallisation and dissolution kinetics for gypsum, based on how fast the nanopipette blocks/unblocks with the changes in bias. For crystallisation, tartaric acid and STMP have about a four times increase in the blocking time, while the dissolution times have increased by about five times. Clear inhibition of both of these steps has been shown, and adds to the argument that these additives work by hindering steps in the local pressure solution creep mechanism.

Also shown in this study was a novel approach for following the nucleation and growth of MOFs, here specifically HKUST-1 was studied through the use of a two-electrode SICM setup. The differences in the mechanisms of formation of HKUST-1 microparticles from the different precursors of copper nitrate and copper acetate have been proven here, with *in situ* studies of the formation of HKUST-1 being shown. The copper acetate precursor has been confirmed to very quickly form a microstructure whereas the copper nitrate precursor forms nanoparticles which can then grow into the HKUST-1 microparticles. Simulation has allowed a particle size

distribution to be deduced, but future TEM analysis could be performed to verify this particle distribution. To take this further, these nanoparticles can be used as seeds to speed up the initial formation of HKUST-1 microparticles, with potential uses in industry to speed up the formation of the HKUST-1 MOF with respect to other conventional methods.

The scope of potential for formation of other MOFs and inorganic species via nanoprecipitation is huge. There is the potential that these MOFs could be formed at the end of a nanopipette and then used as sensors. For example, nanopipettes containing HKUST-1 could prove useful as gas sensors, where HKUST-1 can adsorb small gas molecules such as nitric oxide and dihydrogen.^{26,35} It has also been shown to selectively detect pentanal down to ranges of 1-2 ppm at room temperature^{36,37}, as well as other gases at higher ppm ranges.^{38,39} This work could pave the way for other MOF formations at the end of nanopipette – for example some MOFs are conductive or semi-conductive, providing new interesting electrodes that show changes in electrical properties upon exposure to certain gases, *i.e.* changes in impedance, resistance, capacitance or work function – all measurable parameters. Although MOFs have not been fully utilized as electronic sensor materials yet (the first MOF based electronic gas sensor was reported in 2009)⁴⁰, new discoveries could lead this to be a viable avenue of gas sensing on the nanoscale.⁴¹⁻⁴⁵ Most previous studies have shown that MOF based gas sensors are powder based or single crystal based, which becomes a challenge when trying to incorporate MOFs into electronic devices.⁴⁶⁻⁴⁹ Creating the MOF at the end of a nanopipette could circumvent these problems as the MOF is already incorporated into the device and does not need to be transferred from one place to another.

Creating MOFs inside a nanopipette means that MOF formations can be studied at the very early stages of nucleation and growth in order to analyse mechanisms of formation. For nanoparticle sizing, previous methods have relied on SEM imaging or X-ray diffraction patterns analysed with the Scherrer equation.^{31, 50} The method shown here is comparatively time effective and has the advantage of giving a particle size distribution based on FEM simulations, instead of just an average.

3.9 References

- ¹ Q. Yu, S. Sucheck, B. Groza, R. Mlinac, F. Jones, F. Boehnert, *Process for reducing creep in a gypsum plaster-based element, gypsum plaster-based composition and method for making a gypsum plaster-based element with reduced creep*, U.S. Patent 6632550, **2003**
- ² R. D. Fisher, M. M. Mbogoro, M. E. Snowden, M. B. Joseph, J. A. Covington, P. R. Unwin, R. I. Walton, *ACS Appl. Mater. Interfaces*, **2011**, 3, 3528-3537
- ³ M. M. Mbogoro, M. E. Snowden, M. A. Edwards, M. Peruffo, P. R. Unwin, *J. Phys. Chem. C*, **2011**, 115, 10147
- ⁴ N. B. Singh, B. Middendorf, *Prog. Cryst. Growth Charact. Mater.*, **2007**, 53, 57
- ⁵ E. Finot, E. Lesniewska, J. C. Mutin, J. P. Goudonnet, *Langmuir*, **2000**, 16, 4237
- ⁶ E. Finot, E. Lesniewska, J. P. Goudonnet, J. C. Mutin, *App. Surf. Sci.*, **2000**, 161, 316-322
- ⁷ E. Finot, E. Lesniewska, J. P. Goudonnet, J. C. Mutin, M. Domenech, A. A. Kadi, *Sol. State Ion.*, **2001**, 141-142, 39-46
- ⁸ E. A. Pachon-Rodriguez, J. Colombani, *AlChE J.*, **2013**, 59, 1622-1626
- ⁹ E. A. Pachon-Rodriguez, E. Guillon, G. Houvenaghel, J. Colombani, *Cement and Concrete Research*, **2014**, 63, 67-74
- ¹⁰ D. Perry, A. S. Parker, A. Page, and P. R. Unwin, *ChemElectroChem*, **2016**, 3 (12), 2212–2220
- ¹¹ W. Chen *et al*, *CrystEngComm*, **2018**, 20, 1662

- ¹² L. P. Sarma, P. S. R. Prasad, N. Ravikumar, *J. Raman Spectroscopy*, **1998**, *29*, 851-856
- ¹³ B. Schug *et al.*, *Cement and Concrete Research*, **2018**, *107*, 182-187
- ¹⁴ G. Férey, *Chem. Soc. Rev.*, **2008**, *37*, 191–214
- ¹⁵ J. L. C. Rowsell and O. M. Yaghi, *Synthesis (Stuttg.)*, **2004**, *73*, 3
- ¹⁶ P. Horcajada, *et al.*, *Chem. Rev.*, **2012**, *112*, 1232
- ¹⁷ T. Devic, *et al.*, *Mater. Chem.*, **2012**, *22*, 10266
- ¹⁸ Y. Lin, C. Kong, Q. Zhang and L. Chen, *Adv. Energy Mater.*, **2017**, *7*, 1601296
- ¹⁹ L. E. Kreno, K. Leong, O. K. Farha, M. Allendorf, R. P. Van Duyne and J. T. Hupp, *Chem. Rev.*, **2012**, *112*, 1105
- ²⁰ J. Lee, O. K. Farha, J. Roberts, K. A. Scheidt, S. T. Nguyen and J. T. Hupp, *Chem. Soc. Rev.*, **2009**, *38*, 1450
- ²¹ S. S.-Y. Chui, *Science*, **1999**, *283*, 1148
- ²² P. Schäfer, F. Kapteijn, M. A. Van Der Veen and K. F. Domke, *Cryst. Growth Des.*, **2017**, *17*, 5603
- ²³ A. U. Czaja, N. Trukhan and U. Müller, *Chem. Soc. Rev.*, **2009**, *38*, 1284
- ²⁴ C. Prestipino, *et al.*, *Chem. Mater.*, **2006**, *18*, 1337
- ²⁵ J. Gascon, S. Aguado and F. Kapteijn, *Microporous Mesoporous Mater.*, **2008**, *113*, 132
- ²⁶ B. Xiao, *et al.*, *J. Am. Chem. Soc.*, **2007**, *129*, 1203
- ²⁷ Q. Min Wang, *et al.*, *Microporous Mesoporous Mater.*, **2002**, *55*, 217

- ²⁸ M. D. Allendorf, et al., *J. Am. Chem. Soc.*, **2008**, *130*, 14404
- ²⁹ K. Schlichte, T. Kratzke and S. Kaskel, *Microporous Mesoporous Mater.*, **2004**, *73*, 81
- ³⁰ L. Alaerts, E. Séguin, H. Poelman, F. Thibault-Starzyk, P. A. Jacobs and D. E. De Vos, *Chem. - A Eur. J.*, **2006**, *12*, 7353
- ³¹ J. Huo, M. Brightwell, S. El Hankari, A. Garai and D. Bradshaw, *J. Mater. Chem. A*, **2013**, *1*, 15220
- ³² M. Todaro, A. Alessi, L. Sciortino, S. Agnello, M. Cannas, F. M. Gelardi and G. Buscarino, *J. Spectrosc.*, **2016**, Article ID 8074297
- ³³ S. D. Worrall, et al., *Electrochimica Acta*, **2006**, *222*, 361
- ³⁴ W. N. Martens, R. L. Frost, J. Kristof, J. T. Kloprogge, *J. Raman Spectroscopy*, **2002**, *33*, 84
- ³⁵ S. Bordiga, et al., *Phys. Chem. Chem. Phys.*, **2007**, *9*, 2676
- ³⁶ R. Pohle, A. Tawil, P. Davydovskaya, M. Fleischer, *Procedia Eng.*, **2011**, *25*, 108
- ³⁷ P. Davydovskaya, R. Pohle, A. Tawil, M. Fleischer, *Sens. Actuators, B*, **2013**, *187*, 142
- ³⁸ M. Hosseini, S. Zeinali, M. Sheikhi, *Sens. Actuators, B*, **2016**, *230*, 9
- ³⁹ S. Sachdeva, et al., *Small*, **2017**, *13*, 1604150
- ⁴⁰ S. Achmann, G. Hagen, J. Kita, I. Malkowsky, C. Kiener, R. Moos, *Sensors*, **2009**, *9*, 1574
- ⁴¹ L. Sun, S. S. Park, D. Sheberla, M. Dincă, *J. Am. Chem. Soc.*, **2016**, *138*, 14772

- ⁴² Y. Kobayashi, B. Jacobs, M. D. Allendorf, J. R. Long, *Chem. Mater.*, **2010**, 22, 4120
- ⁴³ L. Sun, T. Miyakai, S. Seki, M. Dincă, *J. Am. Chem. Soc.*, **2013**, 135, 12932
- ⁴⁴ D. Sheberla, J. C. Bachman, J. S. Elias, C. -J. Sun, Y. Shao, *Nat. Mater.*, **2017**, 16, 220
- ⁴⁵ G. Wu, J. Huang, Y. Zang, J. He, G. Xu, *J. Am. Chem. Soc.*, **2016**, 139, 1360
- ⁴⁶ P. Falcaro, R. Ricco, C. M. Doherty, K. Liang, A. J. Hill, M. J. Styles, *Chem. Soc. Rev.*, **2014**, 43, 5513
- ⁴⁷ M. D. Allendorf, A. Schwartzberg, V. Stavila, A. A. Talin, *Chem. Eur. J.*, **2011**, 17, 11372
- ⁴⁸ I. Stassen, N. Burtch, A. Talin, P. Falcaro, M. Allendorf, R. Ameloot, *Chem. Soc. Rev.*, **2017**, 46, 3185
- ⁴⁹ J. Liu, C. Wöll, *Chem. Soc. Rev.*, **2017**, 46, 5730
- ⁵⁰ M. Mazaj, T. Čendak, G. Buscarino, M. Todaro and N. Zabukovec Logar, *J. Mater. Chem. A*, **2017**, 5, 22305

Chapter 4: Studying the Wetting of Gypsum Plaster and Common Humid

Creep Inhibitors via SECCM

4.1 Abstract

This chapter studies an often overlooked area of gypsum plasterboard: the velocity of water spread throughout gypsum plaster. Using an SECCM setup to apply a droplet to a surface of gypsum plaster with different additives incorporated reveals that the change in additive does not affect the wetting distance within reasonable doubt. Altering the humidity does alter the extent of wetting, leading to an interesting phenomenon – at higher humidity water spreads further through plaster. We theorise that the increase in humidity leads to a larger water layer coating the crystals, leading to easier movement of water across the surfaces or that the water must travel further to find gypsum environments that are not already oversaturated with water.

Tartaric acid and STMP and the effect they have on plaster wetting is explored, with tartaric acid seeming to accelerate wetting at the humidities tested, while STMP only increases wetting at room temperature humidities, showing no effect at high humidities. Future work analysing these hypotheses are outlined and the problems with testing the wettability of gypsum plaster and measuring its porosity are commented on, with potential solutions outlined.

4.2 Introduction

One area of gypsum that is understudied is the wetting of plaster, or how liquid spreads through plaster, and how these additives affect the wettability. Most studies into the wetting of surfaces are performed on smooth homogenous surfaces which are applicable in industries such as coating, printing or painting.¹⁻⁵ Most surfaces in the real world though have a roughness to some degree and this lends some porosity to most surfaces, which changes the wetting conditions.⁶⁻⁸ Studies into the wetting of fully porous materials have been also done before, with Starov *et al.* studying the wetting of nitrocellulose membranes of different porosities being wet by silicone oils of different viscosities and aqueous SDS solutions.⁹ The porosities of the membranes were measured by taking the difference in weight between a saturated membrane and a completely dry membrane. Their results are shown in Figure 4.1 which show a fast initial wetting which slows down as the volume of the inner wetting (shown in Figure 4.2) increases. He showed that essentially the wetting speed is related to the porosity of the substrate as well as the viscosity of the droplet used.

In this study the interest is of how water penetrates gypsum plaster. Here the viscosity of all wetting media is kept the same, with the only difference between samples being the humid creep additive incorporated into the plaster. Whether this incorporates different porosity into the plaster is analysed and the wetting of different samples discussed with respect to the additives used and the local humidity in the experiment setup.

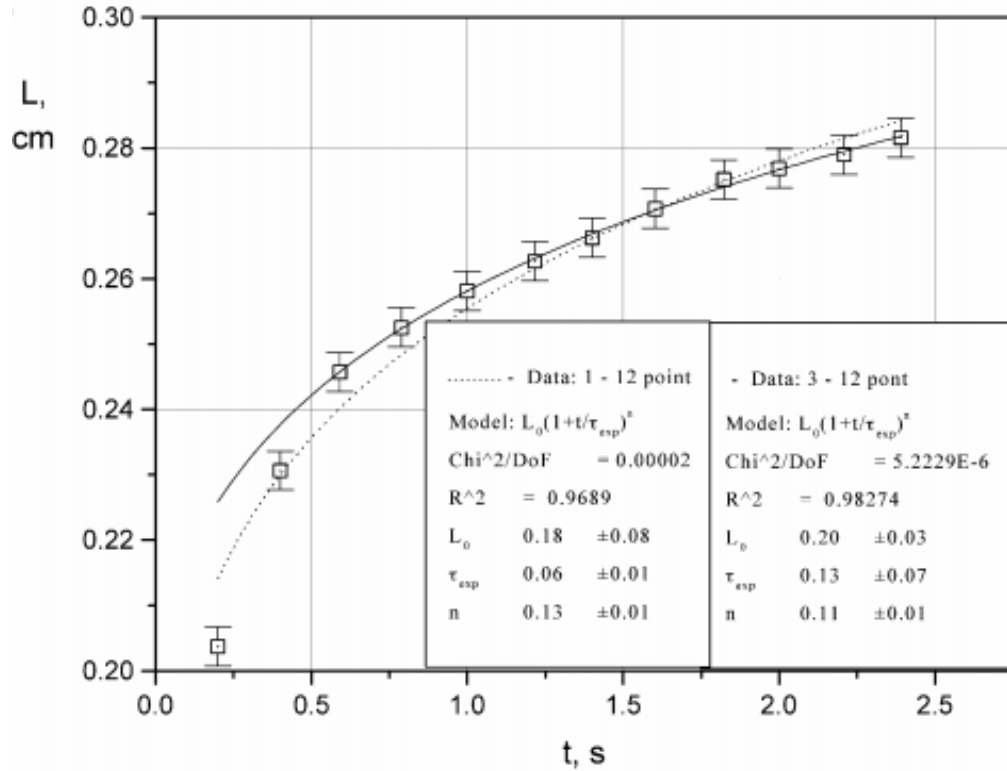


Figure 4.1: Radius of the drop base vs. time. The droplet is a silicone oil with viscosity of 0.554 P being placed on a nitrocellulose membrane with an average pore size of 0.2 μm . Graph taken from Starov *et al.*⁹

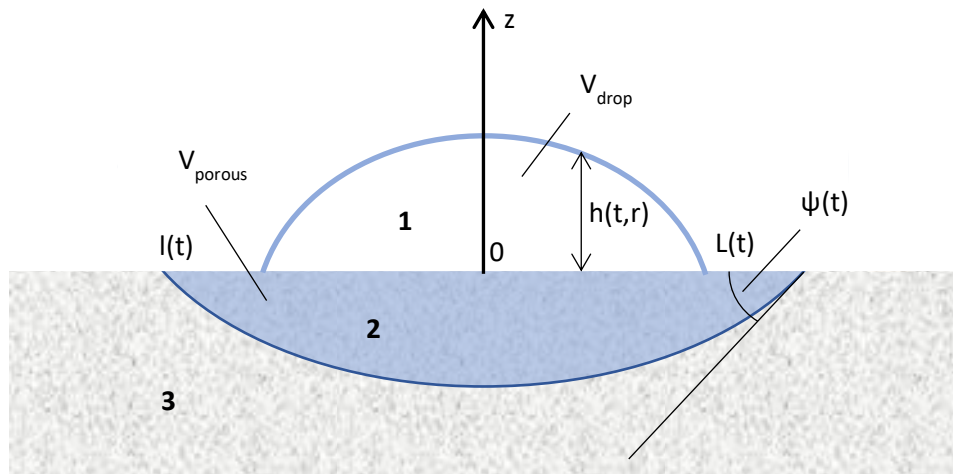


Figure 4.2: Schematic of a spreading of a liquid droplet over a dry porous substrate. Areas are 1) the spherical drop, 2) the wetted region inside the porous substrate and 3) the dry part of the porous substrate. $L(t)$ is the radius of the drop base, $l(t)$ the radius of the wetted circle on the surface of the porous substrate, $\psi(t)$ is the effective wetting contact angle inside the porous substrate and $h(t,r)$ is the height profile of the spreading droplet. V_{drop} refers to the volume of the droplet and V_{porous} refers to the volume of the wet area inside the porous substrate.

4.3 Materials and Methods

4.3.1 Solutions and Sample Preparation

All solutions were made in ultrapure 18.2 M Ω water (Purite, Select HP). Calcium chloride dihydrate ($\geq 99\%$), STMP ($\geq 95\%$) and tartaric acid ($\geq 99\%$) were purchased from Sigma-Aldrich. Calcium sulfate hemihydrate powder ($\geq 99\%$) and polymethylhydrogensiloxane (also known as silicone oil, a hydrophobic additive) were provided by Saint Gobain. Methylene blue dye was purchased from Fisher Scientific.

All plaster was made from the same method except where stated. For plaster with a water gauge of 50, 50 ml of water was placed in a beaker, and 100 g of stucco was slowly added evenly over 30 seconds. The stucco was left to wet for a further 30 seconds before vigorous mixing by hand for 1 minute. The slurry was then poured into the respective mould and gently agitated to remove air bubbles. Dry plaster samples would then be placed in an oven at 40 °C overnight and the mould broken off once dry.

4.3.2 SECCM Setup

Double barrelled nanopipettes were fabricated by laser pulling theta quartz capillaries. Nanopipettes were initially 50 nm in diameter, but later 50 μ m diameter micropipettes were fabricated. Pipettes were silanised on the outside in order to keep the outside hydrophobic, so that the meniscus did not travel up the outside of the pipette. The experimental setup is shown in Figure 4.3. Both barrels were filled with electrolyte (CaCl₂, 100 mM) and methylene blue dye (100 mM) for better conductivity and optical clarity respectively. A two-electrode system was used here

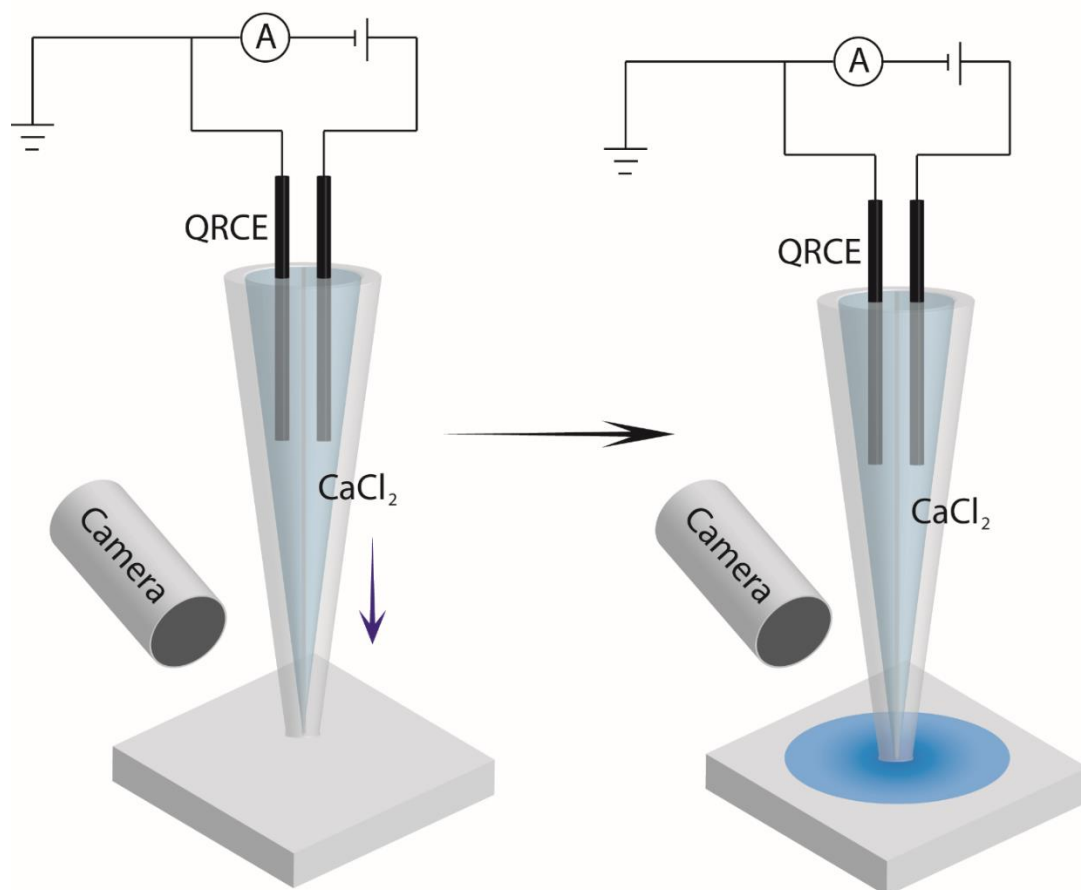


Figure 4.3: Schematic setup of SECCM for video capture of wetting. The schematic shows the spread of liquid as the nanopipette meniscus makes contact with the surface.

with Ag/AgCl QRCEs in each barrel. The micropipette movement was controlled using piezo micropositioners connected to a specialized LabView computer programme, as were all other affairs. A DC current was applied to one of the channels in the nanopipette and a circuit was formed through the meniscus at the end of the pipette. An AC current was applied to the piezo micropositioners, and a change in the AC current associated with contact of the substrate was detected, stopping the micropipette from crashing into the surface. This method allowed for controlled microdroplets to be applied to the substrate.

Eventually much larger micropipettes were used ($\sim 50\ \mu\text{m}$) where an SECCM setup was not needed. In this case a single barrelled micropipette was used and the

meniscus at the end applied to the surface by hand. All videos were acquired by a 6× PixeLink camera focussed on the end of the pipette using a framerate capture of 15 frames per second.

4.3.3 BET Theory

BET surface area analysis was undertaken with a Quadrasorb Evo Gas surface area and pore size analyser. Nitrogen gas absorption was utilised at 77 K in this technique to measure porosity of samples, as this would be a significant factor in the wetting process. Samples were dried at ~40 °C overnight in preparation for BET.

4.3.4 Video Analysis

Videos of wetting were analysed using a specialised MATLAB script to automate calculation of the wetting radius. Videos were converted to black and white, with each pixel having assigned a number between 0 (black) and 256 (white). A straight horizontal line was manually drawn over each video and pixels along this line were analysed for a change in the pixel number. The line was always drawn from the nanopipette outwards, and the line was analysed outwards from this line, with the furthest darkening pixel from the centre being used as the in-situ wetting radius.

4.2.5 Scanning Electron Microscopy (SEM)

SEM images were taken with a Zeiss Gemini ultra-high resolution SEM with a resolution of 0.6 nm at >1 kV. Samples were coated with ~80 nm gold Quorum Sputter Coater to combat local charging of samples.

4.3.6 Atomic Force Microscopy (AFM)

AFM images of cast plaster were recorded in air using an Innova® AFM (Bruker) in contact mode with triangular silicon cantilevers (RESP-10, Bruker), with the images analysed with SPIP software (6.0.14, Image Metrology).

4.4 Results and Discussion

4.4.1 SEM and Creation of Samples

Samples were created as stated in the experimental section earlier, with the casting in the petri dish being important as to give a flat surface for the crystals to cast against. A flat surface was important for the use of a nanopipette as roughness in the surface can very easily break the thin walls at the end of a nanopipette. AFM imaging was used to quantify the roughness of the surfaces. Initially it was clearly seen from SEM that the surface was incredibly rough, due to the matrix of needles that gypsum setting forms (Figure 4.4a). To work around this, the samples were ground with very fine sandpaper (~5 μm grain). This gave much less roughness as seen from AFM (micrometre roughness compared to nanometre roughness), but this was eventually abandoned as this was considered not close to the actual structure of plaster as all the surface pores were filled with gypsum dust. An SEM image of a ground surface is also shown in Figure 4.4b.

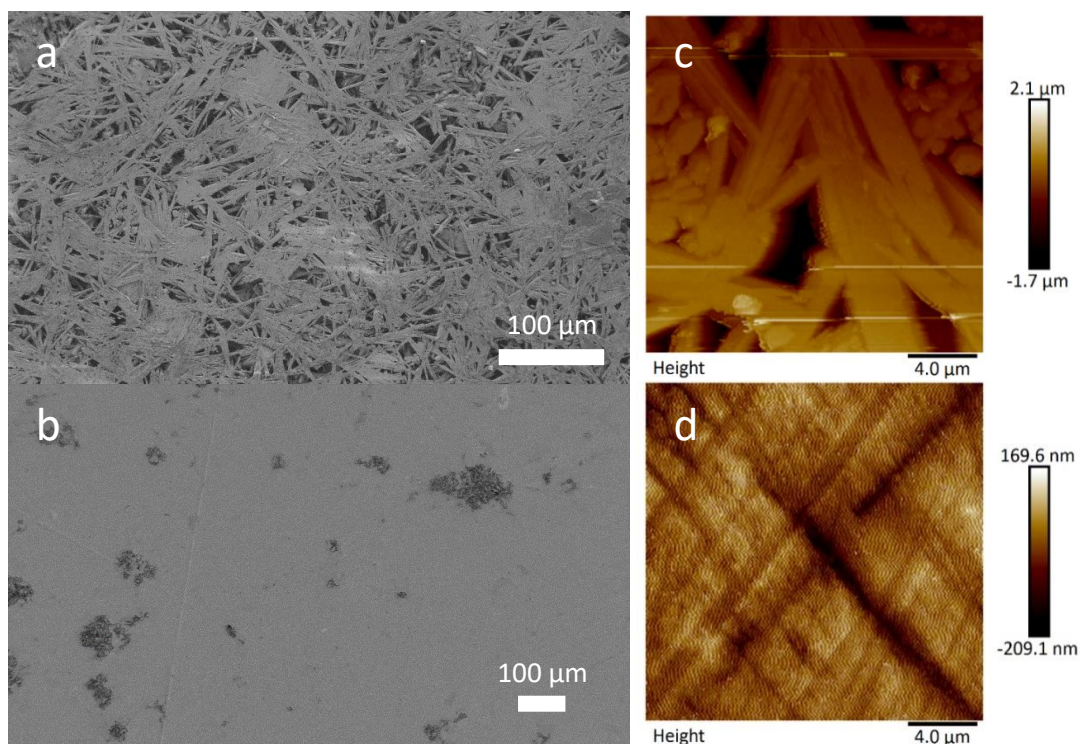


Figure 4.4: a) SEM image of gypsum plaster cast against the flat bottom of a petri dish and b) a plaster surface ground with fine sandpaper to make a smooth surface. AFM images of gypsum plaster are shown in c) cast against the flat bottom of a petri dish and d) a plaster surface ground with fine sandpaper to make a smooth surface. The lines on the smoothed surface are from the sanding process.

4.4.2 Wetting and SECCM

Initially the SECCM experiment was designed to look at dissolution on the surface of the plaster, but it was quickly discovered that aqueous droplets would not sit on the surface similar to how was expected due to the high hydrophilicity of gypsum. The samples were analysed under AFM and viewed under SEM after wetting experiments were done and no dissolution pits were seen. Upon watching videos from the camera, it was quickly discovered that the droplets were being absorbed by the plaster, with a darkening of the plaster travelling across the surface showing how far the liquid had spread through the plaster. The wetting could also be a useful parameter in how the different additives work so this was explored.

Plaster is a matrix of gypsum needle shaped crystals, so the macrostructure has a very high porosity. This coupled with the high hydrophilicity of gypsum means that any aqueous solution wets extremely far and fast through the porous structure. An example of a sample before and after wetting is shown in Figure 4.5.

Wetting videos were taken and analysed as described in the Experimental section. The wetting was not very clear without the methylene blue dye incorporated. Methylene dye was chosen due to its dark colour and high extinction coefficient ($\sim 100000 \text{ dm}^3 \text{ mol}^{-1} \text{ cm}^{-1}$) and added in a low enough concentration to be visible, but not so high as to potentially interact with the plaster. Results from wetting with a 50 nm nanopipette on 8 different samples using no additive in the plaster are shown in Figure 4.6. There is a fairly large difference between the wetting of each sample, despite the fact that they were all created from the same method. The difference in wetting radii imply a difference in porosity between each sample. The difference in porosities of each sample is most likely caused by the method of mixing, which was done by hand. While the method used was theoretically consistent, human error will unavoidably take effect, with more stirring occurring in some samples than others, leading to high porosity.

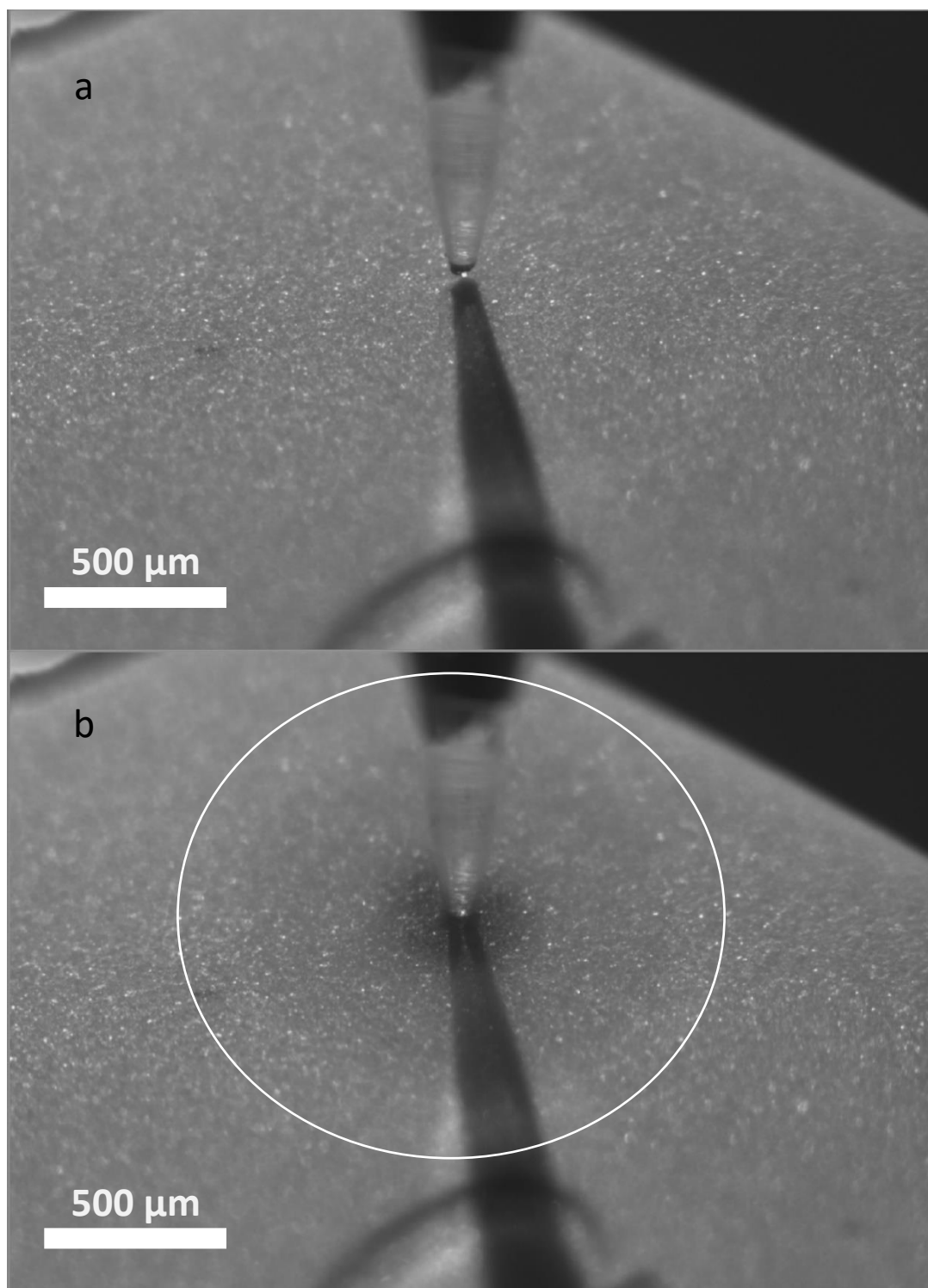


Figure 4.5: Images of a 50 μm nanopipette making contact with plaster: a) before wetting and b) after wetting. The wetting of the plaster can be seen on the surface by a darkening highlighted in picture b).

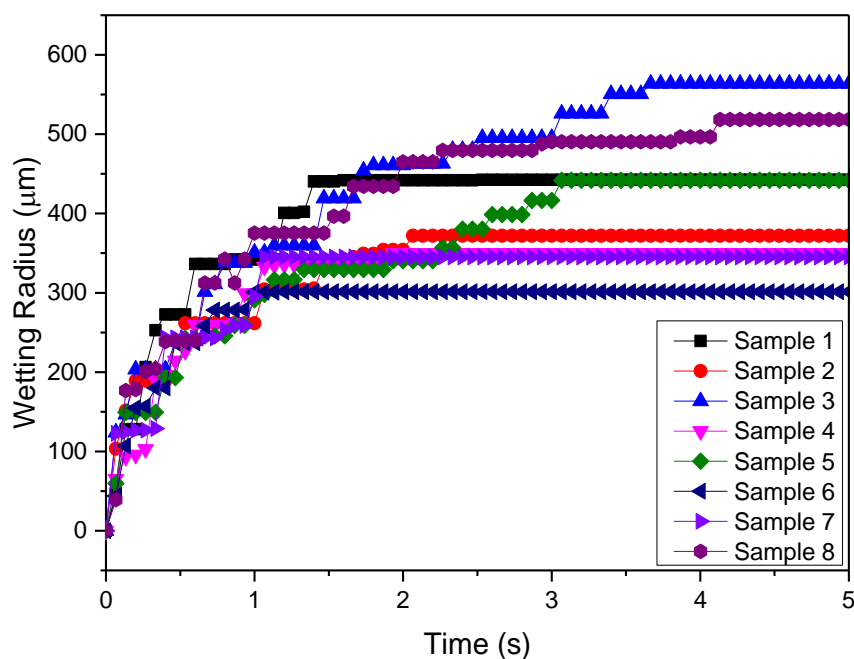


Figure 4.6: Example of the wide variety in wetting from samples prepared by the same method on the same day, using no additive at 50% humidity and a 50 nm pipette.

4.4.3 Changing Humidity

The humidity affected the wetting in a counter-intuitive way. As can be seen from Figure 4.7, the maximum wetting radius increases as the humidity increases. This could be a result of the structure of gypsum, more namely the thin water layers that join crystals, and the hydrophilicity of gypsum. At a very high humidity a thin water layer coats the gypsum crystals, and this makes wetting easier as the water travels along these thin water layers easier than wetting dry gypsum. Another possible hypothesis is that as all of the gypsum crystals have this thin water layer, there is a limit as to how much water each gypsum environment can maintain, and the water added from the droplet must travel further in order to find gypsum crystals that are not already oversaturated with water.

Another interesting aspect of the wetting at different humidities is the rate of wetting. At both low and high humidities, the wetting is slower, although high

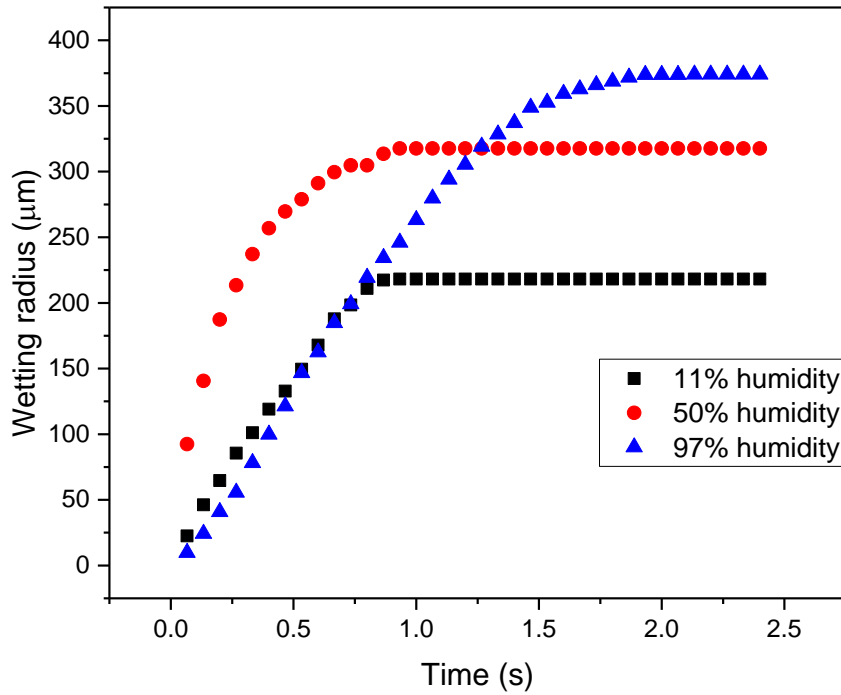


Figure 4.7: Average wetting radius on plaster samples with no additive at differing humidities using a 50 nm pipette.

humidity leads to further wetting distance. At a middle ground humidity, the wetting is faster but reaches a lower maximum wetting radius. It could be that the maximum wetting radius is proportional to the humidity, while the wetting rate has a preferential middle zone where the wetting is fastest. This could be because at low humidities the lack of a water layer slows the wetting process as the water sticks to the crystals, while at high humidities the presence of an already relatively large water layer slows the further wetting. More testing needs to be done to confirm this hypothesis, namely more samples need to be tested with a larger variety of humidities to see if this proposed pattern is real.

Figure 4.8 shows the average wetting results of three sets of three different plaster samples at 97% humidity. From these data it can be seen that the error bars are very large, potentially meaning that the experiment was inconsistent (also there are

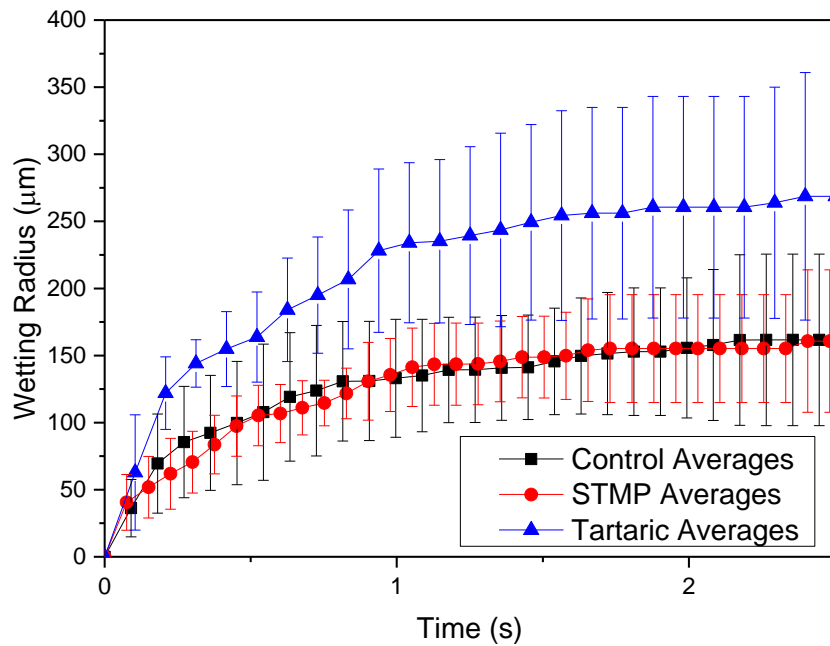


Figure 4.8: Average wetting radius of 3 plaster samples at 97% humidity using a 50 nm pipette.

only 3 datasets to average from, which may lead to the large deviation in the data). These data show tartaric acid increase the wettability of the plaster compared to the other two plaster types. With these sets of plaster samples STMP showed no wetting difference to the control plaster samples with no additive. Figure 4.9 shows the average wetting data of three different sets of three different plaster samples at 50% humidity. Here the results are different again, showing both tartaric acid and STMP increasing the wetting of plaster compared to control samples with no additive. These data seem to imply that the two additives chosen counter intuitively increase the wettability of plaster at “normal” (50%) humidities while at the higher humidity only tartaric acid increases the wettability. There could be some differences between the interaction of tartaric acid and STMP with the water layer on the surface of the gypsum crystals, and at high humidity where the water layer is thicker, this difference becomes apparent and the wettability of the plaster is affected. It seems like tartaric acid is mostly unaffected by the change in humidity (except the expected slight

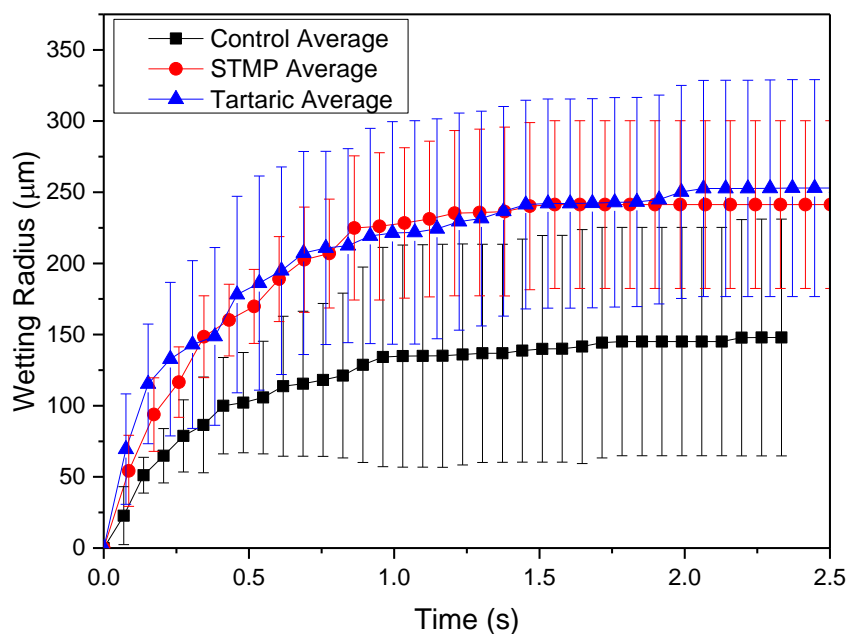


Figure 4.9: Average wetting radius of 3 plaster samples at 50% humidity using a 50 nm pipette.

increase in wettability at higher humidity), while STMP is greatly affected. This could be due to the structure of the two additives, as if the additives are coating the gypsum crystals, then the different properties of STMP and tartaric acid could lead to water spreading more readily over STMP than tartaric acid.

4.4.4 Wetting with Micropipettes and BET Analysis

As can be seen from the SEM of the plaster (Figure 4.4a), the surface is extremely random, and the majority of the vacancies between gypsum needles are much larger than 50 nm, the size of the droplet being used. To eliminate this randomness in the wetting, larger droplets were used. 50 μm single barrelled nanopipettes were used for application of 50 μm droplets. Micropipettes of 5-10 μm were pulled with a laser puller and then polished down until the opening was 50 μm in diameter. Single barrelled micropipettes were used instead of the double barrelled

SECCM setup as a 50 μm droplet was much easier to apply to the surface as this size of droplet could be applied manually. The main use for SECCM was with the 50 nm nanopipettes, as the glass at the end of the nanopipette was so thin, that the slightest touch on the surface would break the end.

The results for the wetting with additives using a larger pipette (50 μm diameter) are shown in Figures 4.10 and 4.11. Upon averaging over 8 different samples there is very little difference in the wetting between each plaster sample with different additives, however the data does seem consistent with the previous data using the 50 nm pipettes as STMP seems to be affected between humidities (relative to tartaric acid and the control sample). While the difference between the wetting radius after 10 minutes between samples seems to be negligible, there does seem to be a difference in the rates of wetting on this larger scale. At both humidities, tartaric acid seems to slightly accelerate the wetting speed compared to the control plaster with no additive, while at the lower humidity (50%), STMP has an even faster wetting

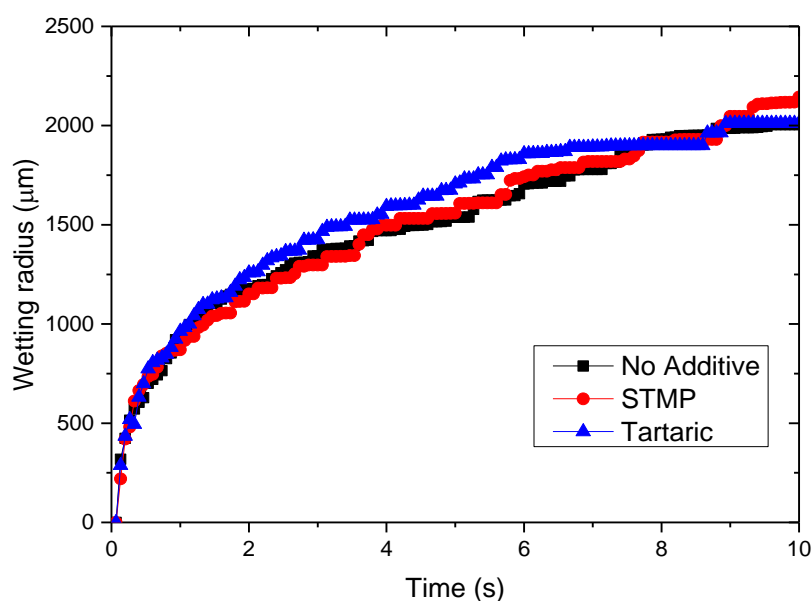


Figure 4.10: Average wetting radii on cross-section of plaster at 97% humidity with a 50 μm micropipette.

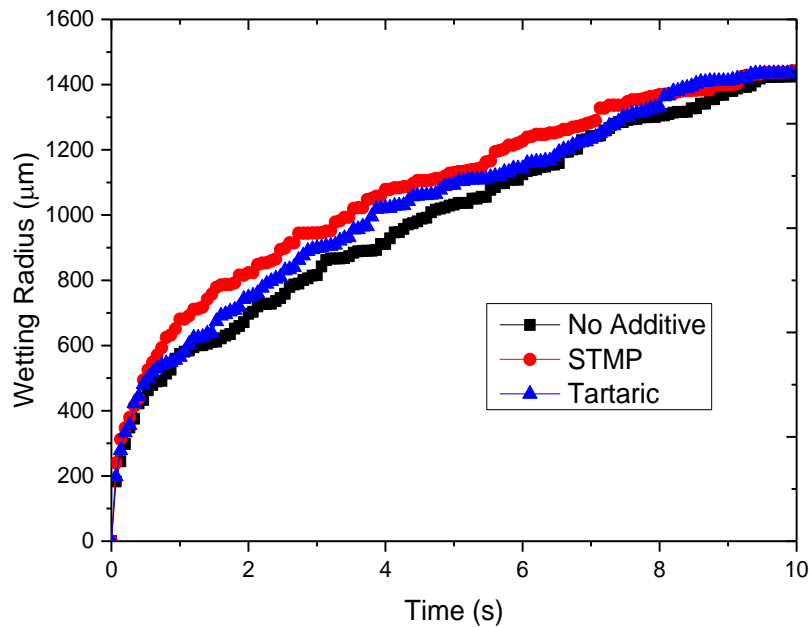


Figure 4.11: Average wetting radii on cross-section of plaster at 50% humidity with a 50 μm micropipette.

that tartaric acid, but at higher humidities the reverse is true, with the STMP samples having an almost identical wetting acceleration as the control samples (on average). This data coincides with the wettability data from the 50 nm pipettes, with STMP showing a reduction in wettability at a higher humidity.

One of the other additives that was explored in the wetting setup was some silicone oil provided by Saint Gobain. This additive is used for specialist plaster that is particularly resistant to water, as the silicone oil is very hydrophobic.¹⁰ As shown in Figure 4.12, the plaster became so hydrophobic that the water did not even penetrate the plaster and no wetting at all was seen.

From these results it could be suggested that the wetting is altered by the additives incorporated into the plaster, with tartaric acid and STMP both behaving differently depending on the humidity of the environment. Sometimes the wetting seemed to differ between samples, randomly increasing or decreasing even with the

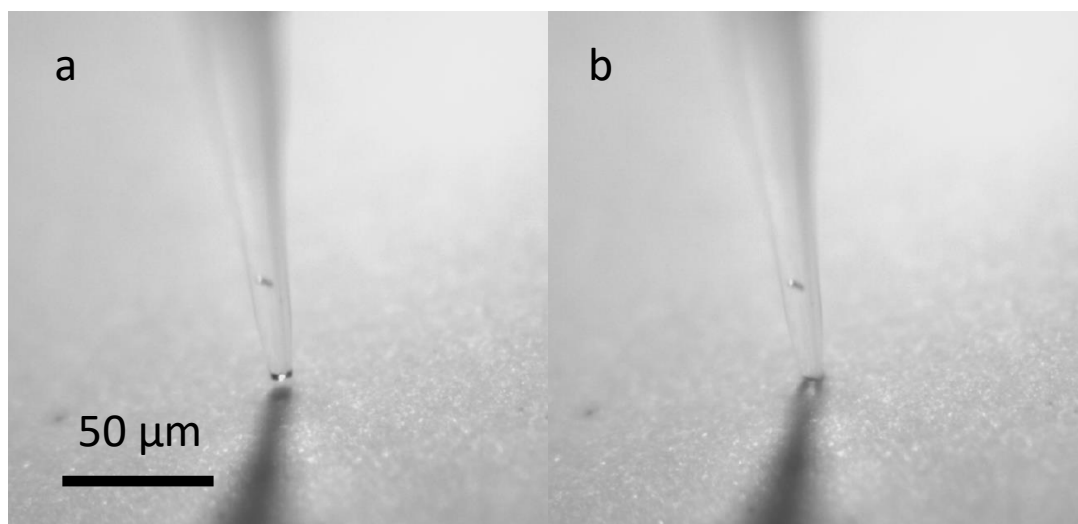


Figure 4.12: Wetting of plaster (50 μm pipette) with silicone oil incorporated; a) the micropipette before making contact with the surface, b) the micropipette after making contact with the surface. The plaster is now so hydrophobic that the droplet does not penetrate the surface and no wetting is seen.

same additive. This was attributed to differing porosity which seemed uncontrollable as every sample was prepared by the exact same method. The only potential error in preparation was with the initial mixing of the plaster, and this may introduce different levels of porosity, which can be measured by BET.

BET measures the surface area and porosity of a powder, however the plaster cannot be powdered as this will destroy all the natural porosity from the gypsum matrix. Instead 3-4 small chunks of plaster were used each time, and while this led to a much lower porosity than a powder, it was theorised that this would give a more accurate porosity for plaster. One of the problems with gypsum for BET was the drying of the samples. Usually samples are dried at $>100\text{ }^{\circ}\text{C}$ to remove water from the surface of the powder, but gypsum deteriorates into bassanite ($\text{CaSO}_4 \cdot \frac{1}{2}\text{H}_2\text{O}$) at temperatures over $40\text{ }^{\circ}\text{C}$. Thus $40\text{ }^{\circ}\text{C}$ was the maximum temperature possible for drying the samples and this unsurprisingly caused some complications. $40\text{ }^{\circ}\text{C}$ is not a high enough temperature to completely evaporate the surface water, but any higher would remove the water molecules from the crystal structure. This could mean that

the porosity of each sample is not completely accurate, but relative to one another the samples were dried the same. An average of surface areas for plaster with the different additives is shown in Figure 4.13.

It seems likely from this data (and a lot of the data collected in this Chapter) that this experiment could be improved. The inconsistencies seen herein (e.g. the large wetting differences seen in Figure 4.6) could be due to the differing porosity of samples created (shown in Figure 4.13 by the large error bars), as even samples created on the same day under the exact same conditions had differing porosities probably due to human error in the mixing/pouring of samples. This difference in each wetting time could also be due to the random nature of each plaster surface, with the droplet from the nanopipette landing on differing environments. The droplet can land on a gypsum crystal or a cavity, or on the edge of a gypsum crystal, all of which would lead to different wetting. While moving to a larger pipette size (from 50 nm to

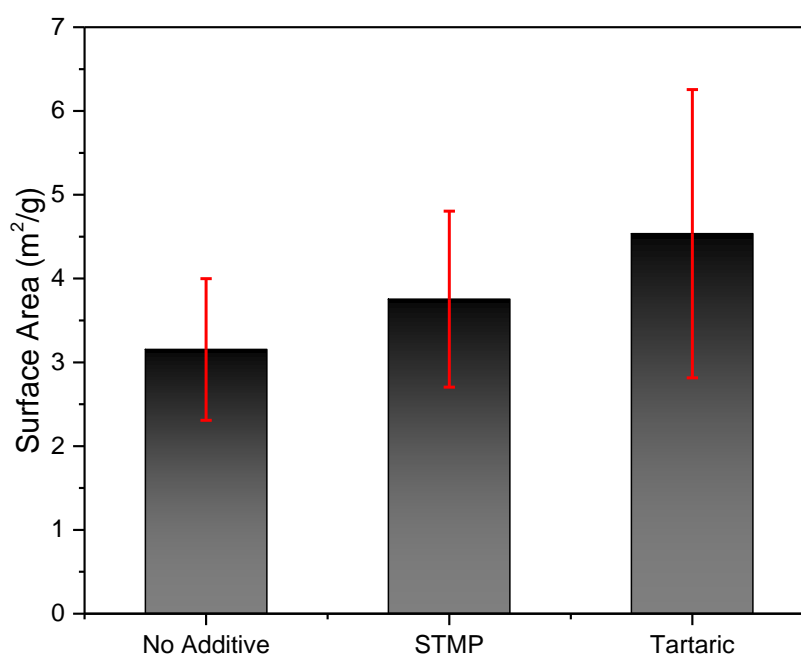


Figure 4.13: Surface area of plaster samples with different additives, measured by BET.

50 μm) removed this random aspect of the droplet contact, the experiment still seems too inconsistent at this point to provide sufficient data to suggest any reasonable hypotheses from the small data sets presented herein. A large amount of plaster samples need to be tested under the exact same conditions in order to determine if there are noticeable differences between the additives for the wetting of plaster. From the data presented herein it cannot be confirmed if the additives effect the wetting of plaster at different humidities (only hypothesised), but a much larger data set of plaster samples would improve accuracy a lot and could help to confirm some of the hypotheses presented.

The humidity also needs to be controlled much more precisely than was done in this experiment. Using salt solutions to control the local humidity is not necessarily very precise, and when working with these small plaster samples in the conditions herein, with the experiments being performed inside of a Faraday cage, the humidity was very difficult to measure and reliably control. Ideally these experiments need to be performed inside an airtight controlled humidity environment such as a glovebox to ensure that the humidity is constant and not fluctuating due to external effects such as opening or closing the Faraday cage or even people walking nearby.

Despite all these problems there does seem to be some merit to further exploration into these findings presented here, just with much better and consistent preparation of gypsum samples (maybe using a motorized stirrer or some sort), better humidity control (with a glovebox as mentioned before), and a much larger number of samples. Referring back to the second Chapter, which looked at droplets containing additives on single gypsum crystals and their contact angles, the studies could be married together to look at single gypsum crystals and how far water spreads on single

crystals treated with different additive, giving some insight to how these additives effect the wettability of plaster, and potentially the humid creep effect.

4.5 Conclusions

Herein a novel SECCM wetting technique has been shown, specifically on plaster with an intent to analyse how additives incorporated into plaster affect the spread of liquid at different humidities. Gypsum has been shown to exhibit interesting wetting behaviours when exposed to different humidities. At higher humidities (~ 97%), gypsum wets much easier than at lower humidities. The least amount of wetting appears to be at medium humidities (~ 50%), with a moderate amount of wetting at low humidities (~ 11%). More experimenting on this hypothesis of a “sweet spot” for wetting needs to be done, with a larger array of humidities tested. A much larger sample range of plaster needs to be tested too, to allow for the large heterogeneity between samples.

It was found that the additives tested (tartaric acid and STMP) affect the wetting, with tartaric acid increasing the speed of wetting while STMP only increased the wetting speed at 50% humidity. Silicone oil incorporated into the plaster exhibited no wetting whatsoever. High humidities (~97%) had no effect on the wetting speed of the STMP incorporated plaster samples compared to plaster samples with no additive.

The wetting is also drastically altered by the porosity of the samples, but the porosity was difficult to control between samples, with samples prepared on the same day by the same method yielding different porosities. Future forays into this study need to use a more consistent method for creating plaster that reduces the deviation in porosity shown here, maybe with a mechanical stirrer of some sort rather than by human hand.

4.6 References

- ¹ V. M. Starov, *Coll. J.*, **1983**, 45, 1154, USSR Academy of Sciences English Translation
- ² P. G. de Gennes, *Rev. Mod. Phys.*, **1985**, 57, 827
- ³ J. F. Joanny, *Mecanique Theoretique Appliquee*, **1986**, 5, 249
- ⁴ G. F. Teletzke, T. H. Davis, L. E. Scriven, *Chem. Eng. Comm.*, **1987**, 55, 41
- ⁵ V. M. Starov, V. V. Kalinin, J. D. Chen, *Adv. Coll. Interface Sci.*, **1994**, 50, 187
- ⁶ E. Raphael, P. G. de Gennes, *Acad. Sci. Paris*, **1999**, 327, 685
- ⁷ L. Bacri, F. Brochard, *Eur. Phys. J.*, **2000**, 3, 87
- ⁸ A. Aradian, E. Raphael, P. G. de Gennes, *Eur. Phys. J.*, **2000**, 2, 367
- ⁹ V. M. Starov, *et al.*, *Advances in Colloid and Interface Science*, **2003**, 104, 123-158
- ¹⁰ D. M. Mahoney, *et al.*, *Environmental, Health and Safety Considerations for Common Moisture Resistant Additive Technologies in Gypsum Wallboard Production*, Published October 2010, accessed September 2018

Chapter 5: Fluorescein as a Potential Plaster Humid Creep Additive

5.1 Abstract

Fluorescein is tested as a humid creep additive and found to have no negative effects on the sagging of gypsum plaster. Fluorescein does not hinder humid creep to nearly the same magnitude as conventional humid creep additives but is considered as a tag for commercial plasterboard to prevent counterfeiting. Common additive tests are performed, assessing fluorescein's viability in an industrial environment and found to have negligible effects on the industrial process. Fluorescein is imaged within gypsum by fluorescence microscopy and can be seen everywhere on gypsum crystals. A droplet evaporation experiment is also performed yielding similar crystal behaviour to when citric acid is used as an additive in Chapter 2.

5.2 Introduction

Fluorescein (Figure 5.1) is a fluorescent organic compound that has many uses as a dye due to its availability and bright colour. It is a red powder that forms a fluorescent yellow solution in water, with a very high fluorescence response. It has been used in the past in a type of dye laser as the gain medium in forensics and serology to detect latent blood stains.¹ Fluorescein is on the World Health Organisation's List of Essential Medicines mainly for its use as a diagnostic tool in ophthalmology and optometry, with fluorescein solutions often being used in eye drops for diagnostics.² It is also used sometimes to diagnose and categorize vascular disorders and is being used increasingly during surgery for brain tumors.³ The fluorescence of fluorescein is very strong, with peak excitation occurring at 494 nm and peak emission at 521 nm. Many fluorescein derivatives exist, with the sodium derivative being most available and cheap.

Initially the reason for studying fluorescein as an additive came from the need to visualise where in plaster the additives reside. The actual position of additives within plaster is fairly unknown – are they coated on the outside of the crystals, incorporated into the crystal structure or focussed within the thin water layers between crystals? A very recent study has shown that certain additives (specifically citric acid

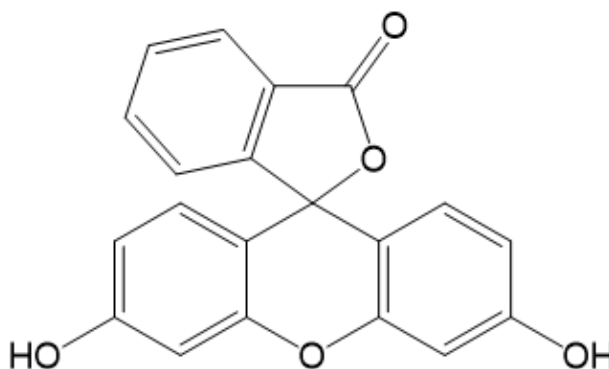


Figure 5.1: The chemical structure of fluorescein.

and tartaric acid) like to bind to the (010) gypsum face in the stand-up configuration.⁹ This finding is almost the exact opposite of what Badens *et al.* reported in 1999, who stated that the (120) and (-111) faces have calcium ions present at the most preferential distances from each other to allow additive binding.⁷ The (120) face is neutrally charged and the closest distance between two calcium ions is 4.0Å. The (-111) face has the same closest calcium ion distance but is positively charged.

Dye molecules have been reportedly incorporated into other single crystals before, and these incorporations can endow the host crystals with a plethora of new properties, such as increased hardness, magnetism and colour. Recent work has shown the inclusion of amino acids within ZnO crystals to tune the bandgap of the semiconducting nature of ZnO.¹⁰ A range of organic and inorganic particles have also been incorporated into calcite (CaCO₃) and most importantly, located using microscopy techniques.¹¹⁻¹⁶ Tunable lasers have also been created from similar practices, with the addition of fluorescent dyes into the crystal structure.^{17,18} One of the unique outcomes of these studies is that they provide methods for understanding crystal/additive interactions. The signature colour of the fluorescent dye molecules reveal the position, while changes in emission spectra give information on the environments within the crystal.^{19,20} A recent study by Green *et al.* looked at the inclusion of fluorescent additives within calcite crystals, and showed that the additives were clearly visible by confocal fluorescence microscopy, yielding more information on the different local environments within single crystals.²¹ Through this, they created a white fluorescent calcite through the simultaneous incorporation of red, blue and green fluorescent dyes.

In this study the viability of fluorescein as a humid creep additive is explored. The effect of adding fluorescein to plaster slurry is studied with respect to the

viscosity of the slurry and how the fluorescein affects the set time compared to plaster with no additive included. Confocal fluorescence microscopy, SEM and the droplet technique from Chapter 2 are used to visualise crystal morphology behaviours and analyse where fluorescein and potentially other additives adhere to within the gypsum structure. Future applications of fluorescein in plaster are also discussed not in reference to use as a humid creep additive, but as a tag in plaster that would be unique to the maker to avoid conflicts when problems within plaster boards arise.

5.3 Materials and Methods

5.3.1 Solutions

All solutions were made in ultrapure 18.2 MΩ water (Purite, Select HP). Calcium sulfate hemihydrate powder ($\geq 99\%$) was supplied by Saint Gobain. Fluorescein ($\geq 99\%$) was purchased from Sigma-Aldrich.

5.3.2 Tests for Water Demand, Set Time with Additives

To analyse water demand of stucco with fluorescein incorporated, a simple viscosity experiment was performed, schematic shown in Figure 5.2. The gypsum slurry was made up as standard but with a water gauge of 70. A controlled volume of slurry was then placed into the receptacle and after a set time, the bottom was removed and the spread of the slurry over the bottom plate was measured.

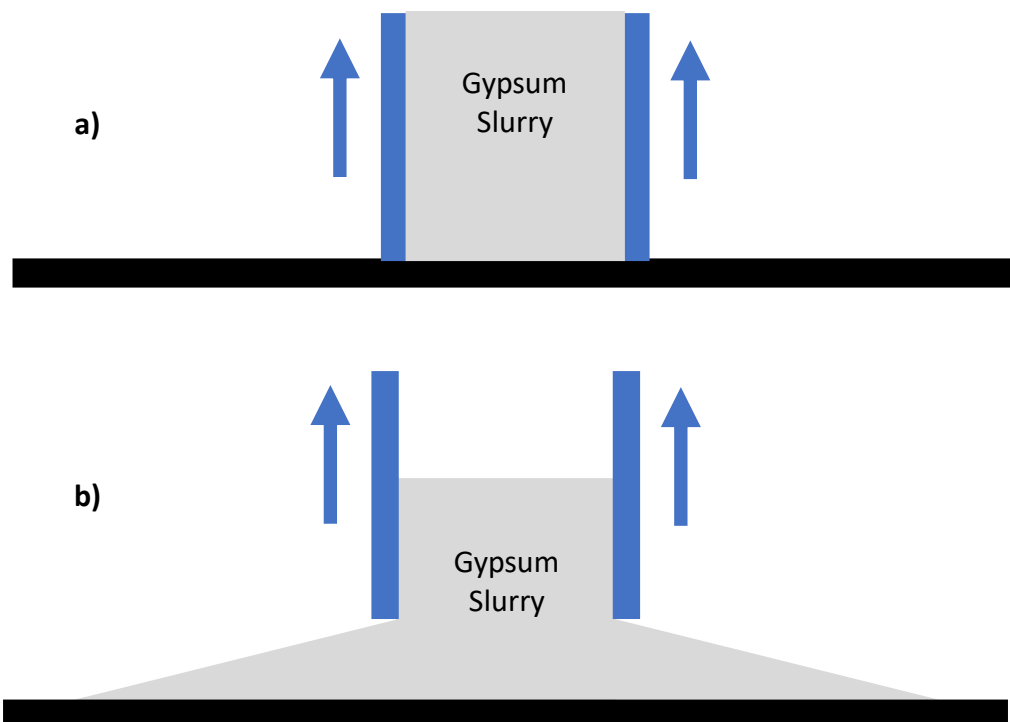


Figure 5.2: Schematic of equipment for testing the viscosity of gypsum slurry. A) shows the slurry in the receptacle before the bottom is removed, and b) shows the spread of gypsum as the bottom is lowered.

To measure the set time of plaster, a simple needle pressure test was applied. The setup is shown in Figure 5.3a. Two set times were necessary to measure; the first was measured as the time taken for the plaster to harden sufficiently so that the needle did not penetrate further than 30 mm. This was referred to as the initial set time. The final set time was measured as the time for the needle in Figure 5.3b to leave no outer ring indent.

Another test needed for commercial plaster was to check the rise of the temperature inside the plaster as it dries. This was accomplished with a thermocouple in two slurry samples, one with additive and one without additive. The slurry samples were held in polystyrene cups and encased in thick polystyrene to avoid external heat sources.

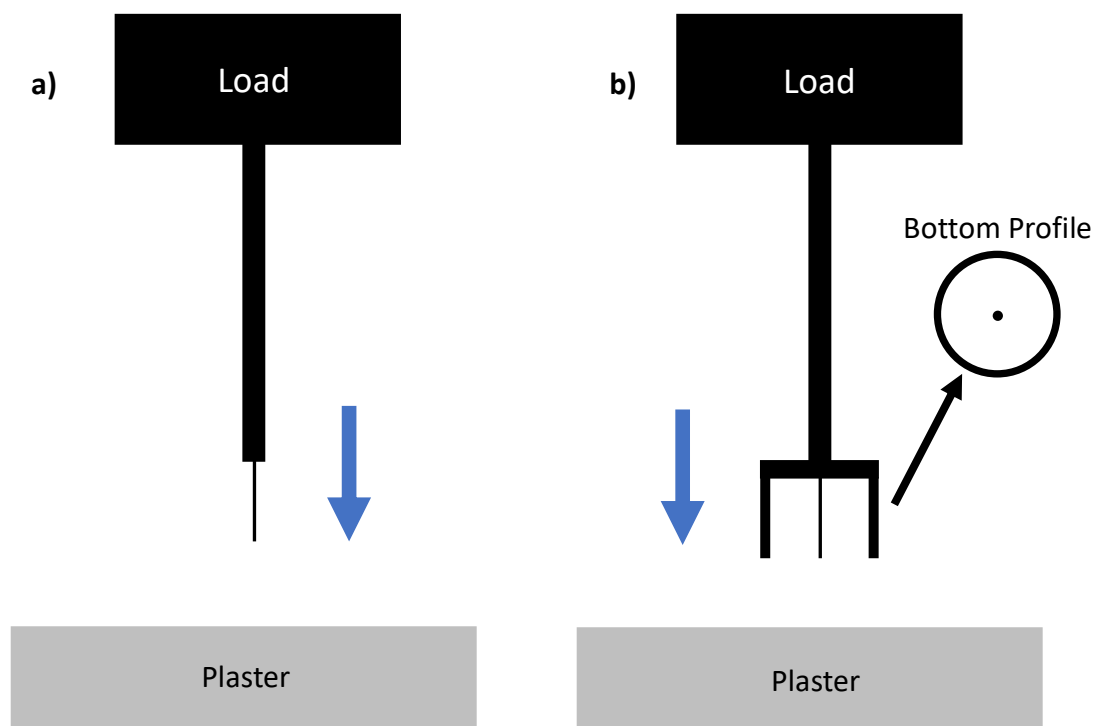


Figure 5.3: Schematic of equipment for testing set time of plaster. The initial set time is measured with setup a) and the final set time measured with b). The profile of the needle from underneath in setup b) is shown inset.

5.3.3 Fluorescence Microscopy

Fluorescence microscopy was performed with a Leica TCS SP5-X confocal microscope with an argon ion laser tuned to a 496 nm wavelength.

5.3.4 Sag Testing

Sag tests were performed at the R&D centre in Saint Gobain Research Shanghai using specialised sag testing equipment. The schematic is shown in Figure 5.4. A long thin plasterboard was created, and secured at either end. A load was then placed directly in the centre, with a laser aimed through the load (which has a hole in) at the plasterboard beneath. The displacement of the plasterboard was then measured

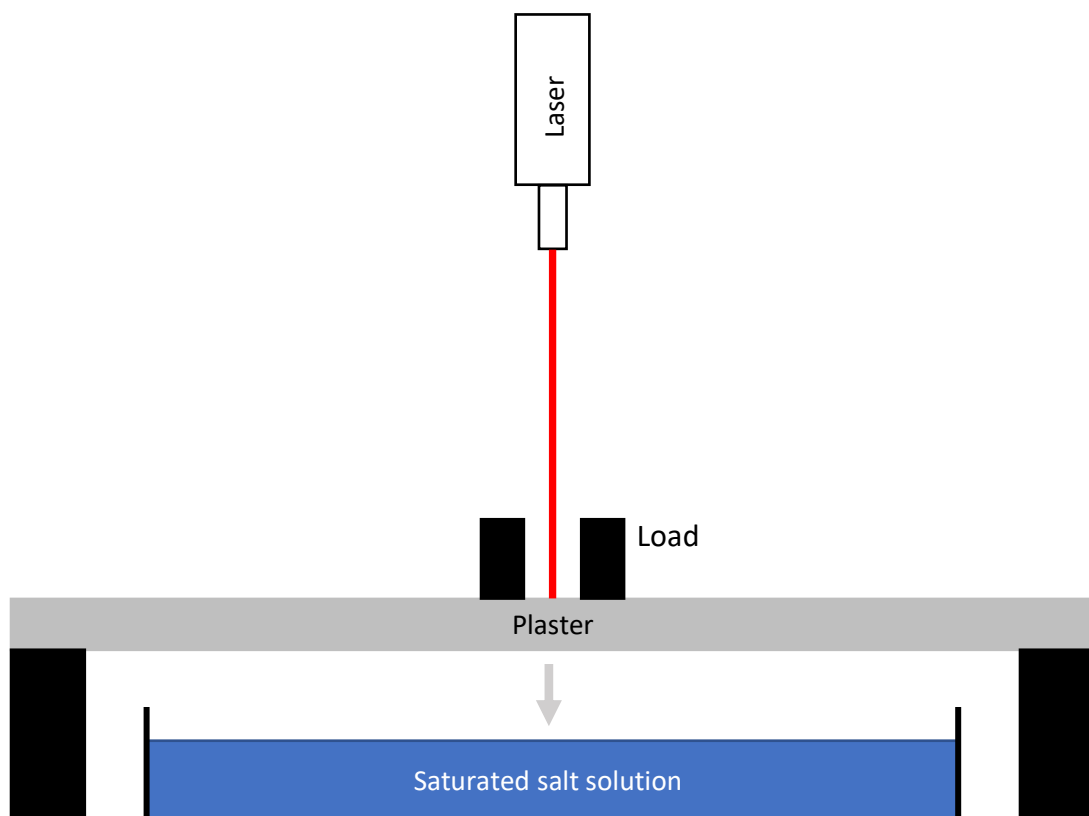


Figure 5.4: Schematic of the sag testing setup. The load on top of the plaster is ring shaped, with a hole in the middle to accommodate for the laser. This ensures the laser is recording the largest displacement.

over time, as the board sags. The entire setup was enclosed to allow control of humidity by addition of saturated salt solutions in a bath at the bottom of the setup.

5.4 Results and Discussion

5.4.1 Fluorescence Microscopy

Fluorescence imaging of gypsum with fluorescein showed that the fluorescein was incorporated everywhere in the plaster. The images shown in Figure 5.5 are of an evaporated droplet of 10 mM calcium sulfate hemihydrate and 0.5 mM fluorescein. While the fluorescein is incorporated everywhere on the crystals, this could be an artifact of the fact that there are many small crystals grown on top of each other. However some of the single crystals seen growing out (for example the crystal labelled as 56 μm in Figure 5.5) are long singular crystals that show fluorescence all along their length, implying that the fluorescein is either coating the crystals or incorporated inside. These images show us that fluorescein is not just focussed in the

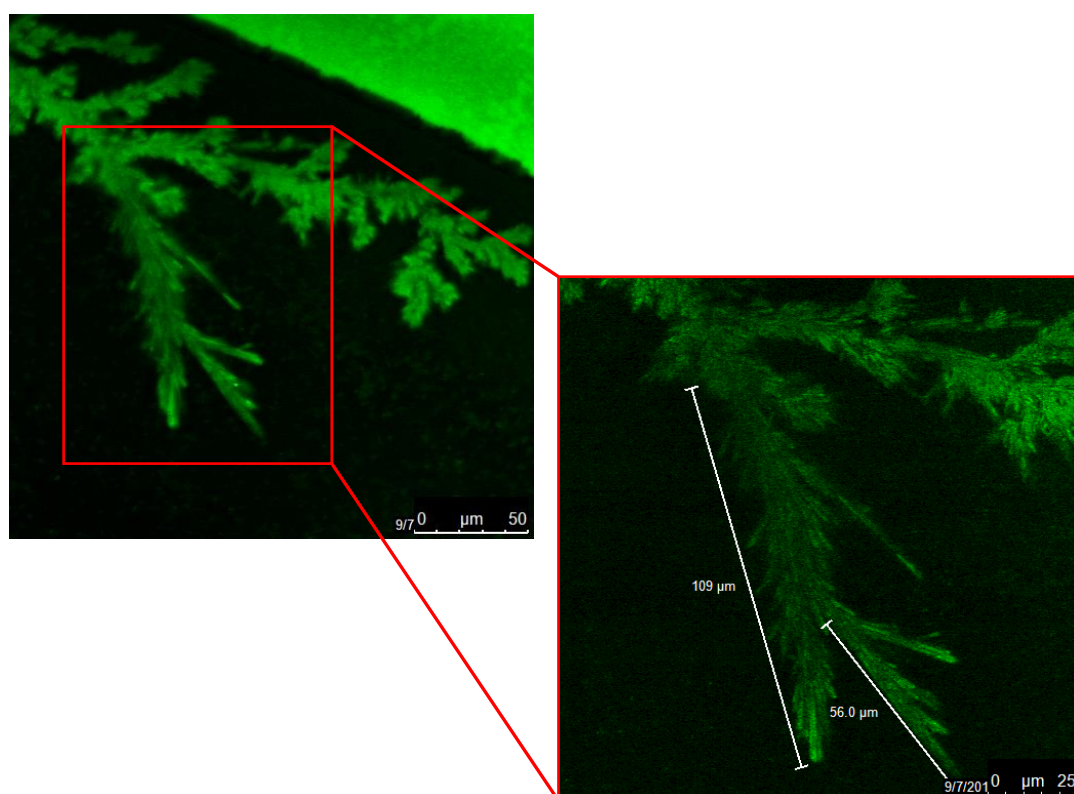


Figure 5.5: Fluorescence microscopy images of gypsum formed from the evaporation of a droplet containing 10 mM $\text{CaSO}_4 \cdot \frac{1}{2}\text{H}_2\text{O}$ and 0.5 mM fluorescein.

thin water layers between crystals, and this behaviour could be present in other humid creep additives.

One of the interesting aspects of the fluorescein structure is that it has an ester COO bond, which is very similar to the carboxyl groups of a lot of common additives. It was therefore theorised that fluorescein could work as a humid creep additive.

5.4.2 The Viability of Fluorescein in Industry

For fluorescein to be even remotely successful as a humid creep additive, its addition cannot influence the setting of plasterboard. For example, fluorescein cannot slow down the time taken for plaster to set, affect the temperature rise set or the viscosity of the gypsum slurry. Tests for all of these were undertaken at Saint Gobain East Leake with the experimental setups shown earlier. The results for the set time and temperature rise set are shown in Table 5.1. Compared to a sample with no additive, the fluorescein did not affect any of these parameters negatively. The water gauge in all the plaster made was 70. For viscosity measurements, slurry without any additives spread to a diameter of 79 mm, while slurry with fluorescein present spread to a diameter of 82 mm. This difference in spread is considered negligible and it can be said that the fluorescein does not affect the viscosity of the gypsum slurry.

Table 5.1: Comparisons of the set times and hydration time of plaster samples created with no additive and 0.5% fluorescein by weight.

Recipe	Initial Set Time (mins)	Final Set Time (mins)	Hydration Time (mins)
No Additive	3.30	4.45	15.15
0.5% Fluorescein	3.30	4.45	15.20

The set times also did not change at all between the two samples. Any increase in the set time would not be favourable, and any decrease in the set time means the fluorescein is acting as a crystallisation accelerator. The temperature rise set also did not increase significantly. This temperature rise set is the time taken for the temperature inside the plaster slurry to reach a maximum temperature, as this implies the hydration is complete. It can be seen that the time taken for each sample to reach its maximum temperature is negligible between samples. Thus, these results show that fluorescein should not affect the production process of forming plasterboard and could be considered as an additive into plaster.

5.4.3 Droplet Evaporation Experiment and SEM

As the droplet experiment was performed on other additives (see Chapter 2), the same experiment was performed with fluorescein as the additive. The gypsum crystallisation behaviour looks very similar to how the gypsum incorporated with citric acid behaved, which was unique. Fluorescein seemed to make the gypsum form one large ring of small crystals around the rim of the droplet. A comparison image of gypsum with no additive is shown in Figure 5.6. This shape is interesting considering that fluorescein does not show the same setting inhibition effects that citric acid exhibits.⁹

5.4.4 Sag Testing

Sag tests were the ultimate test for fluorescein to be a humid creep additive – while it exhibits behaviour that would make it a non-intrusive additive, the uses of a humid creep additive all rest on whether it actually reduces sag or not. The sag results

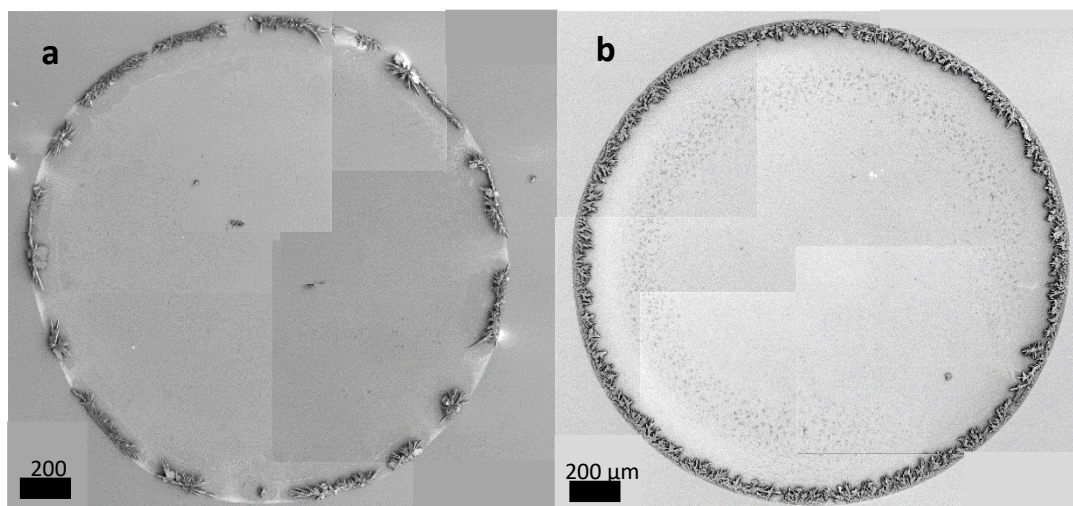


Figure 5.6: SEM images of evaporated droplets of a) gypsum with no additive and b) gypsum with 0.5 mM fluorescein incorporated.

from Saint Gobain Shanghai are shown in Figure 5.7. Boards of plaster with no additive and plaster with tartaric acid (the standard humid creep additive for the company) are compared alongside boards with fluorescein and it can be seen that fluorescein has only a small effect on hindering the sag of plaster, especially compared to tartaric acid.

Despite the humid creep inhibition of fluorescein being effectively negligible, fluorescein might still have a use in the plaster industry. In certain plaster boards tags are used to ensure that problems with plaster boards can be traced back to the creator, and fluorescein could be a useful tagger in the sense that it shows no negative effects on the plasterboard, but would show up and luminescent under UV light. Aesthetically fluorescein can turn the plaster an off-orange colour (depending on the concentration used), but for architecture, most plaster is covered with paint, concealing any colour that is present in the plasterboard. Much more testing with fluorescein needs to be done, for example coupling fluorescein with modern humid creep inhibition additives such as STMP and tartaric acid, to see what effects on the sag this has. It could be that

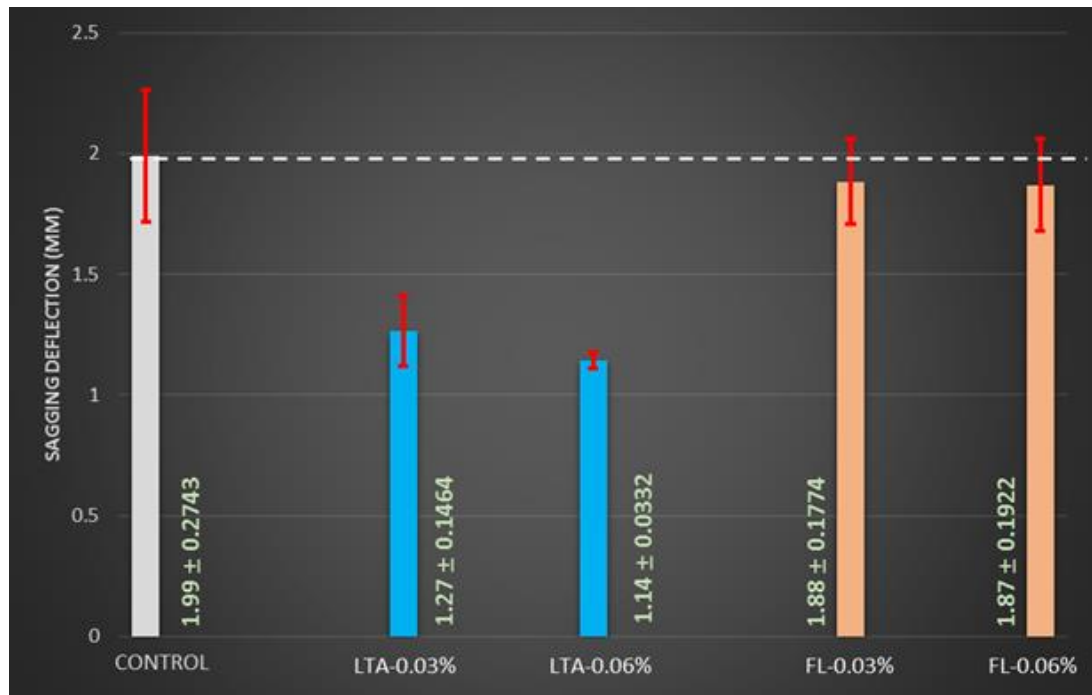


Figure 5.7: The sag of plaster boards made from a standard procedure. In this diagram, LTA = L-tartaric acid and FL = fluorescein.

fluorescein will be seen in the future as a tagging additive alongside some of these humid creep additives.

5.5 Conclusions

Fluorescein has been shown to not work very effectively as a humid creep additive, but it has also been shown to not affect the setting parameters of plaster. Considering the need for non-intrusive tags in plasterboard that cannot be removed easily, fluorescein shows promise for this use: under a UV light the plasterboard would fluoresce and thus be a clear watermark. Since the fluorescein seems to incorporate everywhere within the plaster, and if fluorescence of the entire plasterboard is not preferable, there is potential scope for the addition of fluorescein somewhere near the end of the setting process, even just addition of the occasional drop of fluorescein solution into the slurry will show up under UV light, and the fluorescein should not spread through the entire slurry due to the viscosity of gypsum slurry. This is a potential work around of any aesthetic issues that arise from fluorescein incorporation into the standard dry mixing of reagents at the start of the plaster making process.

There is much future work that could be done with fluorescein in plasterboard, for example combining fluorescein with other humid creep additives to measure any effects that fluorescein has on the inhibition effects of these additives. Also regarding Chapter 4, nanoprecipitation experiments can be done with fluorescein to see what effects the molecule has on the crystallisation and dissolution kinetics.

5.6 References

- ¹ B. Budowle, J. L. Leggitt, D. A. Defenbaugh, K. M. Keys, S. F. Malkiewicz, *J. Forensic Sci.*, **2000**, 5, 1090-1092
- ² *WHO Model List of Essential Medicines 20th List*, March 2017 (Amended August 2017), Accessed July 2018 at <http://apps.who.int/iris/bitstream/handle/10665/273826/EML-20-eng.pdf>
- ³ T. Mathew, *Ann. Thorac. Surg.*, **2014**, 97, e27-e28
- ⁴ R. E. Muller, P. L. Henkels, B. M. O’Kelly, *Gypsum board*, U.S. Patent 3190787, **1965**
- ⁵ Q. Yu, S. Sucheck, B. Groza, R. Mlinac, F. Jones, F. Boehnert, *Process for reducing creep in a gypsum plaster-based element, gypsum plaster-based composition and method for making a gypsum plaster-based element with reduced creep*, U.S. Patent 6632550, **2003**
- ⁶ E. Badens, S. Veessler, R. Boistelle, D. Chatain, *Colloid Surf.*, **1999**, 156, 373
- ⁷ E. Badens, S. Veessler, R. Boistelle, *J. Cryst. Growth*, **1999**, 198, 704
- ⁸ L. Amathieu, *J. Cryst. Growth*, **1988**, 88, 183
- ⁹ W. Chen, *et al.*, *CrystEngComm.*, **2018**, 20, 3581-3589
- ¹⁰ A. Brif, *et al.*, *Adv. Mater.*, **2014**, 26, 477–481
- ¹¹ K. R. Cho, *Nat. Comm.*, **2016**, 7, 10187
- ¹² Y. Y. Kim, *et al.*, *Adv. Mater.*, **2010**, 22, 2082–2086
- ¹³ Y. Y. Kim, *et al. Nat. Mater.*, **2011**, 10, 890–896

- ¹⁴ A. N. Kulak, *et al.*, *Chem. Sci.*, **2014**, 5, 738–738
- ¹⁵ A. N. Kulak, *et al.*, *Chem. Commun.*, **2014**, 50, 67–69
- ¹⁶ Y. Y. Kim, *et al.*, *Adv. Funct. Mater.*, **2016**, 26, 1382–1392
- ¹⁷ B. Kahr, R. W. Gurney, *Chem. Rev.*, **2001**, 101, 893–951
- ¹⁸ M. Rifani, *et al.*, *J. Am. Chem. Soc.*, **1995**, 117, 7572–7573
- ¹⁹ J. B. Benedict, *et al.*, *J. Am. Chem. Soc.*, **2006**, 128, 5548–5559
- ²⁰ A. Barbon, *et al.*, *Angew. Chem. Int. Ed.*, **2004**, 43, 5328–5331
- ²¹ D. C. Green, *et al.*, *Nat. Comm.*, **2016**, 7, 13524

Chapter 6: Conclusions and Outlook

This thesis aimed to understand how anti-sag additives of gypsum plaster inhibit the rate of humid creep, and with this understanding, propose a new idea for a potential humid creep inhibitor that performs better than existing additives. As an abundant material with a wide range of applications, gypsum studies are relevant to modern research. Multiple methods have been employed herein to discern the origin of the humid creep inhibition mechanism, studying crystallisation and dissolution kinetics and behaviours.

The crystallisation behaviour of gypsum has shown to be altered by the introduction of additives in Chapter 2. The droplet evaporation experiment shows that certain additives such as gallic acid hugely hinder nucleation of gypsum crystals, instead largely promoting growth, leading to a small amount of large crystals. Citric acid appears to inhibit crystal growth, but not nucleation, leading to an enormous amount of small crystals. STMP and SHMP both behave unlike any other additives, forming small flower-like crystal clusters, indicating a slowing of both nucleation and growth. The additives did not seem to alter the evaporation rate of the reagent containing droplets, or the time taken for gypsum crystals to crystallise.

Chapter 3 showcases the nanoprecipitation technique with two crystal systems, gypsum and the MOF HKUST-1. Gypsum crystallisation and dissolution kinetics were studied, showing how additives such as tartaric acid and STMP hindered the dissolution of gypsum considerably, without too much effect on the crystallisation, adding weight to the humid creep dissolution/recrystallisation mechanism proposed by Chappuis and Colombani in Chapter 1, as the “best” additives out there affect both dissolution and crystallisation, meaning they could both

play a part during humid creep. Also shown was some of the different crystallisation behaviour by studying the initial current blocking transients. Tartaric acid showed a tendency for large crystals to form inside the nanopipette, whereas STMP exhibited lots of small crystals forming inside the nanopipette, which supports the information found in Chapter 2, where STMP forms smaller crystals. Raman studies were also employed to prove that it was only gypsum forming inside the nanopipette, with no other hydrates of calcium sulfate present.

Nanoprecipitation was also utilised to study the nucleation mechanism of HKUST-1, a commonly studied MOF. Nanoprecipitation was able to prove the mechanism shown in previous literature, which is different depending on the copper precursor used. Copper acetate leads to complete blocking of the nanopipette, indicating the formation of rapid nuclei that agglomerate into large particles. Copper nitrate leads to formation of nanoparticles that fell out of the nanopipette, meaning that sizing of these nanoparticles was possible. In the future a TEM study should be performed in order to confirm this particle sizing. Another study that could be undertaken is to analyse the nanoparticles that form and see if they can be used as seeds for faster HKUST-1 growth. The work in this thesis suggests that this is the case, but TEM or SEM imaging can prove this further. The Raman spectra of the solid created seemed to include some extra peaks compared to literature spectra of HKUST-1, implying that there could be a slight morphological change due to growth in the confinement of the nanopipette. Again, more studies need to be implemented, as there were slight discrepancies in the SEM imaging, showing slight differences in the crystal shaping.

In the wetting study employed in Chapter 4, it was hypothesised that the additives studied had a slight impact on the wetting capabilities of gypsum plaster,

with tartaric acid increasing the wetting speed of plaster and STMP increasing the wetting speed at average humidities (~50%), but not at higher humidities (~97%). Ultimately the experiment proved unreliable, with a wide range of data seen from plaster under the exact same conditions, but several improvements could be made to the experiment to improve reliability. The plaster samples need to be created more reliably, with some sort of automated method of mixing/pouring to remove any human error possibilities. Even with an automated approach however, there is still likely to be differences with the porosity between samples so a much larger sample size would also be necessary. The humidity also needs to be controlled more reliably, with a controlled airtight environment that is kept at a constant humidity being a much bigger improvement on using the ambient environment created by salt solutions. As mentioned earlier in Chapter 4, a study on how far water spreads over single gypsum crystals could be of some merit as this would remove the randomness of the porosity of plaster samples and could provide some data on whether gypsum crystals impregnated with additive are slowing or speeding up the wetting.

Surface area measurements using the BET method were not necessarily reliable due to the fact that gypsum plaster cannot be heated above 40 °C without dehydrating the crystal, meaning that excess water on the surfaces of the crystals could not be properly removed, so full nitrogen adsorption could not take place. If this method was to be used again to study gypsum plaster, a large sample size needs to be taken in order to improve reliability. A different approach needs to be taken in order to study the porosity of gypsum, potentially mercury intrusion porosimetry, which was considered in this project but unavailable at the University of Warwick. With mercury having excellent non-wetting properties and a high surface tension it can give accurate porosity data and is worth considering for future examination.

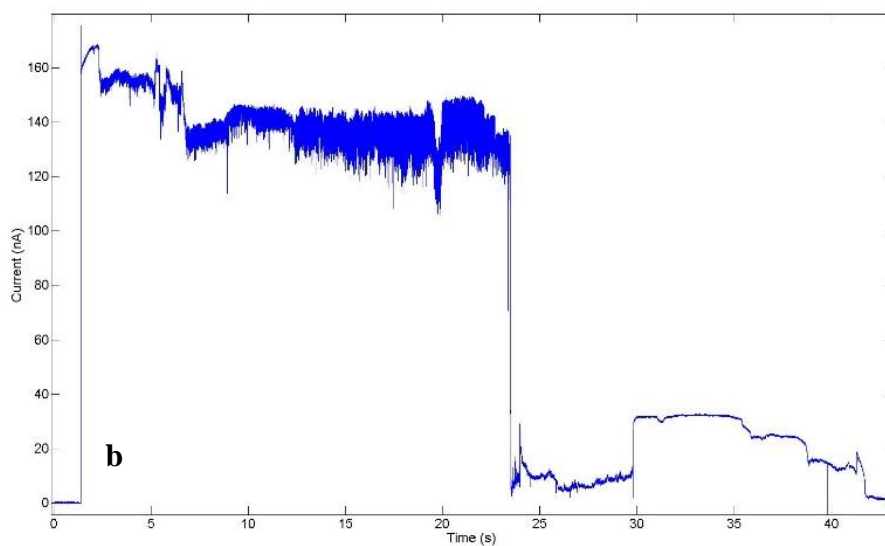
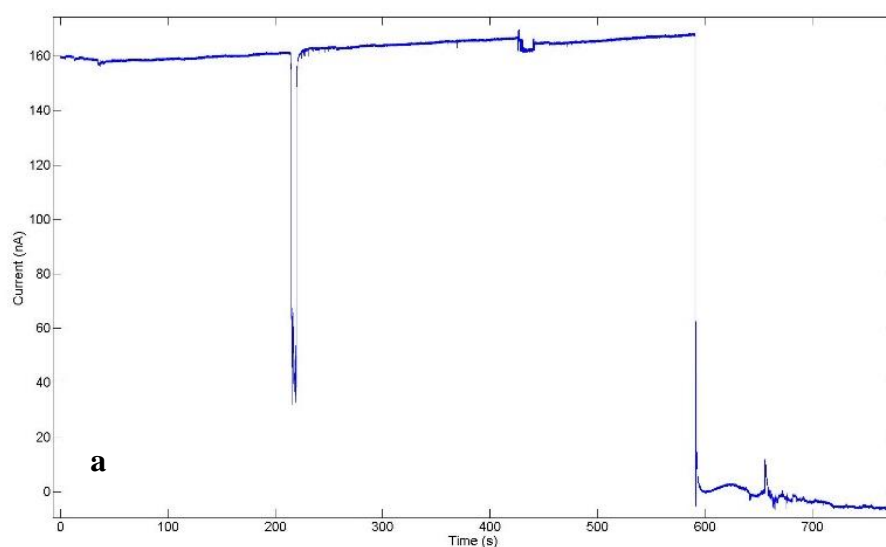
In Chapter 5, fluorescein was studied as a potential anti-sag additive, but was discovered to not work very effectively. It was shown to not alter the setting time for plaster in any way, and while it had no negative effects on the sag of plaster (in that the sag was not accelerated), it has fluorescent qualities which no other additive has, and thus could be used as a tag to combat counterfeiting. This fluorescence also showed that the fluorescein was incorporated all over the gypsum crystals and was not focussed anywhere. This behaviour could be assumed to be the same for other additives, as until recently the position of additives on in plaster has been relatively unknown. Some studies suggest that additives add on certain crystal faces, but the fluorescence data presented herein shows otherwise, although the resolution of the fluorescence microscopy images could be improved, and is perhaps a study for the future to give a better idea as to how the additives incorporate into the plaster.

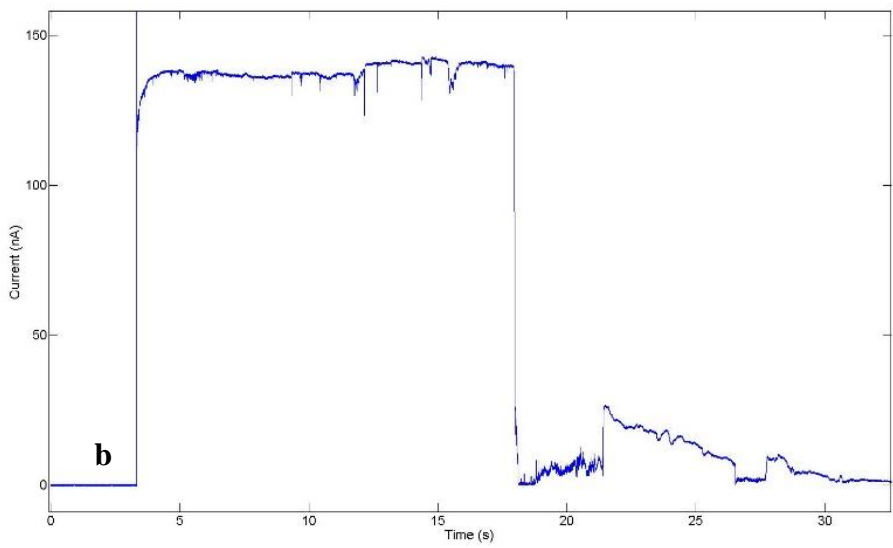
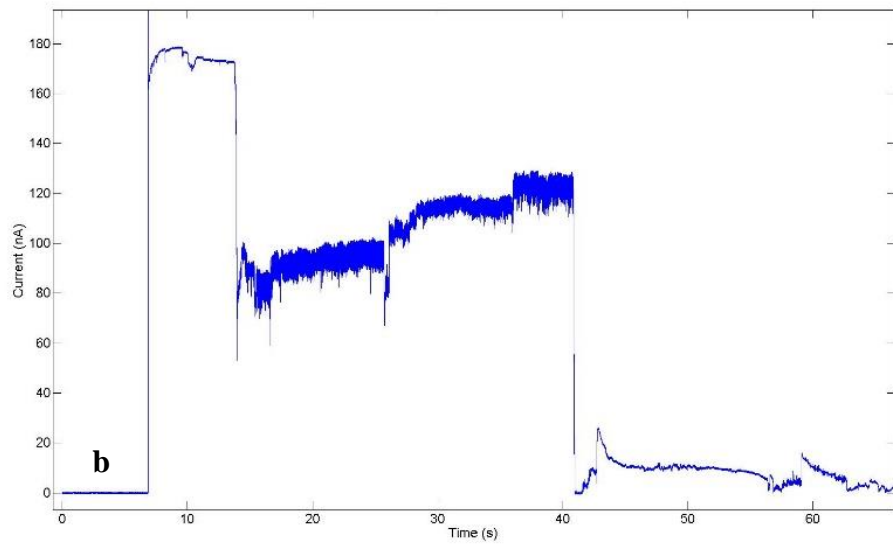
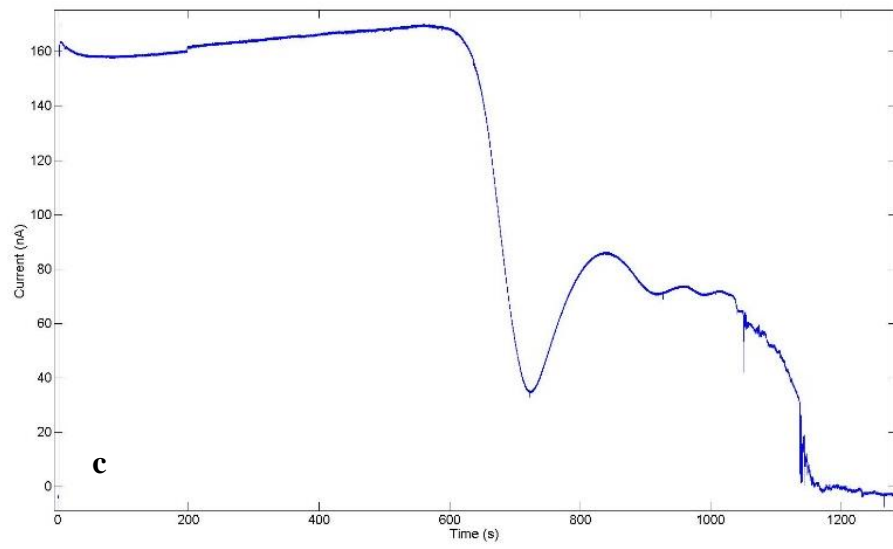
In summary, several plaster anti-sag additives have been tested in different ways to try to understand how the additives work as humid creep inhibitors. It seems clear that the additives effect the crystallisation and dissolution kinetics of gypsum, slowing the dissolution down, while the best additives for industry do not slow the crystallisation much. While the search for a successful new additive yielded no new chemical that reduced the sag effect in gypsum plaster, a potential new chemical tag has been explored in fluorescein, which will help to identify plaster made by a specific company. This will help disputes in the industry for faulty plaster where the creator of the plasterboard is unknown, as the owner can be identified by this chemical tag. The search for a new humid creep inhibitor continues, with nothing trumping the capabilities of STMP without severely hindering the crystal growth of gypsum, which would disrupt and slow production of plasterboard.

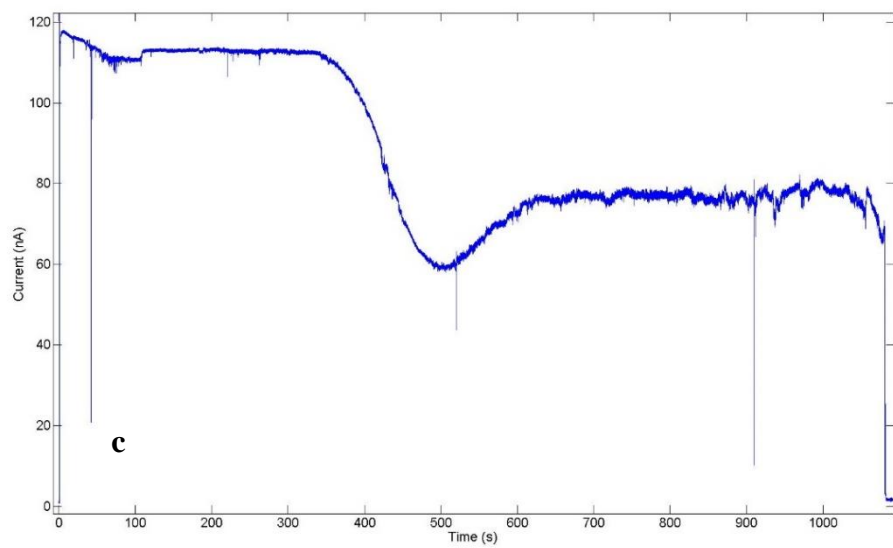
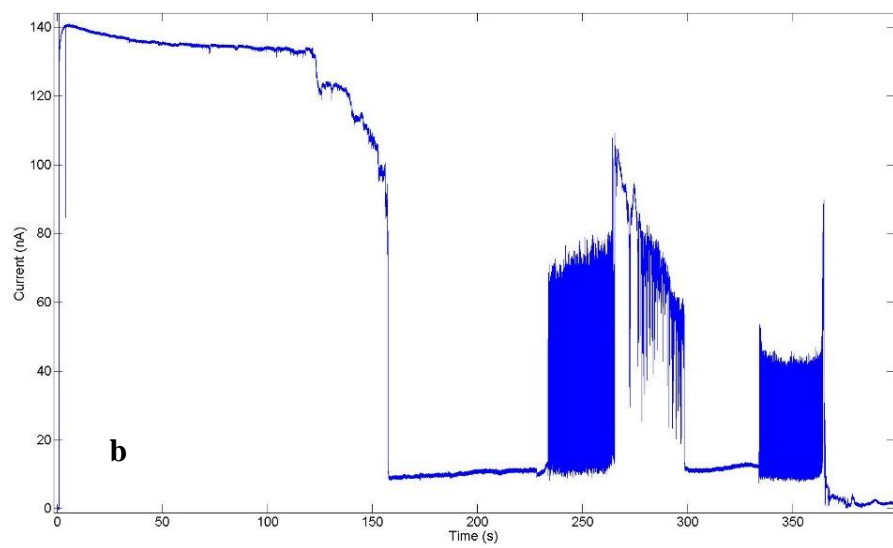
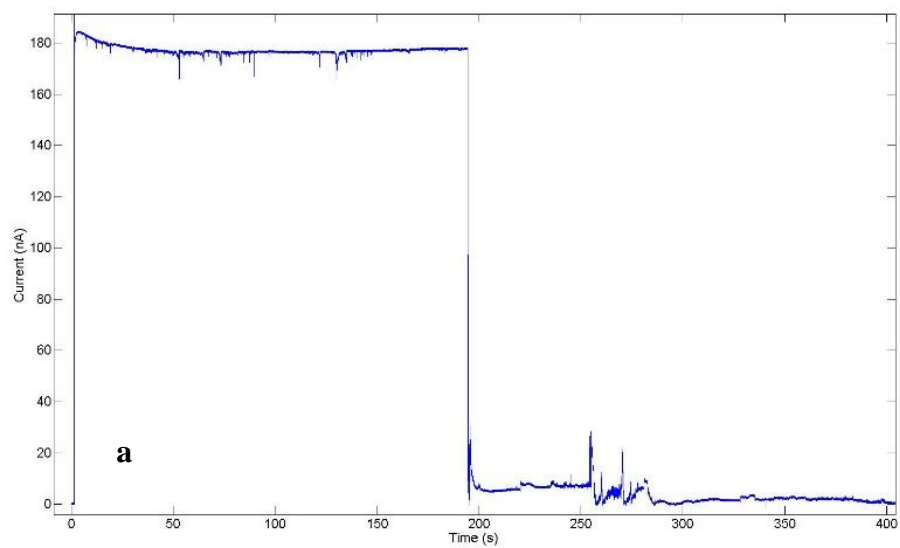
Chapter 7: Appendix

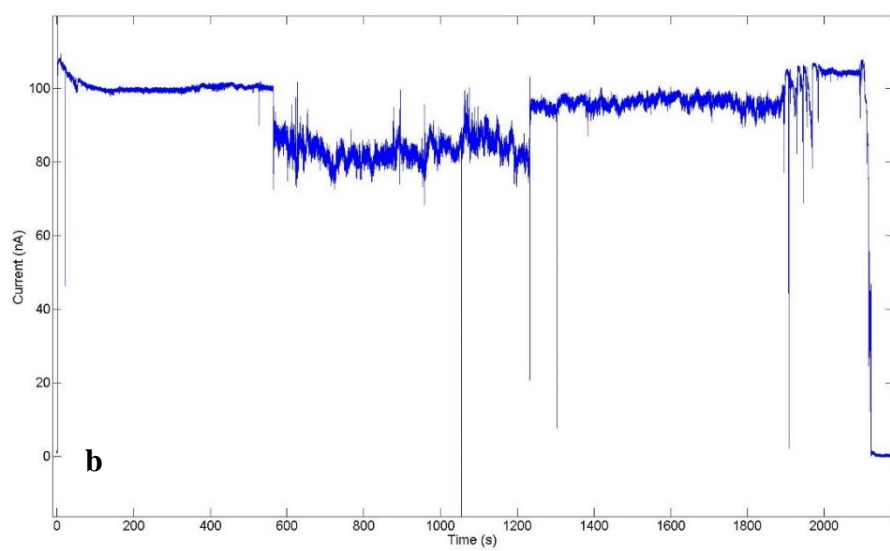
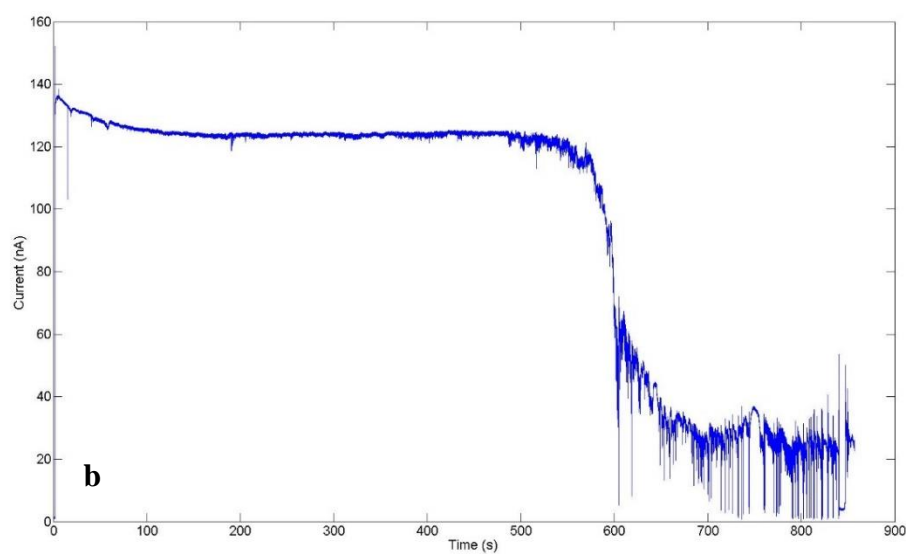
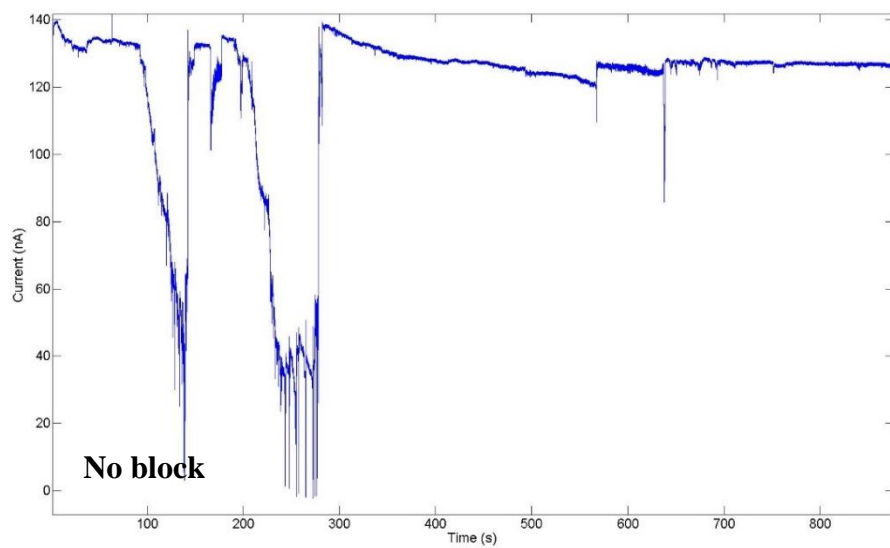
The diagrams in this appendix show more examples of current-time graphs of nanopipettes blocking as gypsum forms as a result of the experiment performed in chapter 3 of this thesis. Three different shapes are seen; a) little activity followed by very sudden blocking, b) large electrical noise followed by sudden blocking, c) 'parabola' shaped transient followed by blocking. Sometimes no blocking is seen. The assigned shape is labelled in the bottom left of each transient.

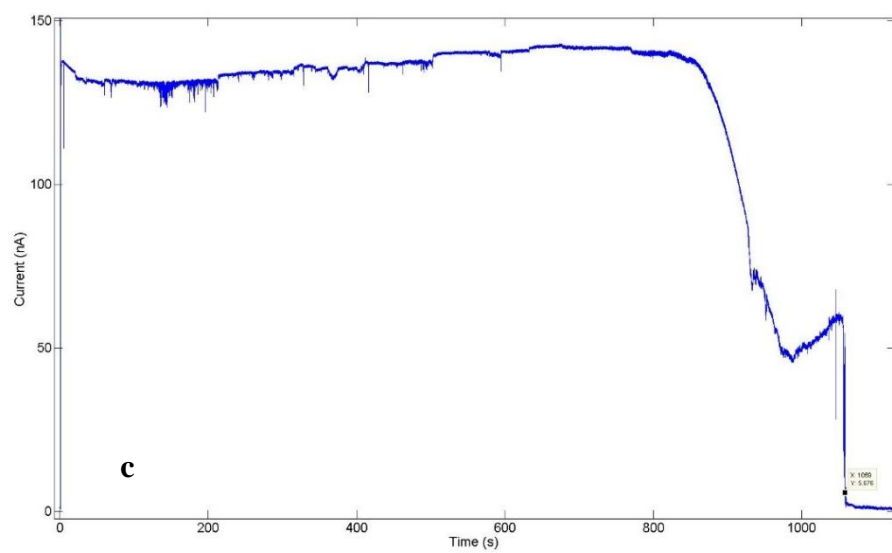
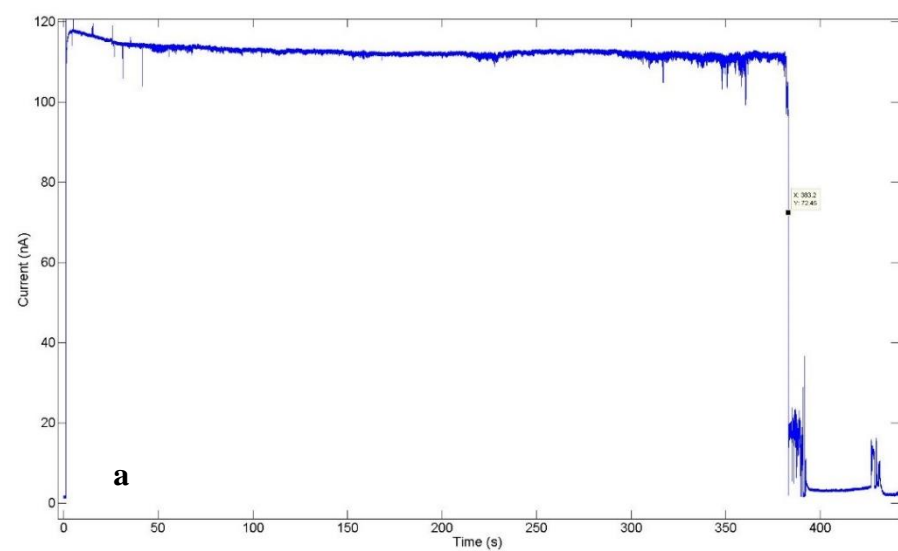
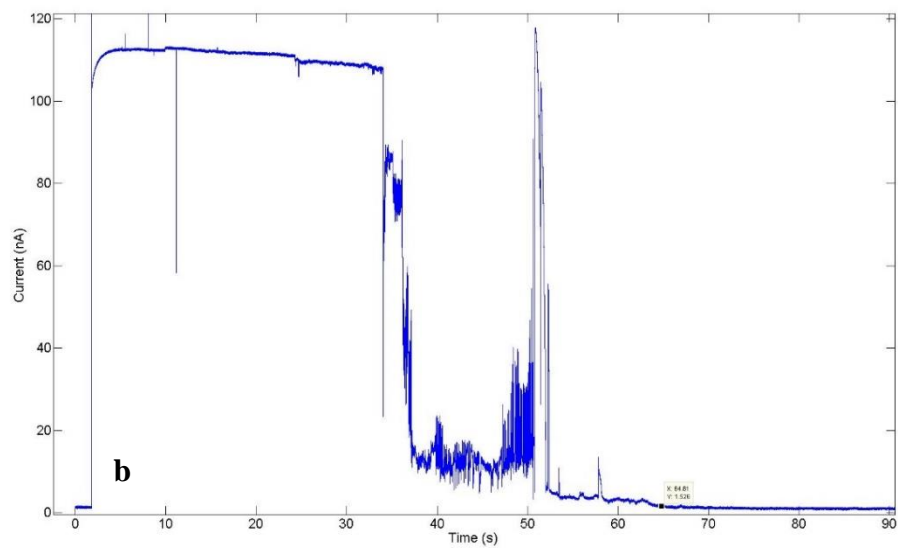
No Additive

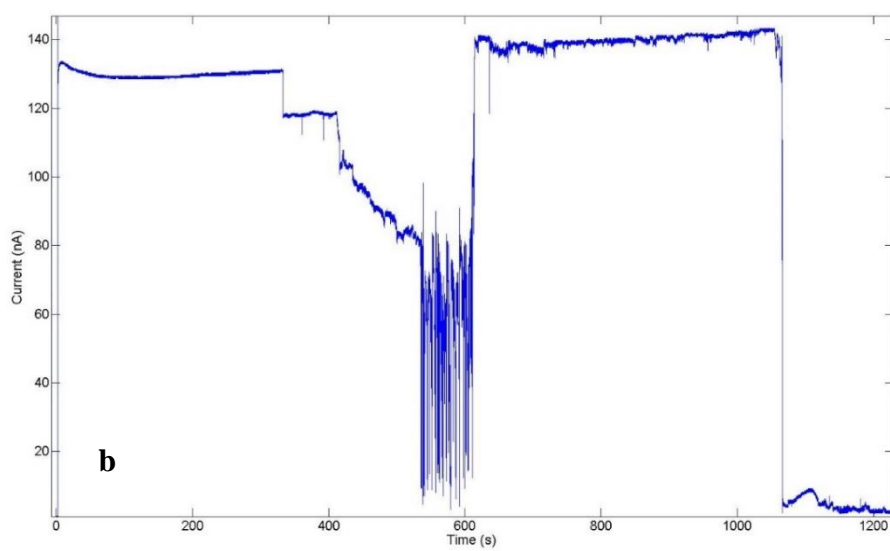
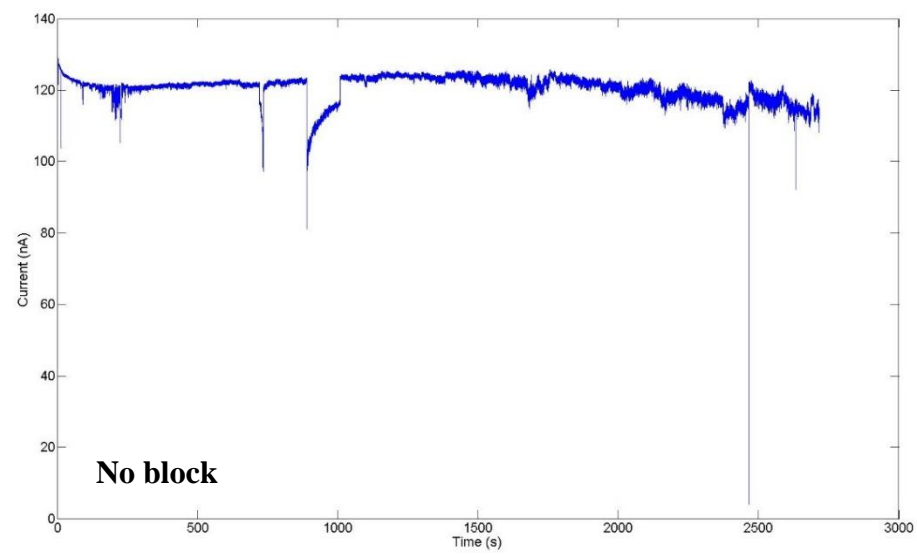
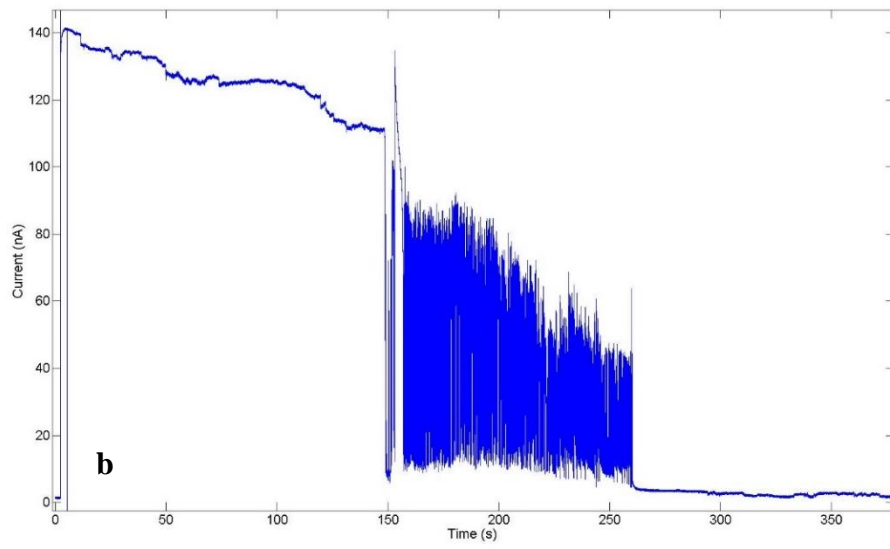


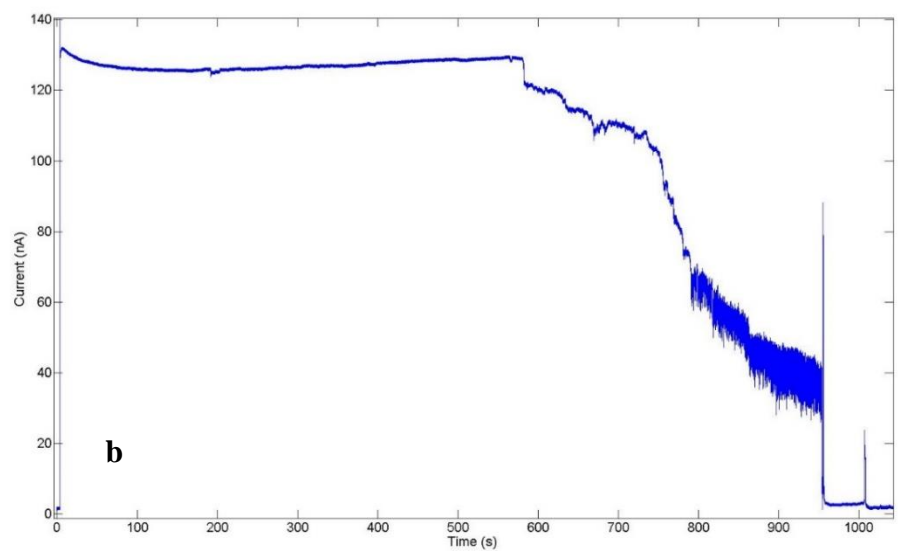
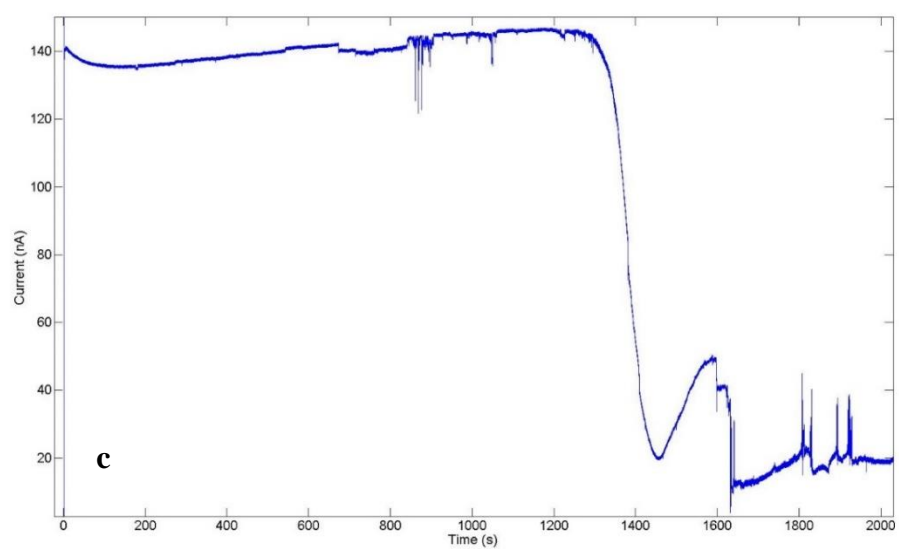
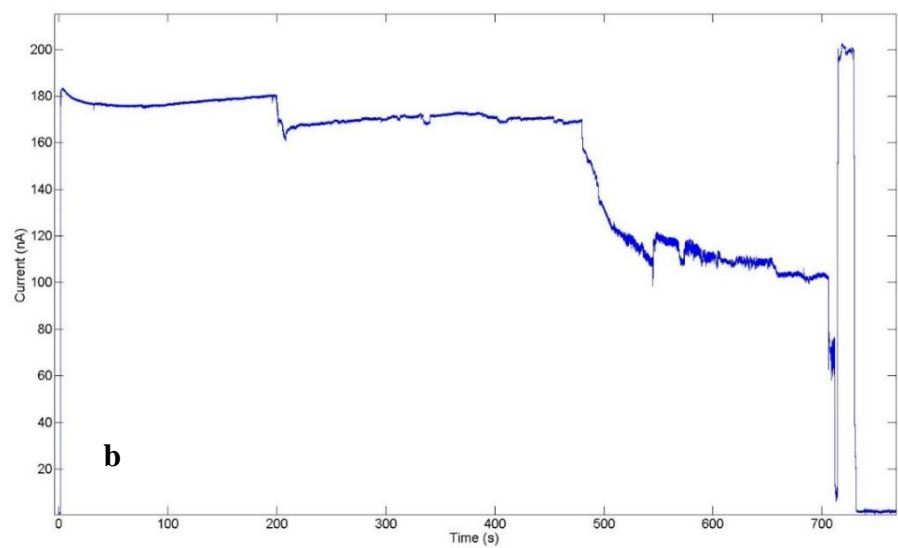


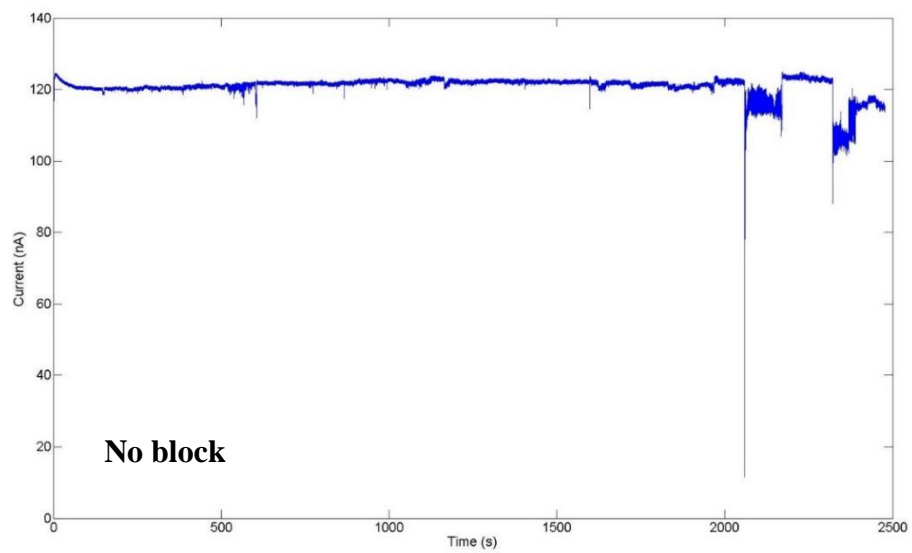
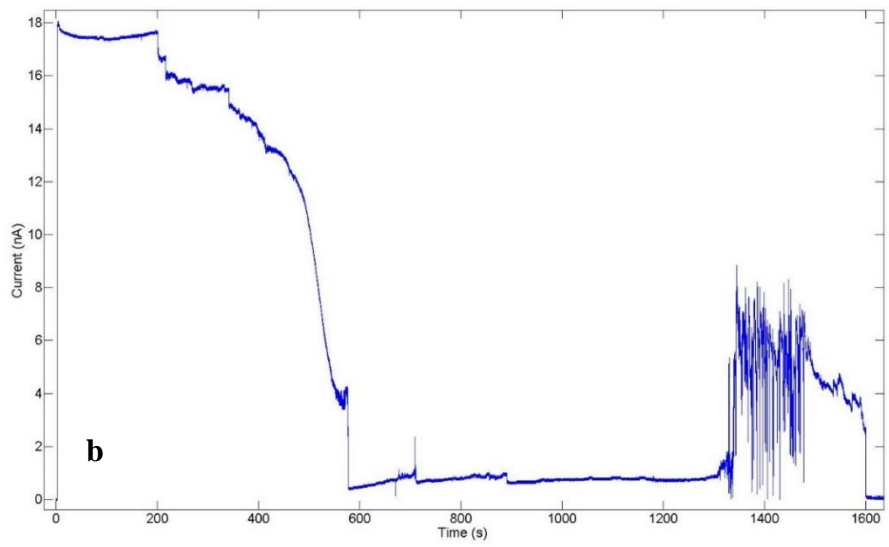
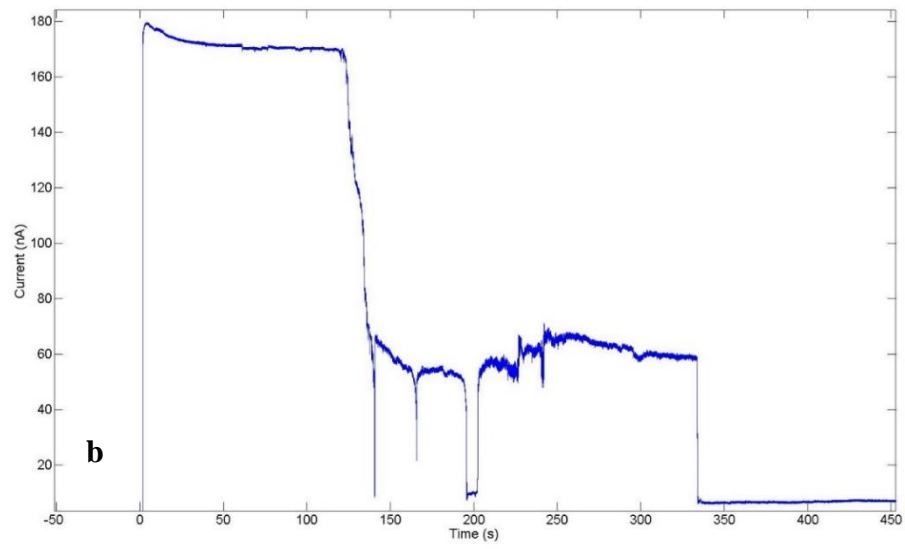




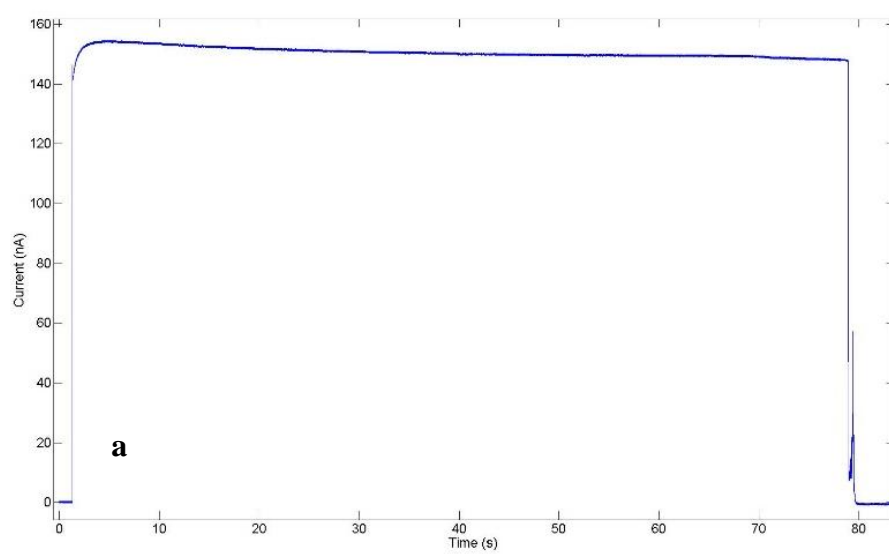
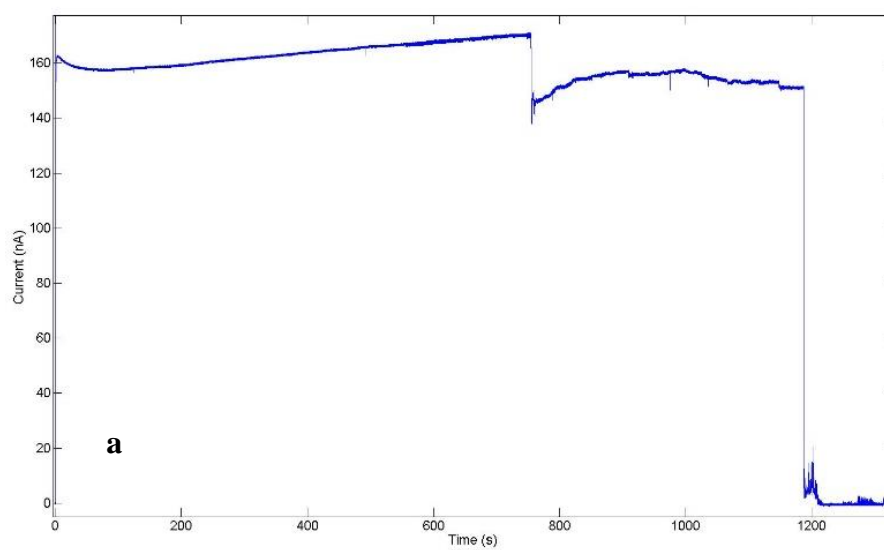


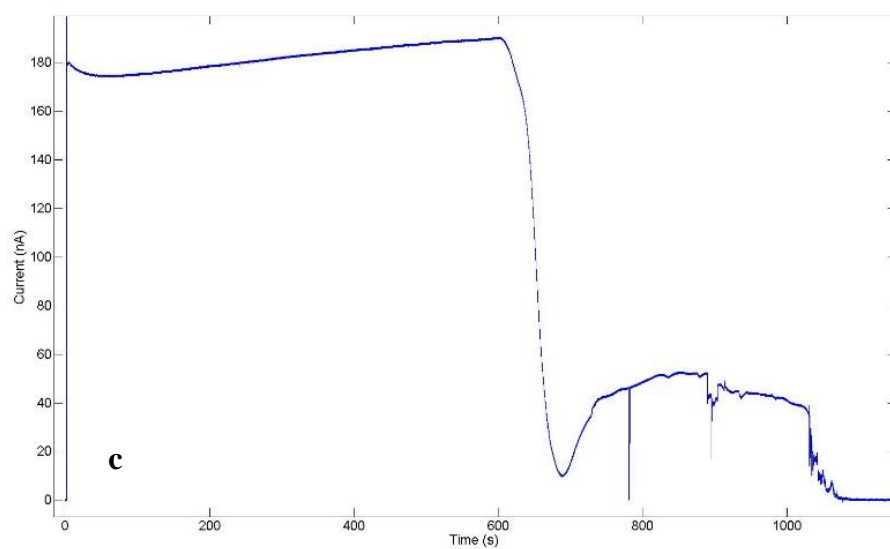
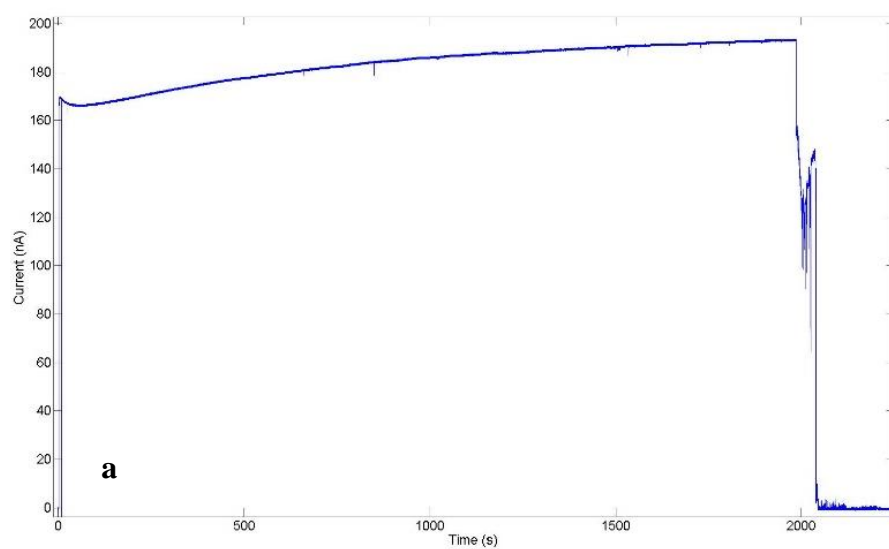
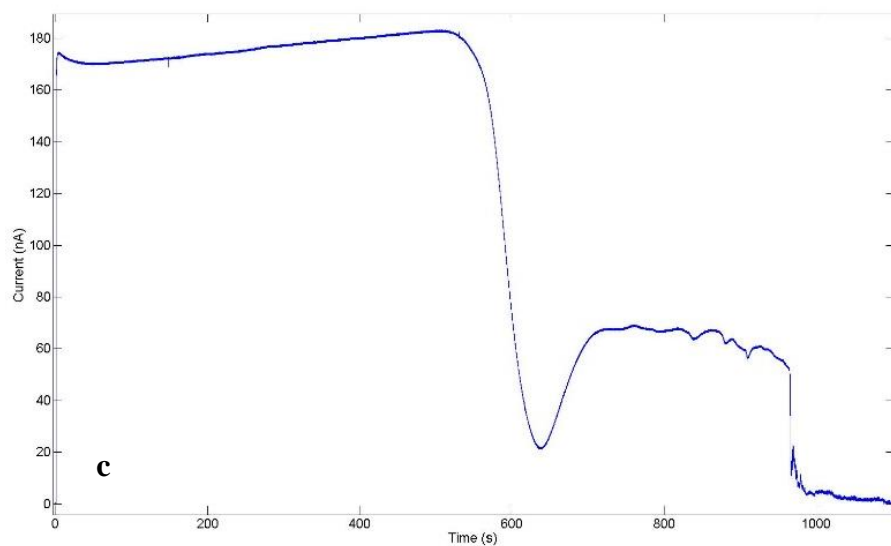


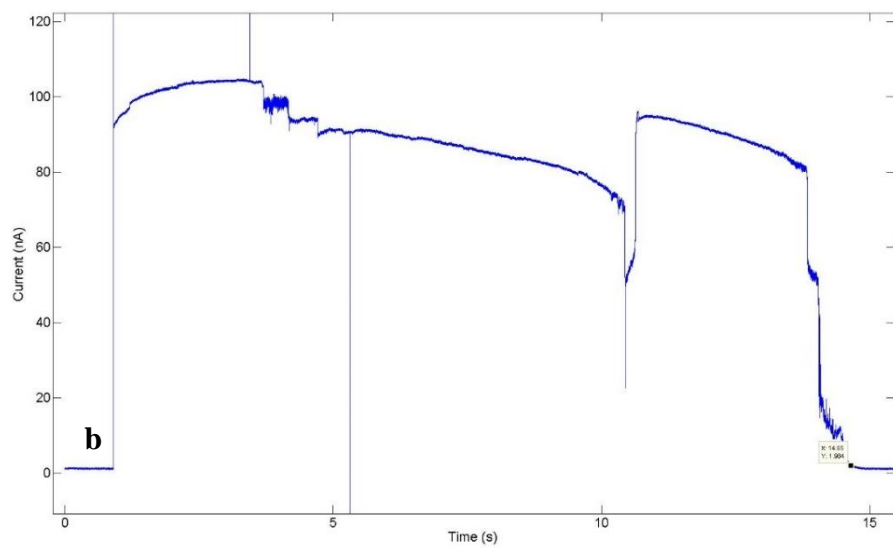
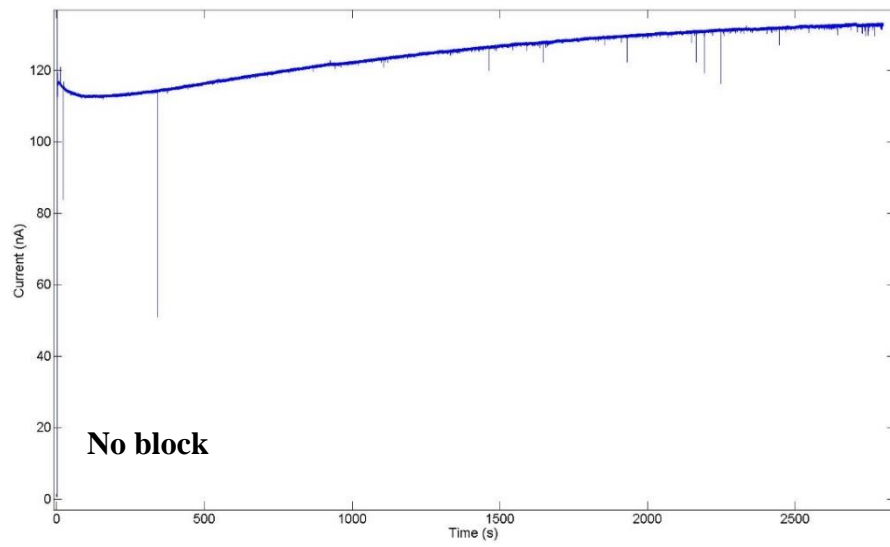
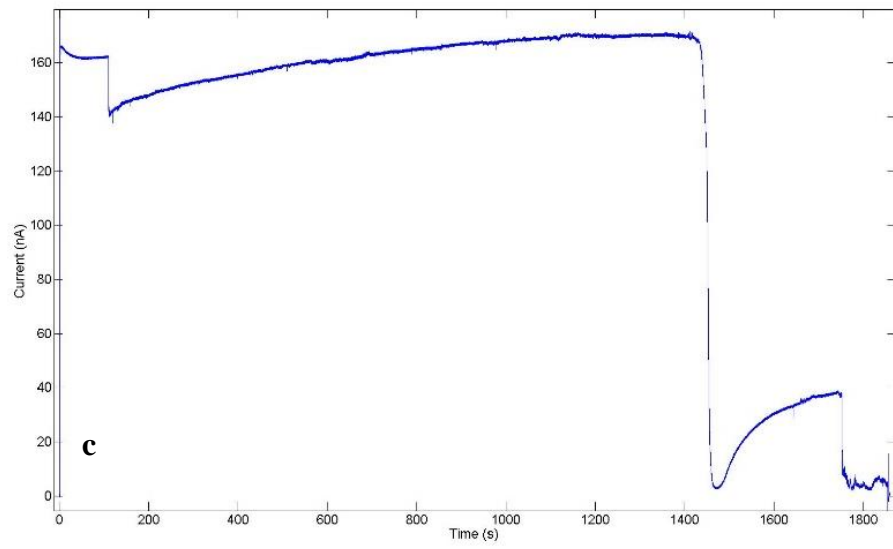


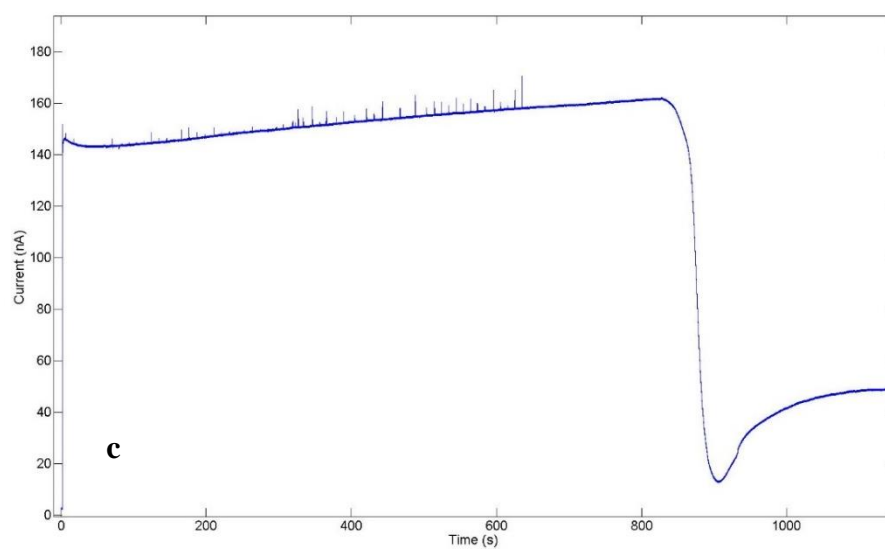
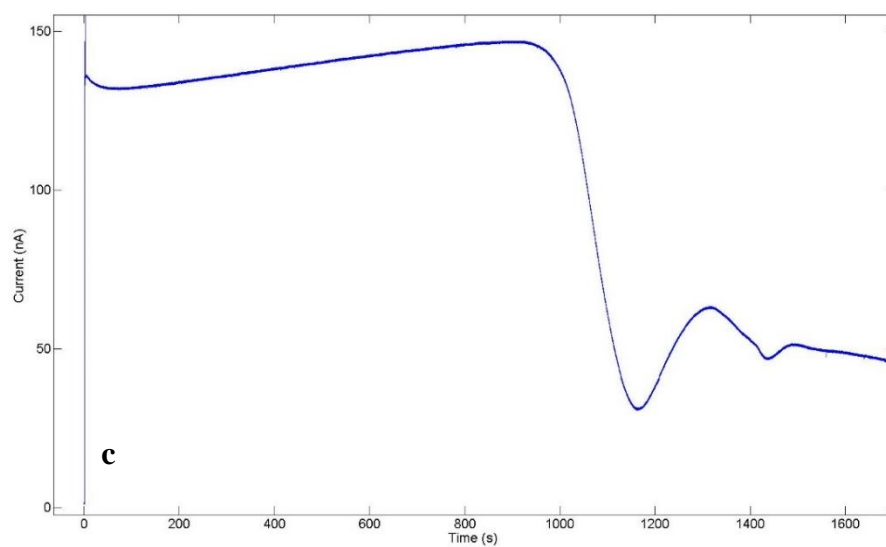
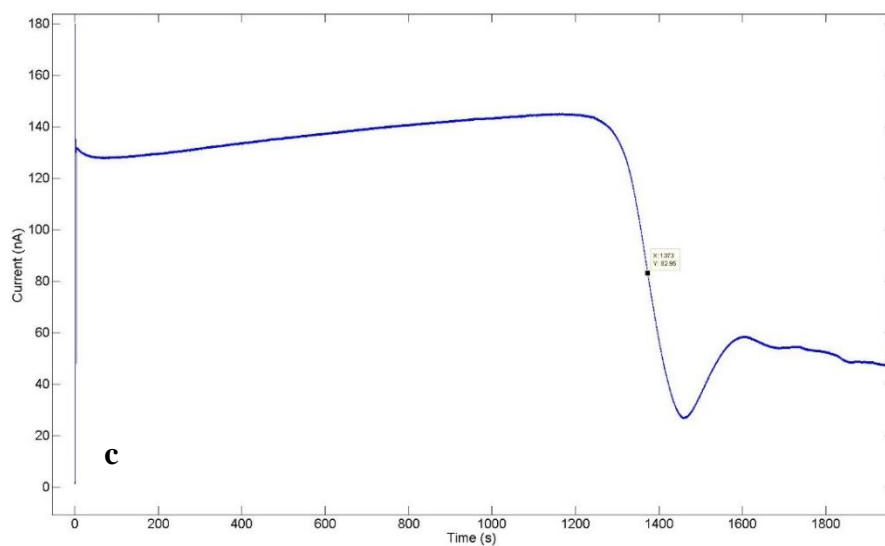


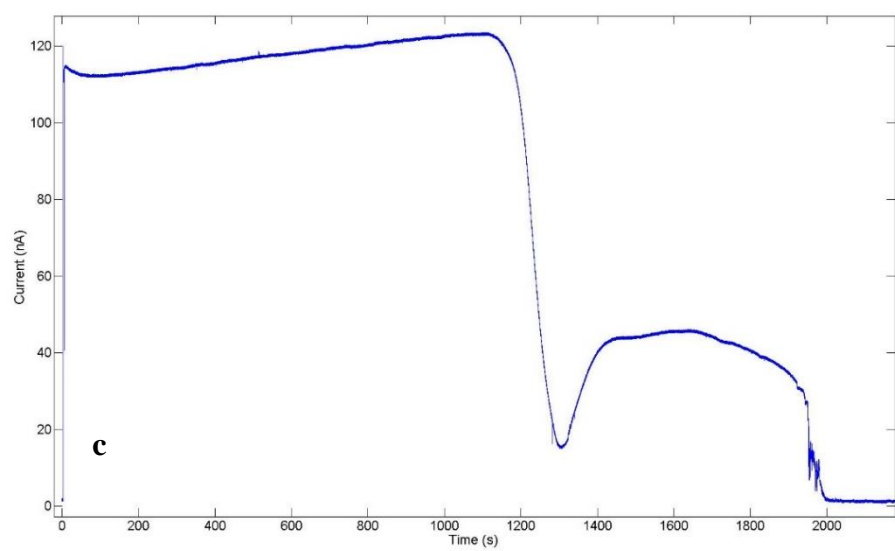
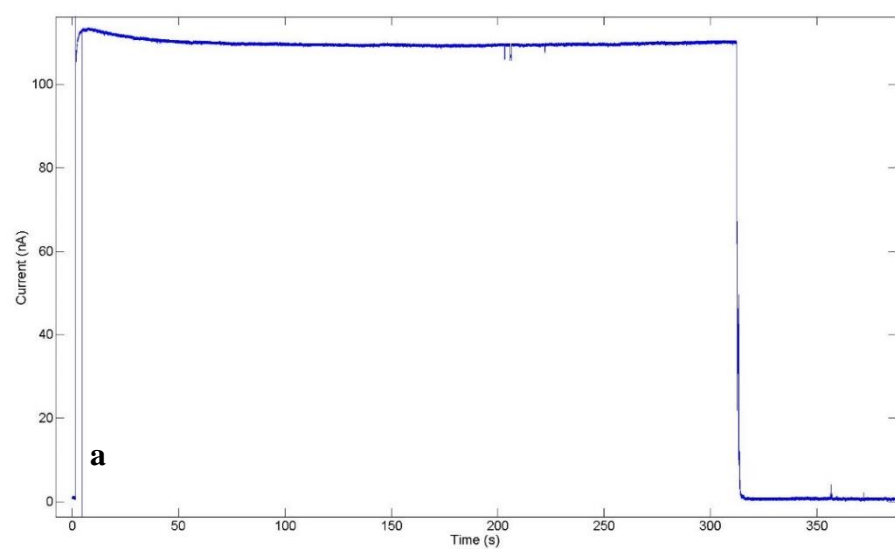
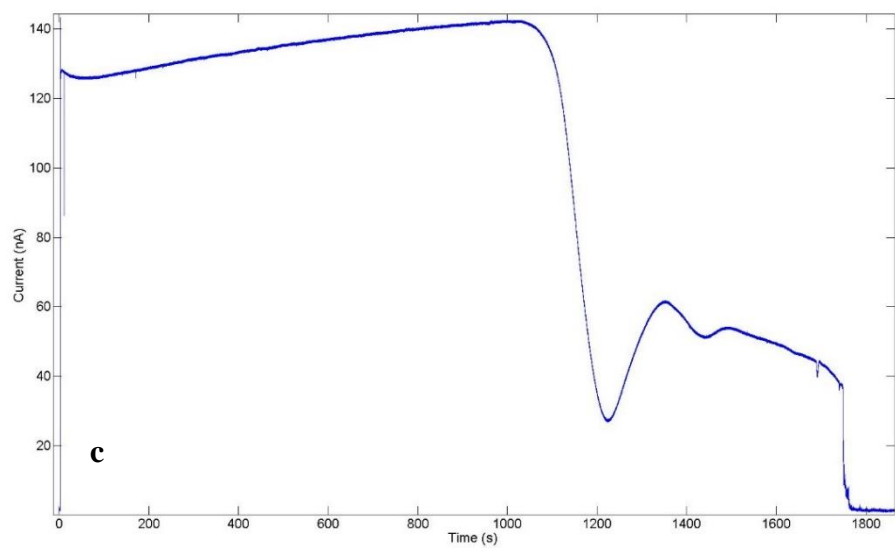
Tartaric Acid

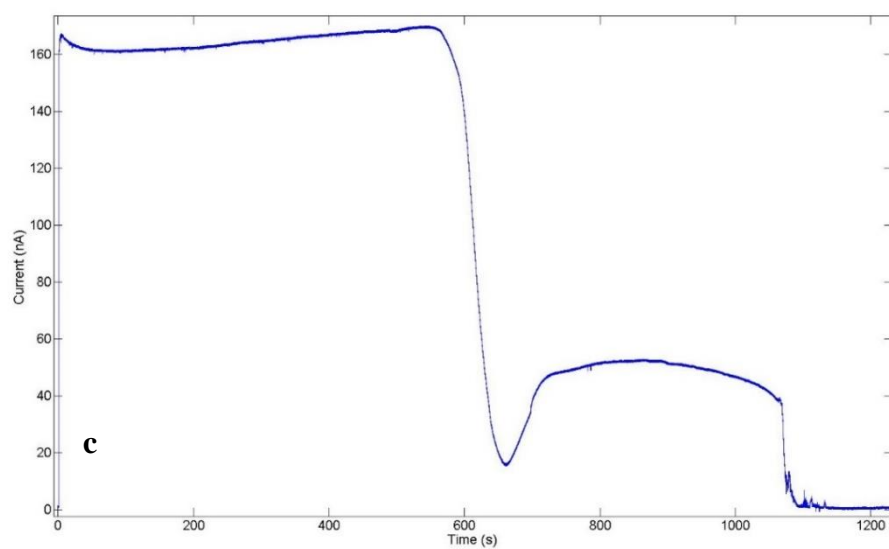
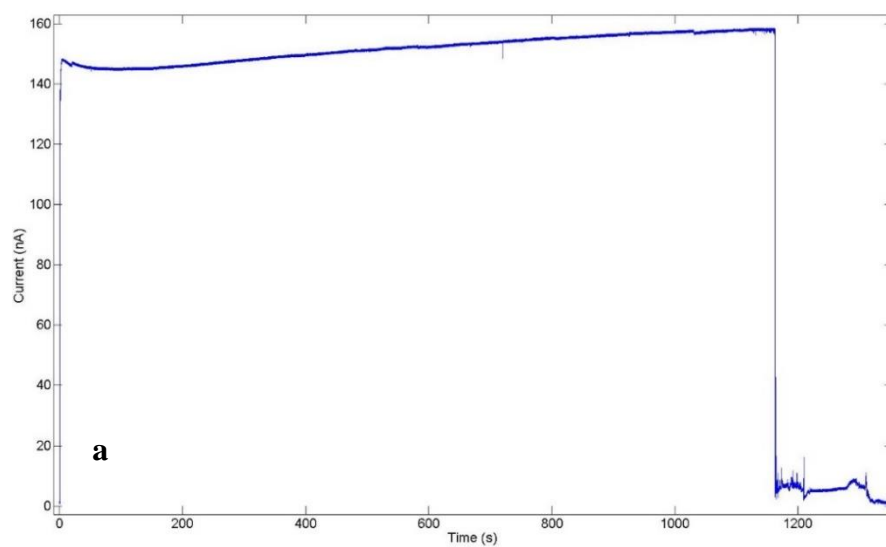
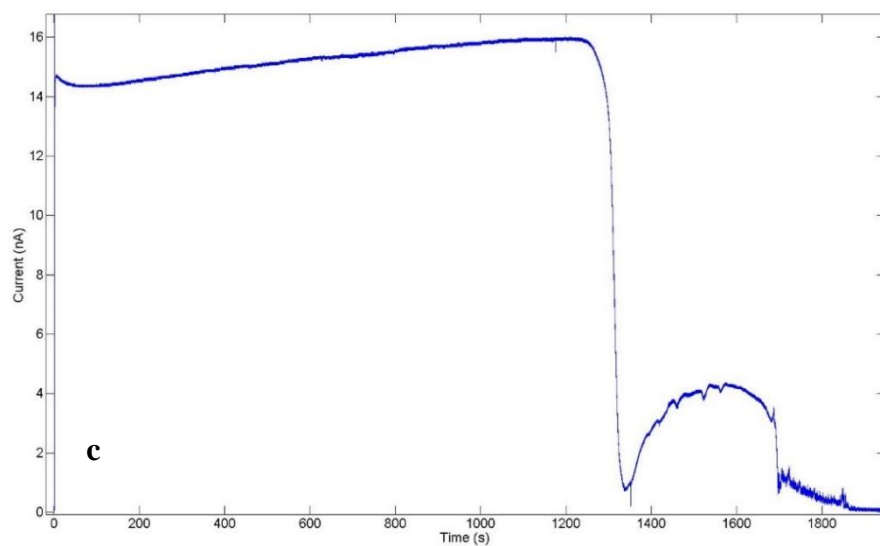


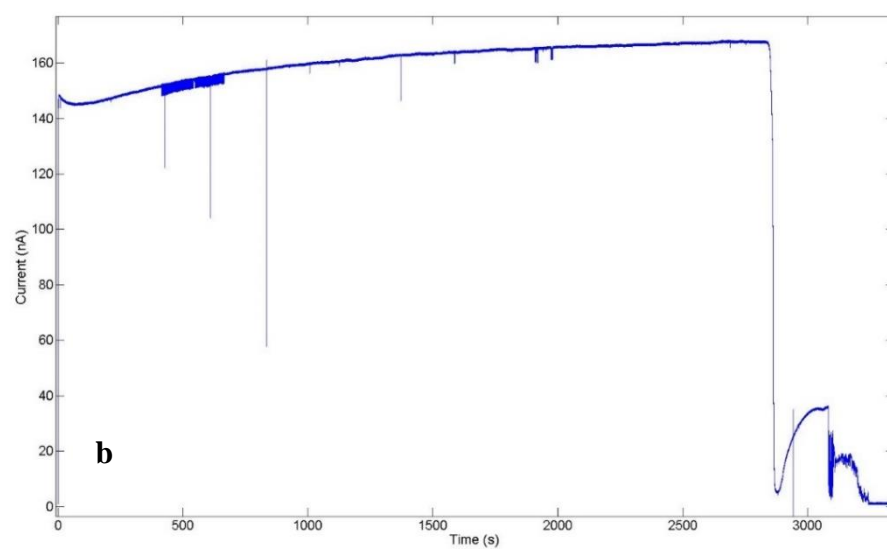
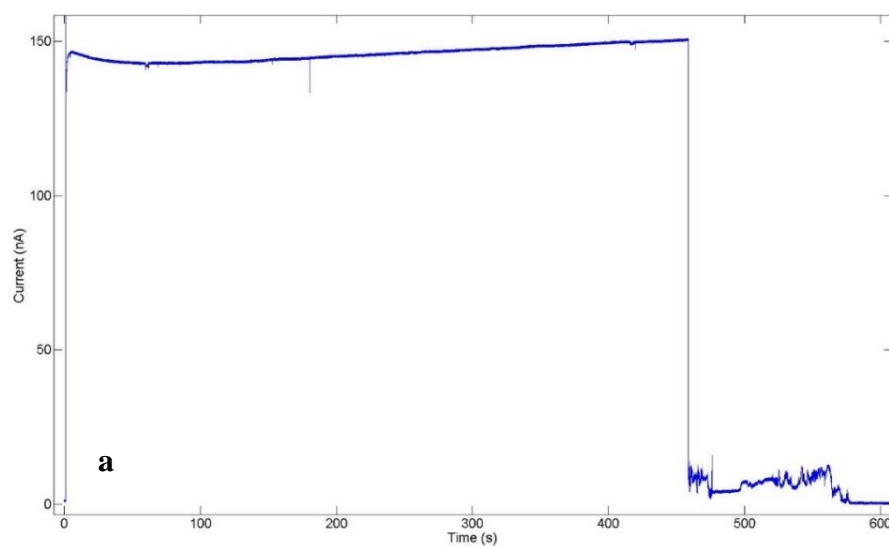
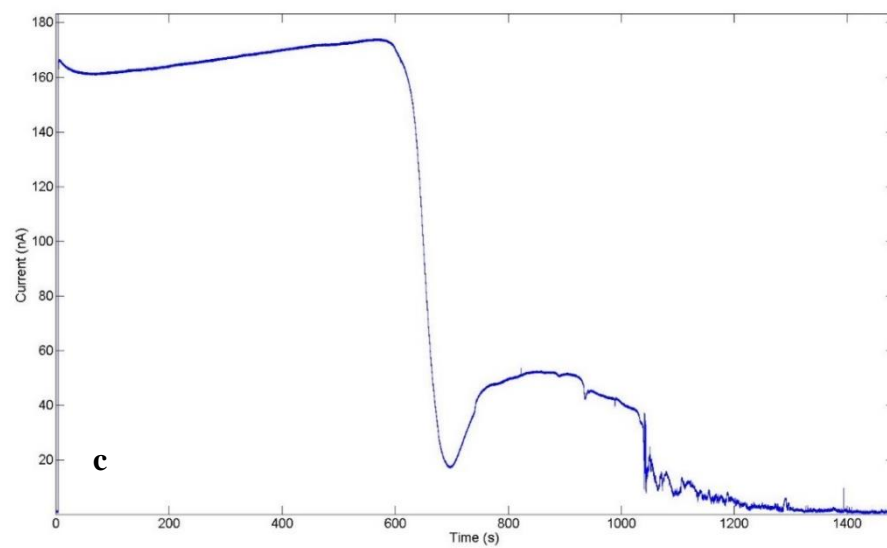


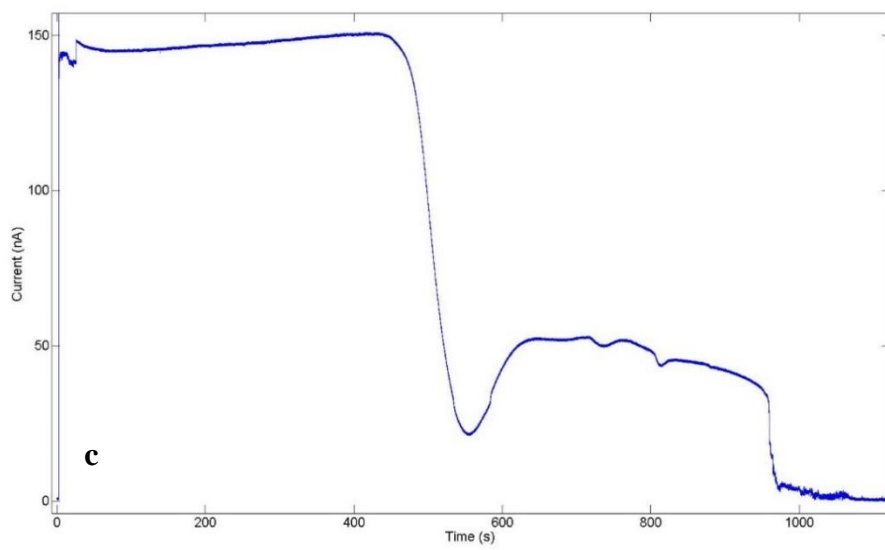
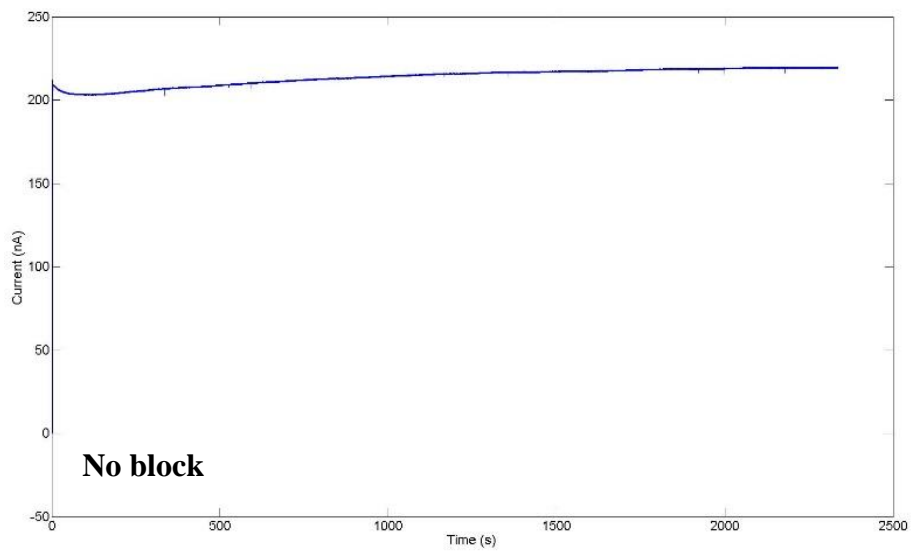
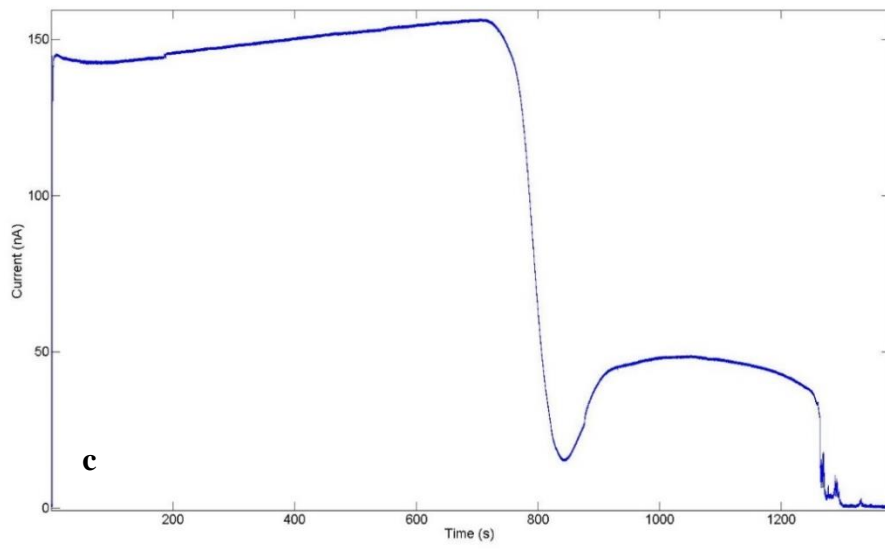




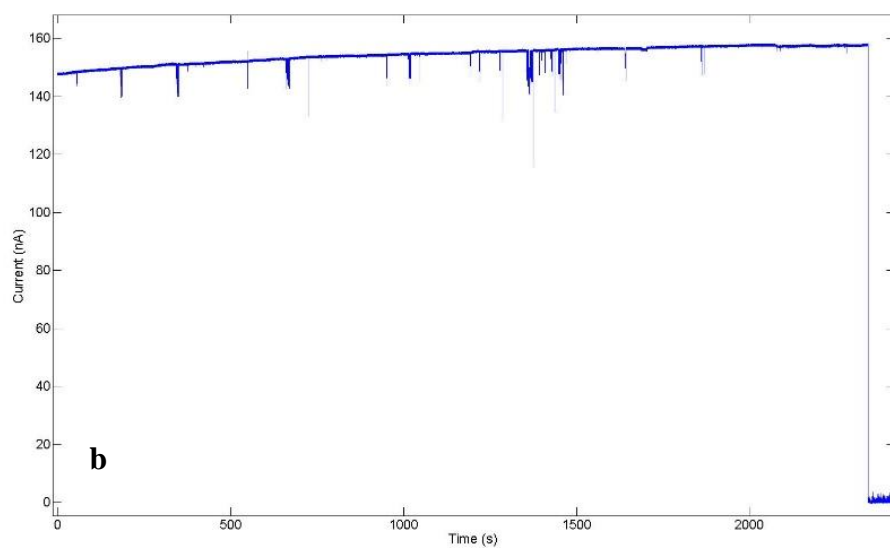
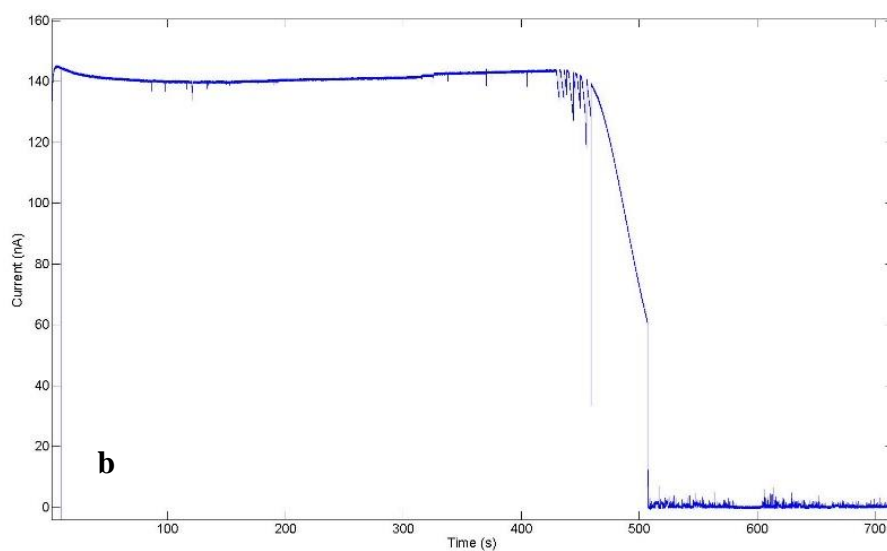


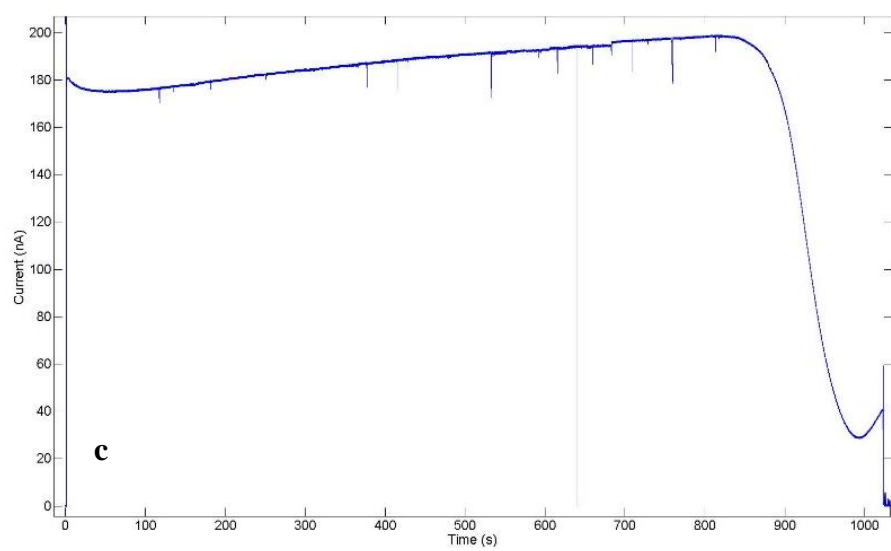
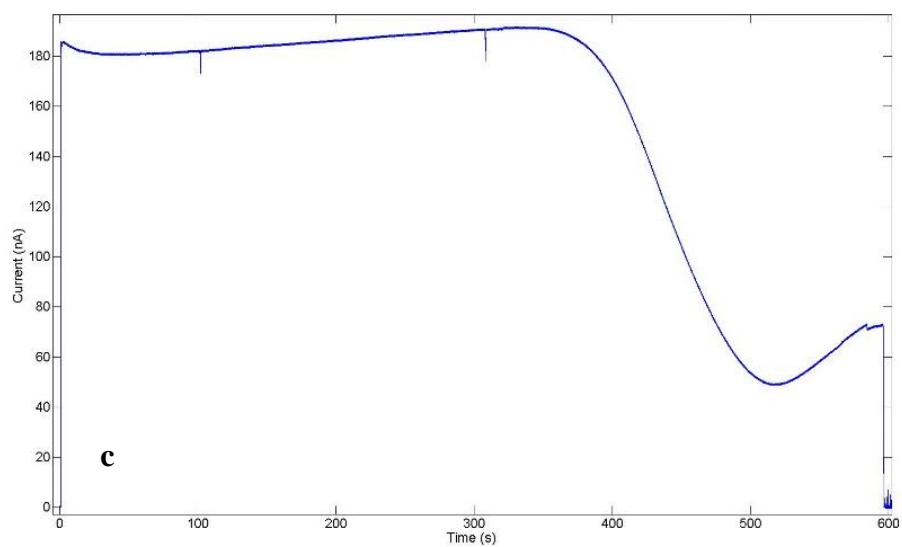
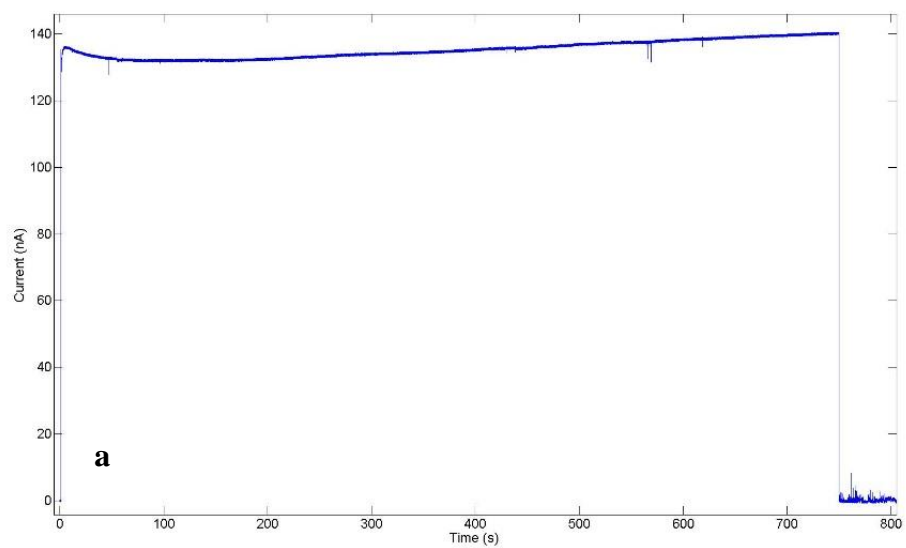


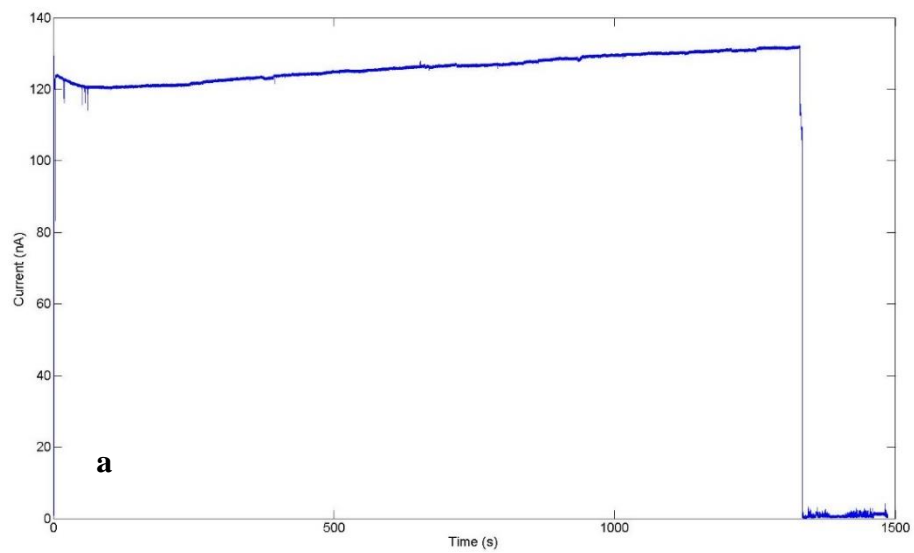
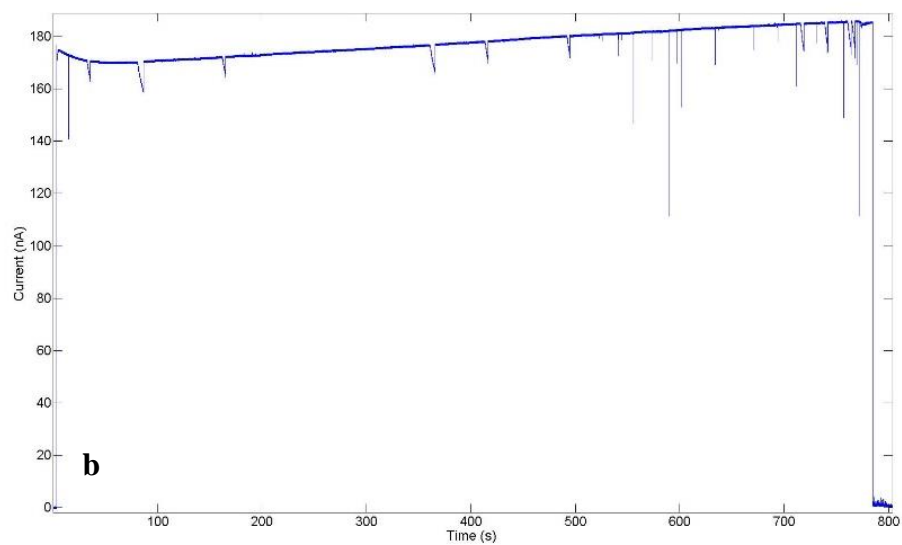
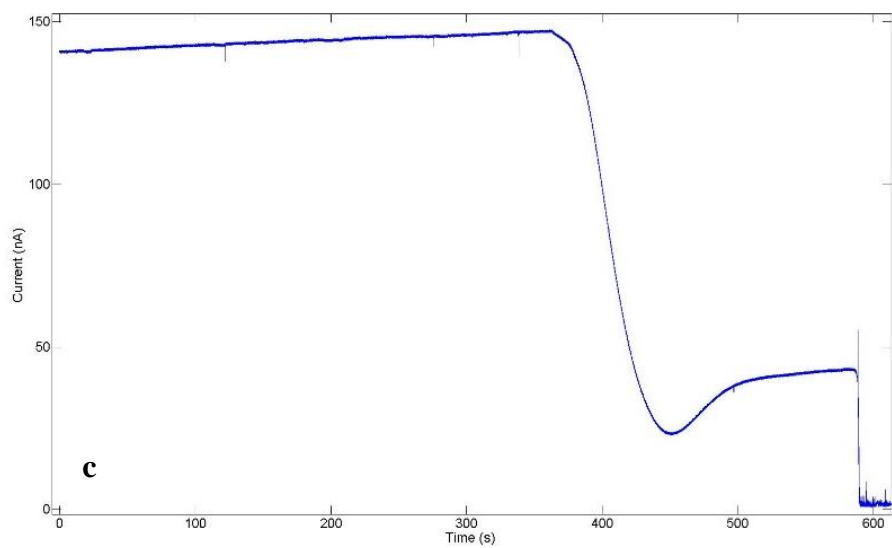


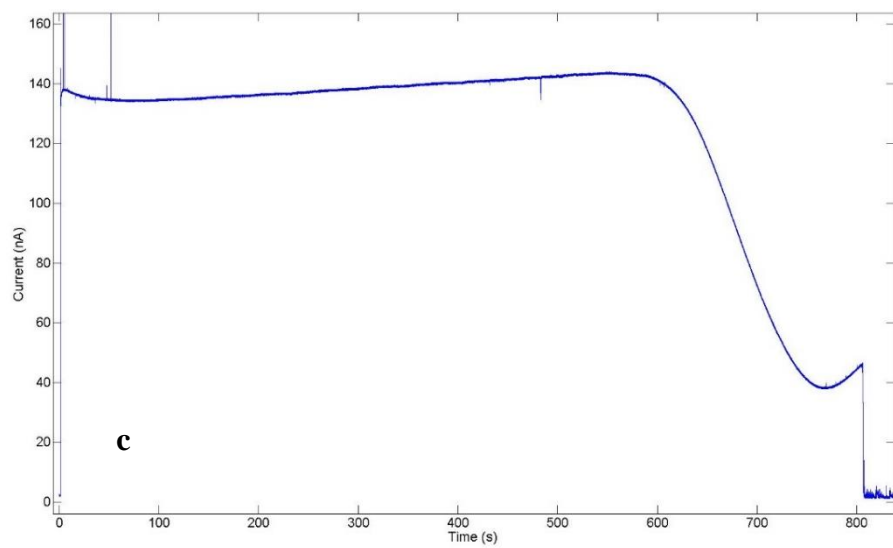
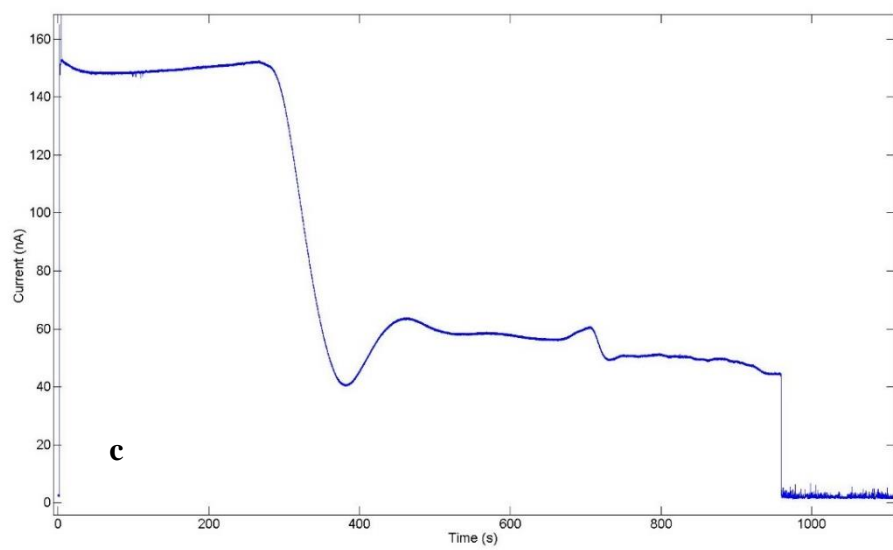
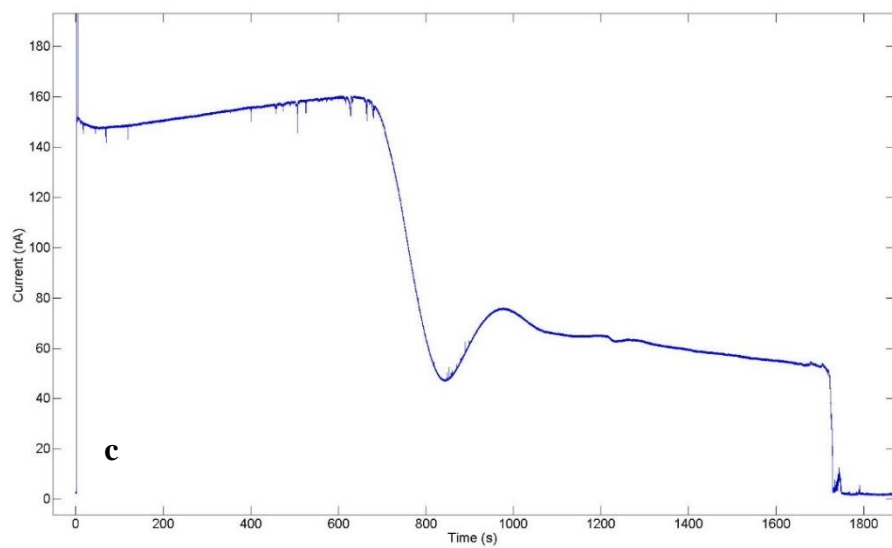


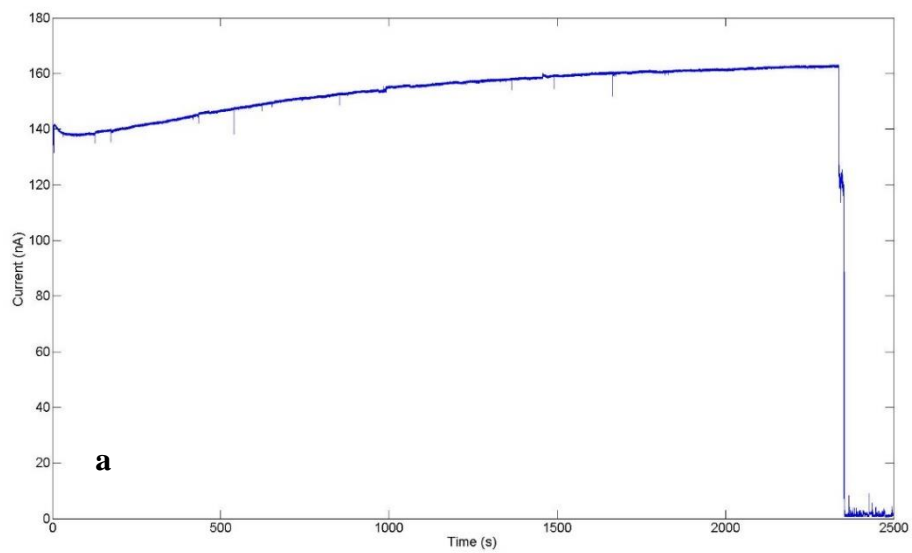
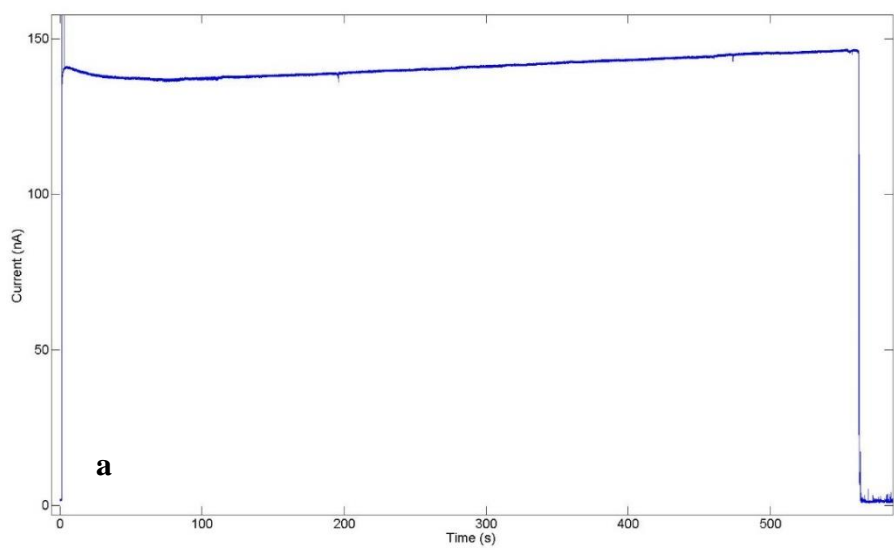
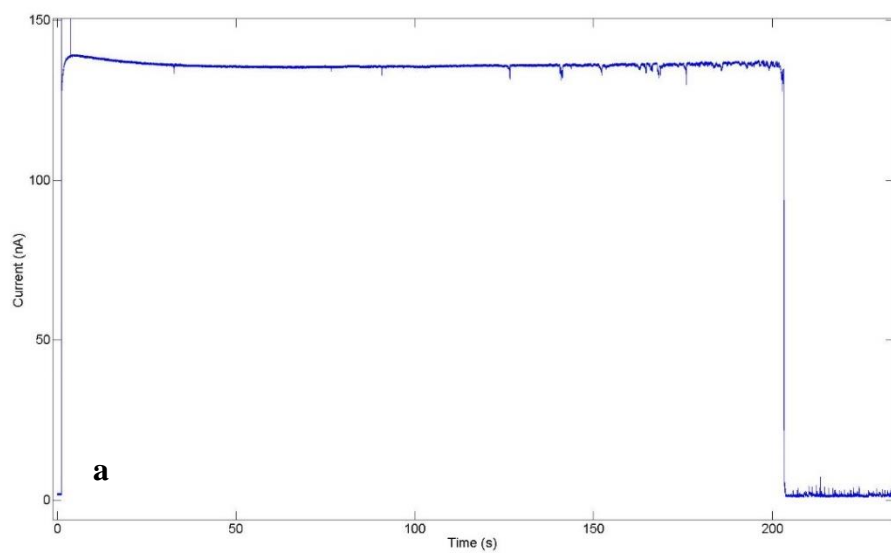
STMP

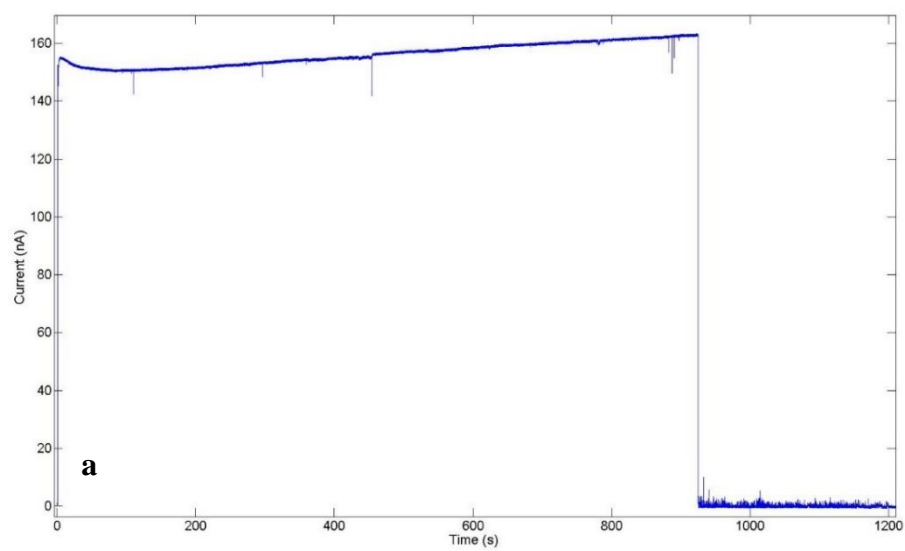
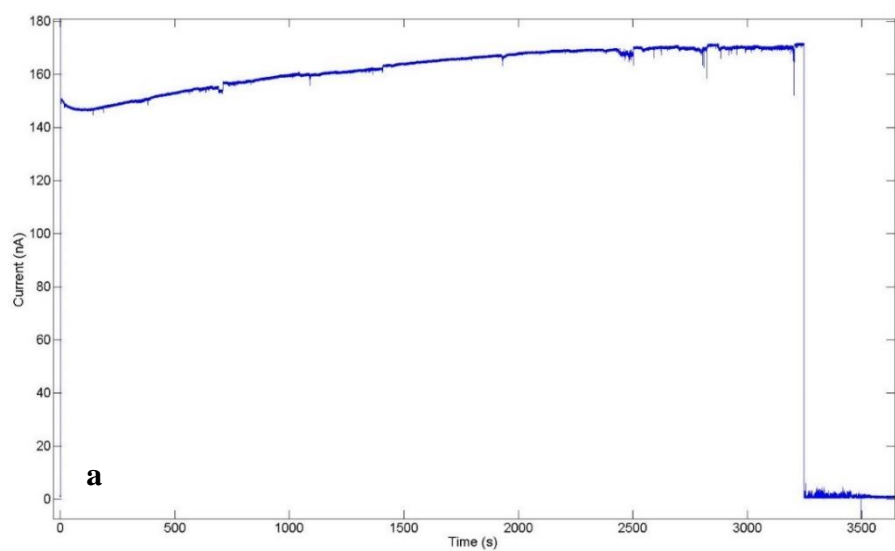
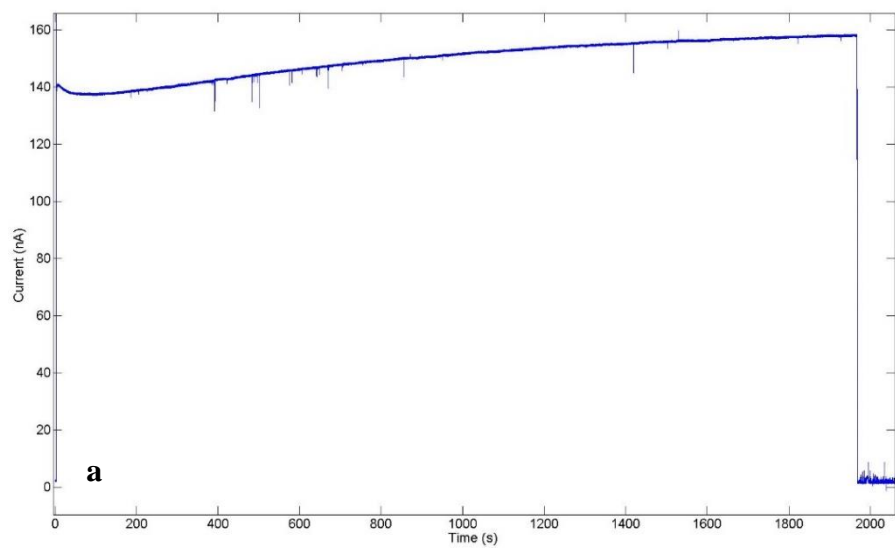


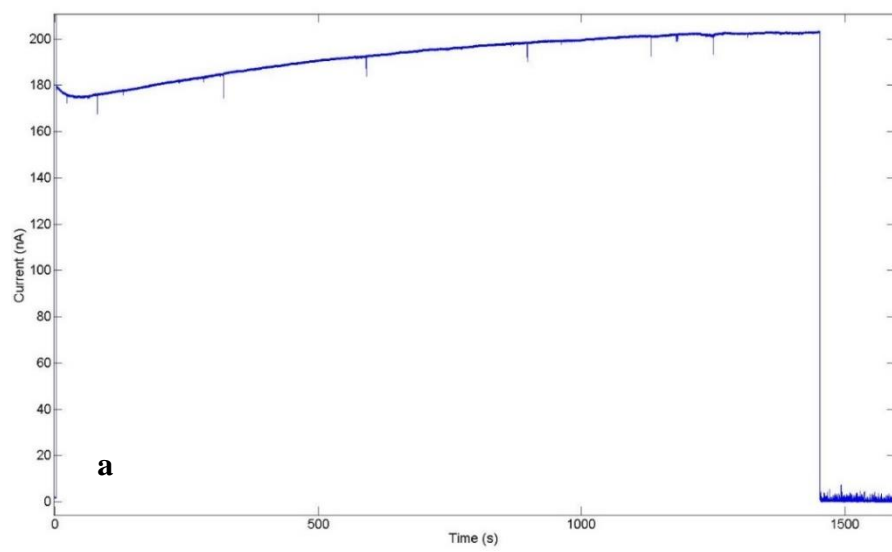
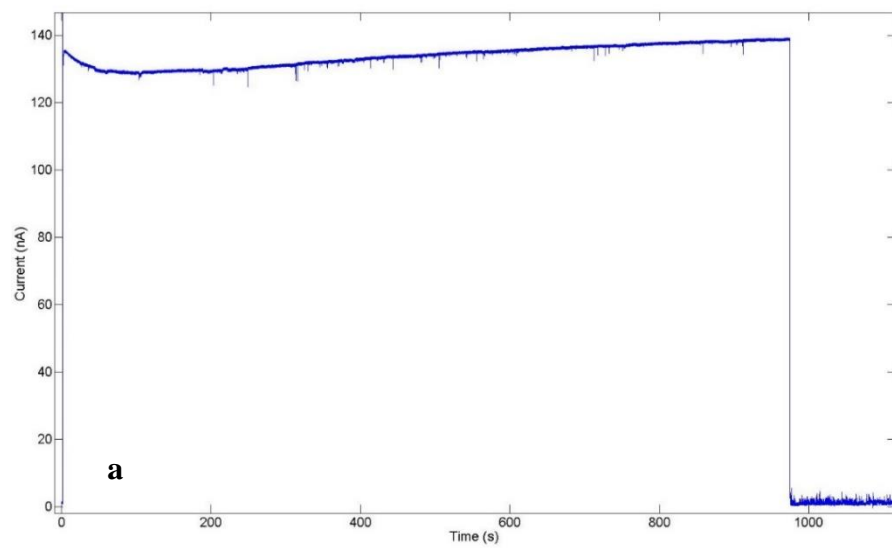
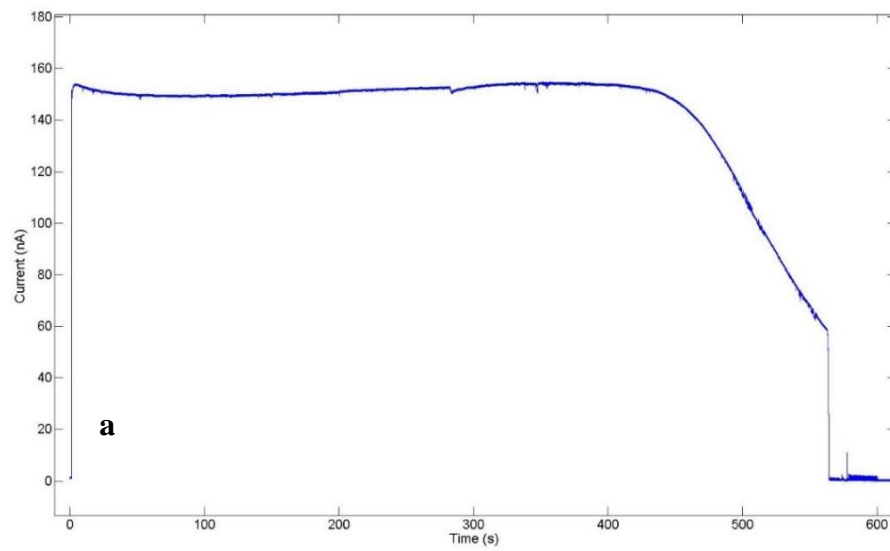


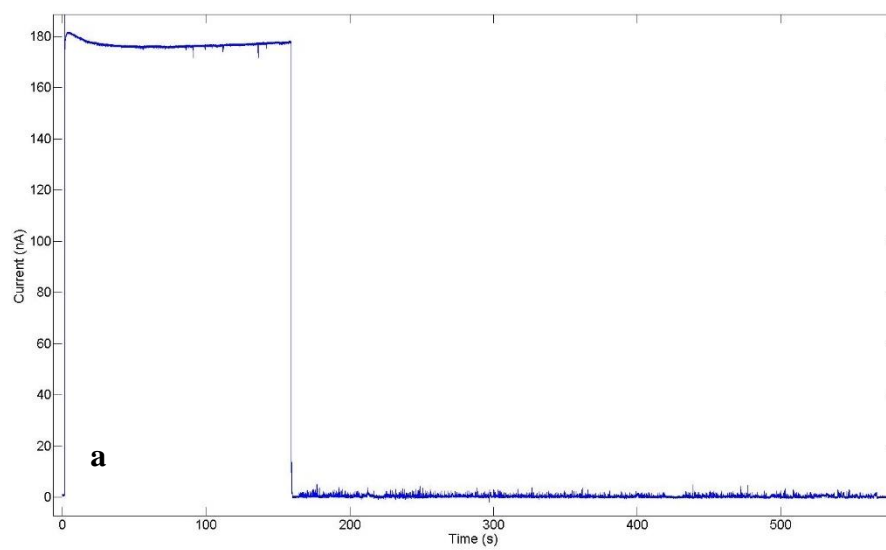
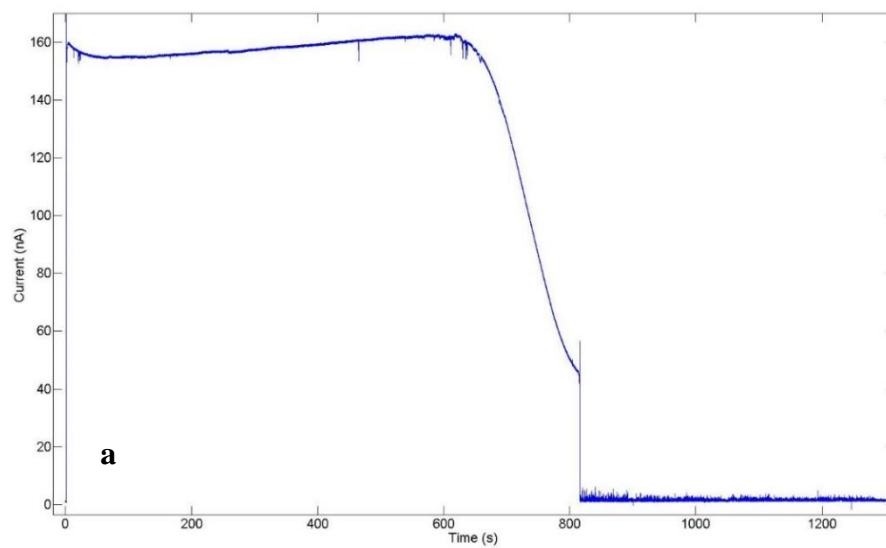




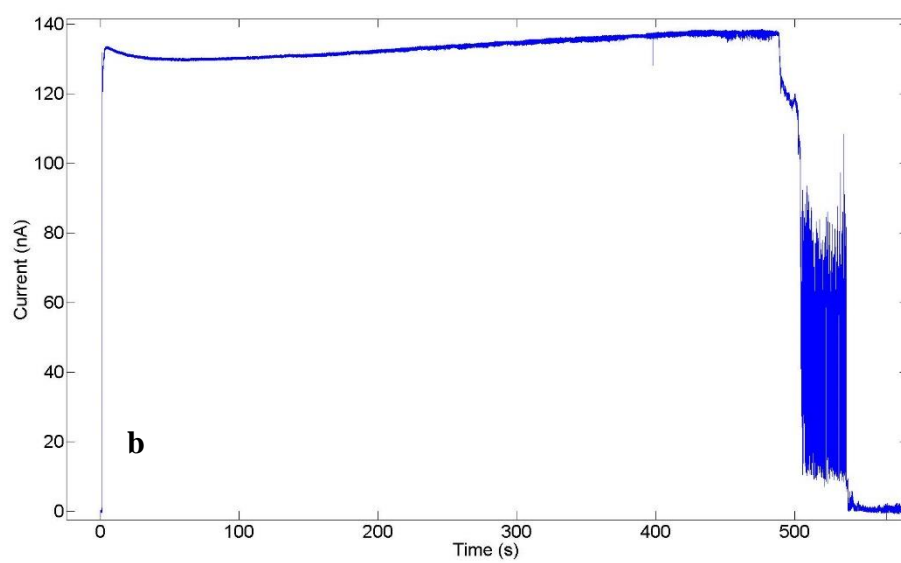
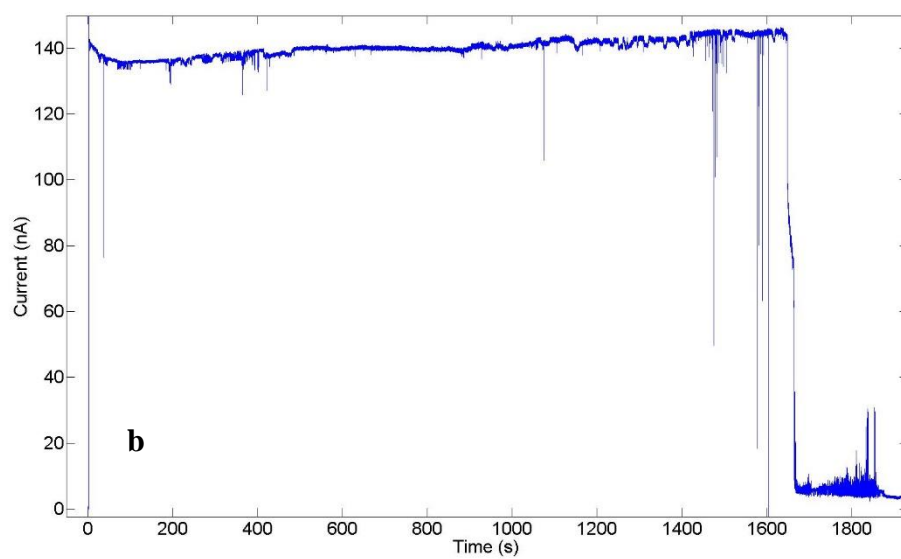


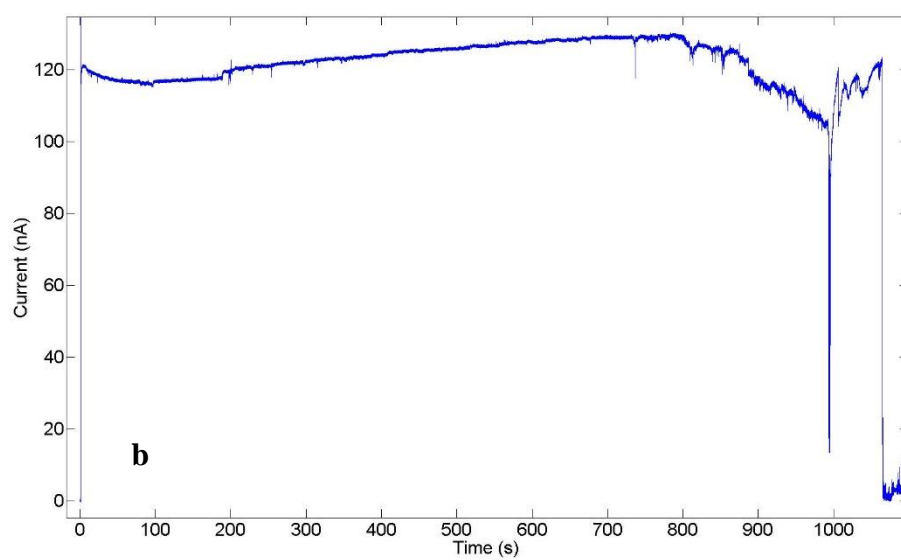
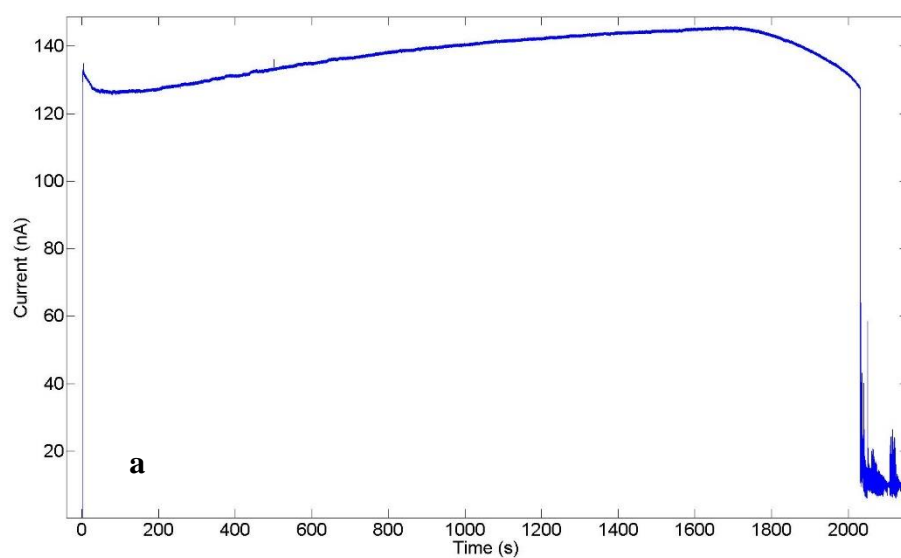
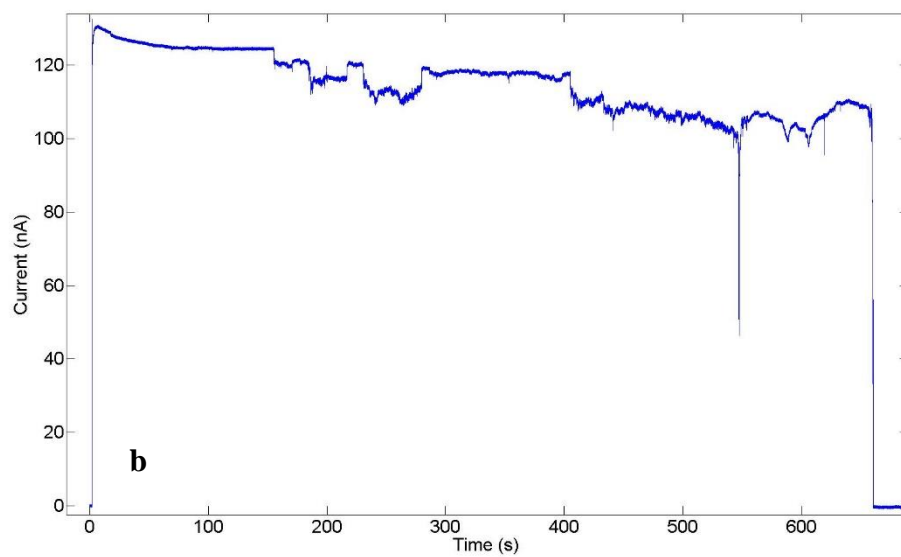


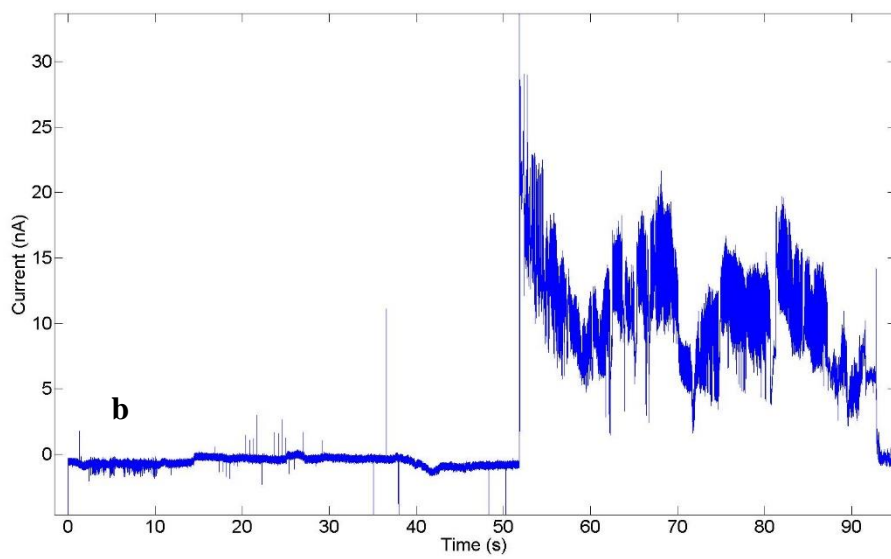
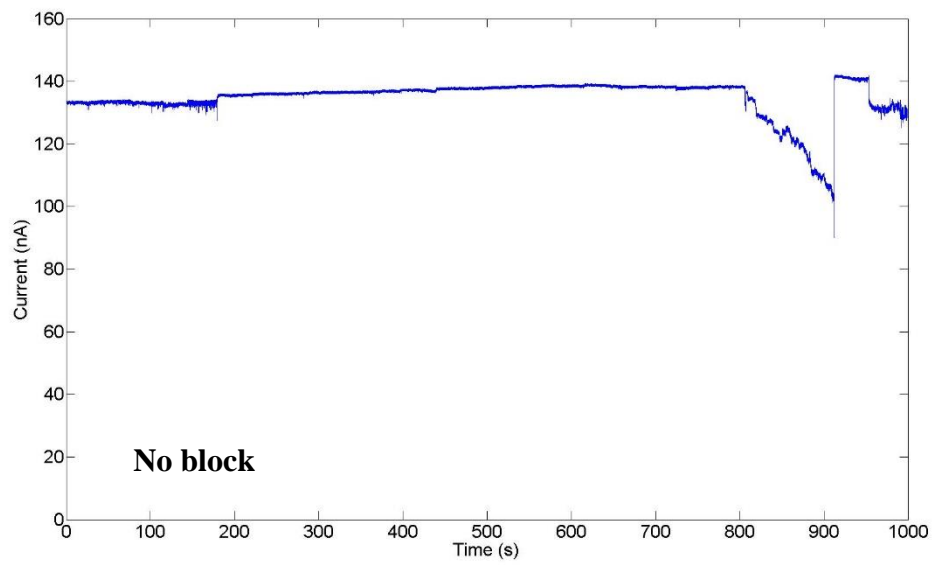
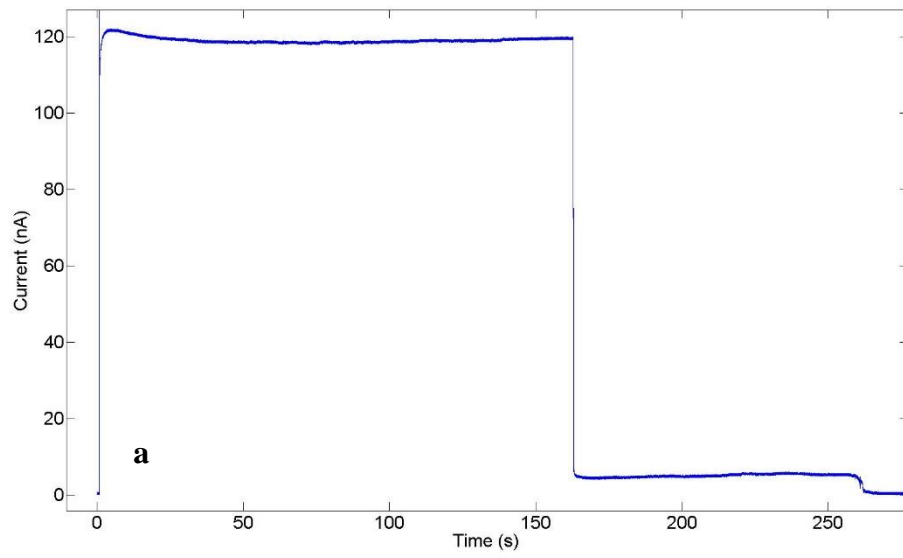


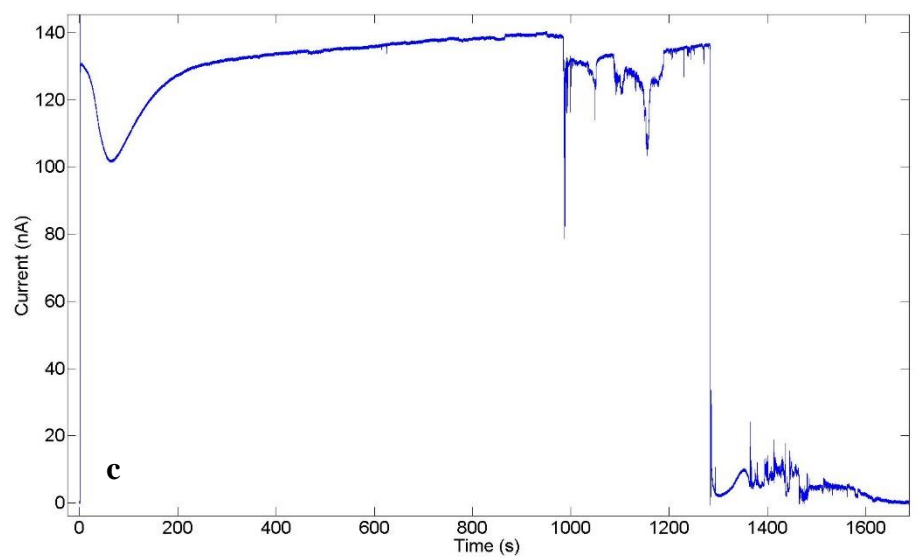
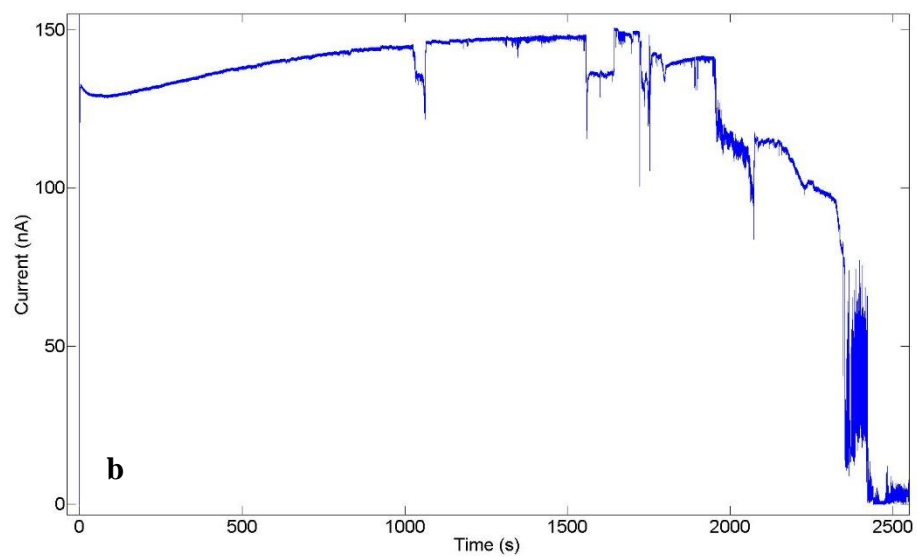


Boric Acid

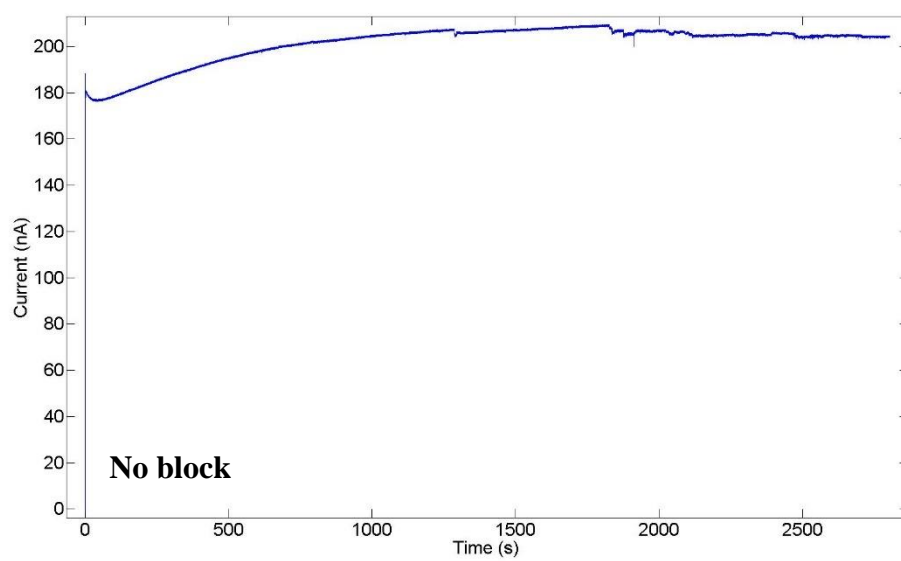
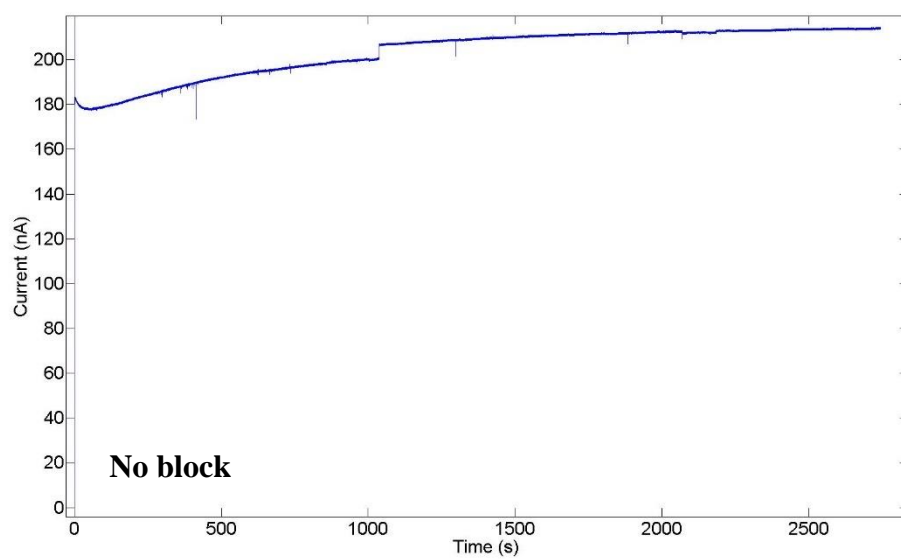


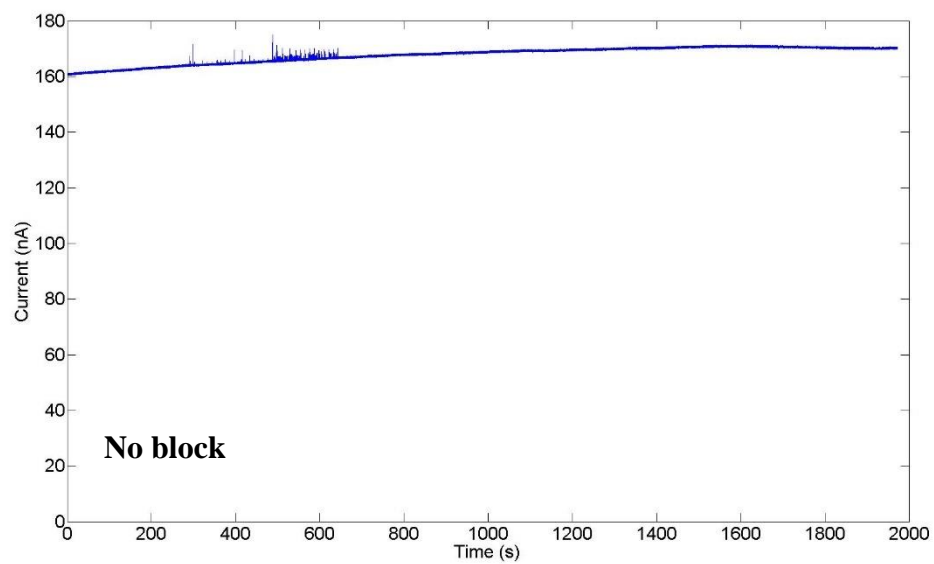
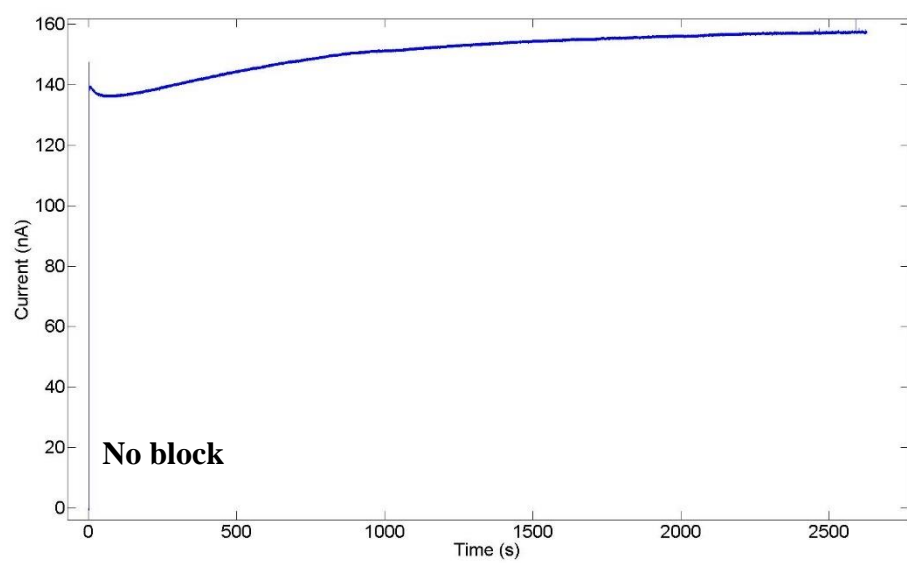
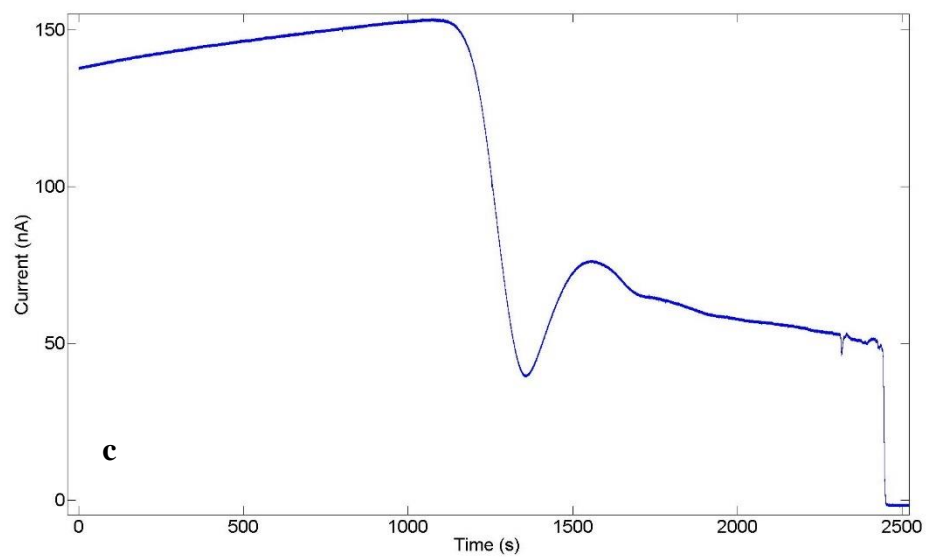


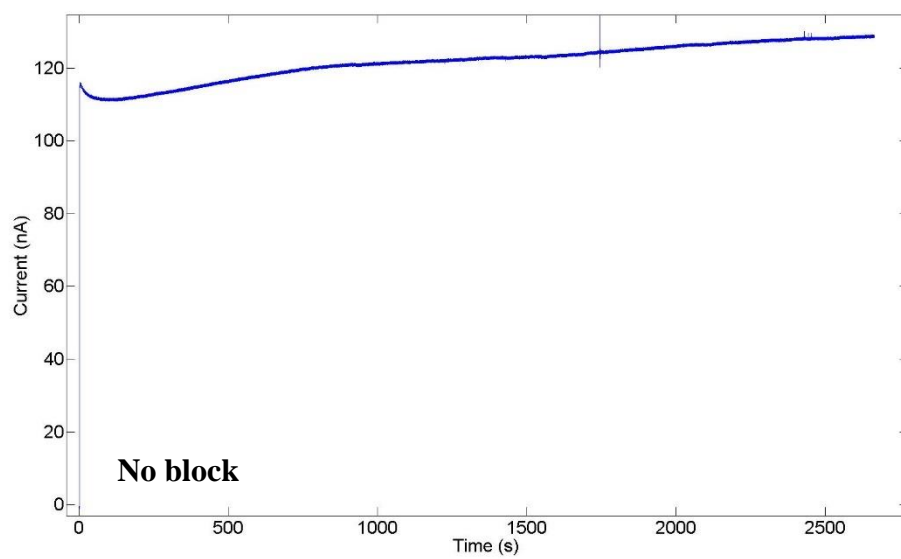
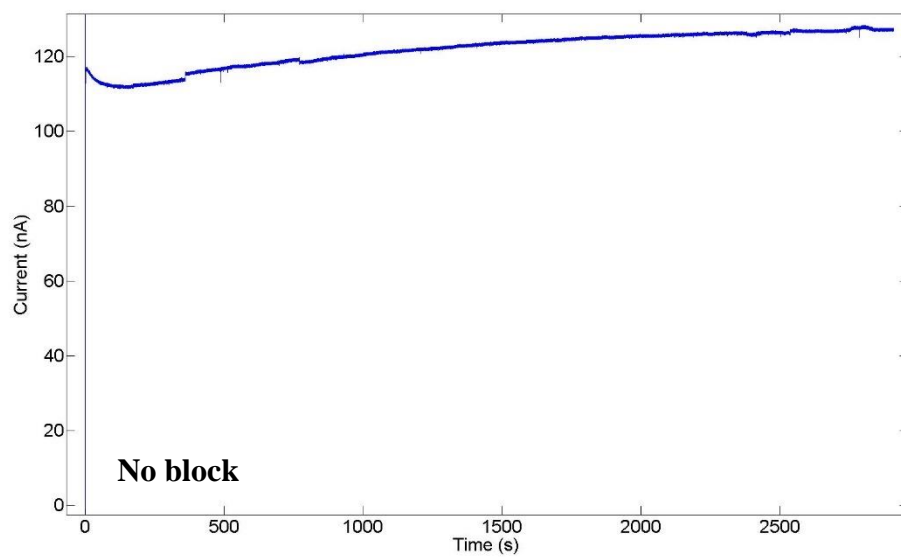




Gallic Acid







Ascorbic Acid

